GEOLOGY, PETROGRAPHY, AND GEOCHEMISTRY OF FISHER PROPERTY ROCKS AND THEIR ALTERED EQUIVALENTS, AND RELATIONSHIP TO AURIFEROUS QUARTZ VEINS, GLENNIE DOMAIN, NORTHERN SASKATCHEWAN

A Thesis Submitted to the College of
Graduate and Postdoctoral Studies In
Partial Fulfillment of the
Requirements For the Degree of
Master of Science in the Department of
Geological Sciences
University of Saskatchewan
Saskatoon

By
COURTNEY CAROL ONSTAD

PERMISSION TO USE

In presenting this thesis in partial fulfillment of the requirement of a Postgraduate degree from the University of Saskatchewan, I agree that the Libraries of this University may make it freely available for inspection. I further agree that permission for copying of this thesis in any manner, in whole or in part, for scholarly purposes may be granted by the professor or professors who supervised my thesis work or, in their absence, by the Head of the Department of Geological Sciences or the Dean of the College of Graduate and Postdoctoral Studies. It is understood that any copying, publication or use of this thesis or parts thereof for financial gain shall not be allowed without my written permission. It is also understood that due recognition shall be given to me and to the University of Saskatchewan in any scholarly use which may be made of any material in my thesis.

Requests for permission to copy or to make other uses of materials in this thesis in whole or part should be addressed to:

Head
Department of Geological Sciences
University of Saskatchewan
114 Geology Building, 114 Science Place
Saskatoon, Saskatchewan S7N 5E2
Canada

Dean
College of Graduate and Postdoctoral Studies
University of Saskatchewan
116 Thorvaldson Building, 110 Science Place
Saskatoon, Saskatchewan S7N 5C9
Canada

ABSTRACT

The Fisher property is part of the Seabee Gold Operation in northern Saskatchewan, which also includes the active Santoy mine and the recently decommissioned Seabee mine. These Paleoproterozoic orogenic gold deposits are hosted by secondary shear zones in the Pine Lake greenstone belt of the Glennie Domain. This region has a complex geological history related to accretionary episodes during the development of the Reindeer zone of the larger Trans-Hudson Orogen. The structures and lithological units, which host the Santoy and Seabee deposits, are interpreted to extend to the Fisher property, located to the southeast of the Santoy mine. However, the characteristics of the supracrustal and intrusive rocks that host the auriferous quartz veins in the Fisher property are not well known. Representative samples of these rocks were collected from 13 drillholes along an 8 km trend of the extension of the Santoy shear zone through the Fisher property. Petrographic, geochemical and mineralogical characteristics were determined for these samples to test their correlation with rocks hosting the Santoy deposit. The host rocks are dominated by transitional to calc-alkaline basalts to dacites, with associated intrusive rocks dominated by granites and diorites, that formed in a maturing arc. All rocks were subsequently metamorphosed to lower amphibolite grade conditions. Sampling of variably altered rocks, and auriferous quartz (+/- pyrite, chalcopyrite, pyrrhotite, arsenopyrite, sphalerite, native gold) veins from outcrop and drill core show evidence of a thin (~50 cm), proximal calc-silicate alteration halo and a distal biotite-sericite halo. The alteration assemblage consists of variable proportions of biotite, chlorite, and sericite (+/- calcite, clinozoisite, epidote, diopside, actinolite, tremolite, tourmaline, scheelite) in mafic rocks, and sericite (+/- biotite, chlorite, tourmaline, epidote, calcite)

in granitoids. Basalts from the Fisher property were further discriminated based on their chromium content. High Cr basalts (HCrB; typically > 60 ppm Cr) have a transitional to calc-alkaline affinity and stronger depletions in the LREEs, especially Nb. Low Cr basalts (LCrB; typically < 60 ppm Cr) have a tholeiitic to transitional affinity and are relatively enriched in LREEs. Textural relationships from auriferous quartz veins observed in thin section analysis have been used to constrain a paragenetic sequence encompassing sulphides, precious metals, and alteration phases. Of note, brecciated textures, Bi-tellurides, and pyrite were associated with high-grade gold. Petrographic observations also noted variations in alteration minerals morphology, colour and structural location. The chemistry of these minerals was studied using microprobe analysis to identify any corresponding chemical changes which were notably observed in chlorite, where a Fe-endmember chlorite is typical of vein-hosted chlorites, but were absent in other phases, such as biotite. Molar Element Ratio diagrams and mass change plots suggest that gains in K and losses in Na reflect feldspar destruction and subsequent sericite and/or biotite/chlorite formation, which tend to be stronger in HCrB relative to LCrB. Zr-weighted enrichment/depletion plots show HCrB have stronger enrichments in K, Rb, Ba, Pb, As, Mo and depletions in Na. Principal Component Analysis identified element clusters reflecting primary igneous features and a possible Au or chalcophile-related signature of Pb, As, As, Mo, W $\pm$ Bi, Te, and Sb. Fluid conditions were likely constrained by low salinities, made evident by low concentrations of base metals, and were likely boron-enriched. Gold mineralization at the Fisher property likely has a strong relationship with structures, however, HCrB, LCrB, granites and metasedimentary rocks all have potential as favourable host rocks.

ACKNOWLEDGEMENTS

This project would not have been possible without the support, guidance, and expertise from my supervisor Dr. Kevin Ansdell. I extend my most sincere gratitude to Dr. Kevin Ansdell who also supervised my undergraduate theses and has been a great mentor and friend to me over the past four years. Dr. Camille Partin is also thanked for her expertise on this research. I acknowledge the Natural Sciences and Engineering Research Council (NSERC) for providing financial support through an NSERC Canada Graduate Scholarship-Master's to Courtney Onstad, an NSERC-SSR Mining Inc. Engage Grant to Dr. Kevin Ansdell, and an NSERC-SSR Mining Inc. Alliance Grant to Drs. Kevin Ansdell, and Camille Partin. A special thanks to the Society of Economic Geologists Canada Foundation and Newmont Mining Corporation for awarding me a Graduate Student Fellowship. Thank you to Tom Bonli at the University of Saskatchewan and Robert Marr at the University of Calgary for their assistance with electron microprobe analysis, the Saskatchewan Resource Council (SRC) for geochemical analyses and Vancouver Petrographics for thin section preparation. Rebecca Kupchinski is thanked for assistance with sample preparation. Thank you to my committee members Dr. Yuanming Pan, and my external examiner Dr. Stefanie Brueckner, for their time in reviewing my thesis and their constructive feedback.

A massive thank you to SSR Mining Inc., especially Paul Kremer and Anders Carlson, for providing funding, logistical support, and access to resources essential to this research. The crew has been very accommodating and managed to retrieve and ship samples to the University of Saskatchewan.

My most sincere gratitude to all my USask friends who welcomed me with open arms; you all made the experience something I will never forget. Thank you to my high school Earth Science 11 and Geology 12 teacher, Jim Milross, who inspired me to pursue a path in geoscience. A

heartfelt thanks to my mother, Glenda, my father, Bryan, my brother and sisters and extended family. I cannot describe how much support I have received from my family and it is truly appreciated. Thank you to my friends Marishka, Anny, Tianna, Robin and Aidan who have all inspired me in various ways. Daniel, thank you for being there for me, your encouragement and love inspires me every day. Lastly, Jojo, Tigger, Tuffy, Levi, Gracie, Chilli and Mookie; thank you for soaking up my tears and keeping me sane through this life.

TABLE OF CONTENTS

LIST OF TABLES

LIST OF FIGURES

CHAPTER 1: INTRODUCTION

1.1 Background Summary and Research Hypothesis

Classically, orogenic gold deposits consist of quartz veins and associated altered rocks hosted by crustal-scale structures, in predominantly greenschist grade metamorphic host rocks. Although Archean cratons include some of the largest and most economic orogenic gold deposits in the world and in Canada (Robert et al., 2007; Goldfarb et al., 2005), there has been increasing recognition that significant orogenic gold deposits also occur in younger, Paleoproterozoic rocks of the Canadian Shield (e.g. Lawley et al., 2016; Wood, 2016; Thomas and Heaman, 1994). In addition, some of these deposits are hosted by amphibolite grade metamorphic rocks (Hardy, 1994) which emphasizes that other terranes of varying age and metamorphic grade in the Canadian Shield may warrant further investigation.

Historical gold exploration in the Reindeer zone of the Precambrian Shield in northern Saskatchewan dates to the early 1900's (Morelli and MacLachlan, 2012). Overall, most of the gold in Saskatchewan has been mined from volcanogenic massive sulphide or orogenic gold deposits. The Seabee Gold Operation, which lies within the Glennie Domain comprises several examples of these orogenic gold deposits and includes the active Santoy mine and the recently decommissioned Seabee mine (Selby, 2017). These Paleoproterozoic orogenic gold deposits are hosted by multiple shear zones (Tourigny, 2003), such as the Santoy Shear zone, which are likely splays off the Tabbernor fault which has a history of early ductile deformation and later brittle reactivation (Wood, 2016; Lewry et al., 1990).

The intent of the project is to determine the petrographic, geochemical, and mineralogical characteristics of host rocks and alteration haloes to auriferous quartz veins. The overarching research hypothesis is that the host rocks to gold on the Fisher property are equivalent to those which host known mineralization at the Santoy deposit. This will be examined through the following objectives:

(1) Characterize host rock lithologies using petrology and lithogeochemistry to constrain those that are favourable for gold mineralization.

(2) Identify alteration haloes and pathfinder elements associated with certain host rocks and the hydrothermal alteration paragenetic sequence.

(3) Evaluate chemical variations associated with host rock, distal and proximal mineral phases.

The host lithologies and structures of the Santoy and Seabee deposits are interpreted to extend into the Fisher property, which is the focus of this study. Overall, this study will provide further constraints on the characteristics of orogenic gold deposits occurring in Paleoproterozoic amphibolite-grade metamorphic rocks and will enhance our understanding of them for continued exploration.

1.2 Research Objectives

The research objectives described above are expanded on here to provide a clear approach on how the overall research hypothesis was assessed.

(1) Characterization of host rock lithologies is crucial prior to making interpretations on alteration/mineralization processes. Hand samples and thin sections will be used to identify primary mineralogy, respective modal percentages, and primary igneous textures. These will

provide suitable rock names and potentially provide insight on primary magmatic processes. Lithogeochemical data aids in rock identification and can be used to interpret tectonic settings and magmatic affinities. Comparisons to host rocks at the Santoy deposit will also be drawn to determine their correlation.

(2) Increasing alteration typically coalesces with quartz veining and associated mineralization due to the presence of hydrothermal fluids (Groves et al., 1998; McCuaig and Kerrich, 1998). The alteration phases and associations with host rocks can be useful information to integrate in an exploration strategy. Alteration haloes will be characterized with core/outcrop samples analyzed using lithogeochemical and petrographic methods. Lithogeochemistry aims to identify pathfinder elements towards gold mineralization, and to understand the alteration framing quartz veins. A paragenetic sequence will be developed based on textural relationships established in thin section and microprobe analysis. Using molar element ratios, which make use of major elements potentially related to alteration, we will also be able to characterize the types of alteration that exist in specific units (Davies and Whitehead, 2006; Stanley and Madeisky, 1996). In addition, various isocon diagrams and density/element-corrected bar plots will be used to identify certain element mobilities, which will aid in understanding relative mobility due to hydrothermal alteration (Gresens, 1967).

(3) Understanding chemical variations/zoning in minerals associated with auriferous quartz veins can reveal important relationships, which may not be apparent through other analytical methods. Microprobe analysis will be used to compare the chemistry between unaltered and altered mineral phases and to identify variations influenced by protolith compositions. Identification of textures associated with mineralization can indicate controls on hydrothermal processes not apparent in petrographic analysis.

1.3 Overview of Canadian Orogenic Gold Deposits

Orogenic gold deposits are typically hosted by secondary splays of crustal-scale structures, within greenstone belt terranes, and commonly in Archean age rocks. These deposits are found especially in the middle Archean to the Phanerozoic and form under higher pressure settings between 1.5 and 5 kbar at depths of 4 to 15 km (Goldfarb, 2001). Formation temperature are moderate relative to magmatic-hydrothermal deposits at 300 to 450 ˚C (Ridley, 2013). Generally, the hydrothermal fluids that form these deposits are CO_2-rich, concentrated in CH_4 and/or N_2 and have consistent fluid compositions indicating a single source influenced the formation of these deposits (Goldfarb, 2015). In Canada, the Archean Superior Province and Slave Craton (Fig.1-1) are well-known terranes with an extensive and well-studied history of orogenic gold production (Gosselin and Dubé, 2005). With recent investigations into exploring northern Canada, the Archean Rae-Hearne Province (Fig.1-1) has proved to be a suitable terrane for orogenic gold mining. In addition, the Paleoproterozoic Trans-Hudson Orogen (Fig.1-1) has a long history of gold exploration and production (Morelli and MacLachlan, 2012).

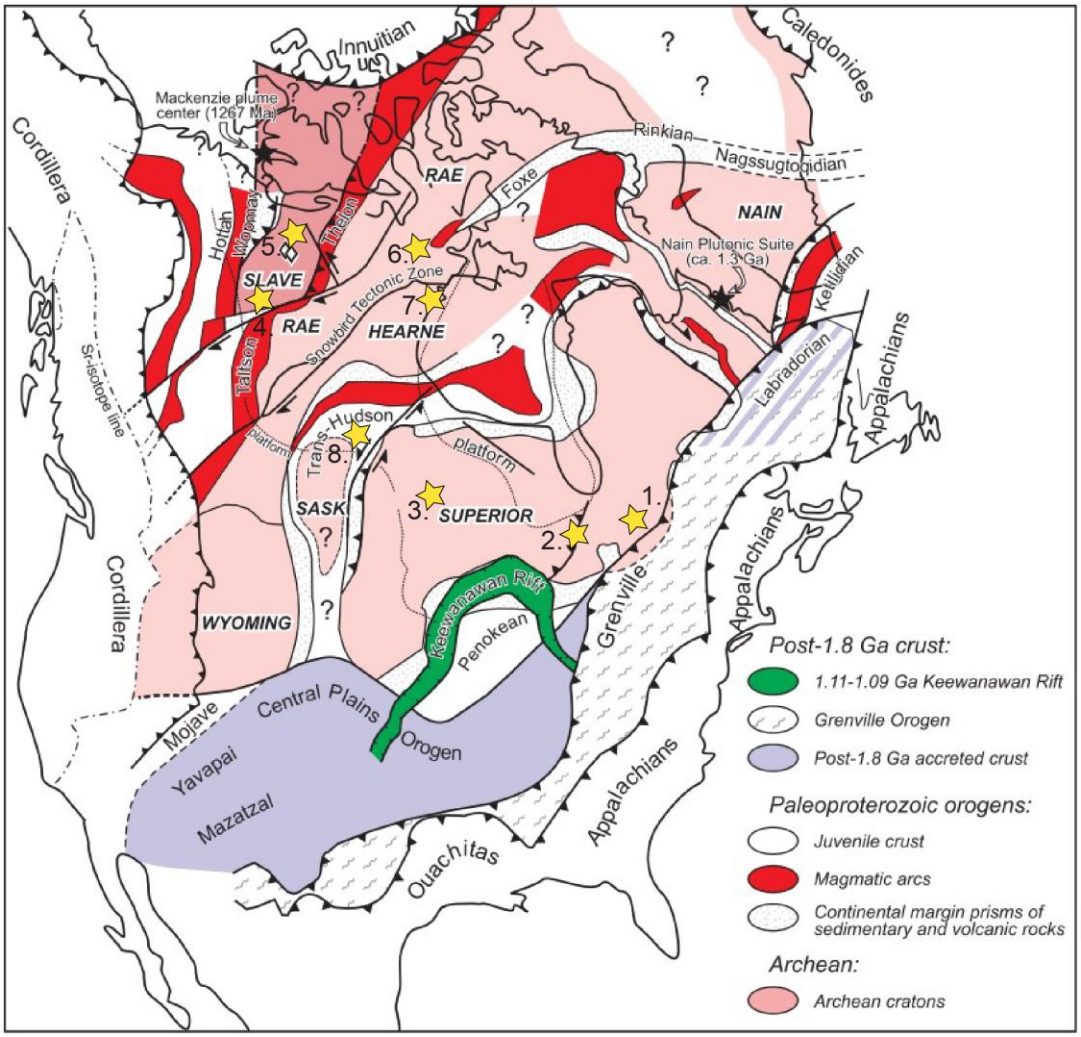

Figure 1-1 Map showing extents of the Archean cratons, including the Superior, Slave, and Rae-Hearne cratons, and Proterozoic orogenic belts, including the Paleoproterozoic Trans Hudson Orogen, in Laurentia (modified after Bleeker and Hall, 2007; Hoffman, 1988; Ross et al., 1991). Selected deposit/camp locations are highlighted with a yellow star and numbered: 1. Val-d 'Or, QC, 2. Timmins, ON 3. Red Lake, ON 4. Giant-Con, NWT 5. Lupin, NU 6. Meadowbank, NU, 7. Meliadine, NU, 8. Lynn Lake, MB.

The Archean Superior Province is exposed over a large portion of Ontario and southwestern Quebec. It comprises many gold-endowed greenstone belts, including the Abitibi, Wawa, Pontiac, and Uchi belts, which account for a significant portion of Canada's gold production. These greenstone belts host many world-class gold camps, such as Timmins, Red Lake, Porcupine, and Val d'Or (Colvine et al., 1988), stressing the relationship between greenstone belts and orogenic gold deposits. No consistencies in host rock lithologies to mineralization have been noted across

the various belts. For example, the Campbell Red Lake deposit is hosted by Fe-rich tholeiitic basalts and basaltic komatiites, opposed to the Sigma-Lamaque, which is hosted by andesitic flows, volcaniclastic rocks and dioritic intrusions (Gosselin and Dubé, 2005). An important relationship also lies in the association of regional-scale shear zones with gold deposits. The orientation of these faults (east – west trending) in the Superior Province suggest they were related to regional north – northwesterly-directed accretionary events (Colvine et al., 1988). Greenschist metamorphism has affected most rocks, however amphibolite metamorphism has affected greenstone belts where aureoles occur adjacent to intrusive bodies (Colvine et al., 1988). The alteration packages associated with orogenic gold deposits vary depending on host-rock compositions. Carbonatization has been noted as the most common alteration product at the regional and mine scale (Colvine et al., 1988). In some deposits, carbonate and phyllosilicate zoning is present around the deposit (e.g. Kishada and Kerrich, 1987), however others lack zoning due to multiple auriferous fluid events (e.g. Andrews et al., 1986).

The Slave Province is exposed in the Northwest Territories with prominent greenstone belts including the Yellowknife, Hackett River, and Courageous Lake belts. Archean orogenic gold deposits are typically associated with 2.73 – 2.70 Ga tholeiitic greenstone belts (Bleeker and Hall, 2007). These tholeiitic greenstone belts typically have a thick, folded turbidite bed adjacent to the belt and have a tightly infolded, synorogenic conglomerate package. The structures which are associated with these gold deposits developed along margins of major basement uplifts (Bleeker and Hall, 2007). The Con-Giant deposit is a well-known orogenic gold deposit in the Yellowknife greenstone belt which is controlled by reverse shear zones (Siddorn, 2011). The Lupin gold deposit is an example of a banded iron formation in which ore bodies are constrained by the limbs of an anticline-syncline pair (Lhotka and Nesbitt, 1989; Gardiner, 1986). Analogous to other Canadian

Archean Au deposits in the Superior, the Slave deposits typically occur proximal to a major structure, such as the Yellowknife River Fault in the case of the Giant-Con mine (Siddorn, 2011). Gold mineralization in the Slave craton is a result of D_2 deformation and subsequent metamorphism which culminated ~2.6 to 2.59 Ga (Davis and Bleeker, 1999).

Increased exploration in Canada's north has brought interest to Nunavut and the northern extents of the Rae-Hearne craton. The Meliadine Deposit in the Archean Rankin Inlet greenstone belt has become of significant economic interest in recent years (Lawley et al., 2015). This deposit differs from those in the Superior and Slave cratons since the auriferous fluids postdate volcanism in the belt by one billion years (Lawley et al., 2016). Gold in the Rankin Inlet greenstone belt is typically hosted within banded iron formations and argillites. The Pyke fault is the primary conduit for gold-bearing fluids (Carpenter and Duke, 2004). It is believed that gold emplacement is linked to Paleoproterozoic reactivation of the Pyke and associated faults related to regional metamorphism at ca. 1850 to 1830 Ma (Carpenter et al., 2005).

Other younger orogenic gold deposits occur in the Cordillera in western Canada and the Appalachians in Atlantic Canada. Of focus to this project, the Reindeer zone of the Trans-Hudson Orogen is an example of a Paleoproterozoic terrane in Canada. The Reindeer zone comprises greenstone belts, which host both volcanogenic massive sulphide and orogenic gold deposits. The orogenic gold deposits were some emplaced due to thermotectonic events throughout the waning stages of the Trans-Hudson Orogen at ca. 1800 Ma (Morelli and Maclachlan, 2012). Typically, orogenic gold is hosted by quartz veins in volcanic, sedimentary, and plutonic rocks. Lithological contacts where competency contrasts exist, like those between gabbroic wallrock and dykes at the Seabee Deposit, are a favourable location for gold mineralization, and is a common characteristic of many orogenic gold deposits. Crustal scale shear zones are common in the Reindeer zone, such

as the Johnson Shear zone in the case of the Lynn Lake gold deposit. Gold mineralization at the Lynn Lake deposit is typically constrained to the Aggasiz Metallotect comprised of picrite, banded iron formation and exhalative sedimentary rocks (Beaumont-Smith and Böhm, 2003).

1.4 Thesis Organization and Structure

This thesis is separated into eight chapters with Chapter 1 introducing the study's objectives and an overview of orogenic gold deposits. Chapter 2 discusses the various methods used to answer the research hypothesis. Chapter 3 provides an overview of the regional geology of the project area including the Trans-Hudson Orogeny, development of the Reindeer zone, and an introduction to the local geology. Chapter 4 is intended to provide a complete overview of unaltered Fisher host rocks and discusses their petrographic and geochemical characteristics. Chapter 5 discusses the electron microprobe results of minerals from unaltered host rocks and altered rocks. Chapter 6 uses various lithogeochemical methods to characterize the alteration haloes associated with host rocks. Chapter 7 addresses interpretations, conclusions, and implications of the findings from previous chapters. This chapter also draws comparisons to work done on the Santoy deposit and provides a preliminary deposit model in which further work can expand on. Chapter 8 summarizes all the findings from this project and identifies areas for future research.

CHAPTER 2: METHODOLOGY

A total of 57 unaltered and representative supracrustal rocks were collected from eight drillholes (FIS-18-001, 003, 016, 017, 018, 022, 023, 028) along an 8 km trend of the Santoy Shear zone (Fig. 2-1). Additionally, 26 variably altered samples were collected along the same trend from seven drillholes (FIS-18-020, 021, 023, 024, 028 & FIS-19-030, 035; Fig. 2-1). Samples were selected based on core images provided by SSR Mining Inc. and include samples from near surface to 720 m at depth. Altered samples were collected at varying intervals, depending on visible alteration and Au grade of the interval. Generally, a least, moderate, and highly altered sample was selected from an interval, ranging from 0.5 – 2.0 m in length, encompassing the extents of the calc-silicate alteration halo. An additional 20 least-altered surface grab samples were collected along two transects across the Fisher shear zone and provide a comprehensive overview of lithologies on the property. The complete list of all samples collected for this thesis and respective analyses is available in Appendix A.

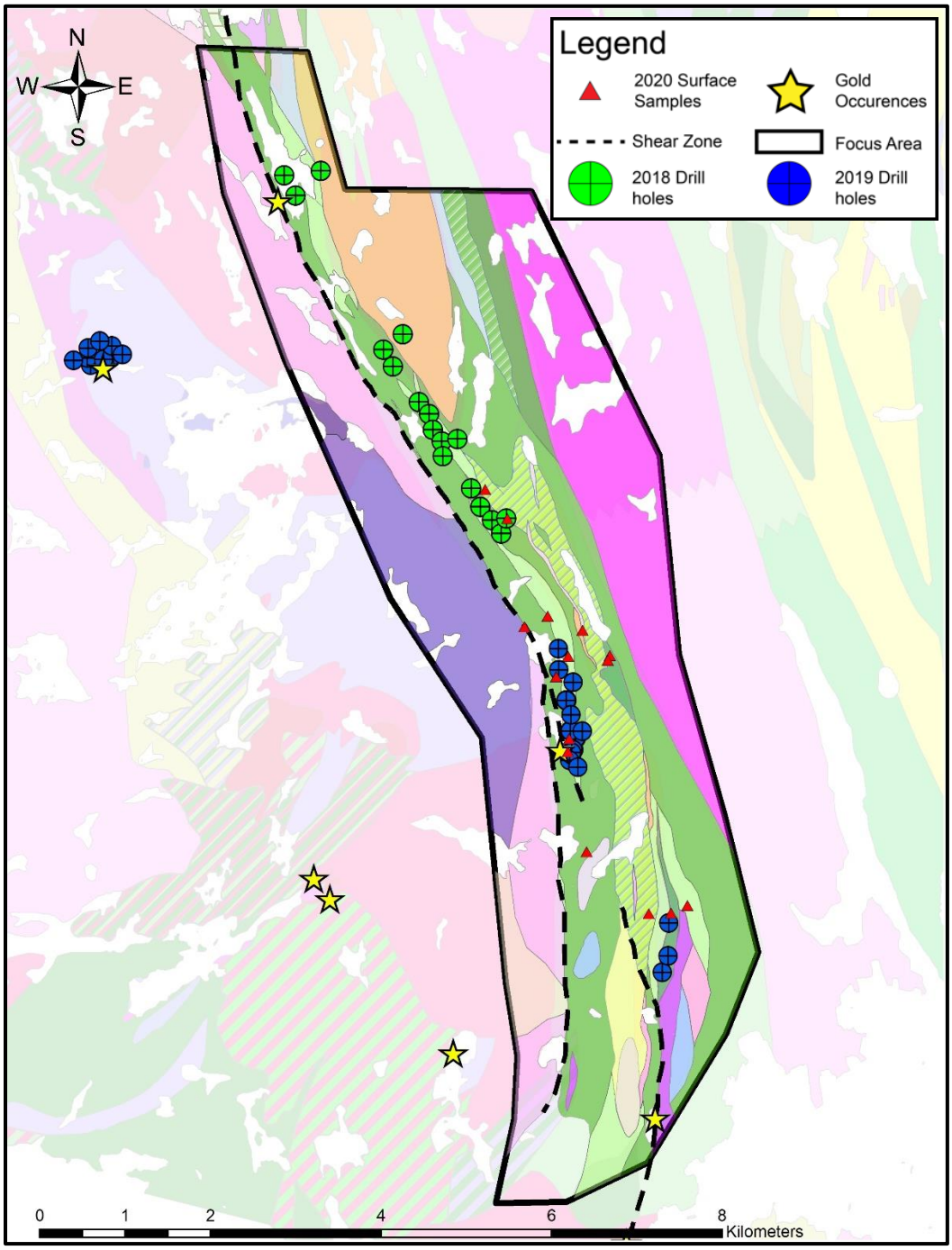

Figure 2-1 Location of drillholes symbolized based on year of drilling program and surface grab samples collected for this thesis. Map was produced in ArcGIS.

2.1 Lithogeochemistry

A total of 100 samples (74 unaltered, 26 variably altered) were sent for ICP Whole Rock analysis to Saskatchewan Resource Council Geoanalytical Laboratories in Saskatoon, SK, Canada. In addition to samples analyzed for this research, quality control and quality assurance (QA/QC) was monitored using duplicates for every 40 analyses, 3 standards, and 1 blank. Samples were crushed, split, and pulverized using an agate ring. Aliquots of samples are combined with a lithium metaborate and lithium tetraborate mixture and subsequently fused. The material is then poured into a dilute HNO_3 solution and dissolved to be analyzed by Inductively Coupled Plasma – Optical Emission Spectrometry (ICP-OES) and Inductively Coupled Plasma – Optical Mass Spectrometry (ICP-MS) as part of the Whole Rock and Trace Element Analysis Package (WR/TR1). ICP-OES was used to analyze Al_2O_3, CaO, Fe_2O_3, MgO, MnO, P_2O_5, K_2O, Na_2O, TiO_2 (detection limit: 0.01%), SiO_2, LOI (detection limit: 0.1%), Cr, V, and Sc (detection limit: 2 ppm). ICP-MS was used to analyze Pb (detection limit: 0.001 ppm), Dy, Er, Eu, Gd, Ho, Lu, Pr, Sm, Ta, Tb, Th, Tm, U, Yb, Y (detection limit: 0.01 ppm), As, Be, Bi, Cd, Cs, Co, Cu, Ga, Ge, Hf, Hg, Mo, Nd, Rb, Ag, Te, Sn (detection limit: 0.1 ppm), Sb, Ba, Ce, La, Nb, Ni, Se, W, Zn, and Zr (detection limit: 1 ppm).

The unaltered samples include texturally consistent intervals of supracrustal felsic to mafic volcanic rocks and various plutonic rocks. Major and trace element constituents of these samples were used to distinguish rock types and to determine the tectonic setting and magmatic affinities. All lithogeochemical plots were created in ioGAS, excel and OriginPro. The complete lithogeochemical data-set is listed in Appendix B.

2.1.1. *Alteration Analysis*

Use of Molar Element Ratios to quantify hydrothermal alteration is an approach commonly used in ore deposit studies, especially in VMS systems where large alteration haloes exist (Stanley, 2013; Piercey, 2009). Molar Element Ratios include General Element Ratios (GERs) and Pearce Element Ratios (PERs) and are an appropriate approach to avoid the effects of closure (Stanley, 2013). PERs are calculated directly from raw geochemical data, using Equation (1), and are used to gain insight on various rock-forming processes. The denominator of the equation, or "z", is a conserved element, which should be identified by prior conserved element analysis (Stanley, 2013), further discussed in section 3.2. GERs differ in that the denominator of the equation (Eq. 2) is not a conserved element. Instead, this element is one that participates in material transfer processes. GERs are intentionally constructed this way to show material transfers such as metasomatism (Stanley, 2013).

(Eq. 1) $$PER_{x/z} = \frac{\frac{x}{GFW_x}}{\frac{z}{GFW_z}}$$

where *x* is the wt. % concentration of element *x*, *z* is the wt. % concentration of conserved element *z* and *GFW* is the oxide gram formula weight.

(Eq. 2) $$GER_{x/y} = \frac{\frac{x}{GFW_x}}{\frac{y}{GFW_y}} = \frac{PER_{\frac{x}{z}}}{PER_{\frac{y}{z}}}$$

Where *x* is the wt. % concentration of element *x*, *y* is the wt. % concentration of non-conserved element *y*, *z* is the wt. % concentration of conserved element *z*, and *GFW* is the oxide gram formula weight.

Isocon diagrams (Grant, 1986; Gresens, 1967) evaluate chemical variations only on a sample-to-sample basis by plotting an unaltered or least altered sample on the x axis, and an altered sample on the y axis. The isocon line is defined by immobile elements of equal concentration and variances from a slope of 1 indicate a volume change (Grant, 1986). If elements are gained through alteration, it will plot above the isocon line. If an element is lost during hydrothermal alteration, it will plot below the isocon line. Isocon lines were either forced through Zr (assuming it was immobile) or forced through a combination of conserved elements in that host rock, from the origin (y=0). As the R^2 value gets closer to 1, there is greater immobility of elements. If the slope of the isocon line is > 1, the elemental gains are stronger than elemental losses, and the reverse is true if the slope is < 1.

Statistical analysis is an alternative approach to understanding elemental relationships in specific suites. Principal Component Analysis (PCA) reduces the dimensionality of data and can help identify element associations (Gazley, 2015). The first principal component is that which accounts for the most variation within the dataset, and each subsequent component accounts for less variance (Fig. 6-13). Eigenvectors are the result of the principal component calculation, and in this case, were calculated using Centred Log Ratio (CLR) transformed data. CLR transformed data is used to remove the effect of closure, which is common when using raw chemical composition data (Buccianti and Grunsky, 2014), by representing each element as a ratio to a central value (Aitchison, 1986). The CLR is calculated by taking the log of the ratio between observed frequencies and their respective geometric means.

An alternative approach to analyzing alteration effects are Zr-weighted enrichment/depletion plots. These plots show elements of interest along the x axis, and their respective enrichments (non-quantitative) on the y axis relative to a least-altered sample (y=1).

Equation 4 is used to calculate the Zr-weighted enrichment/depletion factor (ZWEF). The ZWEF works in a similar way to the density-weighted enrichment/depletion factor (DWEF; Eq.3), which is the reciprocal of Equation 5 from Lesher, 1986. Since density data was not obtained in this study, an assumed immobile element (Zr) is selected as a factor. It is important to note that no quantitative results should be taken from this type of data, only relative comparisons.

(Eq. 3) $$DWEF = \frac{X_i^B * \rho^B}{X_i^A * \rho^A}$$

where X is the concentration and ρ is the density of an element (*i*) of interest, in an altered rock (*B*) or unaltered rock (*A*).

(Eq. 4) $$ZWEF = (\frac{x_{Zr}^A}{x_{Zr}^B})(\frac{x_i^B}{x_i^A})$$

where x_{Zr} is the concentration of zirconium, x_i is the concentration of element *i* of interest, *B* is the altered rock and *A* is the protolith (or least-altered) rock.

(Eq. 5) $$\int_v = \frac{(x_i^A \rho^A)}{(x_i^B \rho^B)}$$

where $\int_v$ is the ratio of the volume of rock A (protolith, or least-altered) to that of rock B (altered), x_i is the concentration of element *i* and ρ is the density.

Analyzing mass changes of elements is another useful approach to quantifying hydrothermal alteration. The single precursor method (MacLean and Kranidiotis, 1987) identified sample CO-2019-123 (HCrB) as a least-altered precursor. Mass percent changes (ΔX_i; Eq. 7) are calculated assuming Zr is conserved by using a Zr factor (f_v; Eq. 6) (Gresens, 1967). Bivariate plots of mass changes of elements can indicate trends towards various types of alteration (Fig. 6-16).

(Eq. 6) $$f_v = \frac{X_{Zr}^A}{X_{Zr}^B}$$

where X_{Zr} is the concentration of zirconium in protolith *A* and altered rock *B*

(Eq. 7) $$\Delta X_i = (f_v * X_i^B) - X_i^A$$

where f_v is the Zr factor, *X* is the concentration of element *i* in a protolith *B* and an altered rock *A*

2.2 Petrographic & Electron Microprobe Analysis

A suite of 45 unaltered samples and 21 variably altered samples were cut perpendicular to or at an angle to the foliation using a rock saw at the University of Saskatchewan. Samples were sent to either Vancouver Petrographics or the University of Saskatchewan Thin Section Laboratory for thin section preparation and were cut at 30 μm thick to be examined using transmitted and reflected light petrography.

Two separate labs were used for microprobe analysis due to circumstances that arose during the Covid-19 pandemic. Three unaltered samples (CO-2019-19, 33, 34) and one altered sample (CO-2019-28A2) were analyzed using a JEOL 8600 Superprobe electron microprobe analyzer at the Electron Microscopy Laboratory in the Department of Geological Sciences, University of Saskatchewan. Polished thin sections were wiped with a methanol-soaked Kimwipe, then given a 30 second wash in methanol to remove fingerprints and contaminants. Carbon coating was applied using a carbon evaporator coater to produce a 200 angstrom carbon coating. The microprobe conditions were pre-set with an accelerating voltage of 15 kV, a beam current of 5-10 nA and diameter of 10 microns. Three unaltered samples include a mafic volcanic, pyroxenite and an andesite, and the altered sample is a mafic volcanic (Appendix C). Samples were collected with

the intent of analyzing host rock mineral compositions, compositional zoning, exsolutions and micro-textures.

In addition, six altered samples (CO-2019-48, 55, 61, 69, 81B, 93A) were analyzed using a JEOL JXA 8200 electron microprobe at the Department of Geoscience, University of Calgary (Appendix C). Polished thin sections were cleaned with methanol to remove fingerprints and contaminants. Carbon coating was applied using a Denton Vacuum DV-502A carbon evaporator. The microprobe conditions were pre-set with an accelerating voltage of 15 kV, a beam current of 20 nA and diameter of 5 microns. A range of well characterized natural and synthetic standards were used. Altered samples were selected to: 1) compare mineral compositions between unaltered and altered host rocks; identify 2) textures associated with mineralization and internal textures of sulphide minerals; 3) alteration minerals not identified in petrographic analysis; and 4) compositional zoning.

Photomicrographs and BSE images were labelled with abbreviations as outlined in Whitney and Evans (2010). The electron microprobe data is listed in Appendix C.

CHAPTER 3: GEOLOGICAL SETTING

3.1 The Fisher Property & Seabee Gold Operation (SGO)

The Fisher property, part of the Seabee Gold Operation, is in east-central Saskatchewan (Canada) in the Glennie Domain of the Reindeer zone. It is approximately 125 km ENE of La Ronge, SK and lies about 7 km southeast of the active Santoy mine. The SGO hosts the Santoy mining complex which accesses numerous deposits including, Santoy 7, 8, 8A, Gap, Gap Hanging Wall. In 2019, the Santoy mine produced 350 000 tonnes of ore milled with an average grade of 9.16 g/T Au (Saskatchewan Ministry of Energy and Resources, 2019). As of January 5, 2021, SSR Mining Inc. exercised a Second Option earn-in with Taiga Gold Corporation for a total interest of 80% of the Fisher property (Taiga Gold Corp., 2021). The Fisher property can be accessed by an all-season road from the Seabee Gold Operation and is accessible by air from Missinipe/Otter Lake (Selby et al., 2017).

Gold discoveries in the area date back to the 1940's (Morelli and Maclachlan, 2012), which brought initial interest to the area. This led to the discovery of the Seabee mine, which lies approximately 10 km west of the Santoy mine. The Seabee mine started producing in November 1991 with an original feasibility study estimating recovery of 379,241 oz Au (Basnett, 1999). The Seabee mine was decommissioned in 2018 with a total of 608,000 oz Au recovered (Saskatchewan Ministry of Energy and Resources, 2019). At present (April, 2021), the Santoy Gold mine is the only actively producing gold mine in Saskatchewan.

3.2 Regional Geology

The Fisher property lies in the northeastern corner of the Glennie Domain within the Reindeer zone of the Paleoproterozoic Trans-Hudson Orogeny (THO; Fig. 3-1). The THO formed

by closure of the Manikewan Ocean (Stauffer, 1984) and delineates the collisional suture zone between the Rae-Hearne, Sask and Superior cratons (Ansdell, 2005). Possible extents have been traced from northern Europe through Nunavut, Saskatchewan, and Manitoba (Hoffman, 1988), and below the Phanerozoic sedimentary units of the Williston Basin. It is then believed to continue south to the Grand Canyon area (Bickford and Hill, 2007; Ansdell, 2005) where it is terminated by the Central Plains orogen (Sims and Peterman, 1986).

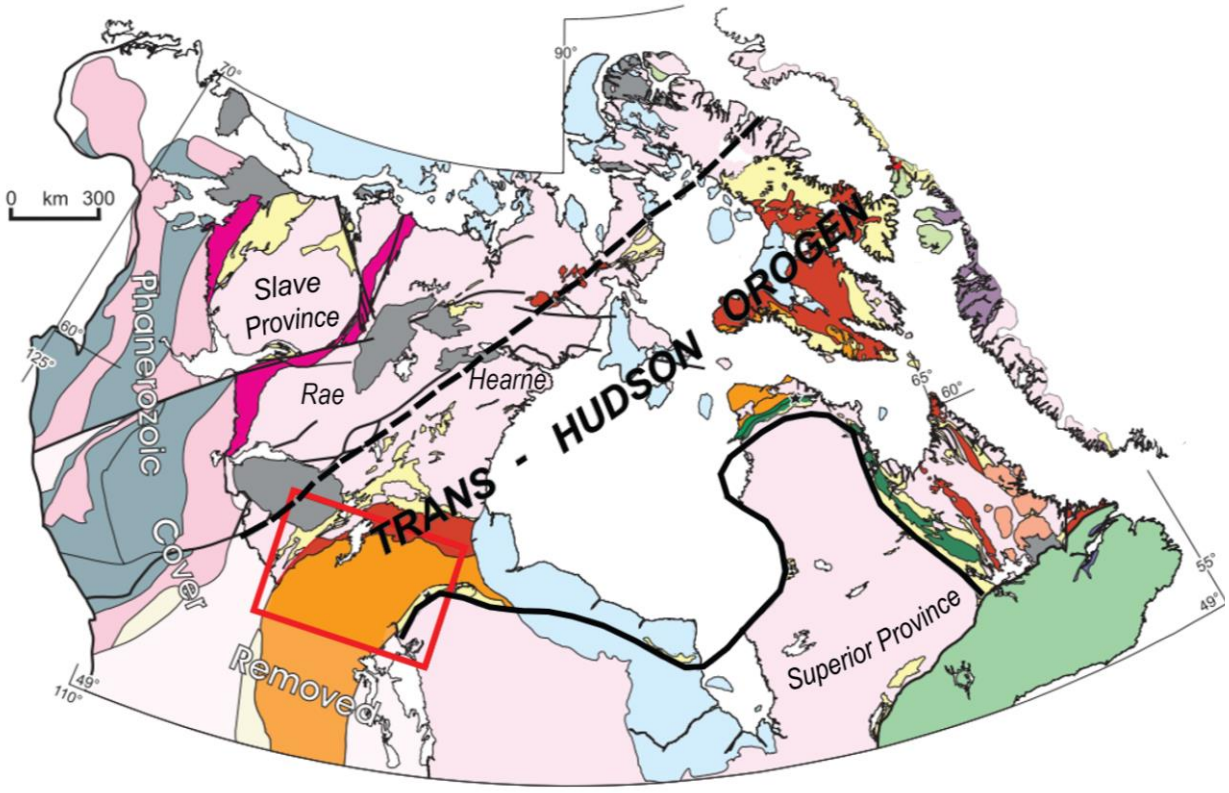

Figure 3-1 Simplified geological map of the Canadian Shield with the approximate boundaries of the Trans-Hudson Orogen shown by black lines (modified from Corrigan et al, 2014). The solid line represents a definite boundary, while the dashed line is approximate. Major Archean provinces (light pink) are labelled and the segment of the Reindeer zone of interest to this research is highlighted by a red box.

The THO in Saskatchewan and Manitoba comprises three distinct segments, including the Cree Lake zone, the Superior Boundary zone, and the Reindeer zone (Fig. 3-2). The Cree Lake

zone, and the Superior Boundary zone, comprise reworked supracrustal rocks which unconformably overly the Archean Churchill, and Superior provinces, respectively. These reworked margins formed during rifting of the Manikewan Ocean where sedimentary rocks were preserved within continental margins (Ansdell, 2005). The Reindeer zone represents various juvenile internides including (from west to east) the Wathaman, Rottenstone, La Ronge, Kisseynew, Glennie, and Flin Flon domains. This 500 km wide zone consists of various subduction-related rocks which formed during closure of the Manikewan ocean (Ansdell, 2005; Stauffer, 1984). These include primitive to evolved oceanic volcanic rocks, plutonic rocks, interarc and successor arc rocks and marginal-basin sedimentary rocks. A minimum age of 1.92 Ga (Ansdell, 2005) provides an age for initial closure of the Manikewan ocean and subsequent arc subduction. The various internides of this zone all evolved separately, and comprise fragments of older continental crust, back-arc basins, oceanic plateaus, and juvenile arc crust. It has been suggested that the Manikewan Ocean had similar characteristics to modern-day southwestern Pacific (Corrigan et al., 2009; Ansdell, 2005).

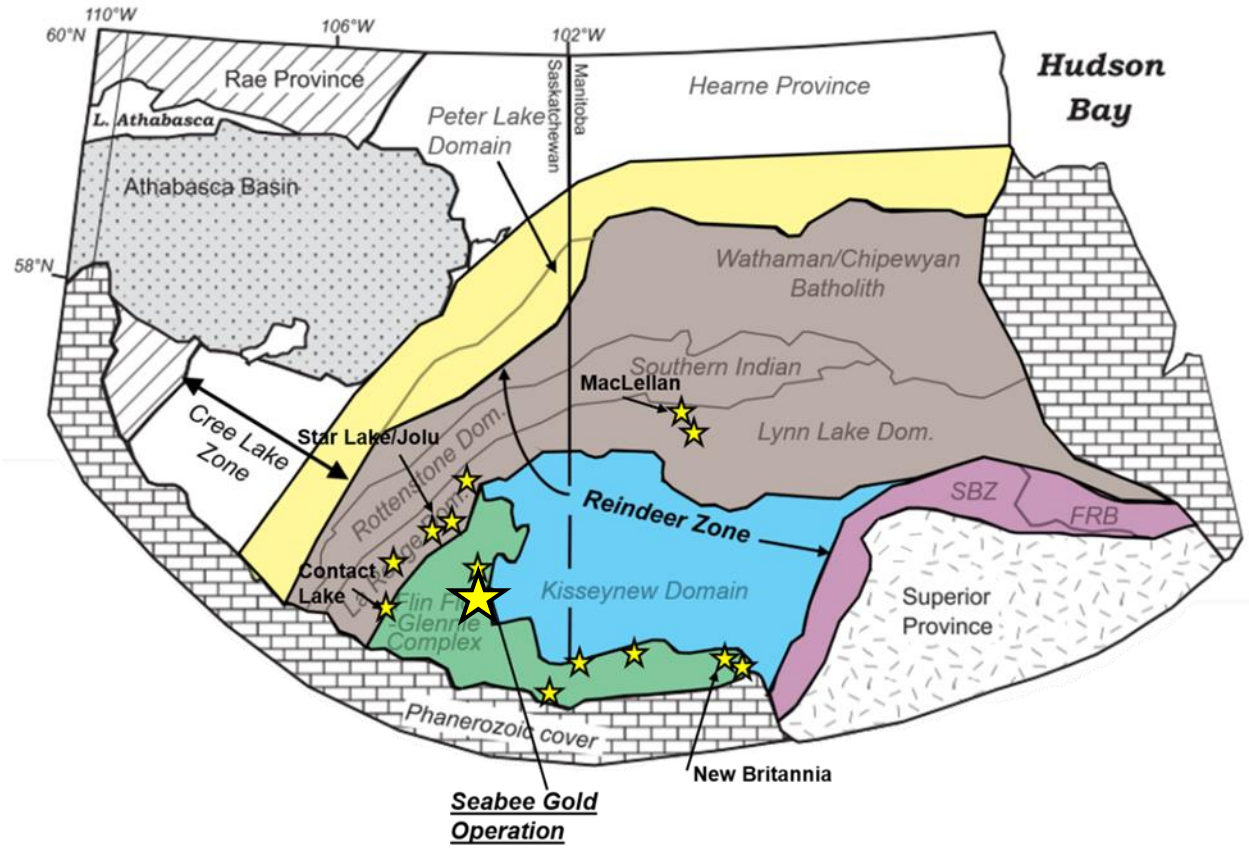

Figure 3-2 Map of lithostratigraphic domains of northern Saskatchewan and Manitoba with relation to major components of the Churchill Province of the Precambrian Shield (Rae, Hearne, Reindeer zone), the Superior Province and northern extents of Phanerozoic cover. Internides of the Reindeer zone are labelled, with yellow stars illustrating the location of orogenic gold deposits. Note the location of the Seabee Gold Operation within the Flin Flon-Glennie complex (modified from Corrigan et al, 2007). SBZ: Superior Boundary zone; FRB: Fox River Belt.

The Flin Flon-Glennie complex (FFGC) within the Reindeer zone comprises various 1895 to 1870 Ma volcanic belts, sedimentary sequences, syn-volcanic and post-tectonic plutonic rocks (Morelli and MacLachlan, 2012; Lucas et al., 1995; Fig. 3-2, 3-3). A range of depositional settings occur across the FFGC including juvenile arc, evolved arc, back arc, and oceanic plateau assemblages (Syme et al., 1998). The greenstone belts (e.g., Pine Lake, Brownell Lake in the Glennie Domain) typically constitute arc or MORB/back-arc constituents. The volcanic assemblages of the Glennie and Flin-Flon domains were accreted between 1880 and 1865 Ma into a single package (Ashton, 1999; Lucas et al., 1996) resulting in the Paleoproterozoic

protocontinent referred to as the Flin Flon-Glennie complex (Ashton, 1999; Lucas et al., 1997). Subsequent subduction beneath this terrane led to successor arc magmatism (1870 – 1835 Ma; Syme et al., 1998) resulting in calc-alkaline to alkaline plutonism across the Reindeer zone (Morelli and MacLachlan, 2012). The development of successor sedimentary basins ensued with siliciclastic sedimentation within and marginal to the Flin Flon-Glennie complex between 1855 – 1840 Ma (Syme et al., 1998). The largest of these basins is now preserved as the Kisseynew Domain, which either developed in a back-arc environment (Ansdell et al., 1995) or along an active continental margin (Zwanzig, 1997).

The metamorphic and deformational history of the Glennie domain is preserved as early tight to isoclinal folds and layer-parallel high-strain zones, termed the D_2 event by Lewry et al., (1990). This event was initiated at ca. 1835 Ma during underthrusting of the Sask craton (3.2 – 2.5 Ga rocks in Fig. 3-3) below Paleoproterozoic rocks of the Flin Flon-Glennie complex (Ashton et al., 2005). D_3 involved late to post-collisional deformation (1800 – 1770 Ma) resulting in north-trending folds and NE-trending D_4 folds. A series of subvertical strike-slip faults (e.g., Tabbernor fault) were formed during D_3 which act as important structural corridors for hydrothermal fluids. These deformational events also coincide with peak metamorphism (1818 – 1794 Ma) and produced a range of metamorphic grades across the Flin Flon-Glennie complex due to the variations in structural relief (Morelli and MacLachlan, 2012). An overview of these deformational events and associated structures, which are relevant for gold mineralization, will be discussed in Chapter 3.3.

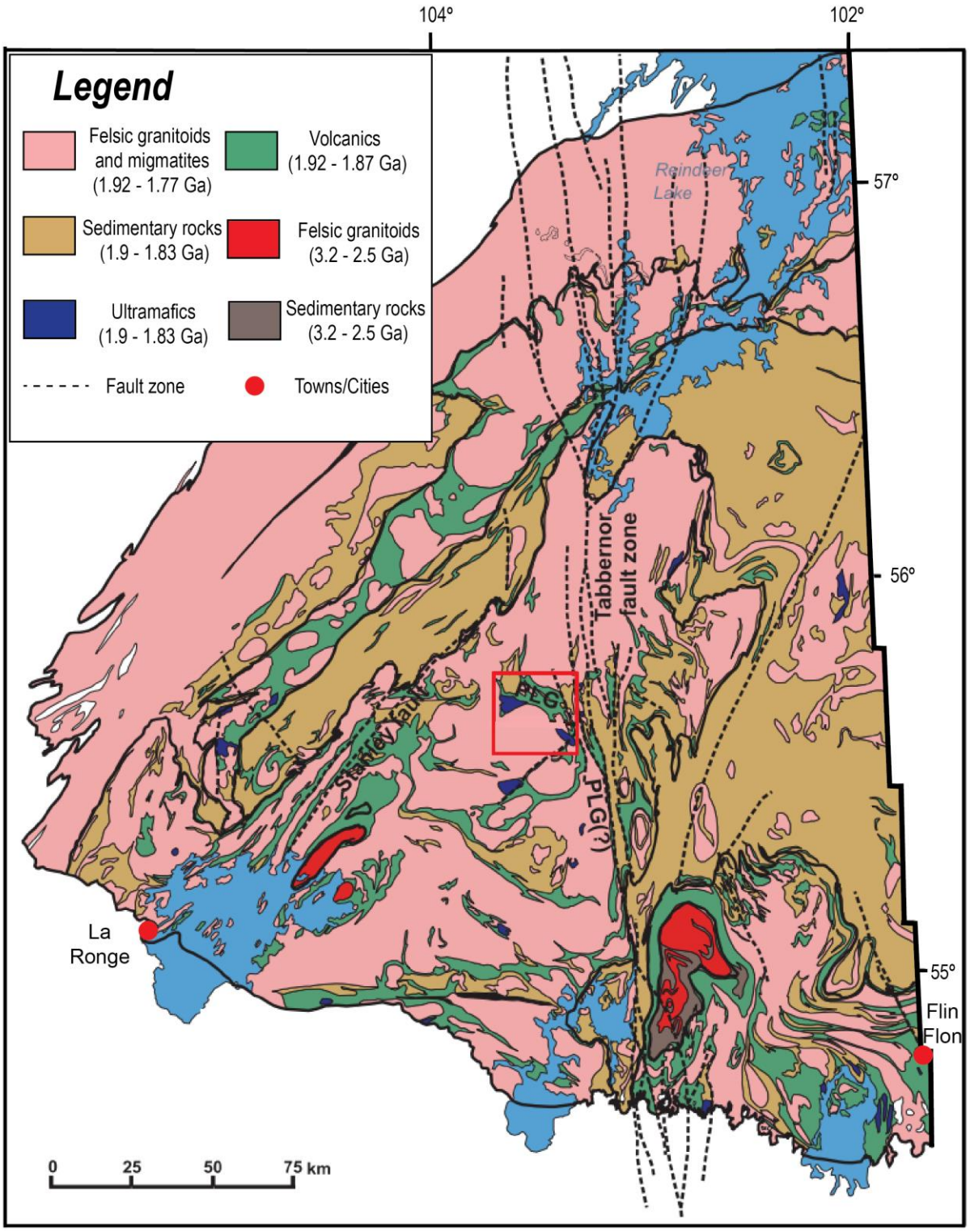

Figure 3-3 Simplified geology of the Saskatchewan segment of the Reindeer zone. Location of the Seabee Gold Operation (outlined in red) and the Pine Lake greenstone belt (PLG) within the Glennie domain (modified from Wood, 2016; Morelli and MacLachlan, 2012; Saskatchewan Geological Survey, 2003).

3.3 Geology of the Seabee Gold Operation (SGO)

The SGO lies within the eastern portion of the Pine Lake greenstone belt of the Glennie Domain (Fig. 3-3). Rocks in this area have been metamorphosed up to amphibolite facies (Wood, 2016; Delaney and Cutler, 1992). The remainder of this chapter will refer to protolith rock names for simplicity since all rocks have been metamorphosed. Delaney and Cutler (1992) delineated two groups of supracrustal assemblages (A & B), and a succession of overlying siliciclastic rocks termed the Porky Lake Group (Fig. 3-4, 3-5).

The oldest assemblage (Assemblage A) at 1.89 – 1.87 Ga, consists of mafic-felsic volcanic, subvolcanic intrusive, volcaniclastic, and minor siliciclastic rocks (Delaney and Cutler, 1992; Chiarenzelli, 1989). The mafic volcanic rocks are typically fine-grained, dark green and consist of dominantly hornblende and plagioclase and display textural heterogeneity. The intermediate volcanic rocks are intercalated with mafic volcanic rocks and volcaniclastics and are identified by medium-grained plagioclase in a finer groundmass of quartz, hornblende, and plagioclase (Delaney., 1986). Felsic volcanic rocks are rare, but are fine-grained rocks comprised of quartz, feldspar with minor biotite. Volcaniclastic rocks consist of both pyroclastics and epiclastics but are difficult to distinguish at amphibolite grade metamorphic conditions. Other minor lithologies in this assemblage include conglomerates, feldspar porphyry flows, pelitic sediments, feldspathic arenites, and mica schists (Delaney, 1987).

The younger Assemblage B (~1840 Ma) comprises variably deformed rocks of mainly volcaniclastics and sedimentary rocks of the Pine Lake greenstone belt (Delaney and Cutler, 1992; Fig. 3-4). This unit comprises felsic volcaniclastics, hornblende volcaniclastics and sediments, lapilli tuffs, chlorite-actinolite schists and a basal polymictic conglomerate. The conglomerate, 3m

at its thinnest to 70m at its thickest, lies at the contact with Assemblage A volcanic rocks and locally intercalates with a rhyolite dated as 1838 Ma ± 2 (McNicoll, 1992). The felsic volcaniclastics are fine-grained and dominated by quartz, plagioclase and minor biotite and magnetite (Delaney and Cutler, 1992).

The Laonil Lake intrusive complex (1889 + 9 Ma) is the oldest pluton within this part of the Glennie Domain and intrudes Assemblage A volcanic rocks (Chiarenzelli, 1989; Fig. 3-4). This composite ultramafic to dioritic plutonic package consists of mostly gabbro and diorite, lesser ultramafic rocks, and minor granodiorite, feldspar porphyry, intermediate and mafic dykes, (Delaney, 1986). The gabbro is a medium-grained and green-grey massive unit that typically forms as sheets. The diorite is texturally variable ranging from medium to coarse-grained and compositionally variable. Predominantly, gabbro and diorite rocks host the mineralization at the Seabee mine.

The Eyahpaise Lake pluton (1859 + 5 Ma) intrudes Assemblage A volcanic rocks and the Laonil Lake and Eisler intrusive complexes (Fig. 3-4). This pluton consists mostly of a medium-grained, massive tonalite (Delaney, 1987). The Lizard Lake pluton (~1874.6 ± 1.9 Ma; Wood, 2016) is a tonalite unit exposed at surface mainly to the East Santoy deposit. It contains xenoliths of the Assemblage A mafic volcanic indicating it post-dates emplacement of these volcanic rocks (Wood, 2016). Deformed, rusty quartz vein intersects the tonalite indicating mineralization post-dates emplacement of these units. The Packman Lake pluton (1807 ± 7 Ma; Wood, 2016; Fig. 3-4) is a quartz syenite unit that likely formed in a syn-collisional environment during peak metamorphic conditions in the Glennie domain (Wood, 2016).

The Porky Lake Group is the youngest unit in the area and comprises a series of arkose/arenites, wackes, conglomerates and biotitic sediments (Delaney, 1986; Fig. 3-4). The arkose/arenite locally preserves crossbedding which denotes a younging direction to the south (Delaney, 1986). Porky Lake siliciclastic rocks are mainly exposed in the northwestern portion of Figure 3-4 in the core of the Ray Lake synform. The siliciclastic rocks of the Porky Lake group unconformably overlie the Assemblage B volcanic rocks (Fig. 3-5) along a highly strained contact, believed to represent a change in depositional environments (Lewry, 1977). It is thought this unconformity may have acted as a conduit for mineralizing fluids during deformational events in the Glennie Domain (Delaney and Cutler, 1992).

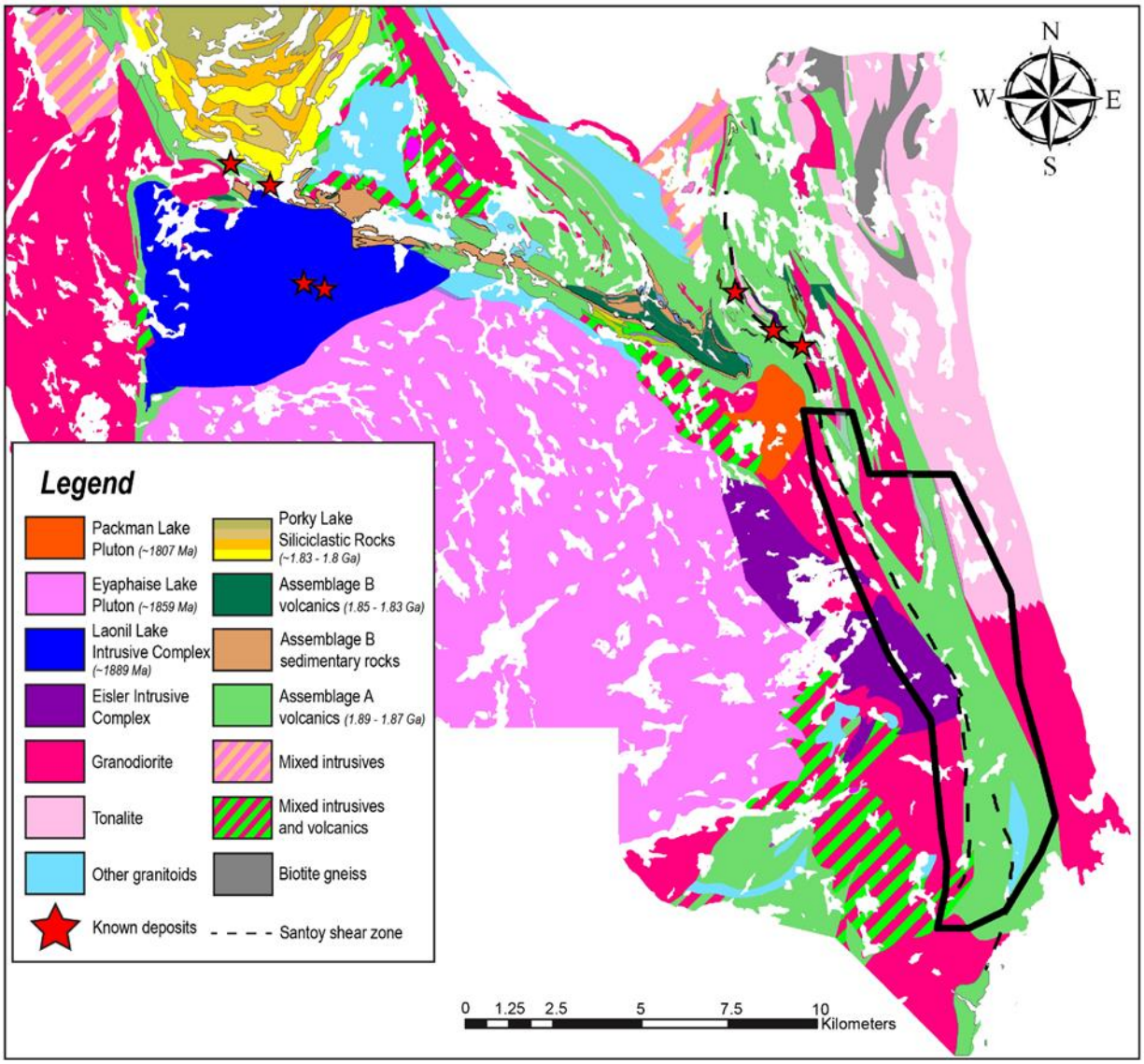

Figure 3-4 Simplified geology of the Pine Lake greenstone belt with Seabee deposits (left-side) and Santoy deposits (right-side) and the focus area of this research within the Fisher property outlined in black (modified from Delaney, 2016).

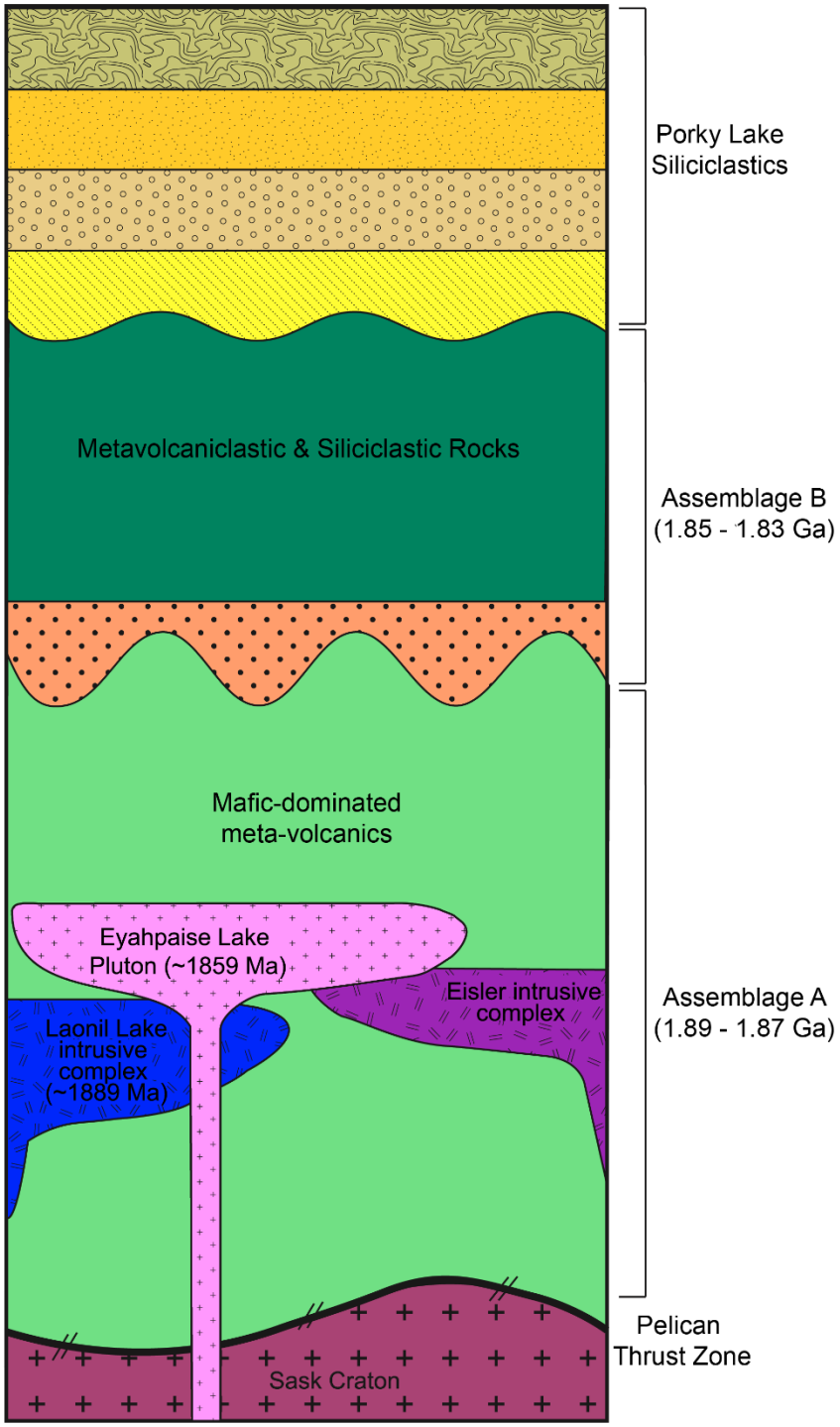

Figure 3-5 Schematic stratigraphic section through the Pine Lake greenstone belt (modified from Wood, 2016). Colours used in this section correspond to those in Figure 3-4.

The important structural feature to the Seabee Gold Operation is the Santoy shear zone (Fig. 3-4), which exact extents are not well defined, but is believed to be at least 3.5 km long (Wood, 2016). Four deformational events can be observed in the Seabee Gold Operation. D_1 included two folding events (F_1 and F_2) characterized by isoclinal recumbent folding and associated foliations related to SW-thrusting (Wood, 2016). D_2 resulted from convergence of the Hearne, Sask and Superior provinces at about 1840 to 1800 Ma, which corresponds to peak metamorphism in the Glennie domain. This event refolded F_2 folds which produced a composite $S_{0/1}$ foliation resulting in an axial planar S_2 foliation. This S_2 foliation is typically defined by hornblende and/or biotite in most suites in the area, parallels bedding and dips moderately-steeply to the NE (Wood, 2016).

During D_3 (~1800 - 1736 Ma; Wood, 2016), F_2 folds and the composite $S_{0/1/2}$ foliation were refolded about a NNW-trending axes, corresponding to the Tabbernor fault zone, which locally produced type two and three interference patterns (Delaney and Cutler, 1992; Ramsey and Huber, 1987). F_3 sheath-like folds are WNW-trending and include the Ray Lake fold, Carruthers Lake antiform and Carruthers Lake synform (Wood, 2016). They along with the Pine Lake greenstone belt, warped around the competent Eyahpaise Lake pluton. The F_3 folds have an S_3 axial planar cleavage typically defined by biotite (Wood, 2016). A L_2 lineation is also locally preserved in these $S_{2/3}$ foliation surfaces as a penetrative mineral lineation defined by the alignment of amphibole and biotite (Wood, 2016).

D_3 is of economic significance as it is believed to be responsible for creating the compressional jog in an early phase of the Santoy shear zone which created the space for gold mineralizing fluids to precipitate. This jog was produced by dextral-reverse oblique slip movement along the Santoy Shear zone. The Packman Lake pluton also had an important role as it acted as a buttress around which the supracrustal rocks were warped (Wood, 2016). A L_3 curvilinear,

stretching lineation has been noted to parallel high-grade ore in the Santoy 8 and 8 East deposits and tend to control the geometry of the folds (Wood, 2016; Helmsteadt, 1987, 1986). Auriferous quartz veins are folded by F_3 folds indicating vein emplacement occurred before F_3.

Evidence of D_4 is not preserved in the Seabee Gold Operation, but regionally can be recognized by F_4 folds refolding F_3 folds along upright, NE-SW trending fold axes resulting in dome-and-basin interference patterns (Lewry et al., 1990). These F_4 folds preserve the L_3 lineations as weak crenulations overprinting L_2 and $S_{2/3}$.

CHAPTER 4: FISHER PROPERTY LITHOLOGIES

The Fisher property of the Seabee Gold Operation is hosted within Paleoproterozoic rocks of the Glennie Domain. The supracrustal rocks exposed across the Fisher property comprise volcanic rocks of intermediate to mafic compositions, various metasedimentary rocks and felsic-mafic dykes which intersect these units. As previously mentioned, amphibolite grade metamorphic conditions affected this area and were accompanied by subsequent alteration and deformation related to the development of the Santoy shear zone, which runs N-S through the Fisher property (shown by black dotted line; Fig. 4-1). The most common lithologies observed at the Fisher Property consist of mafic volcanic, intermediate volcanic, mixed volcaniclastic, and metasedimentary rocks with lesser granites and diorites. Other rock types encountered across the Fisher property include felsic volcanic, quartz diorite and gabbroic rocks, and various schists.

The various supracrustal volcanic, volcaniclastic and metasedimentary rocks across the Fisher property (shown by shades of green and yellow; Fig. 4-1) are attributed to Assemblage A, discussed further in Chapter 3. The metavolcanic and metasedimentary rocks of Assemblage A broadly trend N-S through the Fisher property and dip steeply (70-90˚) to the east. Assemblage A rocks are the oldest rocks (1.89 – 1.87 Ga) in the Fisher property. On the west side of the Fisher property, the Eisler intrusive complex (shown in purple; Fig. 4-1) intrudes Assemblage A volcanic rocks. The Eisler intrusive complex comprises gabbro, quartz gabbro, pegmatitic gabbro, diorite, pyroxenite and tonalite rocks (Witvoet, 2019). Eisler units trend similarly to Assemblage A rocks with near vertical dips. The Uskik granodiorite (shown in magenta; Fig. 4-1) trends N-S on the far east edge of the Fisher focus area, and the Central Granodiorite (shown in orange; Fig. 4-1) pinches out at the surface on the far north of the Fisher property focus area where it intersects metavolcanic rocks of Assemblage A. Various intrusive rocks can be found across the property, and their sharp

and concordant contacts with supracrustal rocks aided in their identification. The origin of these units can only be speculated until age dating confirms their temporal relationship to surrounding rocks.

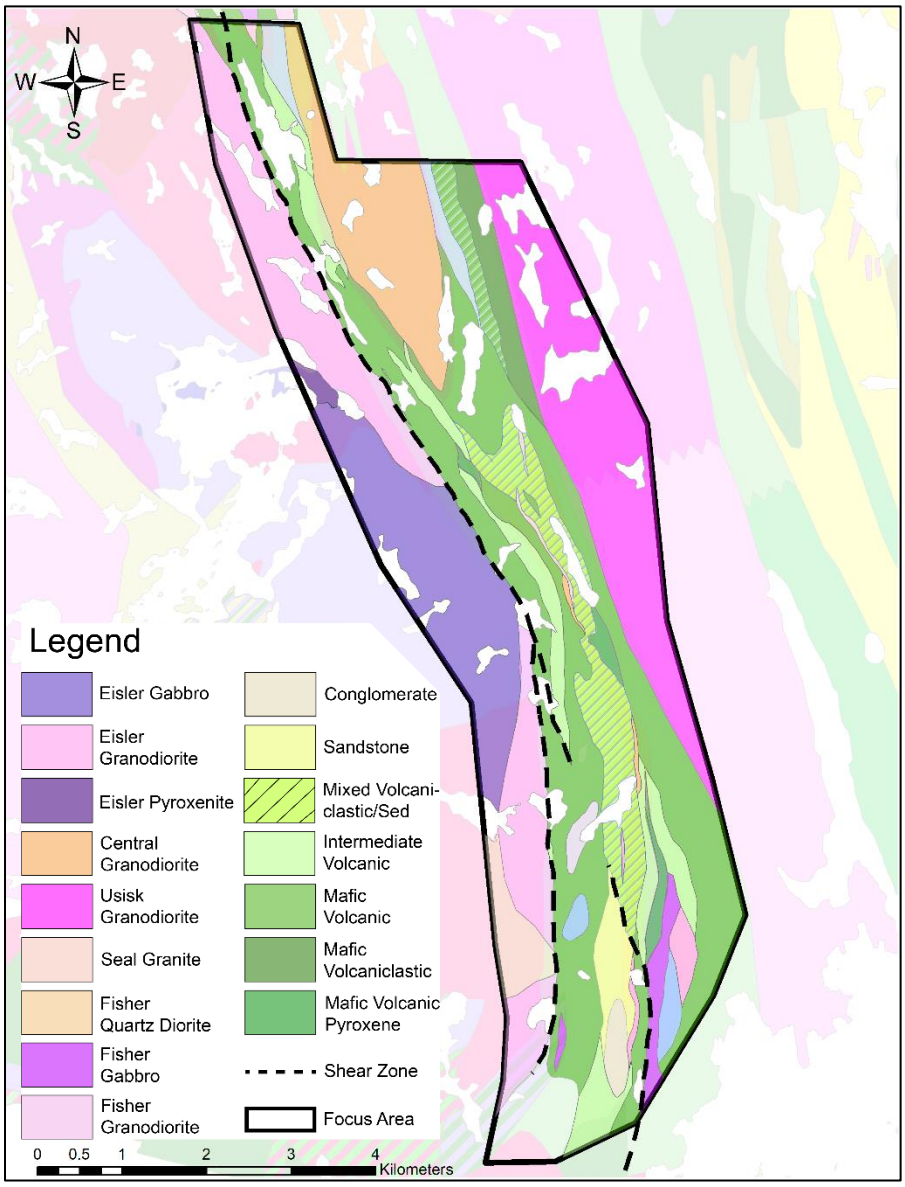

Figure 4-1 Geological map of the "focus area", important to this research, within the Fisher property (extents not shown). Black dashed lines indicate approximate limits of the Santoy shear zone (modified from McEwan, 2013).

4.1 Description of Rock Units

Samples used for this chapter were intended to represent least-altered host rocks to mineralization. The specific samples chosen were based on descriptions and rock names suggested by SSR Mining Inc. logging geologists. However, some of the rock names mentioned in Chapter 4.1 have been reclassified based on geochemical analysis discussed in Chapter 4.2. The overprinting alteration will be discussed further in Chapter 6.

One of the thickest (up to 1km) units at the Fisher property is the Fisher mafic volcanic (Fig. 4-1) which also holds economic significance due to its association with gold mineralization. This unit typically occurs with intermediate volcanic rocks along concordant and gradational contacts. In hand sample, mafic volcanic rocks are fine-grained and medium to dark grey/green in colour (Fig. 4-2a). They are characterized by plagioclase (~10-30%), significant hornblende (20-40%), minor biotite and/or chlorite (5-15%), quartz (~10-25%), and sulphide minerals (0-5%). This predominance of hornblende rather than actinolite (Fig. 4-2e), is typical of basalts that have undergone lower amphibolite facies metamorphism (Spear, 1993). The main fabric associated with D_2 pre-dates gold mineralization and is typically defined by biotite, chlorite and in some cases amphiboles, which becomes increasingly deformed with proximity to the Santoy shear zone. Accessory minerals in this unit include alkali feldspars, apatite, epidote, clinozoisite and titanite. Minor secondary minerals such as sericite and disseminated sulphide minerals are also observed.

A pyroxene-bearing mafic volcanic is differentiated from mafic volcanic rocks based on macroscopic observations of granular relict pyroxenes (Fig. 4-2d) which have been replaced by hornblende (Fig. 4-2h) or secondary chlorite. The unit is locally well-exposed at surface and can

occur up to 250m thick. The unit comprises ~30-60% relict clinopyroxene phenocrysts in a groundmass of fine-grained plagioclase (~30%), and biotite/chlorite (~10%).

The intermediate volcanic rocks are well-exposed at surface on the Fisher property and occur as thick packages (up to 250m) typically in contact with mafic volcanic rocks at surface (Fig. 4-1) and with depth. Hand samples are fine-grained with a medium grey colour (Fig. 4-2b). The intermediate volcanic can be subdivided into two units based on geochemical variations; further discusses in Chapter 4.2. Observations from thin section identified variations in hornblende (Fig. 4-2e) and quartz content between the two units (Andesite-1 and Andesite-2). However, no distinct macroscopic identifiers have been noted. Intermediate volcanic rocks comprise lesser hornblende and plagioclase than the basalt unit, but both exhibit local biotite defining foliation (Fig. 4-2f). Generally, the intermediate volcanic rocks contain 20-40% quartz, 10-30% plagioclase, 5-25% hornblende, and 5-15% biotite and/or chlorite. Accessory minerals are present locally including epidote, titanite, magnetite, diopside, and various sulphide minerals. Myrmekitic textures were locally preserved.

The felsic volcanic unit is a thin package (< 5m) relative to the other volcanic rocks and is not visible at the map scale in Figure 4-1. Overall, the unit does not host significant gold mineralization or exhibit strong alteration, thus minimal samples were collected. The felsic volcanic is a leucocratic, fine-grained unit (Fig. 4-2c) with a groundmass dominated by quartz, minimal biotite defining foliation (Fig. 4-2g) and minor to no hornblende grains. It comprises 30–60% quartz, 10-30% plagioclase, 5-10% alkali feldspars, 5-10% muscovite and/or biotite, and 0-5% hornblende. There is also minor K-feldspar and sericite alteration, but no trace sulphide minerals were identified.

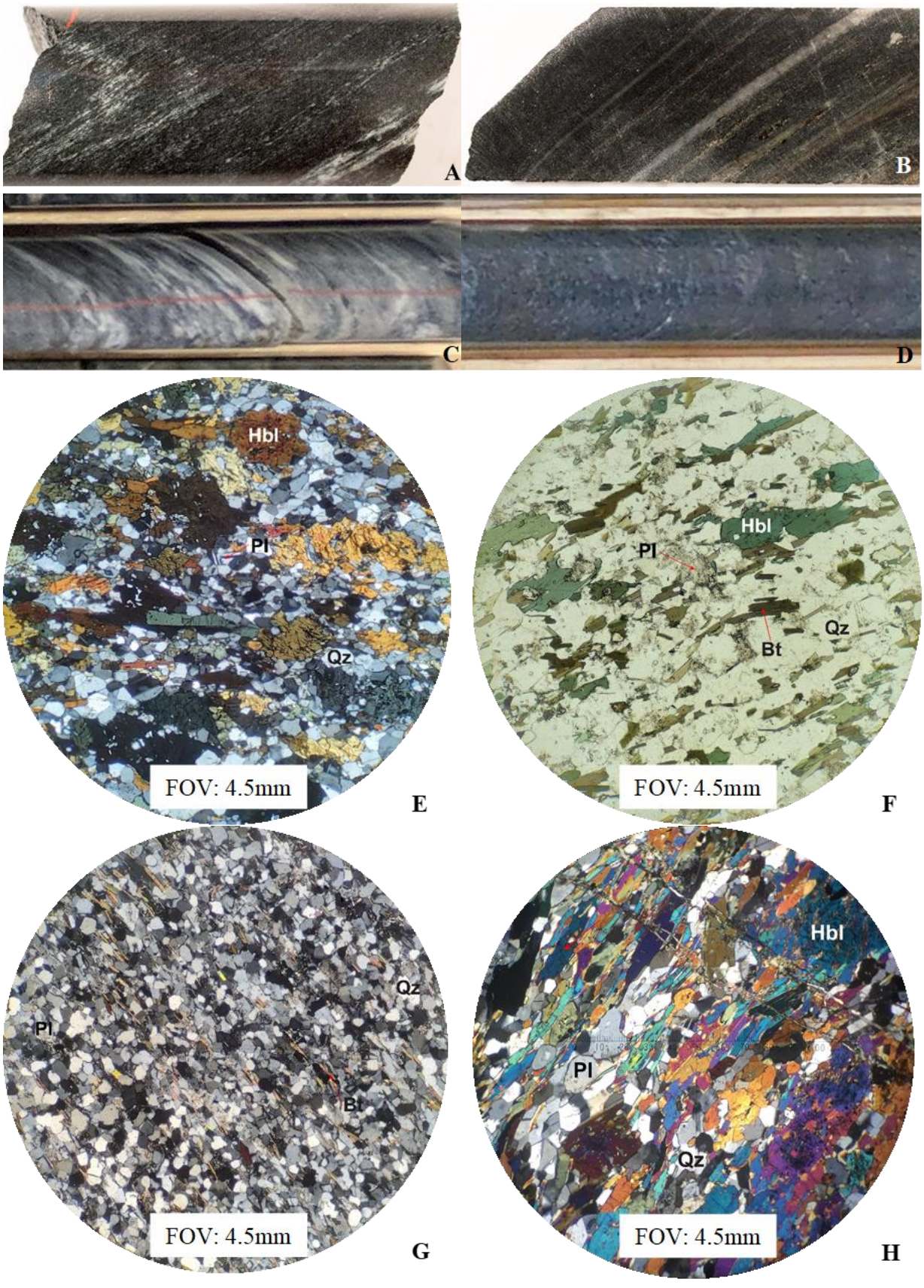
A
B
C
D
Hbl
Pl
Qz
FOV: 4.5mm
E
Hbl
Pl
Bt
Qz
FOV: 4.5mm
F
Qz
Pl
Bt
FOV: 4.5mm
G
Hbl
Pl
Qz
FOV: 4.5mm
H

Figure 4-2 Typical mineral assemblages for representative unaltered extrusive units. A) Fine-grained dark green and moderately strained mafic volcanic with moderate chlorite and biotite alteration (CO-2019-58 135.5m). B) Intermediate volcanic with minor silicification and sericite-pyrite veinlets (CO-2019-57, 108.35m). C) Very fine-grained felsic volcanic exhibiting strain (CO-2019-20, 673.5m). D) A medium-grained dark green clinopyroxene mafic volcanic where granular relict clinopyroxenes have been replaced by hornblende (FIS-18-024; 101.3m). E) Least altered mafic volcanic with coarse hornblende porphyroblasts in a groundmass of finer-grained quartz and plagioclase (CO-2019-123; outcrop). F) Biotite defining foliation in a weakly strained Andesite-1 with hornblende porphyroblasts (CO-2019-11; 157.3 m). G) A fine-grained felsic volcanic with minor biotite along foliation planes (CO-2019-20; 673.6 m). H) Coarse-grained "clinopyroxene mafic volcanic" with hornblende porphyroblasts in a groundmass of mainly plagioclase and lesser quartz (CO-2019-36; 78.1m).

The volcaniclastic units vary in width across the Fisher property. They occur as a mixed package with sedimentary units occurring up to ~500m thick or solely as volcaniclastics up to ~250m (Fig. 4-1). These units are typically distinguished based on macroscopic textures (bedding planes, presence of clasts) which differentiate them from other extrusive rocks. This unit is dacitic-andesitic in composition and includes tuffs. The tuffs are very fine-grained with a groundmass dominated by quartz with minor plagioclase and has biotite and muscovite defining the foliation (Fig. 4-3c). The mineral assemblage includes 20-50% quartz, 10-35% plagioclase, 5-10% alkali feldspars, 10-20% biotite and/or muscovite.

Various sedimentary packages are exposed on the Fisher property and typically occur within the mixed volcaniclastic package (Fig. 4-1). Currently, these include a conglomerate, a greywacke, and a sandstone unit. These units, especially the conglomerate, are identified in the field based on textural and grain size observations at the macroscopic level. The conglomerate comprises felsic to intermediate in composition clasts and can occur interbedded with mafic volcanic or sedimentary rocks of felsic composition. The groundmass has a felsic composition of dominantly quartz with andesitic to rhyolitic, pebble-sized clasts. Trace garnets have also been identified in this unit. The sandstone unit is fine to very fine-grained with very little to no micas present. The

unit comprises ~ 50-70% quartz, 20-40% plagioclase, and ~5% muscovite (Fig. 4-3d). The wacke is fine-grained and of intermediate composition with a groundmass of quartz and plagioclase and biotite altering to chlorite locally along foliation planes (Fig. 4-3e). Throughout the remainder of this paper, these units will be collectively referred to as “metasedimentary rocks”, since few representative samples were collected.

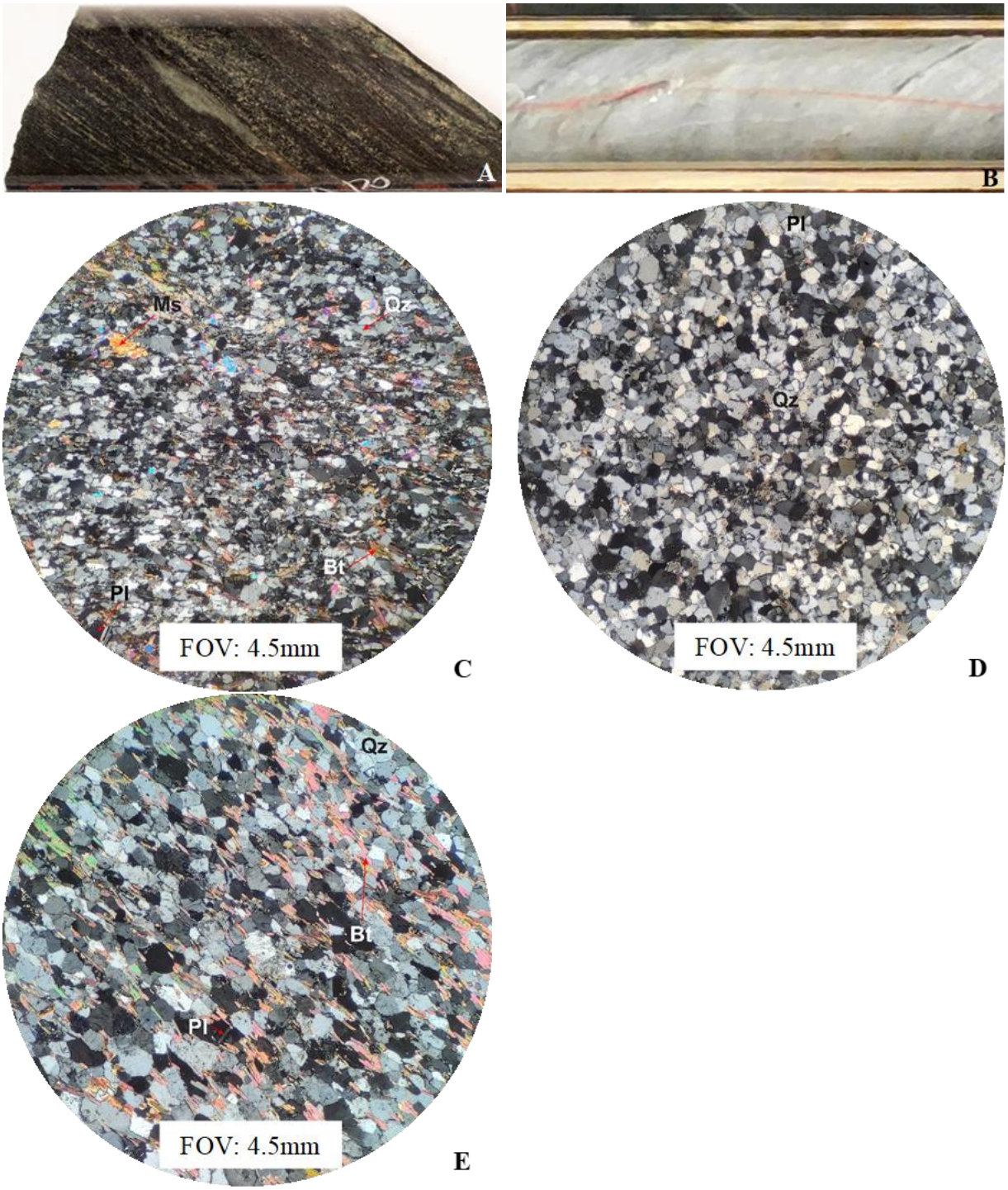

Figure 4-3 A) A fine-grained metasedimentary rock with minor pyrrhotite and chlorite alteration (FIS-19-035; 107.8m). B) A leucocratic very fine-grained metasedimentary rock (FIS-18-017; 409.1m). C) Very fine-grained dacitic ash tuff with minor biotite and muscovite (CO-2019-117; surface). D) A fine-grained sedimentary rock with a groundmass of dominantly quartz (CO-2019-17; 409.2 m). E) Metamorphosed wacke with biotite along foliation planes and minor sericitization of feldspars (CO-2019-56A; 107.8 m).

The granite unit, referred to as “Fisher Granodiorite” in Figure 4-1, typically intrudes the mafic volcanic unit, and is exposed on surface near the southern margins of the “focus area” of this research. In hand sample, granites are light grey with a pink tinge and black flecks (Fig. 4-4a). The rock is roughly equigranular and coarse-grained with a quartz-dominated groundmass and minor biotite and muscovite (Fig. 4-5a). The mineral assemblage includes approximately 30–60% quartz, 20-30% alkali feldspars, 10–20 % plagioclase, 5–15 % muscovite and/or biotite and trace sulphides. Accessory minerals include apatite, zircon, and orthopyroxene. The unit exhibits minor to moderate sericitization of feldspars. Foliation fabrics are not well-preserved in the unit, but grains are locally elongated where shear zones intersect. Pyrite is a common disseminated sulphide in this unit.

The diorite, referred to as “Fisher Gabbro” in Figure 4-1, is a unit that is commonly mis-logged as a gabbro unit. The melanocratic appearance observed in core samples (Fig. 4-4c) makes identification difficult. The rock is finer-grained relative to the granite and granodiorite units with a groundmass of relatively equal quartz to plagioclase and larger crystals of hornblende (~1-2mm; Fig. 4-5c). It comprises 15-35% quartz, 20-40% plagioclase, 5-25% hornblende, and 5-15% biotite and/or chlorite. Zircon, titanite and calcite are accessory within this unit and trace pyrrhotite is common.

The quartz diorite is a less-common unit, and its surface extents are currently unknown. The unit can be difficult to distinguish from granites in the field. However, in hand sample the unit has a distinct salt and pepper appearance (Fig. 4-4d), while in thin section, more hornblende and biotite are noted (Fig. 4-5b). This unit is coarse-grained and equigranular with polygonal quartz similar to the granite. It is characterized by plagioclase (20-40%), quartz (20-40%), biotite and/or chlorite

(5-15%), and hornblende (5-10%). Accessory minerals include titanite and zircon and overall has minor sericitization of feldspars.

The extent of the gabbro unit through the Fisher property is currently unknown since many selected samples had a dioritic composition. Hand samples are mainly black with white specks throughout (Fig. 4-4c). The unit does not show any clear relationships with sulphide minerals and gold grades. It is coarse-grained with large crystals of hornblende (~2.5mm) in a finer groundmass of quartz and plagioclase. Locally, large relict plagioclase grains are moderately sericitized with twinning still preserved (Fig. 4-5d). The unit has 10-20% quartz, 25-45% plagioclase, 10-30% hornblende and ~10% biotite/chlorite. Accessory minerals such as epidote, titanite and magnetite occur as well as minor sericite and tremolite.

The pyroxenite unit is not very common throughout the Fisher property and occurs as 5-10m thick packages (Fig. 4-1). Coarse-grained relict pyroxenes have been replaced by hornblende and ilmenite exsolutions are commonly observed (Fig. 4-5e). The unit has a finer groundmass of mainly cummingtonite and lesser plagioclase and quartz.

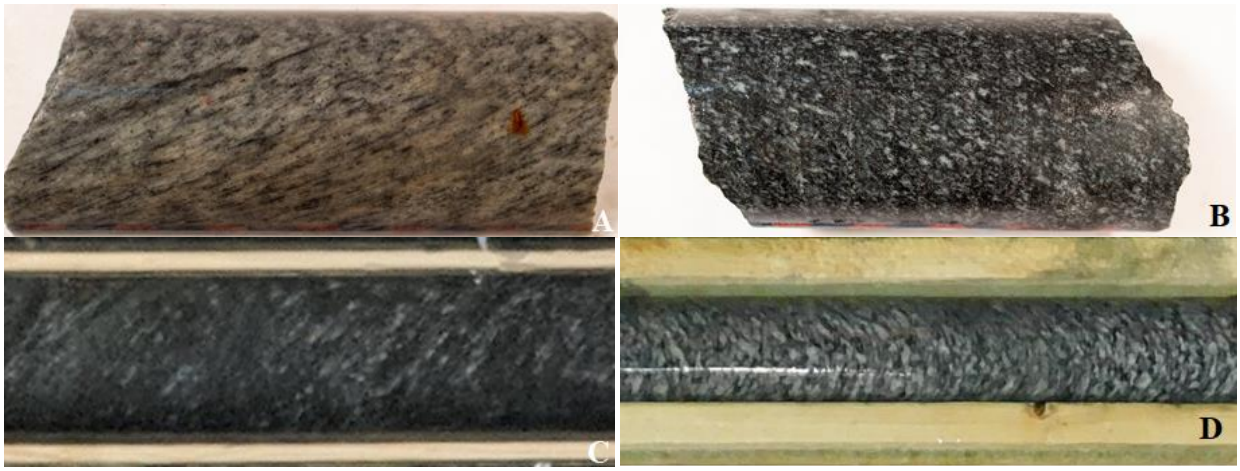

Figure 4-4 Typical mineral assemblages for various unaltered intrusive suites. A) A medium to coarse-grained granite with a weak fabric defined by biotite (FIS-18-021, 249.5m). B) A medium-grained least-altered diorite (FIS-19-030, 136.6m). C) A coarse-grained melanocratic gabbro (FIS-18-017; 720m). D) Coarse-grained quartz diorite with a speckled-appearance (FIS-18-001; 244.6m).

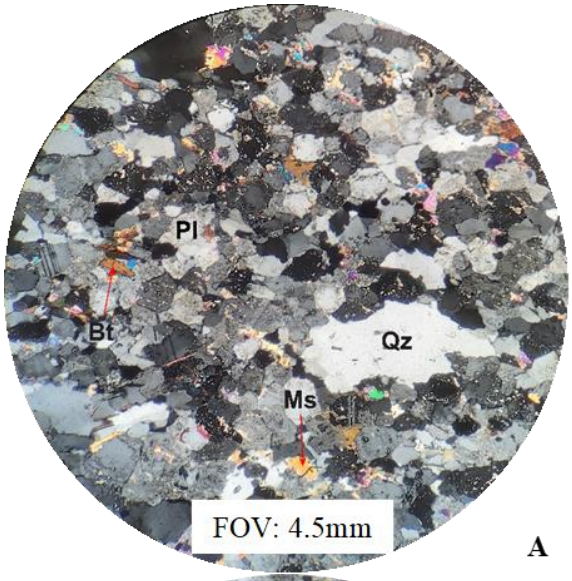
Pl
Bt
Qz
Ms
FOV: 4.5mm

A

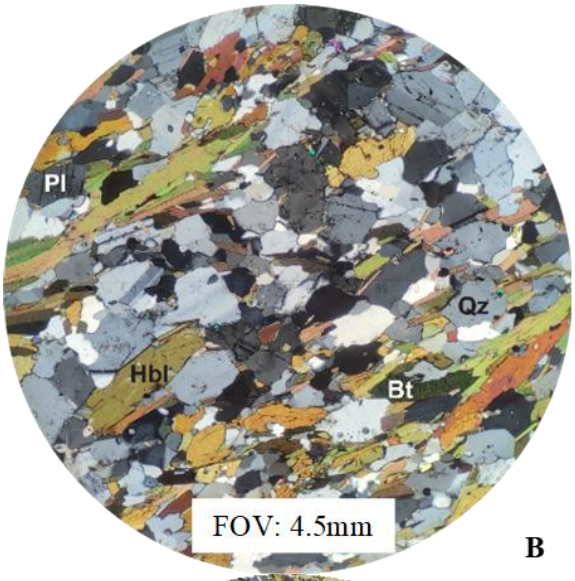
Pl
Qz
Hbl
Bt
FOV: 4.5mm

B

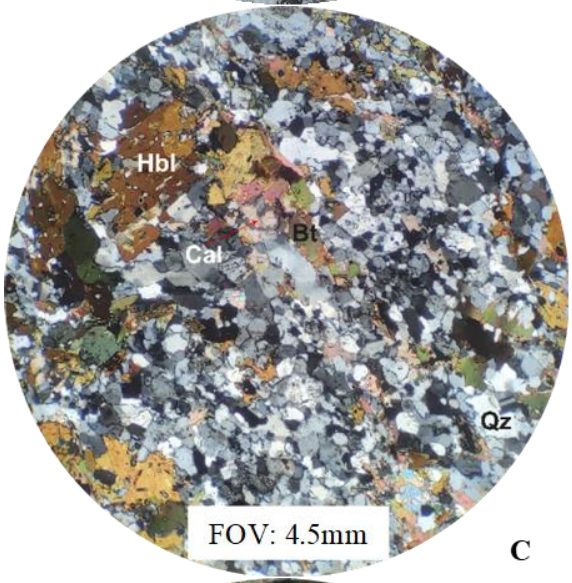
Hbl
Bt
Cal
Qz
FOV: 4.5mm

C

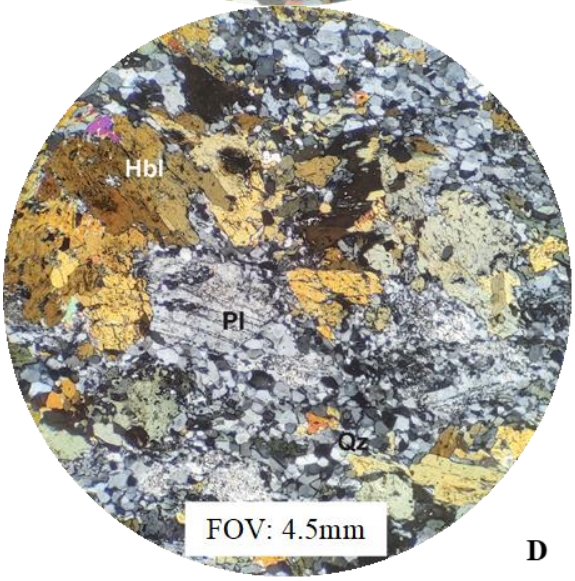
Hbl
Pl
Qz
FOV: 4.5mm

D

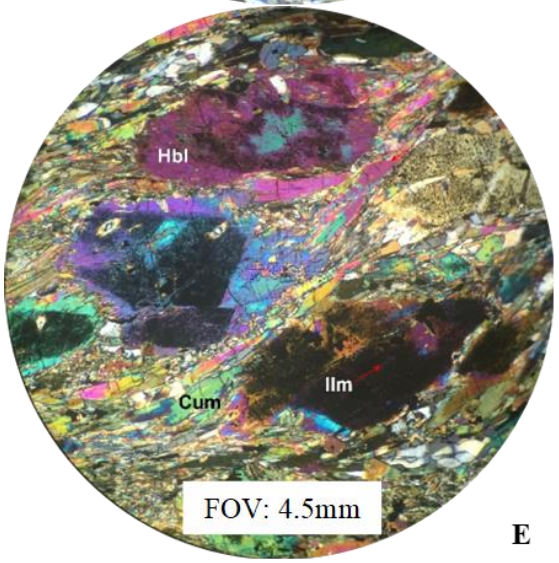
Hbl
Cum
Ilm
FOV: 4.5mm

E

Figure 4-5 A) A granite dominated by coarse-grained quartz and finer plagioclase exhibiting minor sericitization (CO-2019-48; 249.1 m) B) Coarse-grained quartz diorite with minor deformation of hornblende porphyroblasts (CO-2019-08, 392.5 m). C) Diorite unit with a finer groundmass of quartz and plagioclase and hornblende porphyroblasts (CO-2019-81B; 56 m). D) A gabbro with sericitized coarse grains of plagioclase in a finer groundmass of quartz (CO-2019-31; 60.8 m). E) Hornblende porphyroblasts with ilmenite exsolutions in a groundmass of cummingtonite and plagioclase (CO-2019-33; 191.1m).

4.2 Lithogeochemistry

When classifying rocks which have undergone alteration and/or metamorphism it is important to differentiate units using conserved elements. Conserved elements are those which are not actively involved in material transfer processes, and thus stay relatively constant or immobile as rocks undergo chemical processes (Nicholls, 1988). All elements were plotted in bivariate Harker diagrams to assess their mobility (Fig. 4-6). At the Fisher property, most high field strength elements (HFSEs) and rare earth elements (REEs) exhibit conserved element behavior (Fig. 4-6) and are acceptable to use for interpreting magmatic affinities. Zirconium and titanium were identified as conserved elements, while also displaying variations due to host rock chemical compositions and were used to classify the host rocks of the Fisher deposit. This approach identified five intrusive suites: a gabbro, pyroxenite, diorite, quartz diorite and granite unit (Fig. 4-7a). At least four extrusive units including basalts (mafic volcanic rocks from Ch.3.1), two andesite units (intermediate volcanic rocks from Ch.3.1) and rhyolites (felsic volcanic rocks from Ch.3.1) were identified (Fig. 4-7a).

The basalts were further discriminated into High Cr Basalts (HCrB) and Low Cr Basalts (LCrB) based on their respective chromium content. HCrB are those with greater than 60ppm Cr, while LCrB are those with less than 60ppm Cr. Sedimentary and volcaniclastic units were identified using a combination of hand sample and thin section observations and are also shown in selected classification diagrams (Fig. 4-7a,b,c). A conserved element classification diagram

(Pearce, 1996) using Zr/Ti and Nb/Y ratios (Fig. 4-7b) also agrees with the bivariate Zr vs Ti classification diagram. When compared to classification diagrams using major elements for volcanic rock classification (Fig. 4-7c) and plutonic rock classification (Fig. 4-7d), similarities are observed. It is important to note that the discrepancies in host rock classification between figures 4-7c and 4-7d are likely due to effects of metamorphism and/or alteration. Geochemical characteristics of rock units identified by Figure 4-7a will be discussed below.

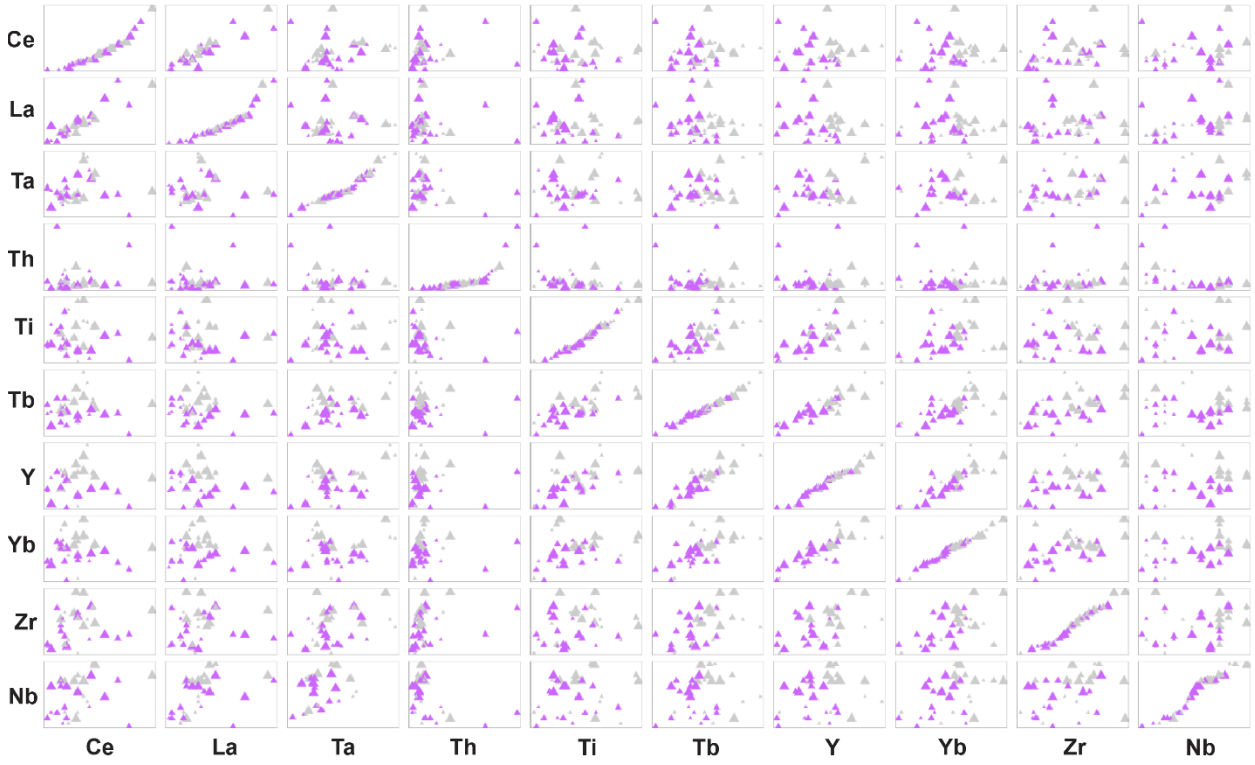

Figure 4-6 Scatterplot matrix of selected conserved elements in HCrB and LCrB (n=36). Probability plots are shown along the diagonal and show the shape of the distribution of the unit.

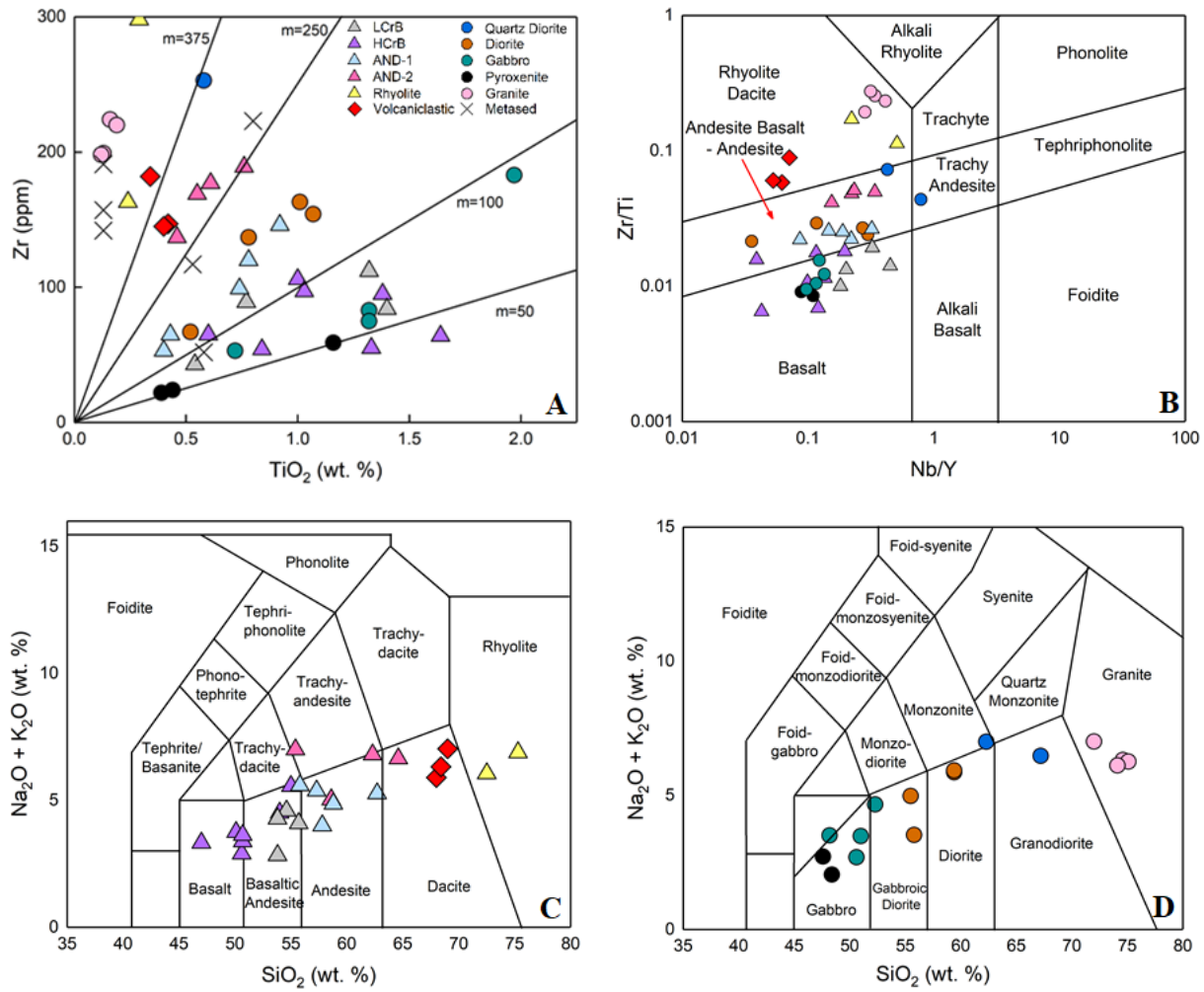

Figure 4-7 Various trace element (A,B) and major element (C,D) plots for classifying igneous rock types. A) Zr vs. TiO2 classification diagram makes use of Zr/Ti ratios (from Hallberg, 1984) and natural breaks in the data. B) Zr/Ti vs. Nb/Y classification diagram for volcanic rocks from (Pearce, 1996). Note that Nb may be relatively mobilize in the Fisher area (Fig.6-15c) and should be used with caution. C) TAS classification diagram for volcanic rocks (from Le Maitre et al, 1989). D) TAS classification diagram for plutonic rocks (from Middlemost, 1994).

Table 4-1 Average chemical compositions of least-altered Fisher host rocks.

Lithology			HCrB	LCrB	AND-1	AND-2	Rhy	VCLST	PYRX	GAB	DIO	GRNT	QD
# of samples			8	4	4	2	2	3	3	4	3	4	2
		Detection Limit											
SiO_2	(%)	0.10%	51.85	54.03	58.40	61.90	73.90	68.47	48.00	50.53	58.47	73.95	62.00
TiO_2	(%)	0.01%	1.06	1.05	0.59	0.53	0.27	0.39	0.66	1.33	1.07	0.15	0.50
Al_2O3	(%)	0.01%	16.03	17.28	15.40	16.85	13.90	13.87	11.90	15.28	15.77	13.88	16.45
Fe_2O_3	(%)	0.01%	11.23	10.95	7.91	6.35	2.17	6.09	12.50	12.09	9.01	2.53	5.61
MnO	(%)	0.01%	0.16	0.16	0.12	0.09	0.03	0.11	0.18	0.15	0.13	0.05	0.09
MgO	(%)	0.01%	5.46	3.33	4.15	2.25	0.62	0.89	13.23	6.13	2.24	0.24	2.94
CaO	(%)	0.01%	8.64	7.54	7.22	4.42	1.91	2.23	10.10	9.36	5.62	1.62	5.23
Na_2O	(%)	0.01%	3.06	3.49	3.30	3.27	3.92	3.12	1.67	3.08	3.14	4.81	4.02
K_2O	(%)	0.01%	1.19	0.96	1.76	2.57	2.56	3.30	0.67	0.50	2.83	1.62	2.00
P_2O_5	(%)	0.01%	0.20	0.31	0.10	0.12	0.03	0.08	0.09	0.23	0.42	0.02	0.14
LOI	(%)	0.10%	0.91	0.75	1.20	1.35	0.85	1.07	1.23	1.15	1.17	1.08	0.70
Ba	(ppm)	1 ppm	348	414	686	1076	1025	854	169	146	725	557	700
Be	(ppm)	0.1 ppm	7.6	9.3	8.4	4.2	10.3	1.6	7.9	8.1	10.5	10.6	8.4
Cs	(ppm)	0.1 ppm	2.7	4.9	3.0	2.8	2.5	0.9	3.3	1.2	0.7	0.6	1.9
Ga	(ppm)	0.1 ppm	16.7	15.6	15.3	17.0	15.6	17.3	11.5	17.0	16.4	15.4	18.2
Ge	(ppm)	0.1 ppm	0.5	0.1	1.2	0.9	1.2	0.4	1.4	1.2	0.1	0.1	1.0
Hf	(ppm)	0.1 ppm	2.1	2.5	2.4	3.8	6.4	4.5	1.0	2.5	4.6	6.9	3.3
Nb	(ppm)	1 ppm	5	11	3	5	12	3	2	3	10	15	8
Rb	(ppm)	0.1 ppm	26.6	23.6	56.4	64.1	53.9	59.2	39.0	8.7	53.9	30.2	50.8
Ta	(ppm)	0.01 ppm	0.27	0.32	0.45	0.51	1.12	0.36	0.31	0.36	0.40	0.95	0.81
Th	(ppm)	0.01 ppm	3.26	2.38	3.49	5.95	11.25	8.21	3.89	1.00	1.98	6.78	7.35
U	(ppm)	0.01 ppm	3.66	2.25	2.70	2.44	3.97	1.84	7.95	0.86	1.96	3.25	21.58
Sr	(ppm)	1 ppm	369	389	396	139	149	133	308	427	252	142	580
Zr	(ppm)	2 ppm	78	94	84	142	231	158	35	99	150	210	126
Ag	(ppm)	0.1 ppm	1.0	0.4	1.2	0.4	0.7	<0.1	1.4	0.8	0.4	0.5	2.4
As	(ppm)	0.1 ppm	2.4	2.7	2.7	1.1	5.4	0.1	1.4	4.7	2.9	4.4	2.6
Bi	(ppm)	0.1 ppm	0.9	0.1	0.2	0.2	0.1	<0.1	0.3	0.1	0.1	0.1	0.3
Mo	(ppm)	0.1 ppm	1.8	2.2	2.4	0.8	2.1	0.8	1.9	1.6	3.1	2.7	1.5
Sb	(ppm)	1 ppm	2	3	1	1	3	<1	1	2	4	4	2
Sn	(ppm)	0.1 ppm	2.1	1.4	3.5	0.7	2.2	0.4	1.4	1.6	1.4	2.4	2.8
Pb	(ppm)	0.02 ppm	8.48	4.44	5.95	7.57	5.33	7.59	4.76	4.29	4.12	6.37	10.62
W	(ppm)	1 ppm	6	2	11	10	3	2	7	2	2	1	14
Co	(ppm)	0.1 ppm	34.2	30.4	24.5	24.1	3.8	3.8	64.1	39.6	18.2	3.1	17.4
Cr	(ppm)	2 ppm	137	23	119	20	9	12	808	170	8	26	108
Ni	(ppm)	1 ppm	71	15	34	9	8	2	279	78	15	12	38
V	(ppm)	2 ppm	242	214	155	73	16	22	236	256	126	31	86
Cu	(ppm)	0.1 ppm	62.1	63.3	32.3	252.9	32.2	10.0	82.4	68.5	47.7	21.5	14.3
Zn	(ppm)	1 ppm	118	129	96	81	48	81	120	111	95	52	102
Ce	(ppm)	1 ppm	30	33	31	48	96	55	14	23	43	74	51
Dy	(ppm)	0.01 ppm	4.00	4.74	3.06	4.15	6.83	7.11	2.24	4.22	6.42	7.19	2.45
Er	(ppm)	0.01 ppm	2.23	2.76	1.39	2.76	3.48	5.18	1.19	2.16	3.41	4.78	1.09
Eu	(ppm)	0.01 ppm	1.16	1.55	1.15	1.14	1.60	1.38	0.74	1.28	1.69	1.32	1.16
Gd	(ppm)	0.01 ppm	3.62	4.55	2.87	4.04	6.71	5.81	1.83	3.40	6.82	7.34	2.77
Ho	(ppm)	0.01 ppm	0.85	1.15	0.67	0.92	1.47	1.61	0.51	0.93	1.42	1.75	0.47
La	(ppm)	1 ppm	15	18	14	23	48	26	5	10	24	38	26
Lu	(ppm)	0.01 ppm	0.37	0.44	0.32	0.58	0.68	0.82	0.22	0.42	0.59	0.84	0.24
Nd	(ppm)	0.1 ppm	18.1	20.1	15.3	23.1	42.0	30.1	8.0	13.8	26.8	36.9	20.1
Pr	(ppm)	0.01 ppm	4.12	4.40	4.03	6.08	11.84	7.42	1.92	3.37	6.11	9.09	6.07
Sc	(ppm)	2 ppm	27	26	20	16	5	13	35	29	16	4	11
Sm	(ppm)	0.01 ppm	3.88	4.29	3.28	4.67	8.30	6.36	1.74	3.44	5.89	7.55	3.52
Tb	(ppm)	0.01 ppm	0.53	0.58	0.45	0.59	0.97	0.95	0.34	0.68	0.81	0.96	0.38
Tm	(ppm)	0.01 ppm	0.38	0.48	0.27	0.44	0.57	0.81	0.20	0.35	0.60	0.87	0.22
Y	(ppm)	0.01 ppm	22.44	27.13	18.23	28.00	39.05	42.73	13.87	25.43	35.10	45.15	13.64
Yb	(ppm)	0.01 ppm	2.49	3.22	1.67	3.32	4.14	5.68	1.30	2.43	4.19	5.91	1.30

The average HCrB unit is characterized by 52 wt.% SiO_2, 11.2 wt.% Fe_2O_3, 5.5 wt.% MgO and 8.6 wt.% CaO (Table 4-1). The average LCrB is characterized by 54 wt.% SiO_2, 11 wt.% Fe_2O_3, 3.3 wt.% MgO and 7.5 wt.% CaO (Table 4-1). Samples with a Cr-CLR value of more than

0.82 were assigned to HCrB and those with less than 0.82 were assigned to LCrB (Fig. 4-8a). The average Cr content in HCrB (137 ppm; Table 4-1) and LCrB (23 ppm; Table 4-1), relative to 170 ppm in an average basalt (Price, 1997) suggests these samples are relatively depleted in Cr. Both units share relatively similar extended trace element variation diagrams with negative anomalies in Nb and Ti, and enrichments in LREEs relative to HREEs (Fig. 4-8b). Specifically, LCrB are more enriched in Y, Yb, and Tb relative to HCrB (Fig. 4-6). The characteristic negative Nb and Ti anomalies and the location of HCrB and LCrB in Figure 4-8e indicate an arc environment. When discriminating magmatic affinities using Jensen's Cation Plot, which uses major elements, LCrB are enriched in Fe relative to HCrB and have a more tholeiitic affinity, whereas HCrB have a more calc-alkaline affinity (Fig. 4-8c). However, when using Ross and Bédard's classification diagram, the distinction in Th/Yb values is not as defined (Fig. 4-8d). The average HCrB is also enriched in Pb relative to LCrB and other Fisher host rocks (Table 4-1).

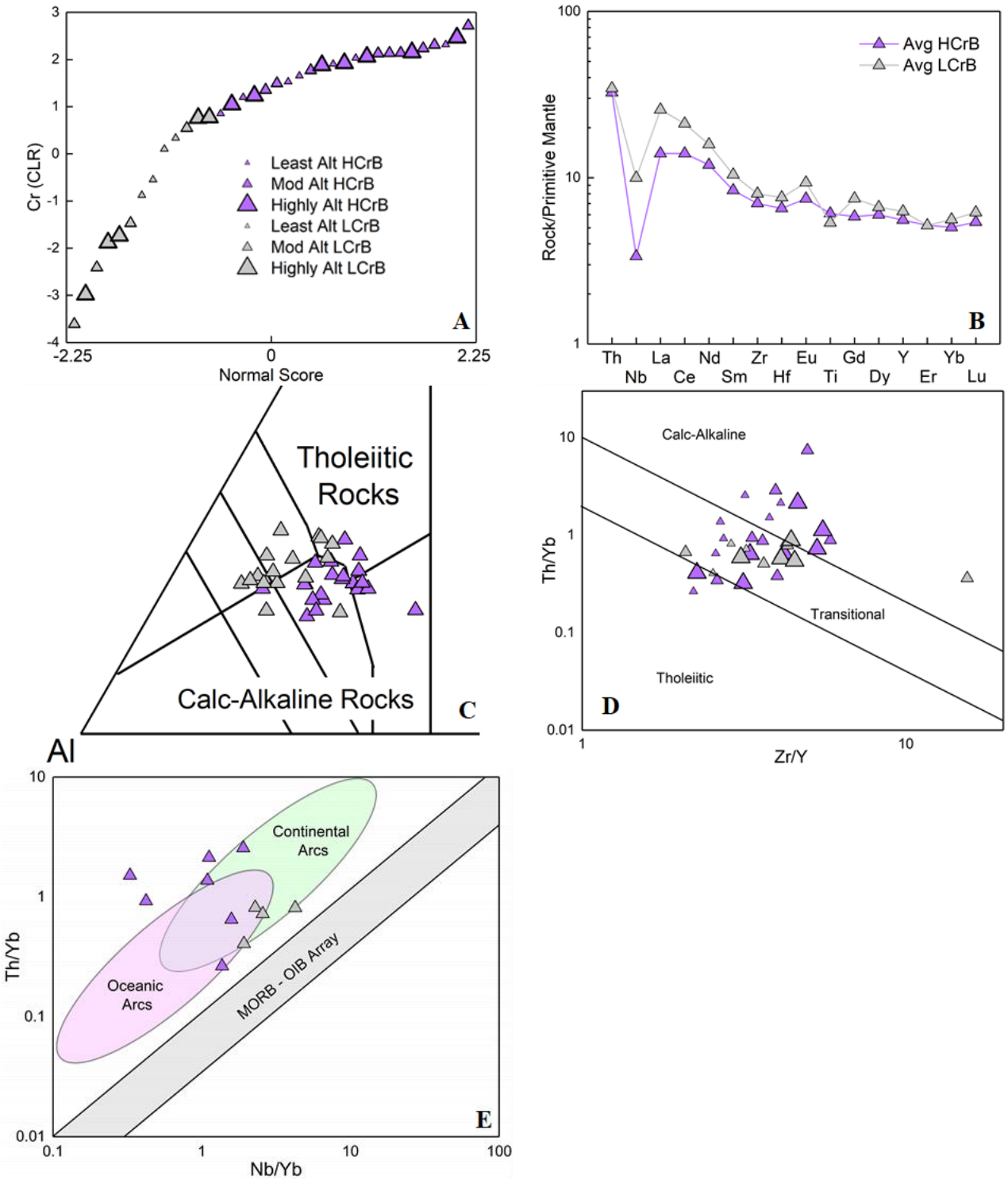

Figure 4-8 Various basalt discrimination diagrams displaying HCrB and LCrB. A) Probability plot of CLR-transformed Cr with normal score of -0.56. B) Extended variation diagram normalized to primitive mantle. Line represents average of all least-altered samples for the corresponding unit. C) Jensen Cation Plot for classification of subalkaline volcanic rocks using cations of Fe_2O_3(total), Al and Mg (Jensen, 1976). D) Th/Yb vs. Zr/Y diagram for discrimination of magmatic affinities from Ross and Bédard (2009). E) Th/Yb vs. Nb/Yb classification diagram of basalts modified from subduction-related settings (Pearce, 2014, 2008).

The average Andesite-1 (AND-1) is characterized by 58 wt.% SiO_2, 7.9 wt.% Fe_2O_3, 4.2 wt.% MgO, 7.2 wt.% CaO and 3.3 wt.% Na_2O (Table 4-1). Andesite-2 (AND-2) is characterized by 61.9 wt.% SiO_2, 6.4 wt.% Fe_2O_3, 2.3 wt.% MgO, 4.4 wt.% CaO and 3.3 wt.% Na_2O (Table 4-1). Andesite-1 and Andesite-2 have calc-alkaline Th/Yb values (Fig. 4-9a,b) and have a trace element signature typical of arc environments (Fig. 4-9c). Andesite-2 is enriched in LREEs relative to Andesite-1 (Fig. 4-9d), indicating a more felsic composition. Andesite-2 is especially enriched in Zr, Hf, Ce, La, Y, Th and Nb relative to Andesite-1 (Table 4-1).

The average rhyolite (Rhy) is characterized by 74 wt.% SiO_2, 2.2 wt.% Fe_2O_3, 1.9 wt.% CaO and 3.9 wt.% Na_2O (Table 4-1). The average volcaniclastic (VCLST) is characterized by 69 wt.% SiO_2, 6.1 wt.% Fe_2O_3, 2.2 wt.% CaO and 3.1 wt.% Na_2O (Table 4-1). The rhyolite has a calc-alkaline affinity, while volcaniclastics have a transitional to calc-alkaline affinity (Fig. 4-9a,b). Rhyolites exhibit strong enrichments in trace elements (Fig. 4-9c) and have slightly steeper LREE trends (Fig. 4-9d) relative to all volcanic rocks.

The average pyroxenite (PYRX) is characterized by 48 wt.% SiO_2, 12.5 wt.% Fe_2O_3, 13.2 wt.% MgO and 10.1 wt.% CaO (Table 4-1). The average gabbro (GAB) is characterized by 51 wt.% SiO_2, 12.1 wt.% Fe_2O_3, 6.1 wt.% MgO and 9.4 wt.% CaO (Table 4-1). Fisher gabbro rocks and pyroxenites also have tholeiitic to transitional Th/Yb values (Fig. 4-9a,b). Pyroxenite and gabbro rocks are enriched in Ni, Cr, Co, and Cu and depleted in Zr, Th, Tb, Pr, Nd, Lu, La, and Ce.

The average diorite (DIO) is characterized by 59 wt.% SiO_2, 9.0 wt.% Fe_2O_3, 2.2 wt.% MgO, 5.6 wt.% CaO and 3.1 wt.% Na_2O (Table 4-1). The average granite (GRNT) is characterized by 74 wt.% SiO_2, 2.5 wt.% Fe_2O_3, 1.6 wt.% CaO and 4.8 wt.% Na_2O (Table 4-1). The average quartz

diorite (QD) is characterized by 62 wt. % SiO_2, 5.6 wt.% Fe_2O_3, 5.2 wt.% CaO and 4.0 wt.% Na_2O (Table 4-1). Diorites, quartz diorites and granites have a transitional to calc-alkaline signature (Fig. 4-9a,b).

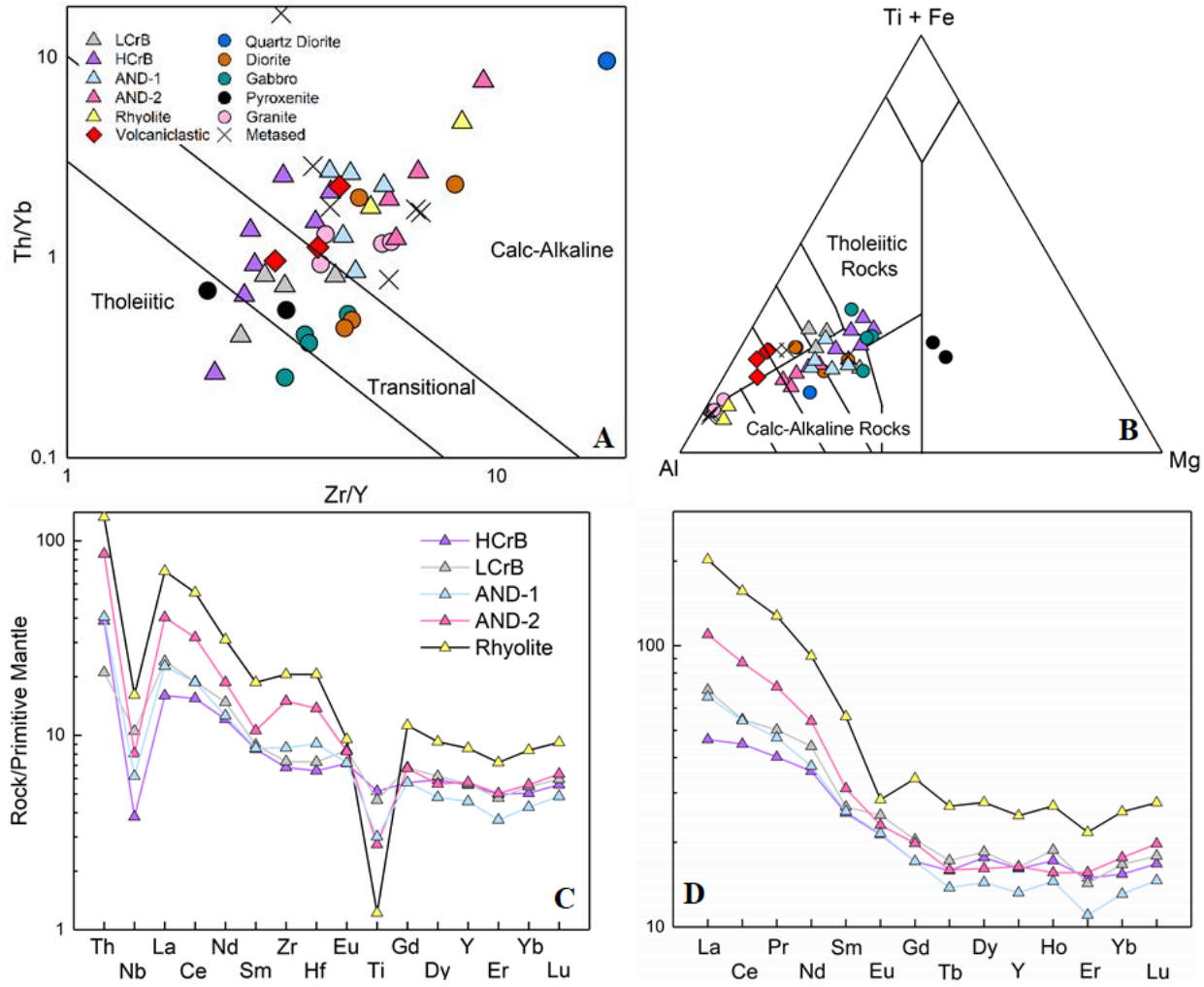

Figure 4-9 A) Fisher rocks plotted on a Th/Yb vs. Zr/Y diagram for discrimination of magmatic affinities from Ross and Bédard (2009). B) Jensen Cation Plot for classification of subalkaline volcanic rocks using cations of $Fe_2O_{3(total)}$, Al and Mg (Jensen, 1976). C) Representative volcanic rocks normalized to primitive mantle (from Sun and McDonough, 1989). Line represents average of all least-altered samples for the corresponding unit. D) Representative volcanic rocks normalized to chondrite (from McDonough and Sun, 1995). Line represents average of all least-altered samples for the corresponding unit.

CHAPTER 5: MINERAL CHEMISTRY

Unaltered and altered rocks were selected for electron microprobe analysis (EMPA). Least altered samples were analyzed with the intent of gathering additional information on the mineralogy of least-altered samples to provide a reference for altered samples. Understanding chemical variations of minerals associated with alteration in orogenic gold deposits has been well studied (Dubosq et al., 2019, Gaillard et al., 2018; Lawley et al., 2015). Identification of phases related to mineralization versus those related to metamorphism is difficult at a macroscopic level, especially in amphibolite facies metamorphosed rocks. Thus, characterizing the variations with microprobe analysis can provide additional insights.

Fisher Host Rocks:

Least-altered samples analyzed included an Andesite-2 (CO-2019-19), an altered HCrB (CO-2019-28A2), a pyroxenite (CO-2019-33) and an unaltered HCrB (CO-2019-34). Minerals of interest in these samples were hornblende, chlorite, titanite and plagioclase (Appendix C). The composition of amphiboles analyzed varies depending on the host rock, but for the most part magnesiohornblende is the dominant amphibole at the Fisher property across all rock types analyzed (Fig. 5-1b; Hawthorne et al., 2012; Leake, 1997). Edenite is locally present in HCrB and Andesite-2 (Fig. 5-1a). Cummingtonite was also identified occurring in the groundmass of the pyroxenite unit (Fig. 4-5e). Plagioclase is commonly of an oligoclase-andesine composition (Fig. 5-1c), and chlorites are of a Mg-Fe composition between clinochlore to chamosite (Fig. 5-1d). The altered HCrB showed a distinct chemical phase of biotite occurring closer to the chamosite end-member (Fig. 5-1d), suggesting this could be a phase related to the alteration.

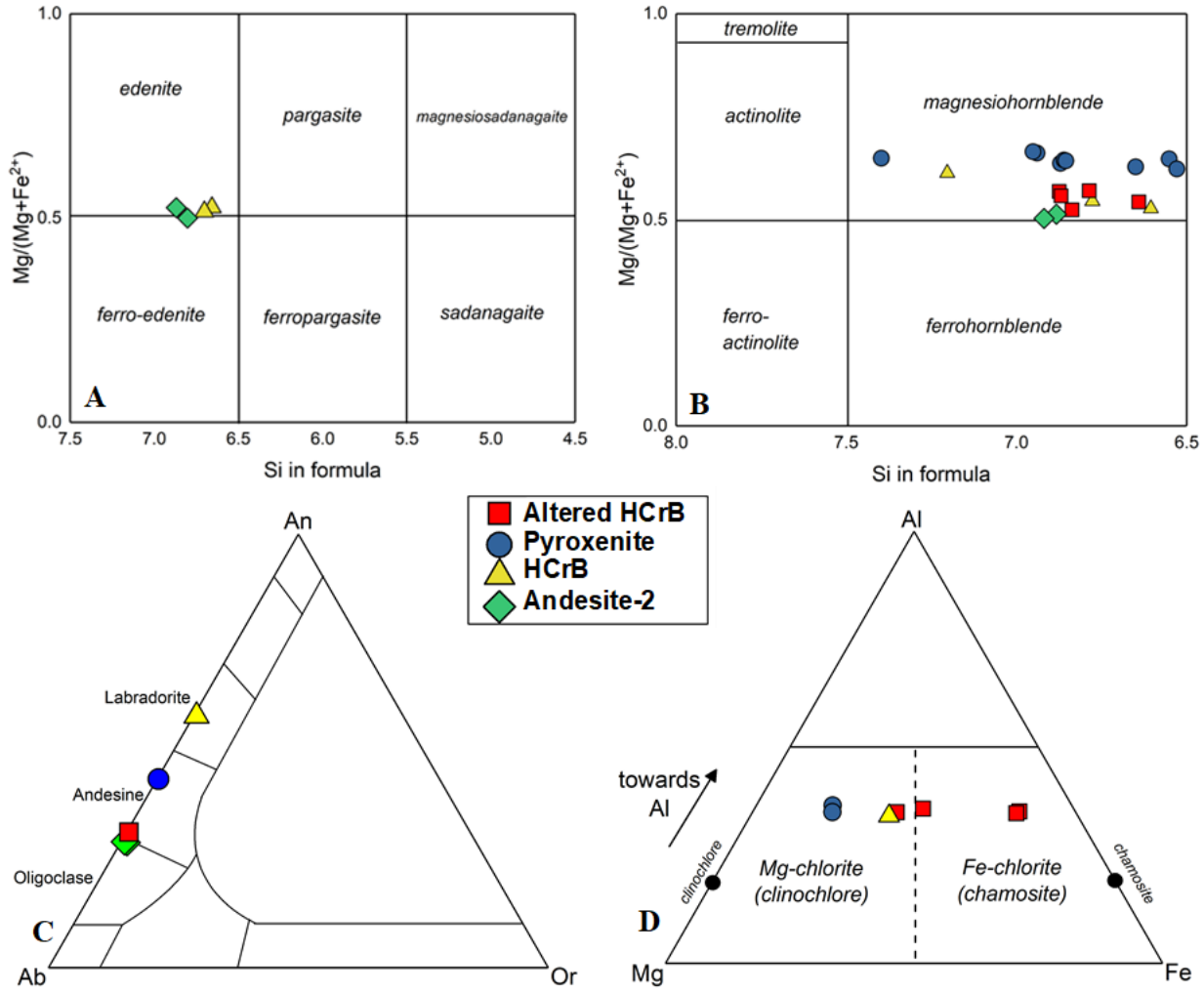

Figure 5-1 Classification diagrams of various pre-alteration minerals from samples using electron microprobe analysis. A) Calcic amphibole classification diagram with parameters from (Leake, 1997): $Ca_B \geq 1.50$; $(Na+K)_A \geq 0.50$, Ti < 0.50 . B) Mg-Fe-Mn-Li amphibole classification diagram with parameters from (Leake, 1997): ($Ca_B \geq 1.50$; $(Na+K)_A < 0.50$), $Ca_A < 0.50$. C) Ternary classification diagram for feldspars. An = anorthite, Ab = albite, Or = orthoclase. D) (Al+Q)-Mg-Fe compositional classification diagram of chlorites from the Fisher property (according to Zane and Weiss, 1998).

Fisher Alteration Assemblage:

Microprobe analysis was also completed on six highly altered samples including two HCrB (CO-2019-55; CO-2019-93A), a LCrB (CO-2019-61), a granite (CO-2019-48), a diorite (CO-2019-81) and a metasedimentary rock (CO-2019-69). Variations in mineral phases were noted during thin section investigation and warranted further investigation to determine if chemical changes corresponded with variations in petrographic attributes such as pleochroism, grain size, crystal form and association/occurrence. Mineral "types" were assigned based on mineral's context in host rocks, including "HR_" referring to minerals either found with; 1) no obvious association, or 2) defining a foliation not believed to be related to alteration. "H_" refers to any mineral phases which is believed to be part of the alteration halo and "V_" refers to minerals identified in quartz veins. These phases will be described in detail below with reference to biotite, chlorite, titanite, calcite and epidote.

Biotite:

Biotite (B) showed the greatest phase variations (Table 5-1) during thin section investigations (Fig. 5-2a,b,c). HRB phases were sampled distal to quartz veins and alteration haloes and were assumed to be a metamorphic fabric. HB were sampled within alteration haloes of quartz veins and typically occurred with chlorite, titanite, hornblende, and epidote. VB were those sampled from within quartz veins or within sulphide mineral veins (Table 5-1). The chemical compositions of biotite phases, however, did not correspond with the phase variations. When plotted on the Mg vs. Al^{VI}+Fe^{3+}+Ti vs. Fe^{2+} +Mn ternary classification diagram (Foster, 1960), most biotite phases plot in the "Ferrous Biotite" space (Fig. 5-3a). The ratio of Fe/(Fe+Mg) in biotite phases ranges between 0.438 – 0.676 and tetrahedral aluminum varies between 0.95 – 1.26.

This further confirms that biotite phases are ferrous and are mainly of annite composition (Fig. 5-3b). Biotites analyzed from the metasedimentary sample are of a phlogopite composition (Fig. 5-3b). Minor variations in biotite chemistry do exist but appear to reflect host rock compositions rather than changes associated with alteration or veining.

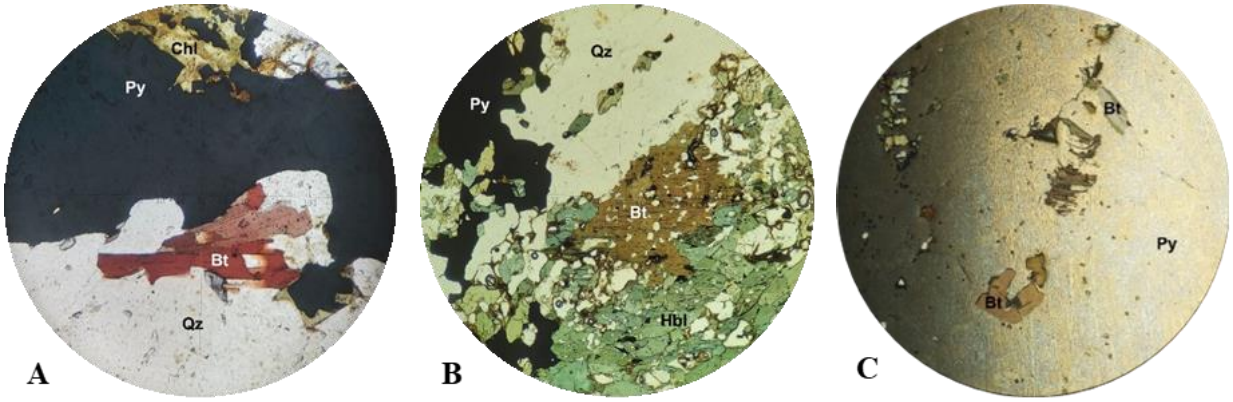

Figure 5-2 PPL photomicrograph images of various biotite phases. A) B_1 along a pyrite vein margin in a granite (CO-2019-48; 249m; FOV: 1.8mm). B) B_1 along a quartz vein in a HCrB (CO-2019-55; 107.45m; FOV: 4.5mm). C) B_3 in a pyrite vein in a HCrB (CO-2019-55; 107.45m; FOV: 4.5mm).

Table 5-1 Descriptions of phase variations of biotite (B) where "H" = halo, "V" = vein, "HR" = host rock.

Phase	**Pleochroism**	**Grain Size**	**Crystal Form**	**Association/ Occurrence**	**Biotite "Type"**
B_1	deep red - brown	fine – very coarse	an - euhedral	along pyrite or quartz vein margins or in sheared quartz veins	HB
B_2	deep red - brown	medium	sub-euhedral	defines foliation	HRB
B_3	brown	medium to coarse	euhedral	vein-hosted	VB

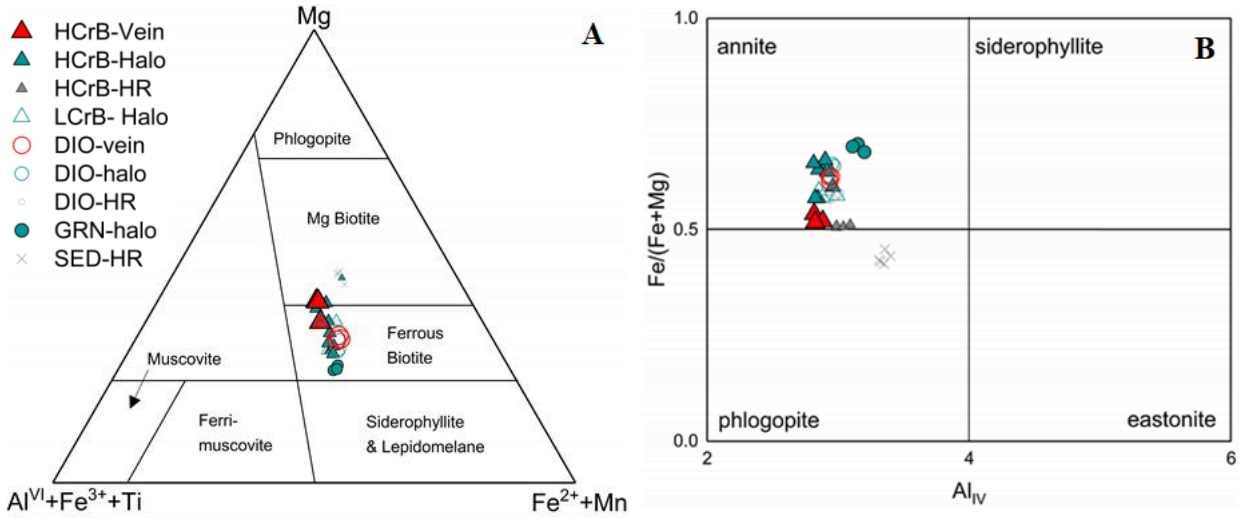

Figure 5-3 A) Mg vs. (Fe^{2+} + Mn) vs. (Fe^{3+} + Al^{VI} + Ti) ternary classification diagram of biotites (Foster, 1960). B) Tetrahedral Al vs. Fe/(Fe+Mg) classification diagram of biotite (Deer et al., 1992).

Chlorite & Titanite:

Chlorite (C) showed similar mineral phase variations to biotite (Table 5-2) during thin section investigations (Fig. 5-4c) and particularly were of interest due to its occurrence along sulphide boundaries and interstices (Fig. 5-4a,b). Two types of HC were identified and either occurred along quartz vein margins with biotite, titanite, hornblende or occurred along shear zones, typically with sericite. VC was observed in quartz vein margins within the interstices of sulphide minerals (Table 5-2). The chemical compositions of chlorite phases analyzed, had a distinct correspondence with phase variations. Vein chlorites were of a chamosite end-member chlorite composition (Fig. 5-5a), which further supports findings from Fig. 5-1d. Halo chlorites tend to occur as an Fe-Mg chlorite but show a progression from the host rock chlorites (Fig. 5-1d). This boundary is not as well-defined since two granite halo chlorites occur in the vein chlorite "zone".

The variations in titanite (T; Table 5-2) showed less variation in thin section (Fig. 5-4c,d,e) but the association of coarse-grained (Fig. 5-4e) and locally euhedral titanite (Fig. 6-3b) associated

with alteration haloes was of interest. HRT were typically anhedral and deformed along foliations, while HT typically occur within alteration haloes in association with biotite and chlorite. The subhedral crystal form likely suggests these titanites were recrystallized primary titanites. VT were not common, but when noted, had a distinct euhedral shape suggesting they had been precipitated from hydrothermal fluids (Table 5-2). Very minor variations were identified, such as increases in Ca in vein titanites, but did not prove to be a robust approach to differentiation titanites (Fig. 5-5b).

Table 5-2 Descriptions of variations in phases of chlorite (C) and titanite (T) where "H" = halo, "V" = vein, "HR" = host rock.

Phase	**Pleochroism**	**Grain Size**	**Crystal Form**	**Association/ Occurrence**	**Mineral Type**
C_1	green	very fine - fine	anhedral	interstices of pyrite	VC
C_2	green	medium - very coarse	subhedral	along quartz vein margin	HC
C_3	green	fine - medium	an - subhedral	shear/fracture controlled	HC
T_1	dirty sand	medium	subhedral	associated with chlorite and biotite alteration	HT
T_2	dirty sand	medium	sub - euhedral	hosted in quartz vein	VT
T_3	dirty sand	medium	an - subhedral	not associated with veins	HRT

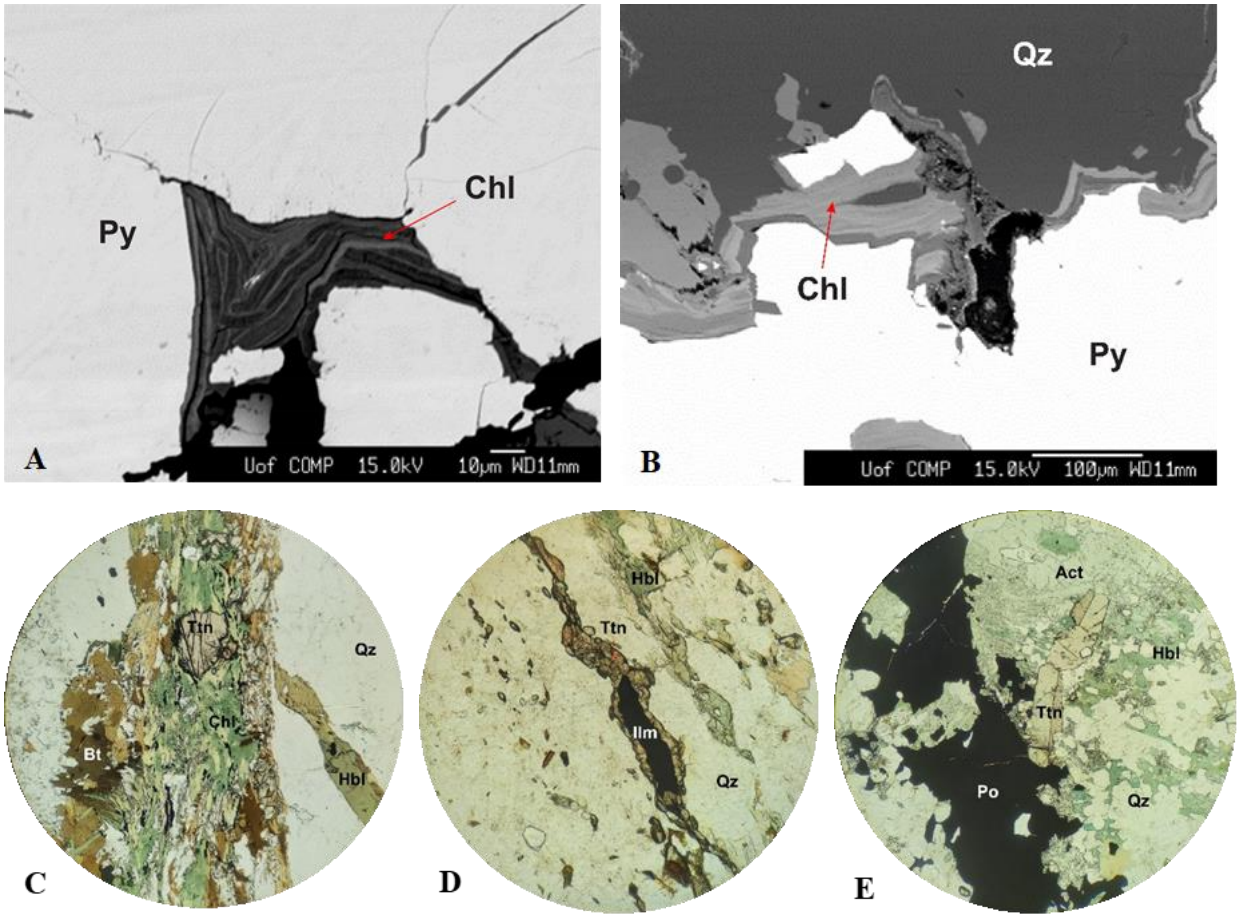

Figure 5-4 A) BSE image – interstitial C_1 in pyrite grains along the margin of a quartz vein in a HCrB (CO-2019-55; 107.45m). B) BSE image- C_1 along the margins of pyrite grain in a HCrB (CO-2019-55; 107.45m). C) PPL- C_2 in an alteration halo with T_1 and biotite in an altered diorite (CO-2019-81B; 55.9m; FOV: 4.5mm) D) PPL- T_3 with ilmenite core defining foliation in a LCrB (CO-2019-61; 139.1m; FOV: 4.5mm) E) PPL- T_1 in a LCrB in an alteration halo (CO-2019-61; 139.1m; FOV: 4.5mm).

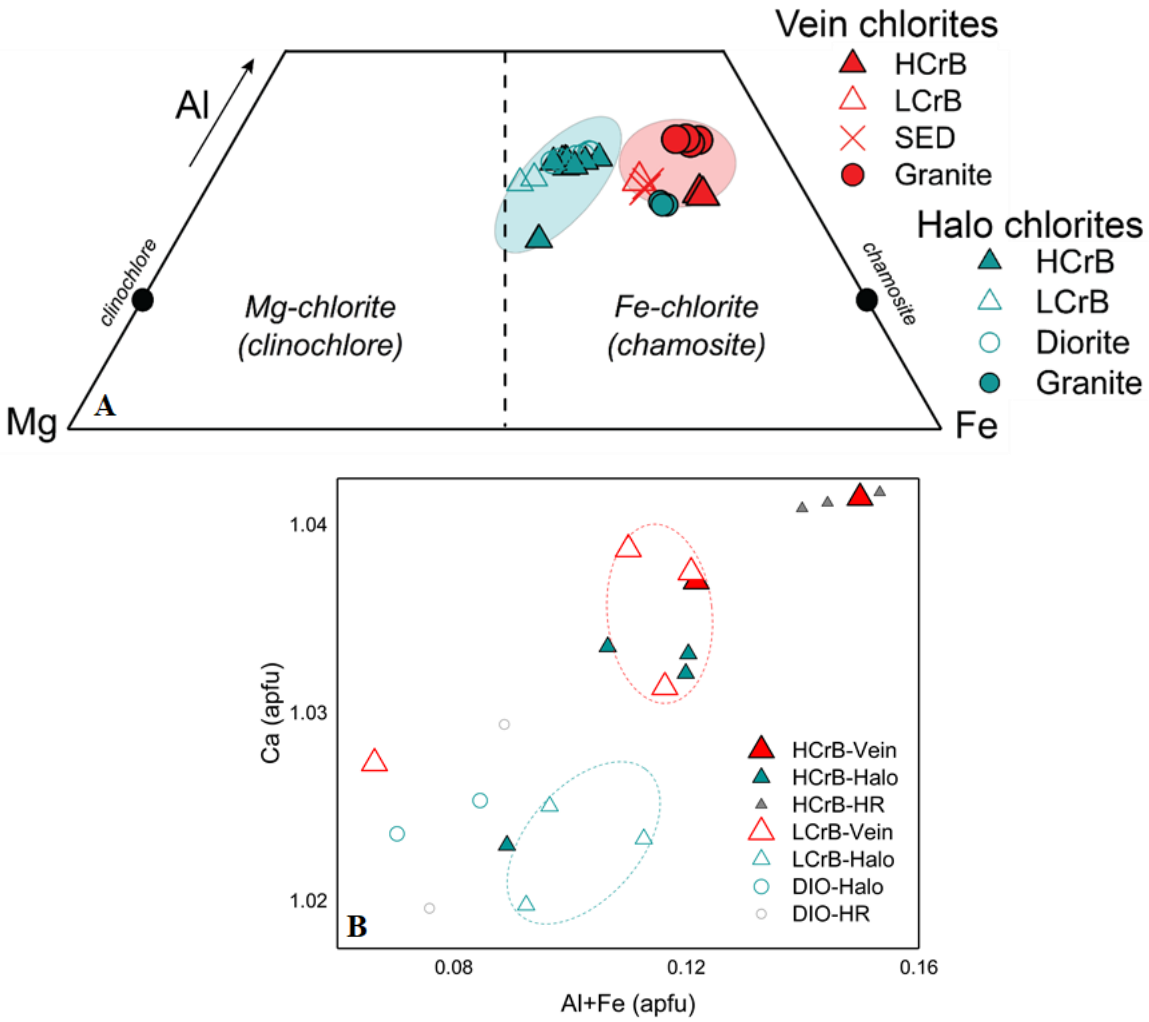

Figure 5-5 A) Al-Mg-Fe ternary compositional diagram of chlorites analyzed from various Fisher host rocks. Black dots represent end-member chlorites, red area represents vein-type chlorites, turquoise area represents halo-type chlorites. B) Bivariate diagram plotting Ca vs. (Al + Fe) of titanite analyses.

Calcite & Epidote:

Variations in calcite (Cal; Table 5-3) were noted during thin section analysis and included late stages of calcite (Fig. 6-5e), large calcite veins (Fig. 5-6a) and calcite occurring in association with pyrite grains (Fig. 5-6b,c). HRCal was typically anhedral calcite occurring within interstices of various host rock minerals. The HCal commonly occurred within interstices of sulphide minerals or, less-commonly, within alteration haloes. VCal was a phase of late cross-cutting calcite veins (Table 5-3). Minimal calcite was observed within quartz veins, but these were not analyzed. No obvious chemical variations were identified apart from calcite occurring in metasedimentary rocks which was slightly higher in Fe and Mg (Fig. 5-7b). Epidote (E) was noted to occur as a clinozoisite-quartz symplectite (Fig. 6-6c), as euhedral clinozoisite (Fig. 6-5h) and as euhedral epidote (Fig. 6-3c). These phases were always found in association with alteration haloes surrounding quartz veins suggesting a hydrothermal origin, rather than a primary or metamorphic origin. Clinozoisite typically occurred in association with plagioclase, muscovite and actinolite. Microprobe analysis was mainly used to confirm the presence of clinozoisite as opposed to epidote, which was confirmed (Fig. 5-7a). No other major chemical variations to distinguish these phases were observed.

Table 5-3. Descriptions of variations in phases of calcite (Cal) and epidote (E) where "H" = halo, "V" = vein, "HR" = host rock.

Phase	**Pleochroism**	**Grain Size**	**Crystal Form**	**Association/ Occurrence**	**Mineral Type**
Cal_1	clear	fine - coarse	subhedral	interstices of pyrite, or along QV margins	HCal
Cal_2	clear	fine - medium	anhedral - subhedral	late crosscutting veins	VCal
Cal_3	clear	medium	sub - euhedral	no association with veins/alt	HRCal
E_1	clear - yellow	fine - medium	anhedral	symplectite texture	HE
E_2	clear	fine - medium	anhedral - euhedral	no distinct association	HE

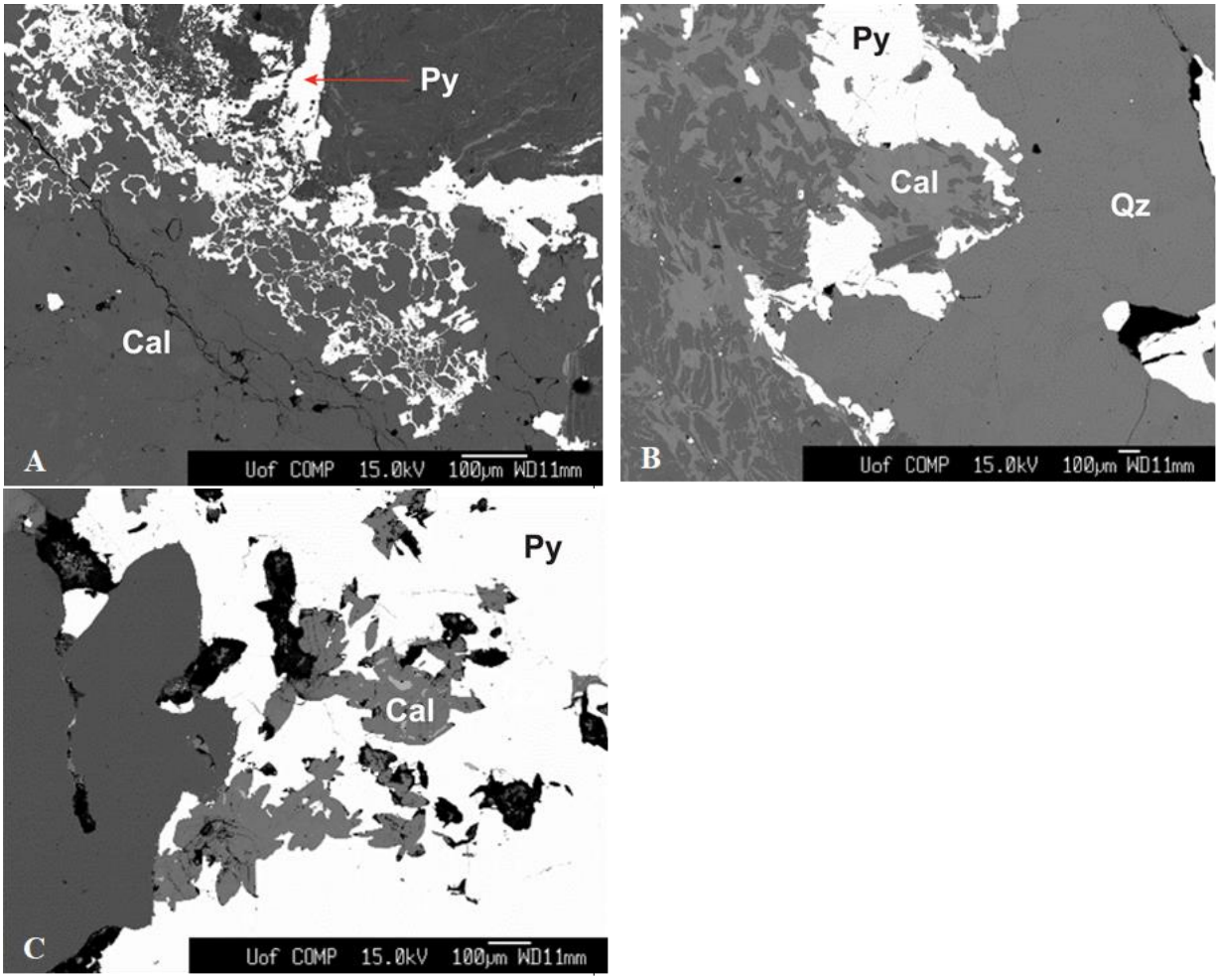

Figure 5-6 A) BSE image of Cal_2 with pyrite occurring on calcite vein margin in a metasedimentary rock (CO-2019-69; 316.1m). B) BSE image of Cal_1 along a quartz vein margin in a metasedimentary rock (CO-2019-69; 316.1m). C) BSE image of a Cal_1 in pyrite interstices of a HCrB (CO-2019-55; 107.45m).

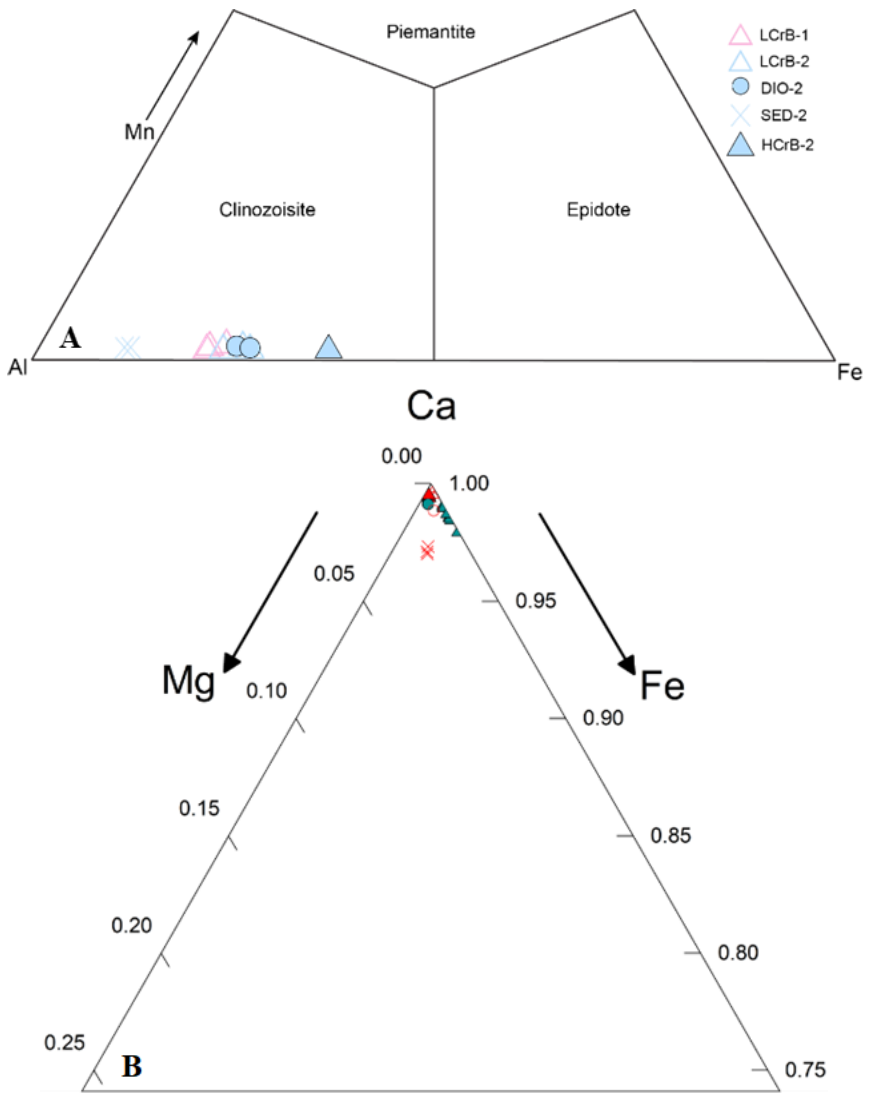

Figure 5-7 A) Mn vs. Al vs. Fe ternary diagram for classification of epidote group minerals. "1" refers to symplectite texture and "2" refers to non-symplectite texture. B) Ca vs. Mg vs. Fe ternary diagram for classification of carbonate minerals with all samples plotting as calcite.

In summary, vein-chlorite has a distinct chemical signature (Fe-rich; chamosite) which may be useful in identifying proximity to mineralized veins. Variations observed in biotite in thin section did not correspond to any accompanying chemical changes. Though other mineral does not have distinct chemical variations, their presence (based on associations with sulphide minerals) is still a useful indication of alteration haloes.

CHAPTER 6: HYDROTHERMAL ALTERATION

Alteration haloes in the Fisher property are typically narrow (~50 cm), cryptic and mineralogically variable. Most commonly, the alteration assemblage is obvious adjacent to quartz veins ranging from 0.10 m to 2 m in thickness. The absence of pronounced zoning of alteration minerals makes identifying proximity to ore difficult and is complicated by host rock type and distance to the Santoy shear zone. However, ore zones can be identified by: 1) understanding the alteration assemblage for host rocks; 2) identifying small geochemical signatures and patterns; and 3) detecting chemical changes in alteration phases at the mineralogical level. Only units which exhibit alteration will be discussed in this chapter including granites, diorites, metasedimentary and metavolcanic rocks.

6.1 Textures & Mineralogy

The alteration assemblages at the Fisher property vary considerably with the host rock, and thus the development of a paragenetic sequence is difficult, which is exacerbated by the narrow alteration haloes, and multiple fluid events. However, Fig. 6-1 provides the best summary of the timing of minerals associated with hydrothermal alteration, including sulphide minerals and gold. The alteration assemblages for each host rock type will be described below.

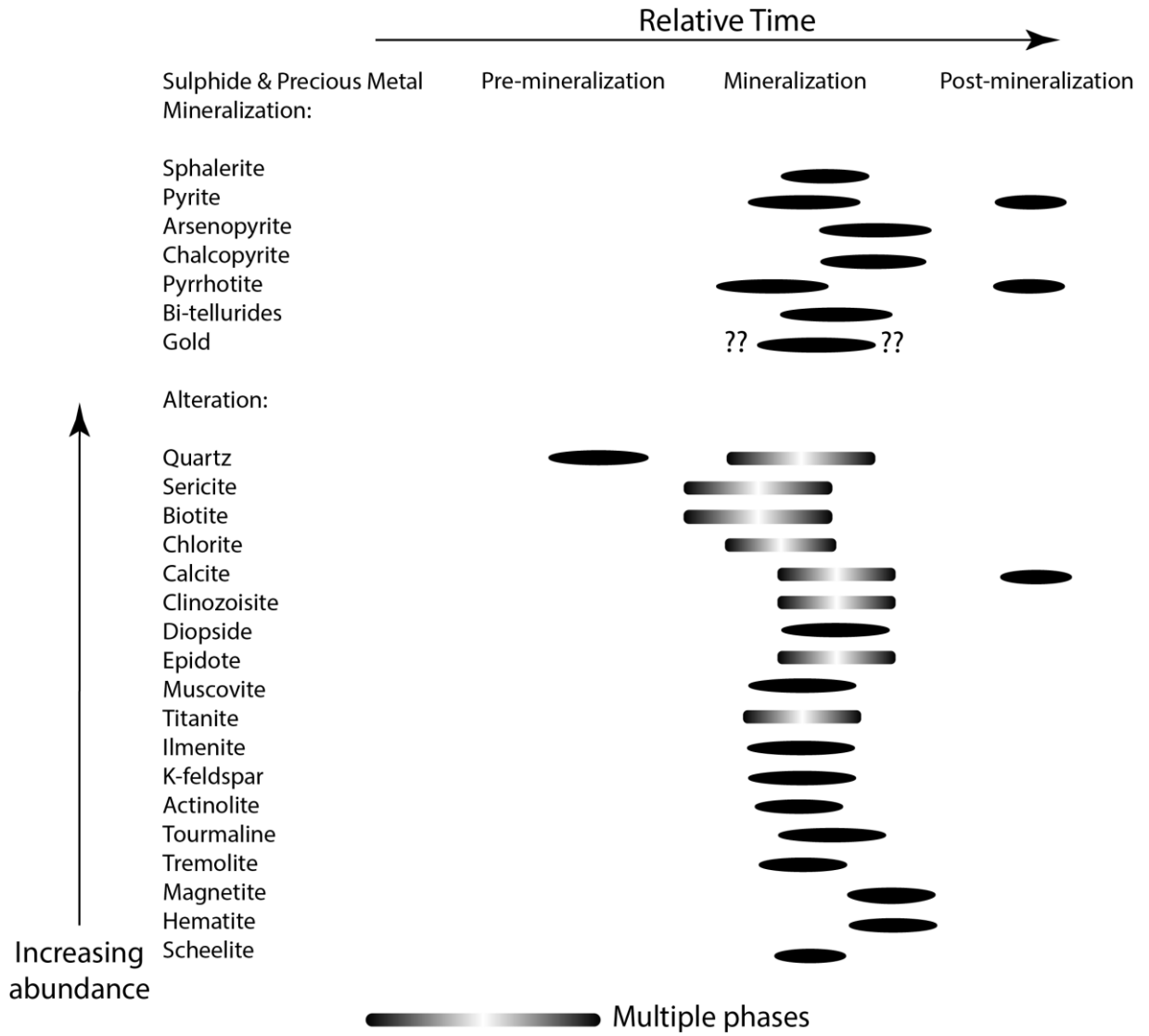

Figure 6-1 Paragenetic chart for the Fisher Deposit including sulphide and precious metal phases and hydrothermal alteration products. It should be noted that the paragenetic sequence with reference to sulphide phases was primarily based on relationships observed in one sample (CO-2019-72) and should be interpreted with caution.

The alteration halo in granites in the Fisher property typically include calcite and chlorite ± biotite, clinozoisite, epidote, sericite (fine-grained muscovite), muscovite, titanite, and diopside. Calcite occurs late in the alteration assemblage within interstices of pyrite grains (Fig. 6-2d) or along quartz vein margins with clinozoisite. Sericitization of feldspars was noted in many samples,

and locally, fine to medium-grained muscovite occurs along quartz vein margins (Fig. 6-2e). Locally, medium to coarse-grained biotite (Fig. 6-2b), fine-grained chlorite and muscovite concentrate along quartz vein margins and in interstices of pyrite (Fig. 6-2a,b,e). Clinozoisite occurs as coarse-grained anhedral crystals along quartz vein margins altering plagioclase (Fig. 6-2f). Titanite forms in minor amounts and locally where diopside and clinozoisite alteration has occurred. The anhedral crystal form indicates these titanite grains were likely primary titanites which were subsequently recrystallized. The granite unit tends to host pyrite, chalcopyrite and arsenopyrite.

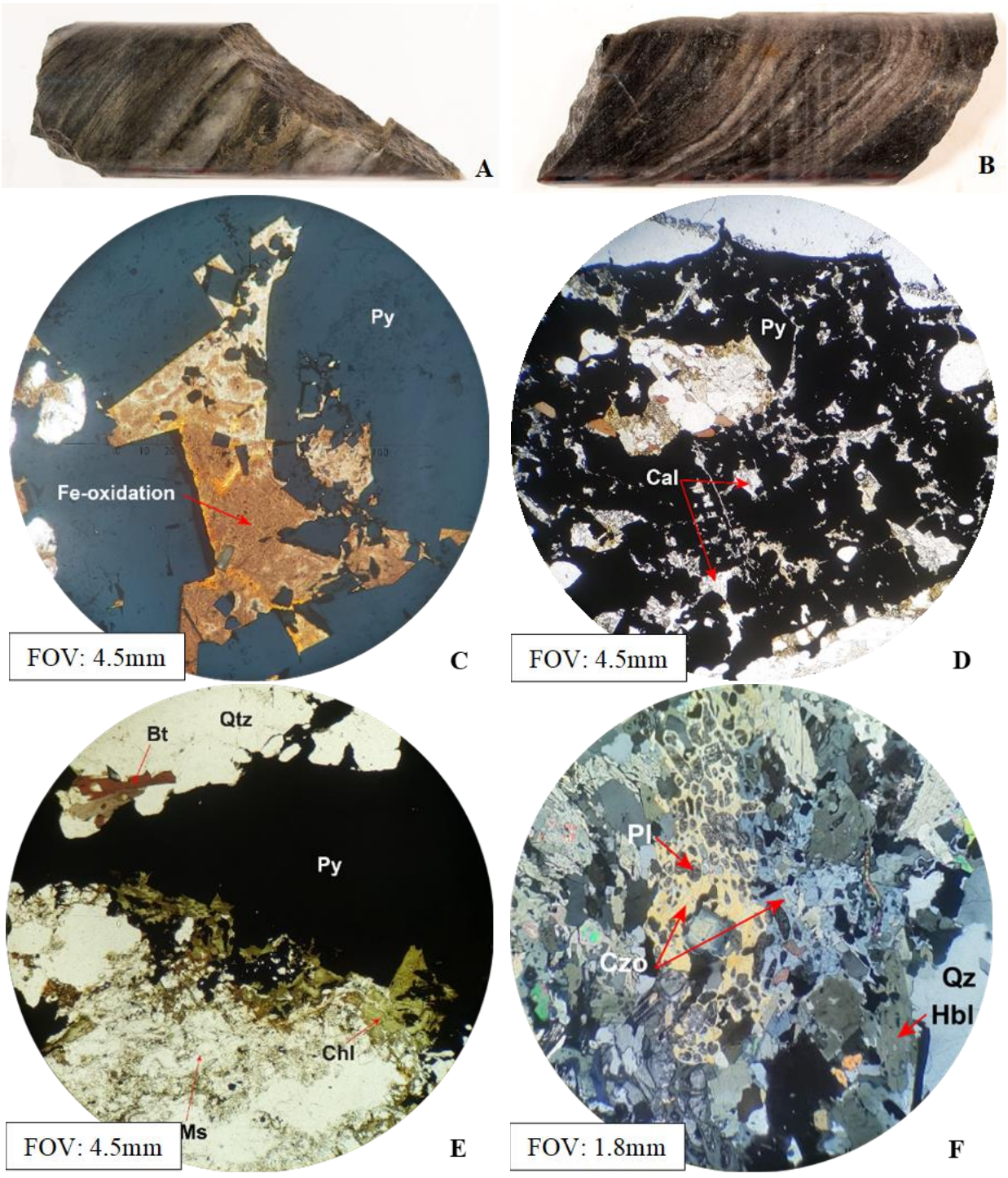

Figure 6-2 Alteration assemblages and textures of granites observed at the Fisher property. A) Bands of wispy biotite alteration along quartz vein margin with pyrite (CO-2019-74; 185.8m) B) Gradational contact between an altered mafic volcanic a granite exhibiting strong silicification, patchy chlorite, bands of epidote-diopside and foliation-controlled pyrite (CO-2019-77; 184.4m). C) XPL- Interstitial Fe-oxidation of euhedral pyrite grains in an altered granite (CO-2019-48, 249 m). D) PPL- Fine-grained, anhedral calcite within pyrite interstices in an altered granite (CO-2019-74, 185.8 m). E) PPL- Sub-euhedral pyrite along a quartz vein margin with proximal fine-grained, anhedral chlorite alteration, muscovite and medium to

coarse-grained biotite (CO-2019-48; 149m). F) XPL- Coarse-grained, anhedral clinozoisite alteration of Ca-feldspars along a contact between a granite and mafic volcanic (CO-2019-77, 184.5 m).

The alteration halo in diorites from the Fisher property typically comprise calcite, biotite, chlorite, epidote, sericite and titanite. Anhedral, fine – coarse-grained calcite crystals form within quartz veins along sutured quartz grain boundaries, along the margins of quartz veins with epidote, chlorite, and pyrite, or as late cross-cutting microveinlets indicating at least two generations of calcite exist. Multiple generations of biotite were observed including fine to medium-grained biotite locally defining foliation, a coarse-grained biotite locally altering to chlorite along quartz vein margins with titanite and recrystallized hornblende (Fig. 6-3a,b,c), fine-grained biotite occurring with chlorite in microshears, and a fine-grained biotite along quartz vein margins with a distinct association with epidote. Fine-grained and euhedral epidote only occurs locally along quartz vein alteration haloes with calcite, biotite, and chlorite (Fig. 6-3c). Sericitization is less commonly found in this unit compared to other felsic units. Titanite occurs as euhedral crystals in the host rock away from the alteration as subhedral crystals closer to the quartz vein, and as coarse-grained euhedral crystals within the alteration halo of quartz veins (Fig. 6-3b).

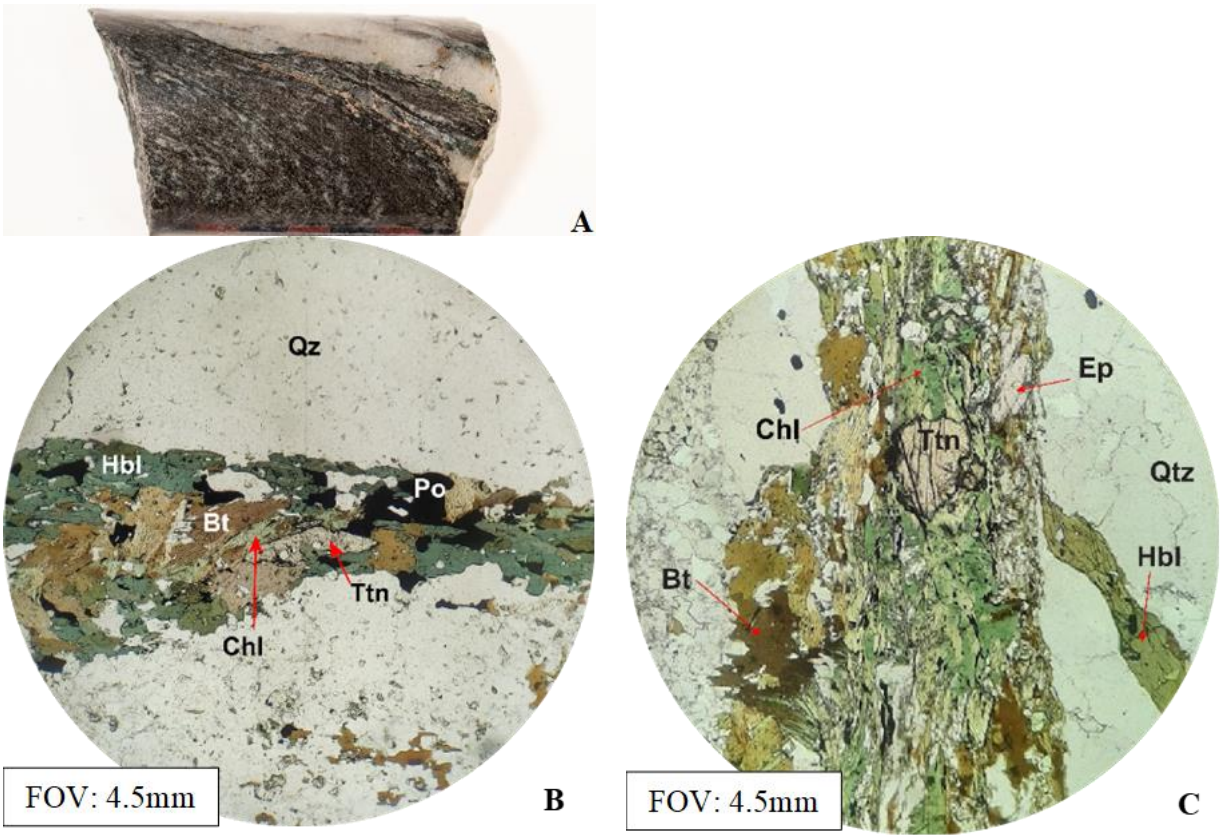

Figure 6-3 Alteration assemblage of diorites from the Fisher property. A) Pyrrhotite and chlorite-biotite alteration along quartz vein (~3cm) margins and within vein in a diorite (CO-2019-81; 55.9m). B) PPL- A thin vein of alteration minerals including biotite altering to chlorite and euhedral titanite in an altered diorite (CO-2019-82B; 56.6 m). C) PPL- Thin alteration halo (2.5mm) of chlorite, biotite, epidote and titanite along a quartz vein margin (CO-2019-81B; 55.9m).

Various metasedimentary units exist on the Fisher property and tend to have considerable alteration along contacts with mafic volcanic rocks. These metasedimentary units have less variable alteration assemblages, except when in contact with volcanic units. The common alteration minerals for the sedimentary units consist of sericite-muscovite-chlorite-calcite $\pm$ K-feldspar, tourmaline. Along contacts with mafic volcanic rocks the alteration assemblage can be influenced by those assemblages (Fig. 6-4d). Sericitization of feldspars occurs throughout all samples with increasing concentration proximal to quartz veins (Fig. 6-4a). Medium-grained muscovite completely alters plagioclase (Fig. 6-4d) and forms with chlorite along quartz vein margins with trace euhedral pyrite grains. Tourmaline alteration was locally identified in

association with sphalerite (Fig. 6-4c) and within calcite veins (Fig. 6-4e). Calcite occurs as coarse-grained anhedral alteration, especially in contact with mafic volcanic units (Fig. 6-4d,f). K-feldspar occurs locally with bands of diopside and epidote (Fig. 6-4b).

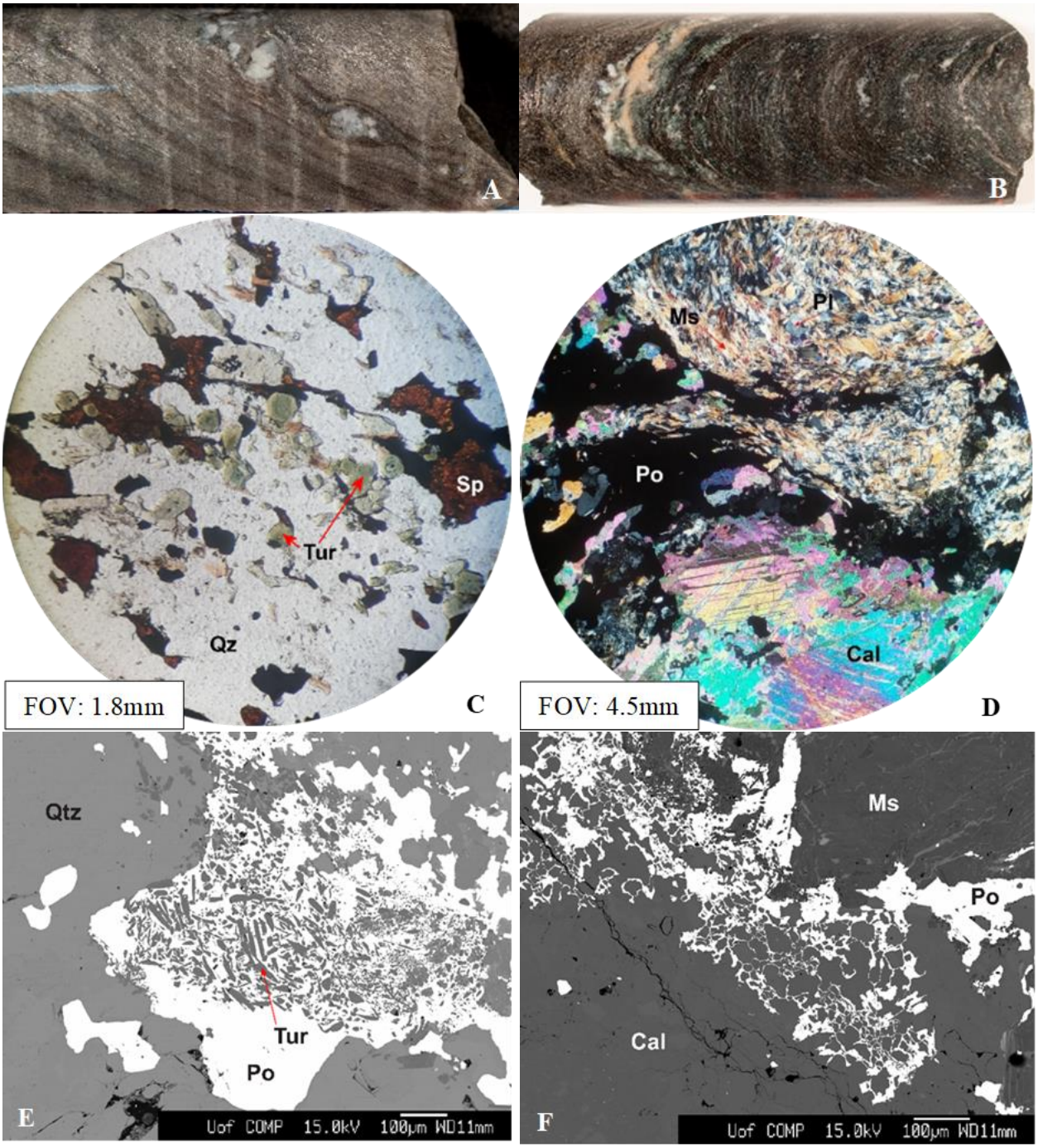

Figure 6-4 Alteration assemblages of metasedimentary rocks from the Fisher property. A) Quartz boudins in a strongly sericitized and biotite altered metasedimentary rock (CO-2019-73; 329.8m). B) Intensely altered metasedimentary rock with bands of diopside-epidote-K-feldspar and strong biotite and chlorite alteration (CO-2019-69; 316.2m). C) PPL- Tourmaline alteration in a metasedimentary unit showing sphalerite, arsenopyrite and pyrite mineralization (CO-2019-72, 329.2 m). D) XPL- Coarse-grained calcite and strong muscovite alteration of plagioclase in a contact between a mafic volcanic and a metasedimentary rock (CO-2019-69; 316.2 m). E) BSE image- Fine-grained tourmaline alteration in an anhedral pyrrhotite vein along a quartz vein margin (CO-2019-69; 316.2m). F) BSE image- Anhedral calcite vein with pyrrhotite (CO-2019-69; 316.2m)

The HCrB and LCrB alteration assemblages are significantly more complex than those identified in other units. The HCrB assemblage includes multiple generations of biotite, sericite, calcite $\pm$ chlorite, tremolite, actinolite, titanite, clinozoisite, epidote, diopside and tourmaline. Biotite occurs locally as medium anhedral grains with no preferred orientation, coarse-grain subhedral crystals along quartz vein margins (Fig. 6-5b), a finer-grained variation also along vein margins and as shear bands, a medium-coarse grained "pervasive" alteration in particular samples, and a fine-grained variation defining C-S fabrics. Sericitization of feldspars occurs distally to quartz veins (Fig.6-5d), along quartz vein margins, as a pervasive replacement of plagioclase grains associated with clinozoisite (Fig.6-5c), locally, in association with fibrous actinolite (Fig. 6-5g), and in micro-shear zones (Fig. 6-5f). Calcite forms as coarse-grained subhedral grains directly proximal to pyrrhotite (Fig. 6-4d), medium-grained anhedral crystals along quartz vein margins with biotite and/or chlorite (Fig. 6-5d), and fine-grained microveinlets cross-cutting quartz veins (Fig. 6-5e). Chlorite occurs as either a medium-coarse grained subhedral chlorite along quartz vein/pyrite margins (Fig.6-5d), especially pronounced in the "Mac vein zone" (Fig. 6-5a), or a finer-grained variation occurring along shears and are typically associated with biotite and epidote. Clinozoisite occurs as a clinozoisite-quartz symplectite texture (Fig. 6-6e), or as coarse-grained euhedral crystals (Fig. 6-5h). Medium, anhedral to subhedral titanite grains exit along quartz veins and as fine-medium grained anhedral crystals along foliation planes associated with biotite and diopside. Diopside also occurs boudins (Fig. 6-5b) or as coarse-grained crystals in quartz veins (Fig. 6-5a). Tourmaline alteration is limited and occurs as fine-grained sub – euhedral crystals within pyrite grains with calcite alteration (Fig. 6-4e).

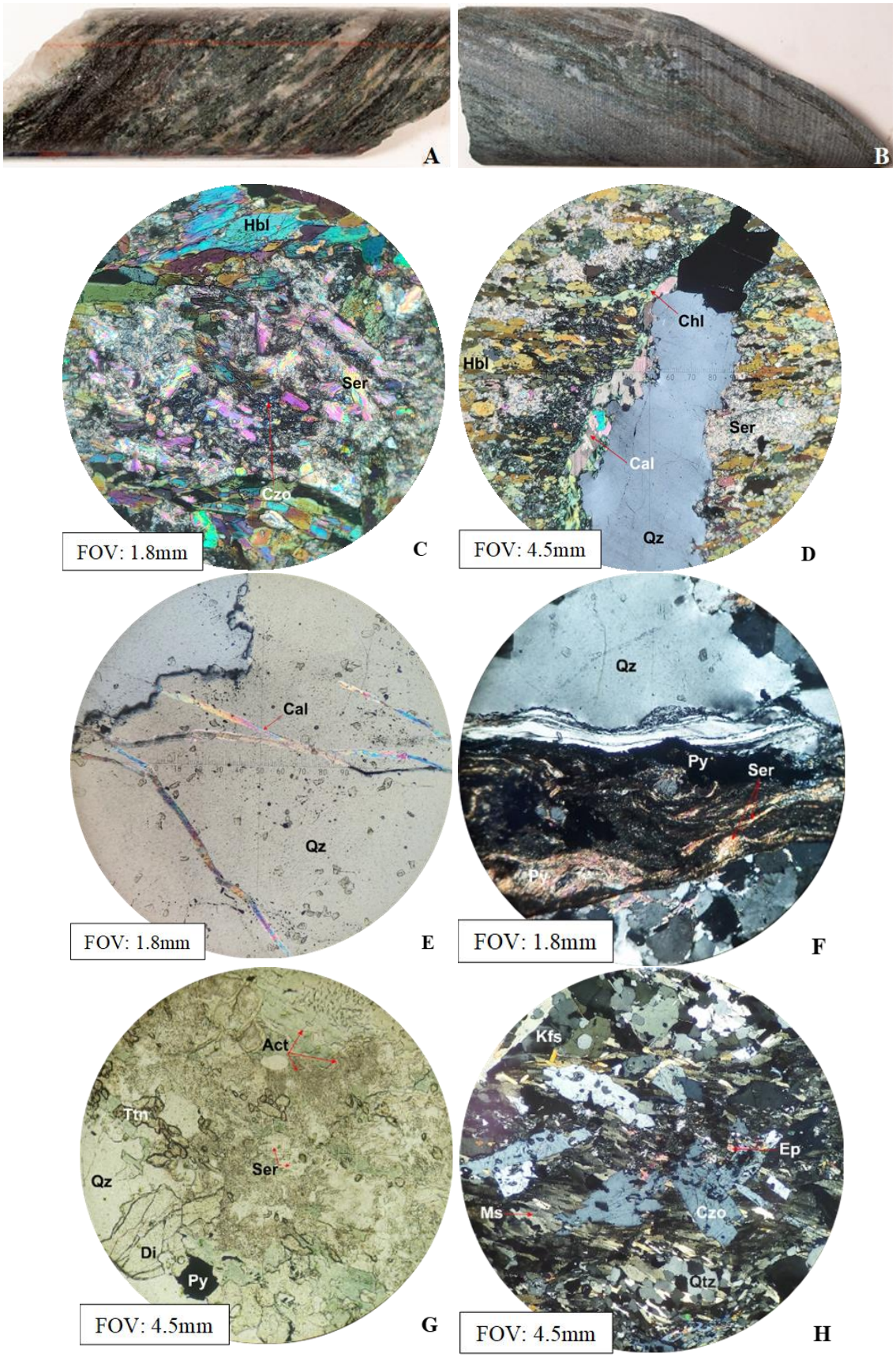
A
B
Hbl
Ser
Czo
FOV: 1.8mm
C
Chl
Hbl
Ser
Cal
Qz
FOV: 4.5mm
D
Cal
Qz
FOV: 1.8mm
E
Qz
Py
Ser
Py
FOV: 1.8mm
F
Act
Ttn
Ser
Qz
Di
Py
FOV: 4.5mm
G
Kfs
Ep
Ms
Czo
Qtz
FOV: 4.5mm
H

Figure 6-5 Alteration assemblages of HCrB. A) Mac Vein intercept exhibiting strong diopside, chlorite, biotite, and sericite alteration within a sheeted quartz vein interval (CO-2019-93; 182.3m). B) Strong chlorite and wispy biotite alteration and a diopside boudin with K-feldspar and recrystallized hornblende (CO-2019-87; 307.5m). C) Strong localized sericitization of feldspars and interstitial clinozoisite alteration proximal to a quartz vein (CO-2019-28A2; 231.8m) D) Quartz vein with associated calcite and chlorite alteration overprinting a distal sericite alteration (CO-2019-28A2; 231.8) F) XPL- A micro-shear zone comprising sericite with ribbon quartz at margins from intense deformation (CO-2019-57; HCrB, 108.6 m). G) PPL- Strong sericitization and fibrous actinolite alteration of feldspars in a mafic volcanic with diopside and titanite on quartz vein boundaries (CO-2019-93A; HCrB, 182.4 m). H) XPL- Euhedral clinozoisite and coarse-grained muscovite alteration along a HCrB contact with a metasedimentary rock (CO-2019-93a; 182.3m).

The LCrB assemblage includes biotite-diopside-clinozoisite-calcite-titanite $\pm$ chlorite, K-feldspar, epidote. Typically, quartz veins in this package occur with chlorite-biotite-clinozoiste margins and calcite-diopside hosted within veins or proximal to veins. Biotite occurs as coarse-grained euhedral grains along quartz veins and a medium-grained biotite altering to chlorite along quartz veins (Fig. 6-6a,b). Diopside is very common in LCrB and occurs as coarse subhedral grains typically within quartz veins or along quartz vein margins and associates with pyrrhotite (Fig. 6-6b,d). Clinozoisite occurs in all samples as a clinozoisite-quartz symplectite texture commonly along quartz vein or pyrrhotite grain margins (Fig. 6-6c). Medium-grained anhedral calcite occurs within quartz veins along pyrrhotite margins and within the host rock along quartz grain boundaries. Titanite occurs in the host rock along foliation planes with biotite as medium-grained anhedral crystals with ilmenite exsolutions, anhedral crystals along quartz vein margins, medium – coarse-grained euhedral crystals (Fig. 6-6d) locally exhibiting twinning along quartz vein margins. Chlorite occurs as fine-grained alteration along shears. Epidote forms as fine-grained crystals with clinozoisite.

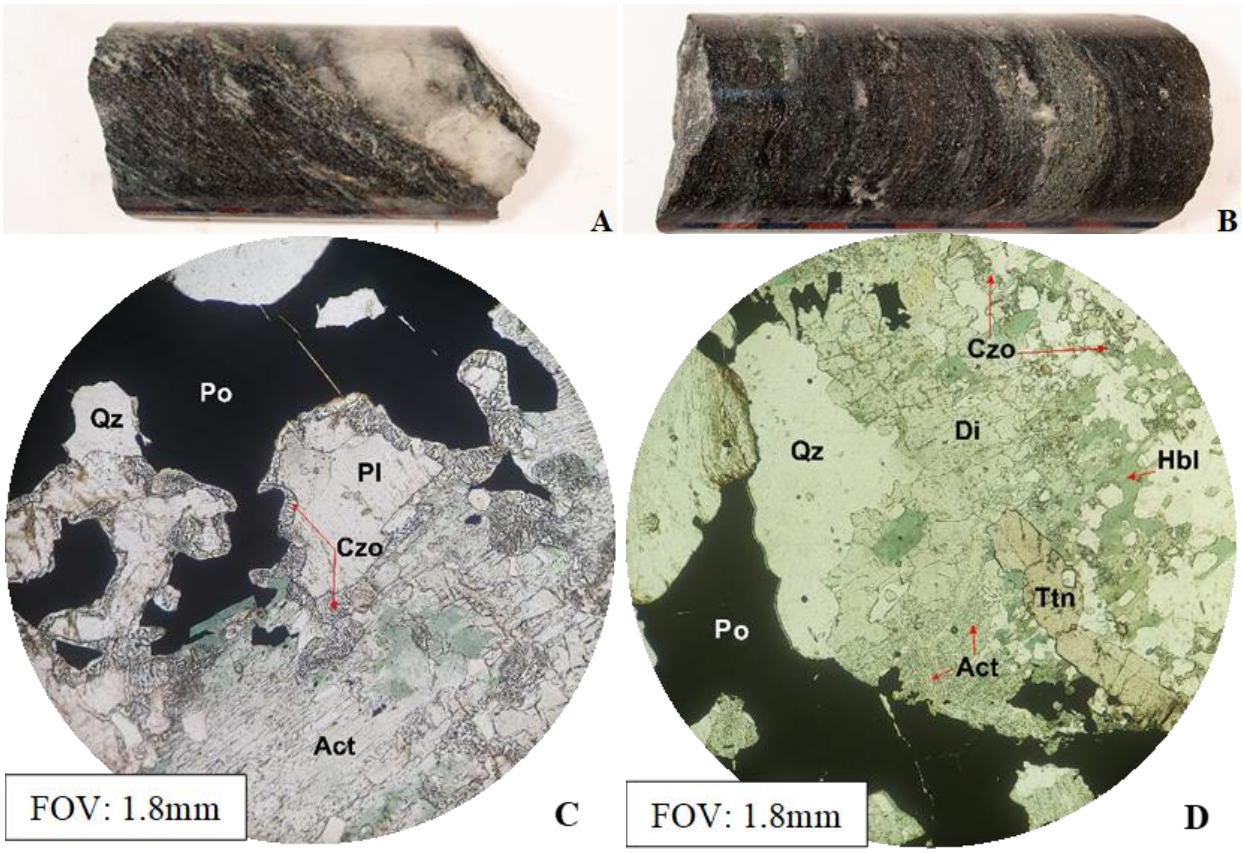

Figure 6-6 Alteration assemblages of Low Cr-Basalts from the Fisher property. A). Pyrrhotite mineralization along quartz vein margins with strong diopside and biotite alteration (CO-2019-61; 139.1m). B). Cm-scale bands of chlorite, biotite and diopside (CO-2019-64; 28.5m). C) PPL- Clinozoesite-quartz symplectite forming along pyrite? grain boundaries (CO-2019-61; 139.1 m). F) PPL- Coarse-grained diopside alteration in a quartz vein (CO-2019-61; LCrB, 139.1 m).

The paragenetic relationship between sulphide minerals (Fig. 6-1) was constructed from the examination of numerous samples, although a metasedimentary sample (CO-2019-72) was particularly useful. Chalcopyrite occurs along grain boundaries of euhedral pyrite crystals (Fig. 6-7a), along fractures in pyrite (Fig. 6-7d) or as veins with hematite inclusions crosscutting pyrrhotite (Fig. 6-7b). Pyrite grains appear to be replaced by pyrrhotite (Fig. 6-7a) suggesting pyrrhotite formed after pyrite. However, in other samples the relationship is less clear, and so they may be broadly coeval (Fig. 6-7c). Locally, relationships between hematite and pyrrhotite indicate early precipitation of pyrrhotite, followed by hematite formation which also post-dates pyrite (Fig.

6-7c). Arsenopyrite also appears to have crystallized relatively late in the mineralization sequence (Fig. 6-7c).

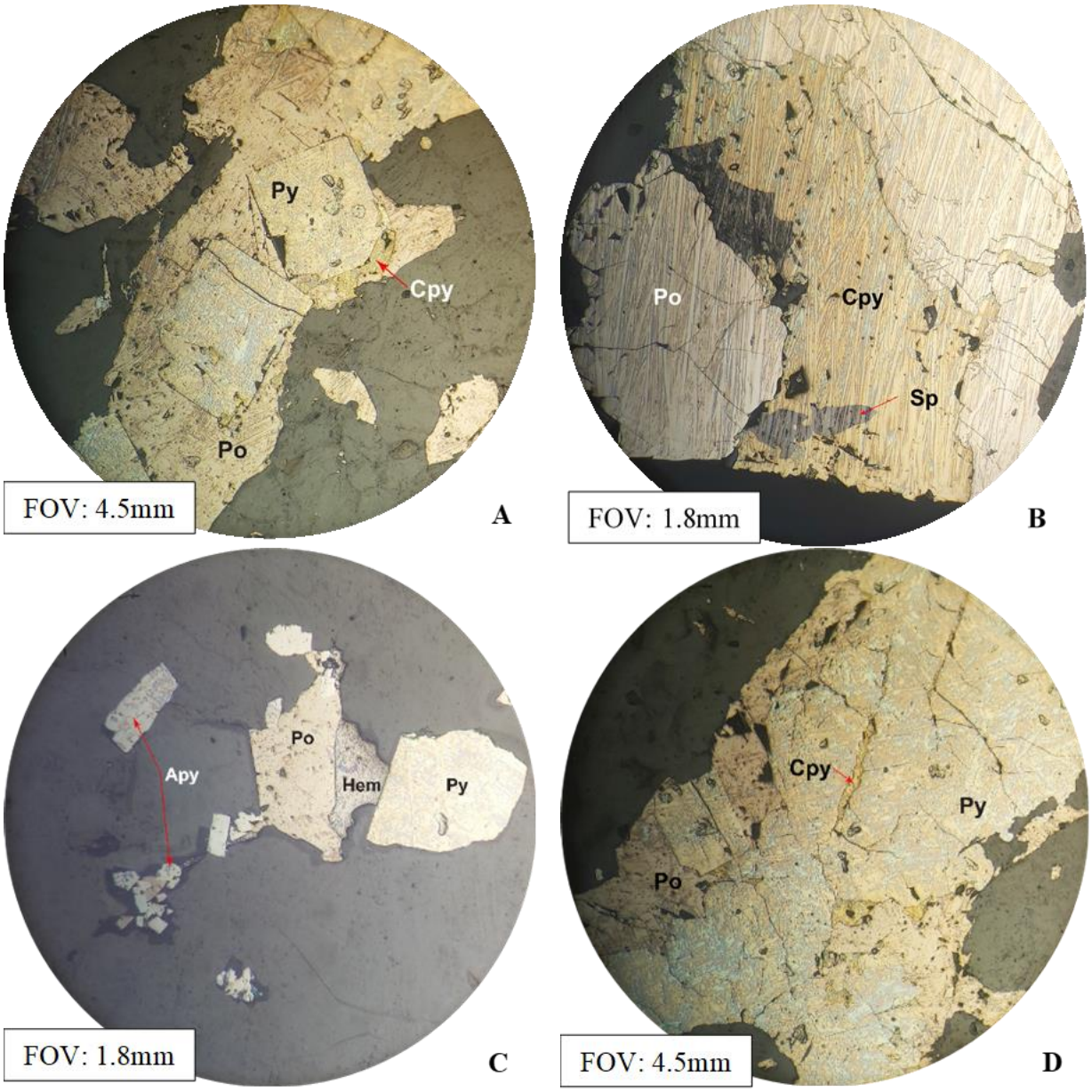

Figure 6-7 Reflected light images of sulphide minerals in a metasedimentary rock (CO-2019-72; 329.2m). A) Pyrrhotite vein with chalcopyrite on margins of euhedral pyrite crystals. B) Late chalcopyrite vein with hematite inclusions cross-cutting pyrrhotite. C) Euhedral arsenopyrite crystals occurring with pyrrhotite, sphalerite and pyrite. D) Anhedral chalcopyrite filling fractures within pyrite grains.

Sulphide minerals in the HCrB and LCrB at the Fisher property commonly include pyrite, chalcopyrite and pyrrhotite. Pyrite and pyrrhotite occur along quartz vein margins, disseminated throughout the unit, and concentrate along fractures in shear zones and along foliation planes. In one HCrB high-grade sample (8.08 g/T over 0.9m), brecciated pyrite was identified (Fig. 6-8b) but typically, pyrite in the HCrB occurs as coarse-grained sub - euhedral crystals in quartz veins (Fig. 6-5a), fine-grained anhedral crystals in micro-shear zones (Fig. 6-5f) and is locally fractured with chalcopyrite infilling fractures. Bi-Tellurides were also identified along pyrite grain boundaries (Fig. 6-8a).

Granites in the Fisher property typically host euhedral, coarse-grained pyrite (Fig. 6-8c) and arsenopyrite in quartz veins. Locally, margins of pyrite crystals are overgrown by tremolite (Fig. 6-8c) or show evidence of dissolution reactions (Fig. 6-8d). Granites also exhibit globular/blebby pyrrhotite, fracture-controlled pyrite/pyrrhotite, disseminated pyrite/pyrrhotite and trace amounts of chalcopyrite. Diorites in the Fisher property commonly host disseminated pyrrhotite, blebby pyrrhotite and coarse-grained pyrrhotite in quartz veins, and minor pyrite and chalcopyrite. Colloform textures suggest pyrite occurs post-pyrrhotite formation (Fig. 6-8e).

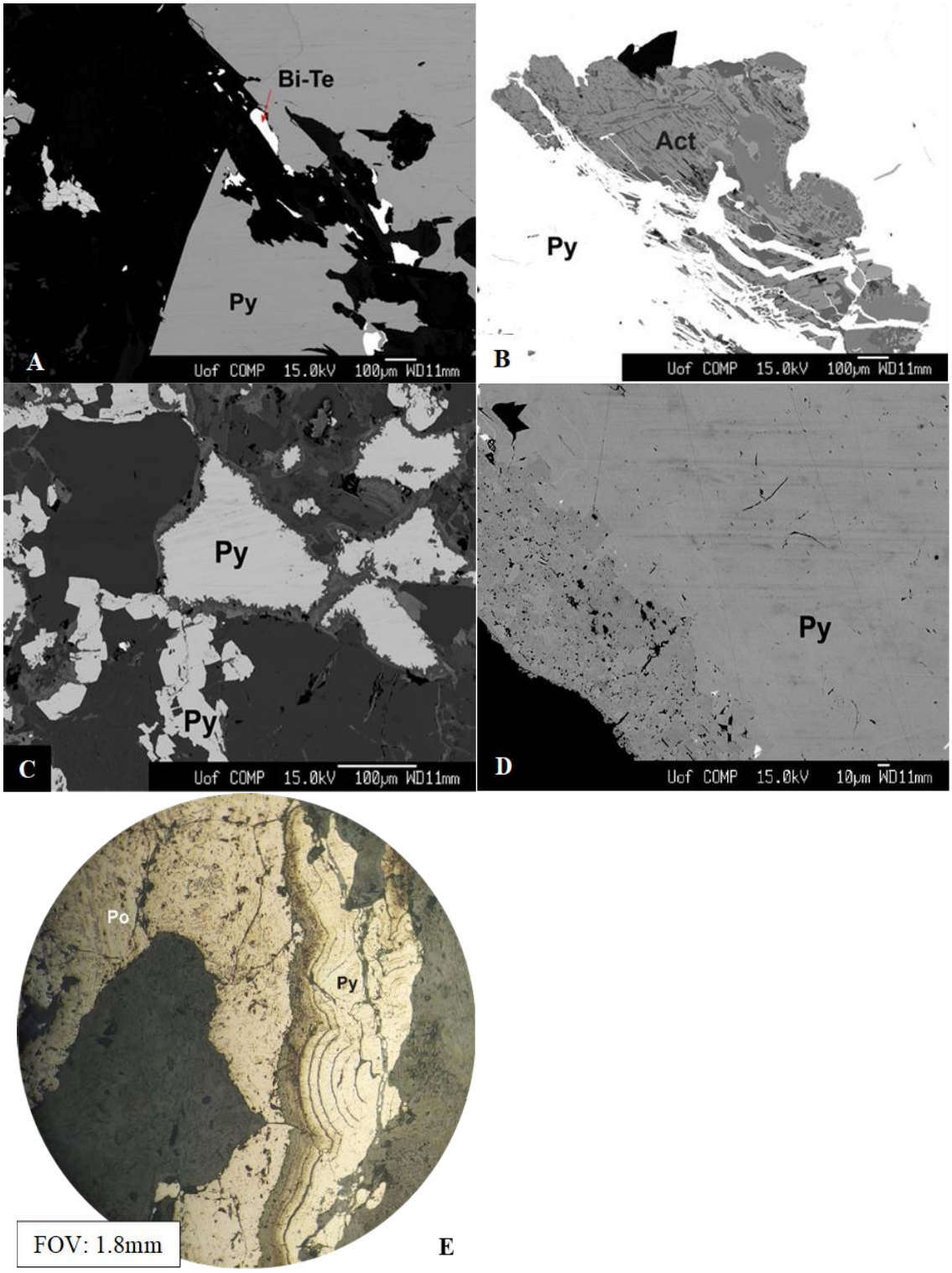

Figure 6-8 Sulphide mineral textures in HCrB (A,B) and granites (C,D,E) from the Fisher property. A) BSE image- Bi-Tellurides occurring along pyrite margins (CO-2019-55; 107.5m). B) BSE image- Brecciated pyrite in a HCrB (CO-2019-55, 107.5 m). C) BSE image- Tremolite? alteration along pyrite grain boundaries (CO-2019-48; 249m). D) BSE image- Evidence of dissolution reactions along pyrite grain boundaries (CO-2019-48; 249m). E) Reflected Light- Colloform banding in pyrite in void space along a pyrrhotite fracture (CO-2019-83, 57.2 m).

6.2 Geochemistry

All units from the Fisher property have undergone varying degrees of hydrothermal alteration, although the alteration appears to be stronger in volcanic rocks relative to intrusive units, likely due to increased chemical reactivity. This section will primarily describe the alteration geochemistry of the HCrB and LCrB. However, one of the highest-grade samples from the Fisher property was from a mineralized granite (CO-2019-48), and metasedimentary rocks locally exhibit mineralization, so these rocks will be briefly described.

Prior to analyzing the alteration effects on host rocks, samples are classified using the same Zr vs. Ti plot (Fig. 6-9) from section 3.2 (Fig. 4-7a). Intrusive units still have consistent Zr and Ti ratios which results in uniform host rock signatures (Fig. 6-9). Some of the HCrB volcanic units, have similar Zr/Ti ratios as Andesite-1, but based on differences in hand sample (Fig. 5-2a,b) and petrographic (Fig. 5-2e,f) observations, the HCrB and Andesite-1 are two distinct units.

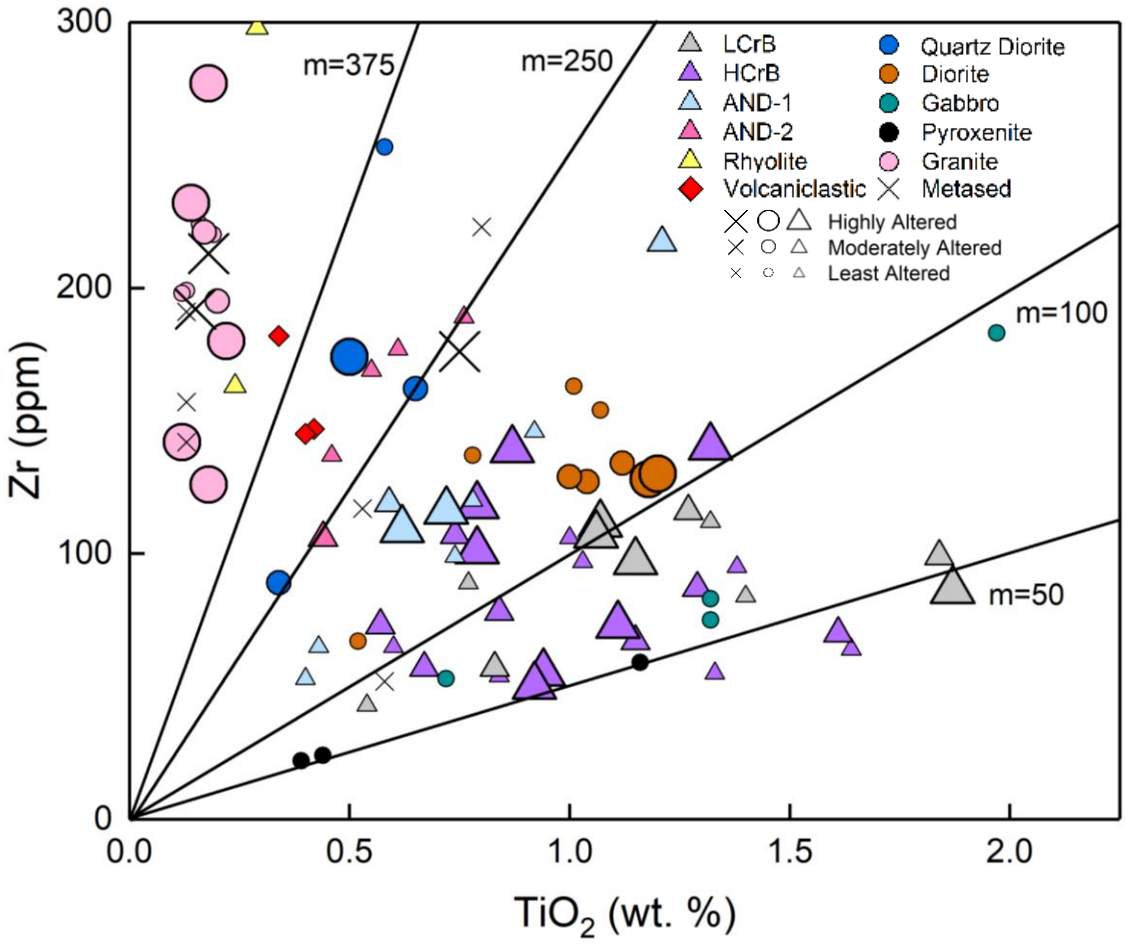

Figure 6-9 Zr vs. Ti plot for variably altered Fisher extrusive, intrusive, and metasedimentary units (modified after Hallberg, 1984). The least altered samples are the same as those shown in Fig. 4-7a.

An important aspect of quantifying hydrothermal alteration is selecting appropriate "least-altered" samples. For this study, five conditions (Table 6-1) are used to determine least altered, moderately altered, and highly altered samples.

Table 6-1 Conditions used to identify least, moderate, and highly altered samples. Note that "x" represents the sample of interest and number corresponds to order of importance (1 = most important condition).

	Alteration Intensity		
Conditions	Least	Moderate	Highly
1) K/Al vs. Na/Al (Fig. 6-11b)	Na/Al: $0.25 < x < 0.35$ K/Al: $x < 0.05$	Na/Al: $0.15 < x < 0.25$, $0.35 < x < 0.45$ K/Al: $0.05 < x < 0.15$	Na/Al: $x < 0.15$, $0.45 < x$ K/Al: $0.15 < x$
2) Visible alteration in hand sample (Ch.5.1) (*subjective*)	Logged as "least altered" in drill core logs	Logged as "moderately altered" in drill core logs	Logged as "highly altered" in drill core logs
3) K_2O+Na_2O vs. $100*K_2O/Na_2O+K_2O$ (Fig. 6-11d)	Values within "Weakly Altered" zone	Values along zone divisions	Values within "K Metasomatism" or "Na Metasomatism" zones
4) Al/Na vs. Na_2O (Fig. 6-11c)	Na_2O: $2.5 < x < 4$ Al/Na: $x < 8$	Na_2O: $4 < x < 5$, $1.5 < x < 2.5$ Al/Na: $8 < x < 12$	Na_2O: $5 < x$, $x < 1.5$ Al/Na: $12 < x$
5) Zr-weighted enrichment/depletion plots (Fig. 6-15a,b) (*subjective*)	Values close to the y=1 line (Fig. 6-15a,b)	Values between least and highly	Values furthest from the y=1 line

Alteration effects on Fisher host rocks are shown below (Fig. 6-10) and emphasize the reactive nature of volcanic rocks. Highly altered Fisher volcanic rocks, especially HCrB and LCrB, typically plot close to mineral nodes such as muscovite "Ms" (Fig. 6-10a,b) or plot off or close to feldspar control lines (Fig. 6-10c). Fisher intrusive rocks and least-altered samples, for the most part, plot away from mineral nodes (Fig. 6-10a,b) or along feldspar control lines (Fig. 6-10c). Based on these finding and less alteration in intrusive rocks observed in hand samples, alteration geochemical analysis will mainly focus on HCrB and LCrB.

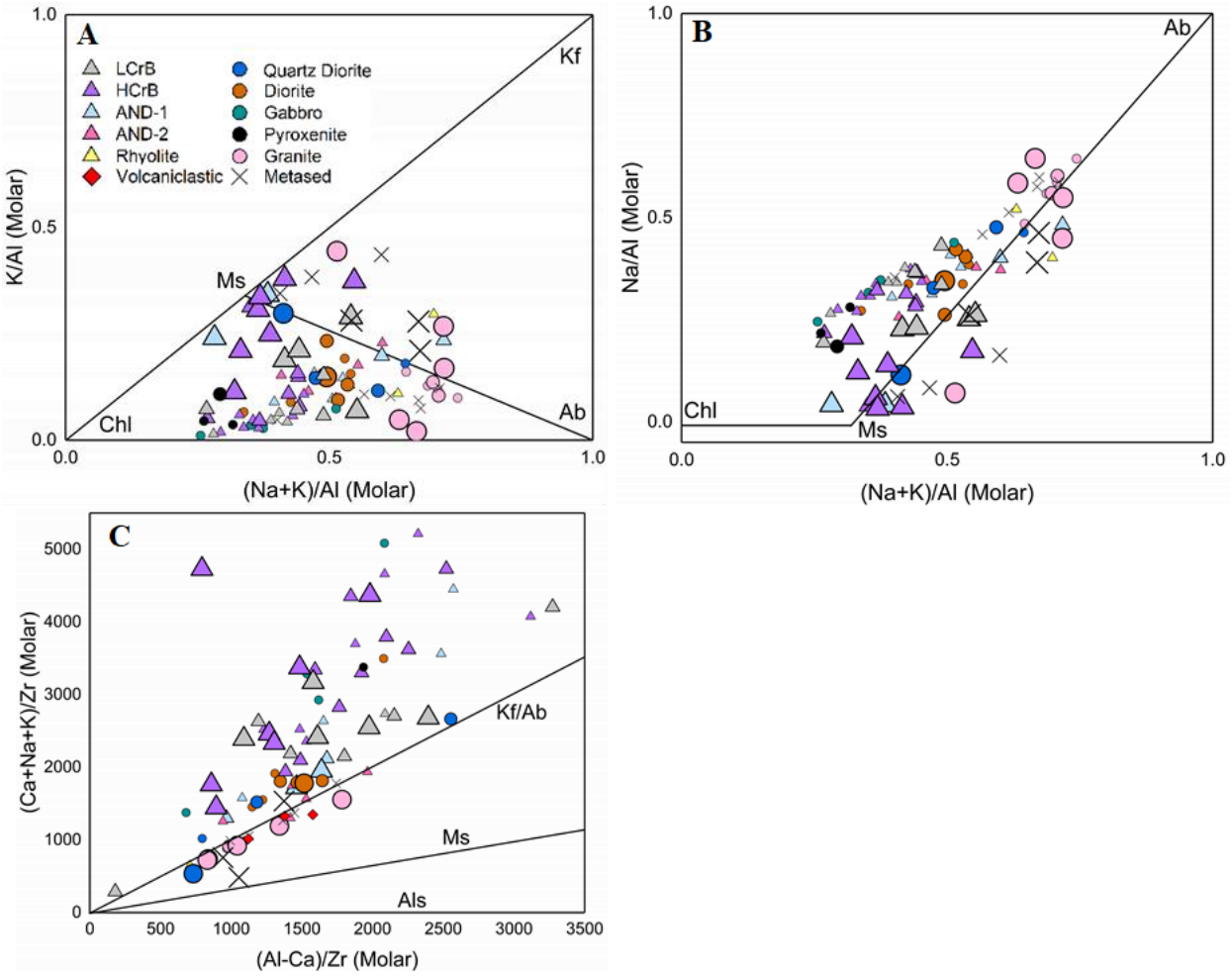

Figure 6-10 PER and GER diagrams displaying all Fisher host rocks. Note "Chl" = chlorite, "Ms" = muscovite, "Kf" = F-feldspar, "Ab" = albite and "Als" = aluminosilicate. Also note that lines on graphs are mineral control lines. A) K/Al vs. (Na+K)/Al Albite Alteration GER Diagram NaK-K Control Diagram B) Na/Al vs. (Na+K)/Al Albite Alteration GER Diagram (Stanley, 2017). C) (Ca+Na+K)/Zr vs. (Al-Ca)/Zr Feldspar Control Diagram (Stanley and Madeisky, 1996).

Fisher property rocks are mainly analyzed using GERs and PERs, due to their effectiveness of emphasizing overprinting alteration effects. Highly altered HCrB plot near the muscovite node signifying that muscovite or sericite alteration affected these rocks (Fig. 6-10a,b; Fig. 6-11a). If samples have a combination of albite and muscovite alteration, samples should plot along the Ab-Ms line (Fig. 6-10a; Fig. 6-11a). However, the trend appears to converge directly from the "unaltered window" to the Ms node suggesting muscovite is a dominant alteration type. HCrB display potassic alteration made evident by K/Al values of >0.2, and significant Na loss shown by

Na/Al values of < 0.2 (Fig. 6-11b). K gains and Na loss are further supported by Figure 6-10c,d and suggest that no sodic metasomatism affected these basalts. Instead, the pairing of Na losses and K gains suggests sericitization of Na-feldspars occurred. In all the figures described above, the “unaltered window” is used to identify least-altered samples for isocon analysis, mass change calculations and Zr-weighted enrichment/depletion plots.

The LCrB has similar trends as the HCrB, but overall, does not show as strong associations with the “Ms” node (Fig. 6-10a,b, Fig. 6-11a). Potassium metasomatism has affected LCrB, but not to the same extent they have affected HCrB (Fig. 6-11b,d). One of the differentiating factors between the LCrB and HCrB is evident in Figure 6-11c where LCrB do not exhibit the losses in Na, which the HCrB does.

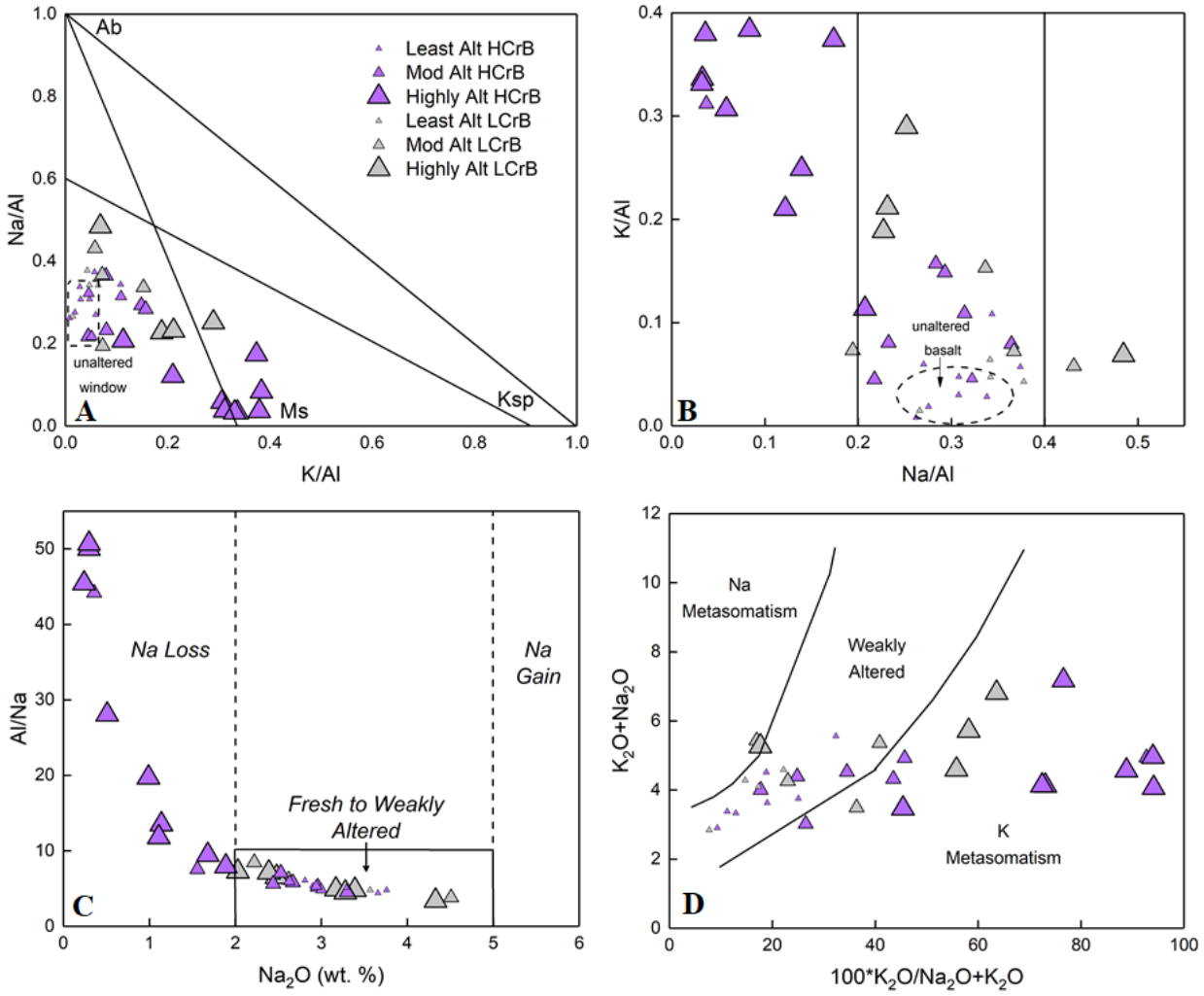

Figure 6-11 . MER diagrams of Fisher basalts. A) Na/Al (molar) vs. K/Al (molar) diagram (modified from Davies and Whitehead, 2006). B) K/Al (molar) vs. Na/Al (molar). C) Al/Na (molar) vs. Na_2O (wt. %) (Spitz and Darling, 1978). D) $K_2O + Na_2O$ (wt. %) vs. $100*K_2O/Na_2O + K_2O$.

Unaltered samples are selected based on Table 6-1 and alteration plots (Fig. 6-11a,b). The highly altered HCrB, sample CO-2019-71, has gains in K, Rb, Ba and As (Fig. 6-12a), suggesting biotite and sericite alteration affected these rocks and potentially the presence of arsenopyrite. The loss in Na paired with K gains (Fig. 6-12a) suggests sericitization. The LCrB, sample CO-2019-61, has characteristic elements associated with potassium alteration (K, Rb, Ba) and gains in W (Fig. 6-12b). Thin section analysis confirmed this rock has an alteration assemblage of biotite-diopside-clinozoisite-calcite with pyrrhotite mineralization (Fig. 6-6d). Gains in W indicate the presence of a W-bearing phase; scheelite, which was confirmed in microprobe analysis. Most elements in the granite occur close to the isocon line (Fig. 6-12c), which suggests that intrusive

units do not show alteration effects as strongly as volcanic rocks. Similar observations were made when analyzing other intrusive rocks using isocon analysis. Sample CO-2019-48 shows gains in Cu and Bi and could related to chalcopyrite and Bi-telluride occurrences. The metasedimentary rock sample (CO-2019-69) has gains in potassic elements and Mo and Pb (Fig. 6-12d). The sample is biotite, muscovite and carbonate altered (Fig. 6-4d).

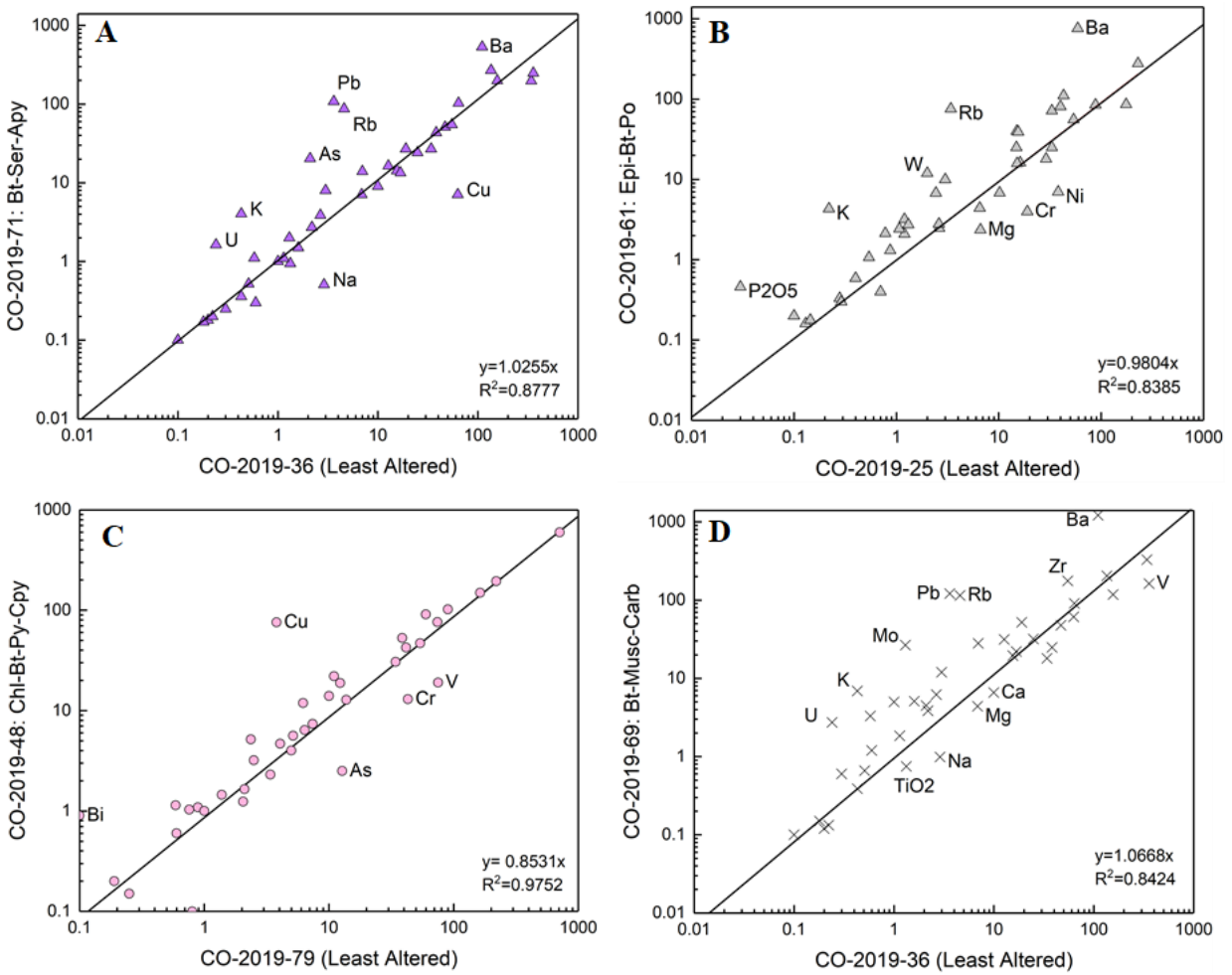

Figure 6-12 Isocon diagrams (based on Grant, 1986) for: A) Least-altered Fisher HCrB vs. an altered HCrB. B) Least-altered Fisher LCrB vs. an altered LCrB. C) Least-altered granite vs. an altered granite. D) Least-altered metasedimentary rock vs. an altered metasedimentary rock. The black line represents the isocon, with element gains plotting above the isocon and losses plotting below. The geochemical data is from Table 4.X.

Groups of similar colours in Table 6-2 have similar covariance and are used to identify element associations. PC1 potentially shows a few processes at play. A unique metallic signature

is made evident by positive loadings (eigenvectors) in As, Mo, Pb, and Ag. K and Rb also have a positive loading which could indicate potassic alteration. Elements with negative loadings were less clear and could represent multiple processes occurring. PC2 shows a major distinction between compatible elements (with positive loadings) and incompatible elements (with negative loadings). The strong positive loadings, especially in Cr, Mg, and Ni, could suggest that all three elements are related to a primary igneous feature. PC3 shows evidence of sericitization by the anticorrelation of Na (positive loadings) and K, Rb, Ba and LOI (negative loadings). PC4 hints that to metal associations may exist: 1) Bi, W, Te which could indicate an association between Bi-Tellurides and scheelite and 2) Zn, Sb, As, and Pb which could represent either pyrite or arsenopyrite with trace metal phases. It is also important to note that many elements behave similarly, such as Ni and Cr. Thus, we would expect lithophile, siderophile and chalcophile elements to associate. Anticorrelations signify that no relationship between the elements of interest exists.

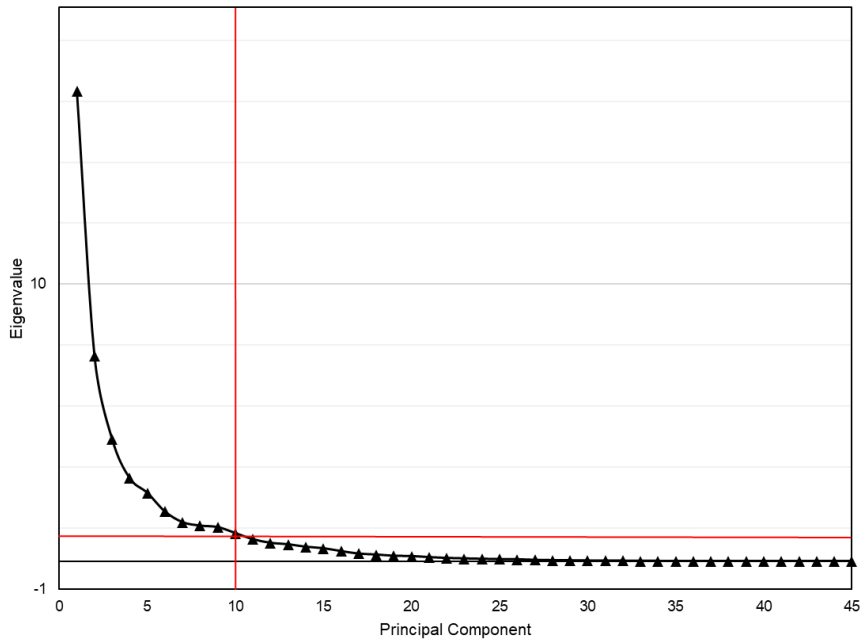

Figure 6-13 Scree plot of PCs 1 – 45 vs. eigenvalues to demonstrate respective variability. The red bold line through PC10 is to highlight that PC1 to PC 10 account for 89% of the data's variance (Cattell, 1966).

Table 6-2 Table of scaled eigenvectors (loadings) for principal components 1 through 10. Eigenvectors calculated from CLR transformed data (n=18 samples; moderate and highly altered HCrB and LCrB), with values ranging between 1 (perfect correlation) and -1 (perfect anticorrelation).

PC1		PC2		PC3		PC4		PC5		PC6		PC7		PC8		PC9		PC10	
As	0.22	Cr	0.31	Na	0.24	Bi	0.41	Cd	0.41	W	0.35	Ta	0.26	Cu	0.46	P	0.25	Hg	0.46
Be	0.20	Mg	0.27	Be	0.21	W	0.36	Ta	0.37	La	0.27	Rb	0.19	Sb	0.32	Zn	0.24	Ba	0.38
Mo	0.20	Ni	0.26	Ag	0.17	Te	0.27	Ni	0.23	Nd	0.24	K	0.16	V	0.27	Ba	0.23	Pb	0.20
Pb	0.19	Ca	0.20	Hg	0.17	Th	0.22	Y	0.19	Eu	0.21	Cu	0.16	W	0.21	Te	0.19	Cu	0.17
Ag	0.17	Co	0.20	Ta	0.17	Ba	0.19	Dy	0.18	Ag	0.18	Al	0.12	Ca	0.21	Ti	0.19	Yb	0.15
Rb	0.13	V	0.17	Sr	0.13	Zr	0.13	Hg	0.17	Pb	0.14	Ag	0.12	Ti	0.19	Mn	0.17	Zn	0.14
Nb	0.11	Zn	0.15	Mo	0.12	Hf	0.12	Ti	0.14	Cu	0.11	Ba	0.11	Te	0.18	Ag	0.16	Y	0.12
Sb	0.11	Sc	0.15	Bi	0.11	Ag	0.12	Cr	0.14	Mn	0.11	Ga	0.10	As	0.14	K	0.16	Al	0.11
K	0.11	Mn	0.09	Cu	0.10	Sr	0.09	Yb	0.13	Si	0.11	Co	0.09	K	0.13	Eu	0.15	Mo	0.11
W	0.09	Al	0.09	Fe	0.07	Cu	0.09	Hf	0.10	Ga	0.10	Th	0.08	Yb	0.12	Rb	0.15	Mn	0.08
Cd	0.08	Si	0.08	Ti	0.07	Ta	0.09	Zr	0.10	Cd	0.10	LOI	0.07	Co	0.08	Na	0.14	Ag	0.06
Cs	0.06	LOI	0.08	Sc	0.07	Rb	0.07	LOI	0.09	Ca	0.09	Gd	0.06	Sc	0.08	Fe	0.13	Th	0.05
Ba	0.05	Sr	0.08	W	0.06	Na	0.07	Ag	0.08	As	0.07	Si	0.06	Si	0.08	Pb	0.12	Cd	0.05
Ta	0.04	Pb	0.07	As	0.05	Cs	0.07	Gd	0.05	P	0.06	Sr	0.06	Fe	0.08	Sr	0.12	Dy	0.05
Te	0.03	Ag	0.06	Cs	0.03	K	0.06	Nb	0.04	Gd	0.06	Dy	0.04	Hf	0.07	Bi	0.08	Ca	0.05
Bi	0.00	Fe	0.06	Y	0.03	Ga	0.04	V	0.04	Ta	0.04	Y	0.04	Cd	0.07	Be	0.08	Ga	0.04
Zn	0.00	Cd	0.06	V	0.03	Al	0.03	Mn	0.03	Zn	0.03	P	0.04	Be	0.06	Ta	0.07	Rb	0.03
Cr	0.00	Ga	0.03	Al	0.02	Cr	0.01	Mg	0.02	Ti	0.03	Cs	0.03	Nb	0.05	Nb	0.05	Si	0.02
Ni	-0.01	Bi	0.03	Nb	0.01	Ni	0.01	As	0.02	Al	0.02	Be	0.02	Mn	0.04	V	0.05	V	0.02
Hg	-0.03	Th	0.02	Ca	0.01	Ca	0.00	Fe	0.02	K	0.02	As	0.02	Ga	0.04	Dy	0.04	Sr	0.01
LOI	-0.03	Cs	0.01	Mn	0.00	Si	0.00	Pb	0.00	Mo	0.01	Pb	0.01	Y	0.03	Ga	0.03	P	0.01
La	-0.04	W	0.01	Co	0.00	Y	0.00	Ga	0.00	Sr	0.00	Eu	0.01	Ag	0.03	Al	0.03	Zr	0.01
Cu	-0.07	As	0.00	Eu	0.00	Mn	-0.01	Zn	0.00	Zr	-0.01	Cr	0.01	Ba	0.03	W	0.03	Fe	0.00
Hf	-0.10	Mo	-0.02	Ga	0.00	Dy	-0.03	Bi	-0.01	Ni	-0.01	Na	0.00	P	0.02	Gd	0.03	K	-0.01
P	-0.11	Cu	-0.03	P	-0.01	Yb	-0.03	Ca	-0.01	Mg	-0.02	W	0.00	Zn	0.01	Y	0.02	Sc	-0.02
Zr	-0.12	Na	-0.04	Dy	-0.01	LOI	-0.03	Te	-0.02	Cr	-0.02	Ti	-0.01	Mg	0.01	Sc	0.02	Na	-0.05
Mg	-0.13	Rb	-0.05	Mg	-0.03	Eu	-0.03	Ba	-0.02	Te	-0.04	V	-0.01	Gd	0.00	Co	0.01	Cr	-0.05
Nd	-0.14	Be	-0.05	Cd	-0.05	P	-0.05	Be	-0.02	Dy	-0.05	Fe	-0.02	Al	-0.01	Ca	0.01	Hf	-0.06
Gd	-0.15	Te	-0.05	Pb	-0.06	Sc	-0.06	Eu	-0.03	Hf	-0.05	Nb	-0.02	Bi	-0.01	Sb	0.01	Be	-0.07
Na	-0.16	Ba	-0.05	Si	-0.06	Cd	-0.07	Co	-0.03	LOI	-0.05	Sc	-0.03	Dy	-0.01	Si	-0.01	As	-0.08
Th	-0.16	K	-0.05	Yb	-0.08	Fe	-0.08	P	-0.03	Fe	-0.05	Yb	-0.04	Zr	-0.04	Yb	-0.02	W	-0.09
V	-0.17	Hg	-0.10	Sb	-0.10	Hg	-0.09	K	-0.04	Th	-0.06	Mg	-0.05	Rb	-0.04	As	-0.03	Cs	-0.09
Yb	-0.17	La	-0.13	Te	-0.10	Mg	-0.09	Rb	-0.05	Y	-0.07	Ni	-0.05	Pb	-0.04	Cr	-0.03	Te	-0.09
Co	-0.17	Ti	-0.14	Gd	-0.11	Ti	-0.10	Sc	-0.05	Ba	-0.08	Ca	-0.08	Cs	-0.06	Mo	-0.04	Gd	-0.09
Eu	-0.18	Ta	-0.14	Nd	-0.11	Be	-0.11	Si	-0.07	Be	-0.08	Sb	-0.09	Mo	-0.07	Mg	-0.06	Sb	-0.10
Ca	-0.18	Sb	-0.15	La	-0.12	Mo	-0.12	W	-0.09	Hg	-0.08	Hf	-0.10	LOI	-0.08	Nd	-0.08	Ni	-0.10
Sr	-0.18	Y	-0.15	Zr	-0.13	Nd	-0.13	Al	-0.10	Rb	-0.10	Zr	-0.11	Ta	-0.08	Cs	-0.09	Eu	-0.10
Ti	-0.18	Dy	-0.15	Hf	-0.13	Gd	-0.13	Na	-0.14	Sc	-0.11	Mo	-0.13	Cr	-0.08	Ni	-0.10	Ti	-0.10
Y	-0.20	Nd	-0.16	Zn	-0.16	V	-0.14	Sb	-0.14	Co	-0.12	Nd	-0.14	Eu	-0.10	Th	-0.12	Co	-0.11
Si	-0.20	Eu	-0.17	Cr	-0.17	Co	-0.15	Sr	-0.14	V	-0.15	Hg	-0.15	Sr	-0.15	La	-0.12	Nd	-0.13
Dy	-0.20	Yb	-0.19	Th	-0.18	Pb	-0.17	Th	-0.16	Bi	-0.17	Mn	-0.19	Th	-0.17	Cd	-0.19	La	-0.14
Mn	-0.21	Gd	-0.24	Ni	-0.18	As	-0.18	Mo	-0.16	Na	-0.17	La	-0.20	La	-0.18	Hf	-0.20	Nb	-0.15
Sc	-0.21	Zr	-0.24	Rb	-0.34	Nb	-0.19	Cu	-0.18	Nb	-0.19	Zn	-0.23	Nd	-0.20	Zr	-0.22	Bi	-0.15
Al	-0.21	Nb	-0.25	LOI	-0.34	La	-0.22	Nd	-0.24	Yb	-0.20	Cd	-0.29	Ni	-0.22	LOI	-0.23	Mg	-0.26
Fe	-0.23	P	-0.26	Ba	-0.35	Sb	-0.25	Cs	-0.29	Sb	-0.22	Bi	-0.33	Na	-0.24	Hg	-0.23	LOI	-0.29
Ga	-0.23	Hf	-0.26	K	-0.38	Zn	-0.31	La	-0.36	Cs	-0.54	Te	-0.57	Hg	-0.30	Cu	-0.50	Ta	-0.36

An additional approach to further identify element associations is achieved by use of biplots (Fig.5.14a) and 3-dimensional plots of PC1, PC2 and PC3 (Fig. 6-14b) which account for 55% of the variance in the dataset. Five groups of element associations can be identified based on the vector's orientation and magnitude: (1) elements associated with potassic alteration: K, Ba, Rb; (2) elements associated with sodic alteration: Na; (3) elements associated with mafic compositions: Fe, Mg, Mn, Ca, V, Sr, Ga, Cr, Ni, Zn, Co, Cd; (4) chalcophile elements: Bi, Cd, Ag, Pb, W, Mo, As and Sb, Te; and (5) immobile elements: Y, Ti, Eu, Yb, Nd, Nb, Ta, La, Zr, Hf, P and Gd. HCrB tend to associate with chalcophile elements, especially Pb, and elements related to potassic alteration (Fig. 6-14b). LCrB do not show any distinct element associations.

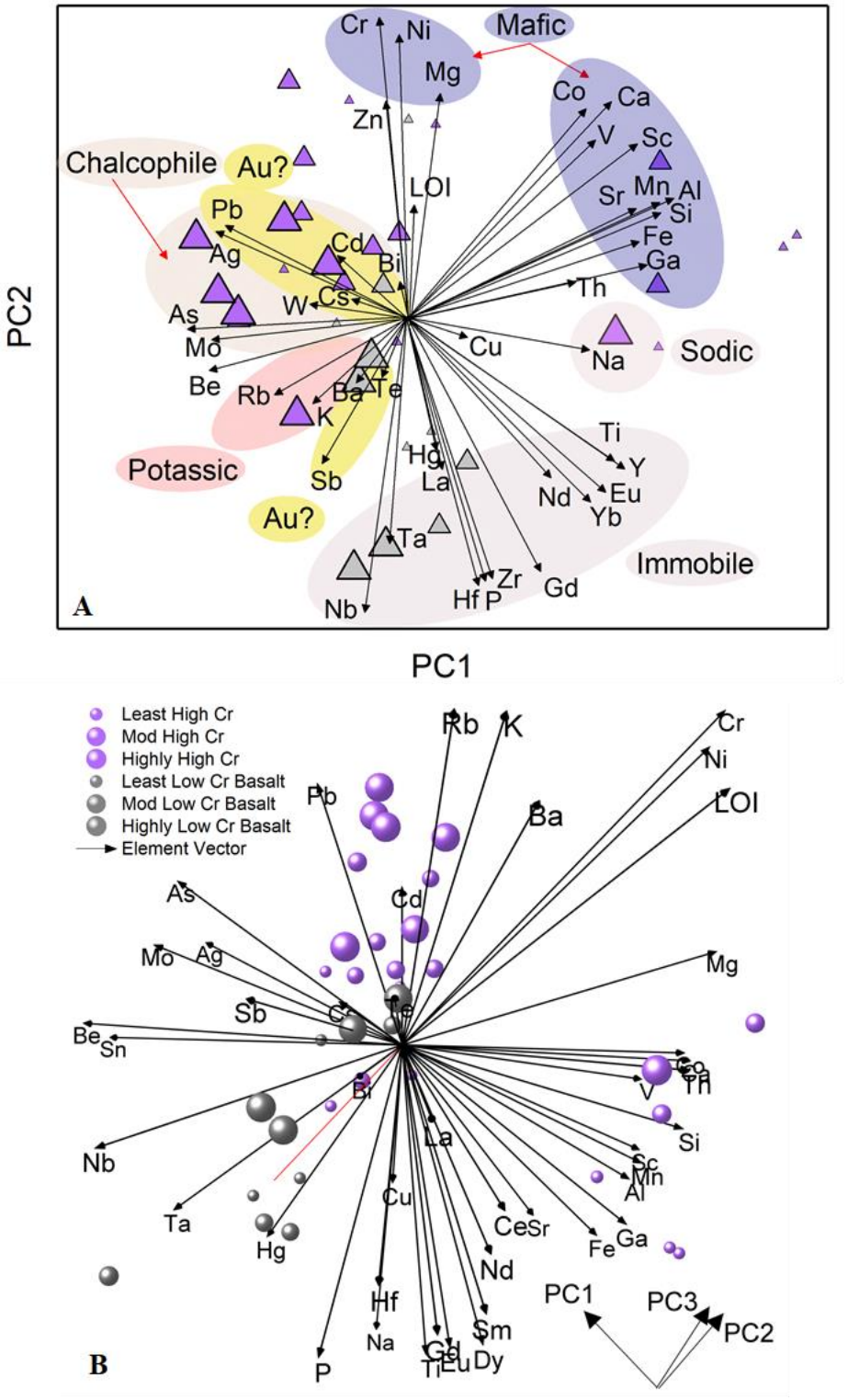

Figure 6-14 A) Bivariate plot of PC1 vs. PC2 and various element groupings. B) Principal Component Analysis results plotted in PC1-3 3-dimensional space. The PC axes have been oriented in two ways to illustrate clusters in geochemical data. PC1-3 account for 55% of the variance in the dataset.

In comparing HCrB to LCrB, four HCrB samples and three LCrB samples with variable alteration assemblages are plotted relative to a least-altered sample (CO-2019-123; HCrB). Both basalts show enrichments in Rb, K and Ba, though these tend to be stronger in HCrB (Fig. 6-15a). Na losses are significantly evident in the HCrB which likely corresponds to feldspar destruction. Slight variation between HCrB and LCrB exist in comparing Ca and Mg (Fig. 6-15a). Increased Ca in HCrB could correspond to a combination of calcite and clinozoisite alteration (Fig.6-5d,h) and/or a primary magmatic feature. Gains in Mg likely correspond to biotite and chlorite alteration, or again, are highlighting a primary magmatic feature. Major elements that are typically immobile, such as Al and Ti (Fig. 6-15a), are plotting with slight variations which further stresses that this approach should only be used to identify major variations.

In terms of mobile elements, both HCrB and LCrB have strong enrichments in Pb, As, and Mo, but are greater in HCrB (Fig. 6-15b). Ni and Cr are both depleted, which is expected since this was the source of their classification. Enrichments in Zn in HCrB and LCrB suggest that conditions for sulphide formation were favourable (Fig. 6-15b). The immobile elements do not show major distinctions between the HCrB and LCrB (Fig. 6-15c). However, the LREEs (Nd, La, Eu) show larger variations from the y=1 line relative to HREEs, suggesting these are relatively mobile.

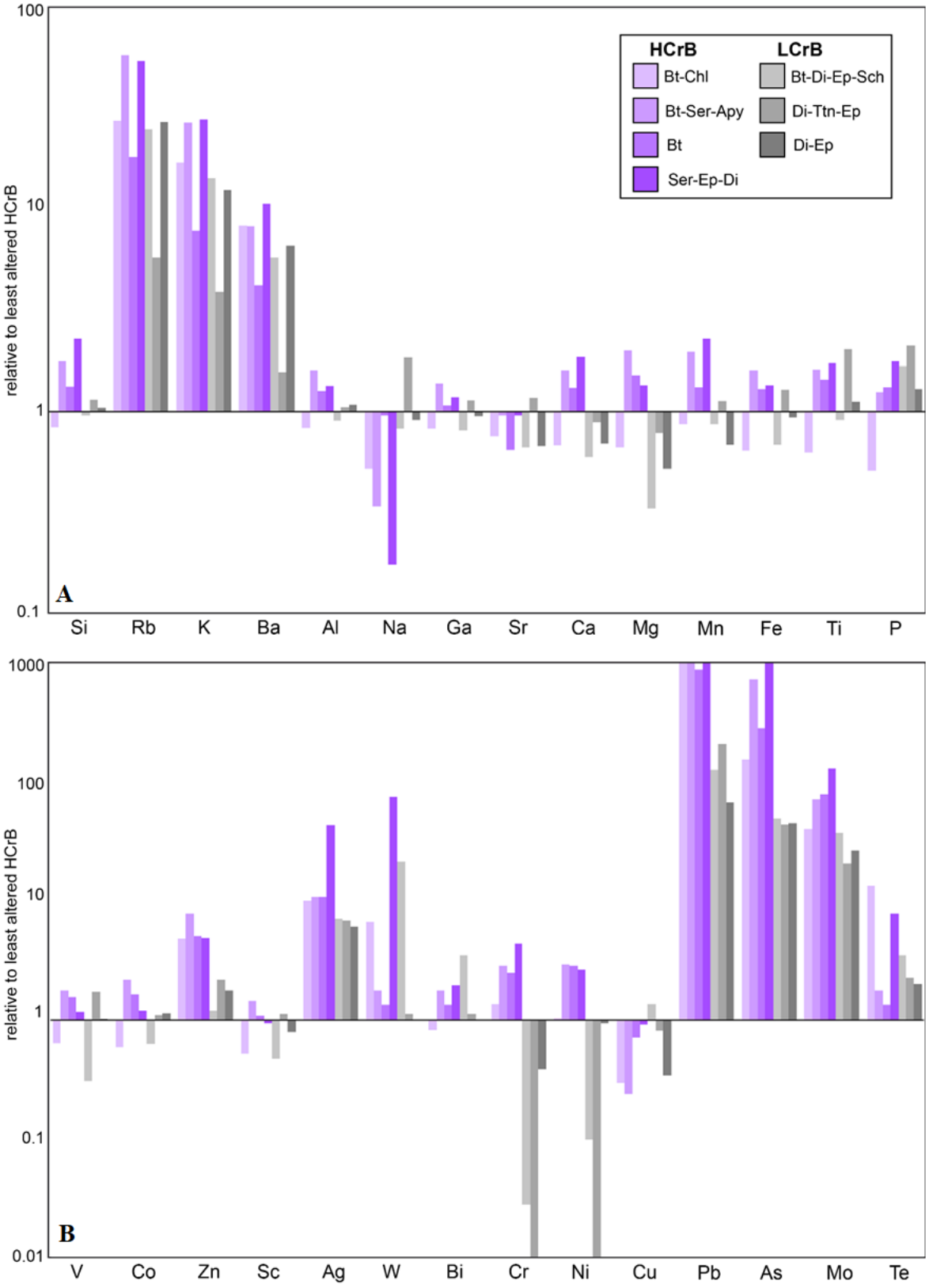
HCrB
Bt-Chl
Bt-Ser-Apy
Bt
Ser-Ep-Di
LCrB
Bt-Di-Ep-Sch
Di-Ttn-Ep
Di-Ep
relative to least altered HCrB
100
10
1
0.1
A
Si
Rb
K
Ba
Al
Na
Ga
Sr
Ca
Mg
Mn
Fe
Ti
P
1000
100
10
1
0.1
0.01
B
V
Co
Zn
Sc
Ag
W
Bi
Cr
Ni
Cu
Pb
As
Mo
Te

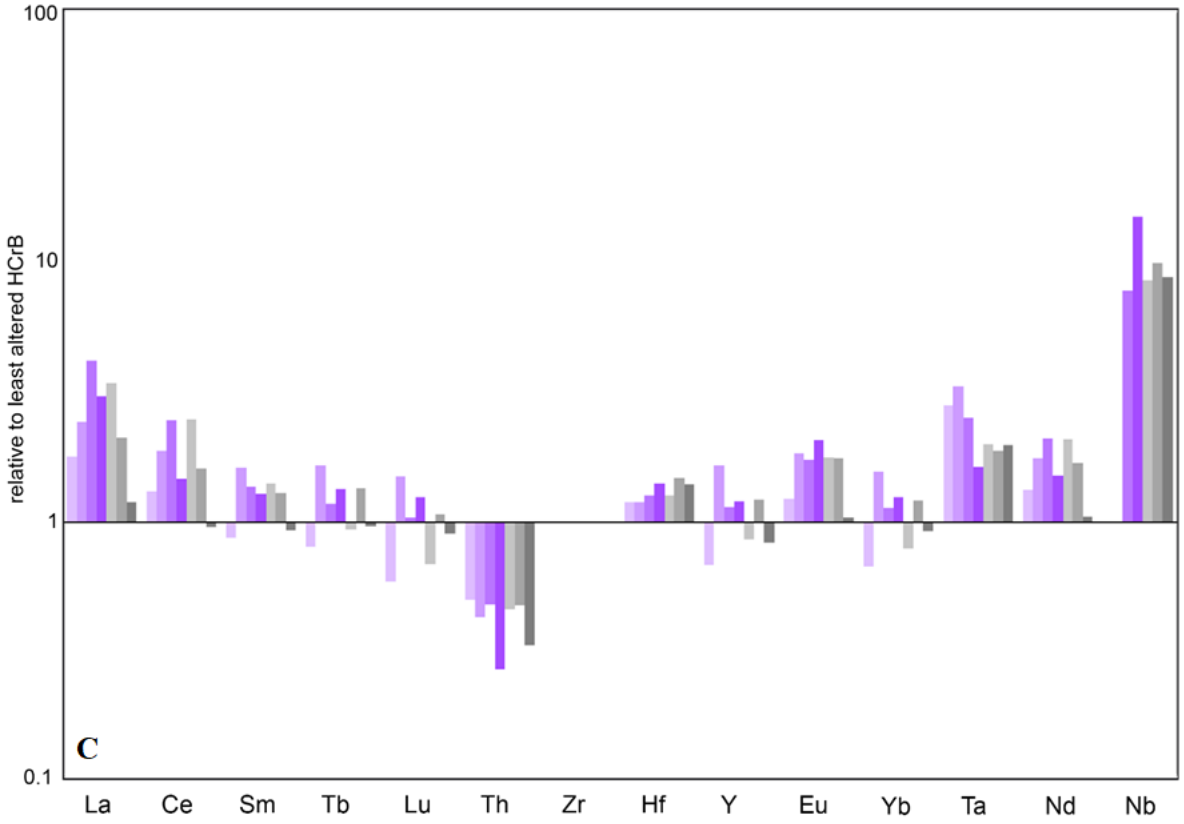

Figure 6-15 Zr-weighted enrichment/depletion plot showing major elements and ionic substitutions (A), mobile elements (B) and immobile elements (C).

Based on mass change calculations, various trends can be identified. Most highly altered samples trend towards a combination of sericitization, silicification and possible biotite alteration, made evident by mass gains in K_2O (Fig. 6-16a). Mass losses in Na_2O are typically attributed to feldspar destruction, which, accompanied by K_2O gains is typical of sericitization (Fig. 6-16b). Biotite and chlorite alteration are shown for those samples with gains in FeO_T, MgO and MnO, which is stronger in HCrB (Fig. 6-16c). Sericitization in both HCrB and LCrB is made evident by losses in CaO and NaO (Fig. 6-16c). These trends are also observed in hand sample and thin section (Fig. 6-5c,d,g). Various mobile elements also demonstrate the growth of minerals in alteration, such as arsenopyrite (Fig. 6-16d).

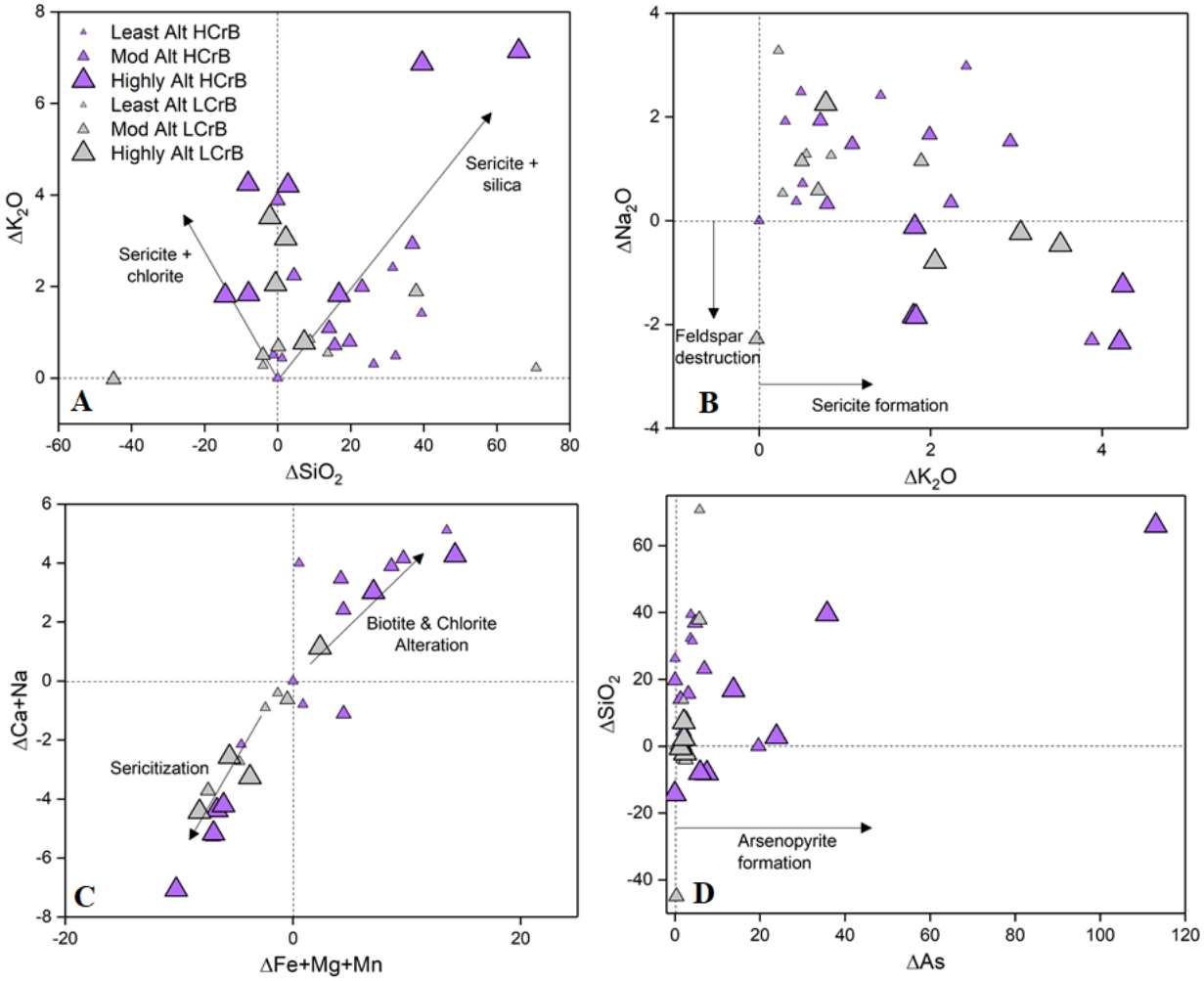

Figure 6-16 Mass change plots of Fisher HCrB and LCrB basalts showing selected element losses and gains, and the various processes associated with mass gains (sericite, apatite) and losses (feldspar destruction). A) ΔK2O vs. ΔSiO2. B) ΔNa2O vs. ΔK2O. C) ΔCa+Na vs. ΔFe+Mg+Mn. D) E) ΔSiO2 vs. ΔAs.

In summary, the approaches described in this chapter which quantify hydrothermal alteration can be summarized by:

<u>HCrB:</u>

(1) K, Rb & Ba gains associated with potassic alteration (Fig. 6-11b,d; Fig. 6-12a; Fig. 6-14b; Fig. 6-15a; Fig. 6-16a)

(2) Na and Sr loss due to feldspar destruction – mainly sericitization (Fig. 6-11b,c; Fig. 6-12a; Fig. 6-15a; Fig. 6-16b,c)

(3) Gains in Fe, Mg, Mn potentially related to increased biotite and chlorite alteration or related to a primary igneous feature (Fig. 6-15a; Fig. 6-16c)

(4) Enrichments in Pb, Ag, W, As, Mo, Zn (Fig. 6-12a; 6-14a,b; Fig. 6-15b; Fig. 6-16d)

LCrB:

(1) K, Rb & Ba gains associated with potassic alteration (Fig. 6-11d; Fig. 6-12b; Fig. 6-15a; Fig. 6-16b)

(2) No significant Na gains or losses (Fig. 6-11c; Fig. 6-12b; Fig. 6-15a)

(3) Enrichments in chalcophile elements but not as strong as HCrB (Fig. 6-12b; Fig. 6-15b)

Granites:

(1) Trending towards muscovite alteration (Fig. 6-10a,b)

(2) Not strongly altered, made evident by localization of most elements along isocon line (Fig. 6-12c)

(3) Enrichments in chalcophile elements (Bi, Cu; Fig 6-12c)

Metasedimentary rocks:

(1) Trending towards muscovite alteration (Fig. 6-10a,b)

(2) Enrichments in chalcophile elements (Mo, Pb; Fig 6-12d)

CHAPTER 7: DISCUSSION

7.1 Host Rock Classification

Geochemically, host rocks can be classified using major or conserved elements (Stanley, 2013; Winchester and Floyd, 1997; Pearce, 1996). The applicable approach depends on the geologic history. For example, major elements can be readily mobilized, especially in hydrothermal systems and metamorphosed rocks. Fisher property rocks have been metamorphosed to lower amphibolite facies and are locally altered; thus, it is best practice to use conserved elements to classify these rocks. A simple approach to identifying conserved elements is by utilizing bivariate plots (Fig. 4-6). All analyzed elements were tested for their immobility and elements such as Zr, Yb, Hf, Eu, Tb, Lu, Al, Mn and Ti were identified as conserved due to minimal variation in relative abundances within lithologies. Figure 7-1 shows the range of variability for selected trace and major elements in basalts. Intrusive units do not exhibit as strong of alteration as volcanic rocks (Fig. 6-2a; Fig. 6-12c) so less variation would be expected in these units.

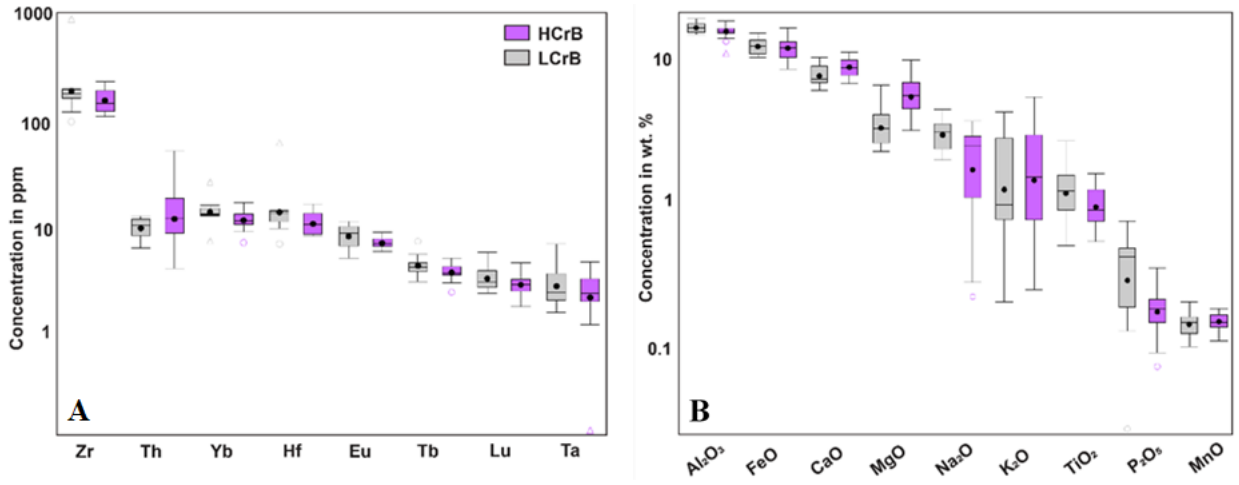

Figure 7-1 Box and Whisker plots of least to highly altered HCrB and LCrB and their respective trace elements (A) and major elements (B) concentrations.

The principal diagram used to classify Fisher host rocks was the Zr vs. Ti bivariate plot (Fig. 4-7a; Fig.5-9). This plot assumes that both Zr and Ti were conserved, which was confirmed for least altered samples. Both titanite and zircon were listed as constituents of the alteration assemblage at the Santoy deposit (Wood, 2016) which would contradict using the Zr vs. Ti plot for classification. However, hydrothermal titanite nor zircon were identified at the Fisher property. The variations in Zr (Fig.5-9) may be attributed to sampling of rocks that were logged as, and appeared to be altered mafic volcanic rocks, but may have been altered by relatively thin, intercalated felsic units/intrusive rocks. Due to the variation in conserved elements in highly altered samples, a combination of using the Zr vs. Ti discrimination diagram, Pearce classification diagrams, petrographic observations and hand sample descriptions were used to classify samples.

When studying magmatic affinities, the use of conserved elements is prioritized over plots which use major oxides. The Ross and Bedard diagram (Fig. 4-8d; Fig. 4-9a) makes use of conserved elements, and specific ratios of these elements which, in theory, are not affected by post-crystallization alteration. The diagram indicates that mafic intrusive rocks are tholeiitic – transitional, felsic intrusive rocks are calc-alkaline, intermediate to felsic volcanic rocks are calc-alkaline, and basalts range from tholeiitic to calc-alkaline (Fig. 4-9a). In general, immature island arc environments are characterized by basaltic rocks with a tholeiitic signature, while mature island arcs are characterized by andesites and dacites with a more tholeiitic to calc-alkaline signature (Miyashiro, 1974). In the case of the Fisher property, there is a combination of these characteristics, but overall basalts have a more transitional to calc-alkaline signature (Fig. 4-8d) suggesting the property preserves a mature island arc. Negative Nb and Ti anomalies (Fig. 4-9d) and the mixed continental-oceanic signatures (Fig. 4-8e) indicate a maturing volcanic arc setting for all Fisher host rocks. Prior work in the Flin Flon-Glennie domain established the tectonic

setting in which volcanic rocks formed was a primitive to evolved oceanic island arc setting (Stern et al., 1995). Observations from the Fisher property agree with regional interpretations.

The distinction between HCrB and LCrB is based on variations in the CLR of Cr. A cutoff value of 60 ppm Cr or a normal score of -0.56 was used to distinguish between the two basalts (Fig. 4-8a). This manually selected cutoff was chosen based on alteration characteristics. Past studies have used a normal score of 0, -1.0 and 1.0 as cutoffs to divide units evenly (Hood, 2019), but that would assume equal samples in each unit. Based on the limited number of samples collected, it is difficult to assume equal number of HCrB and LCrB. The average Cr content of LCrB is 23 ppm Cr and 137 ppm Cr in HCrB, compared to 170 ppm in average basalts (Price, 1997). The HCrB is one of the following: 1) a distinct lithologic unit from the LCrB; 2) a higher Cr end-member of the same lithologic unit as LCrB; or 3) the same unit as LCrB which has been altered by Cr-bearing fluids or Cr has been lost.

Losses in Cr, which define the LCrB and Cr gains in HCrB (Fig. 6-15b) could be explained with one of two ideas; either Cr was removed/added during hydrothermal alteration or it is reflecting a primary igneous feature. If the Cr were added during hydrothermal alteration, chromium-rich micas in the alteration assemblage would be expected. Cr-micas are a more typical alteration product in ultramafic rocks but have been shown to occur in other rock types (Zuo et al., 2016). Petrographic observations, however, did not indicate the presence of Cr-rich micas. If the Cr were reflecting a primary igneous feature, Ni and Mg mass gains/losses would be expected to follow a similar trend as Cr, which is observed at the Fisher property (Table. 6-2). In terms of Cr mobility in hydrothermal fluids, some studies have shown that Cr-enriched, oxidized fluids mixed with Au-enriched, reduced fluids can lead to precipitation of Au (Dinel et al., 2008). However, other studies have indicated the relative immobility of Cr in hydrothermal fluids and instead relate

the variation to primary igneous fractionation (Hood et al., 2019). Overall, the Cr variations in HCrB and LCrB are minor and are likely more reflective of a primary feature. The variation between the units could correspond to different fractional crystallization histories.

Though geochemical classification was the primary approach for classifying Fisher host rocks, petrographic and hand sample descriptions were used to supplement the geochemistry. The mineral abundances discussed in Chapter 3.1 align well with the geochemical classification in Chapter 3.2. Since distinguishing metasedimentary rocks from other rock types is difficult with whole-rock geochemistry, textural relationships observed in thin section and hand sample greatly aided classification.

7.2 Constraints of Mineralizing Processes and Fluids

The alteration assemblage can be simplified into a distal sericite and biotite and a proximal calc-silicate alteration assemblage. This distal sericite and biotite alteration is most evident in least altered samples, which are typically 2 – 3m away from mineralization along drill core. Magnesiohornblende was identified as the most common amphibole in the Fisher property (Fig. 5-1b). Sericitization of feldspars is common throughout the Fisher property and can be described by Equation (1) which involves the addition of K through hydrothermal fluids. This reaction also results in Na or Ca in solution which could become consumed during the formation of clinozoisite. Biotite alteration from the breakdown of magnesiohornblende and addition of K can be described by Equation (2).

(1) $$3\left[(Na,Ca)AlSi_3O_{8\ (albite)}\right] + K^+_{(aq)} + 2H^+_{(aq)} = 1\left[KAl_3Si_3O_{10}(OH)_{2\ (sericite)}\right] + 6SiO_{2\ (quartz)} + 3(Na^+, Ca^{2+})_{(aq)}$$

(2) $$Ca_2[Mg_4Al]Si_7AlO_{22}(OH)_{2\ (magnesiohornblende)} + 2K^+_{(aq)} + H_{2(aq)} + 6Fe^{2+}_{(aq)} =$$
$$2[KFe^{2+}_3AlSi_3O_{10}(OH)_{2\ (annite)}] + 2Ca^+_{(aq)} + 4Mg^{2+}_{(aq)} + SiO_{2\ (quartz)}$$

The proximal calc-silicate alteration is comprised of various minerals including quartz, biotite, chlorite, sericite, calcite ± clinozoisite, epidote, titanite, diopside, actinolite, K-feldspar, muscovite, tourmaline and scheelite (Fig. 6-1). Textural and spatial observations during petrographic analysis indicated the presence of multiple generations of alteration minerals, which could reflect chemical variations related to the effects of hydrothermal fluids.

Biotite and chlorite are common occurring alteration minerals at the Fisher property. Biotite grains analyzed in most Fisher host rocks were annite in composition (Fig. 5-3b). Biotite in alteration haloes in the metasedimentary unit was the most Mg-rich (phlogopite) in composition (Fig. 5-3b) likely related to the presence of clays in the original rock which were subsequently altered during metamorphism/alteration. Biotite in mafic volcanic rocks has been partially or completed altered to chlorite, possibly by way of the reaction in Equation (3). Chlorite associated with the alteration halo is of a Fe-Mg composition, while those associated with quartz and sulphide veins, are more Fe-rich (chamosite; Fig. 5-5a). It is also likely that chlorite was precipitated directly from the hydrothermal fluids by interactions between fluids and the wall rock.

(3) $$KFe^{2+}_3AlSi_3O_{10}(OH)_{2\ (annite)} + 3Mg^{2+}{}_{(aq)} + 6H_2O_{(aq)} =$$
$$(Fe^{2+}, Mg^{2+})_6(Si, Al)_4O_{10}(OH)_{8\ (chlorite)} + K^+{}_{(aq)} + 6H^+{}_{(aq)}$$

Clinozoisite alteration typically occurs in association with sericitization, calcite and mica alteration. Equation 4 presents a possible reaction where sericitization of feldspars and release of Ca^{2+} into solution (from Eq.1) results in the formation of clinozoisite and calcite and the release

of K into solution. This reaction potentially explains the additional association of micas with clinozoisite (Fig. 6-2f; Fig. 6-5c,h). Electron microprobe analysis confirmed that calcite is the dominant carbonate mineral associated with sulphide minerals (Fig. 5-7b).

(4) $$KAl_3Si_3O_{10}(OH)_{2\,(sericite)} + 3Ca^{2+}_{(aq)} + CO_{2\,(aq)} + 2H_2O_{(aq)} =$$
$$Ca_2Al_3(Si_2O_7)SiO_4O(OH)_{(clinozoisite)} + CaCO_{3\,(calcite)} + K^+{}_{(aq)} + 5H^+_{(aq)}$$

Another dominant association in the calc-silicate assemblage in the mafic volcanic rocks is actinolite-diopside-titanite-chlorite-sericite (Fig. 6-3c; Fig. 6-5g, Fig. 6-6c,d). Magnesiohornblende grains typically exhibit margins which have been altered to actinolite (Fig. 6-6c), which locally occur as needles (Fig. 6-6d). Magnesiohornblende is a source for the Ca present in actinolite, titanite and diopside. The association between ilmenite and magnesiohornblende was locally preserved as ilmenite exsolutions along hornblende cleavage planes (Fig. 4-5e) or as ilmenite grains occurring proximal to magnesiohornblende and explains one possible introduction of Ti to form titanite. As mentioned previously, biotite commonly alters to chlorite which is dominantly preserved in association with the above minerals (Fig. 6-3c).

Minor amounts of other alteration minerals exist such as tourmaline, scheelite, muscovite and K-feldspar. Scheelite was observed in trace amounts in W-enriched samples, and fine-grained tourmaline showed a close association with calcite and higher-grade Au samples. Both have potential as important alteration minerals signifying proximity to high grade gold.

Mass transfer diagrams provide an excellent indicator of how alteration has affected pre-mineralization rocks and what elements have been introduced through the hydrothermal fluids. Figure 7-2 shows overall mass gains in the following U, Pb, As, Mo, Rb, Ag, K, Nb, Ba, Zn, Te

and W and mass losses including Na, Cr, Ni, Th, Cu, Sr and Mg. Quartz veins were intentionally avoided when sampling to better constrain the alteration haloes. However, the presence of quartz veins indicates gains in Si would be expected.

Based on mass change calculation results listed above, the following conclusions can be made. Gains in K reflect the presence of either K-feldspar, biotite, or muscovite in the alteration. The metal enrichments of Pb, As, Mo, Ag, Zn, Te, and W may be useful as pathfinder elements towards gold mineralization. As enrichments directly reflect the presence of arsenopyrite which is often related to Au in orogenic gold systems (Xing et al., 2019). Trace amounts of sphalerite, scheelite and Bi-tellurides exist (Fig. 6-8e), which explain the gains in Zn, W, and Te respectively. No Mo, Pb or Ag-bearing phases were observed in thin section and likely occur as trace phases in sulphide minerals, such as pyrite and/or arsenopyrite, but still have a potential to be used as pathfinders. Rb and Ba gains directly reflect ions which substitute into the chemical formula of micas. A couple of immobile elements such as Nb and Th show evidence of mobilization in the system and should thus be used with caution.

Na and Sr losses, which characterize the HCrB, were observed in proximal and distal samples related to sericitization of feldspars in both proximal and distal alteration assemblages (Fig. 6-5c,d,e). Mg, Cr and Ni mass losses, which are more pronounced in the LCrB, are likely a result of the samples being normalized to a HCrB, and thus, likely reflect a primary igneous feature, rather than a hydrothermal feature. LCrB inherently show losses in Cr and Ni, in which the nature of those elements is discussed further in Chapter 6.1.

The direct relationship between gold and sulphide minerals is not fully understood. However, HCrB tend to show more advanced alteration and stronger metal enrichments suggesting that Cr-

Mg-Fe-bearing wall rock mafic volcanic rocks are suitable for sulfidation reactions which precipitate pyrite. For reference, Fisher HCrB have an average $FeO_{(t)}$ of 12.00 wt. % (avg basalt: 8.65 wt. %; Price, 1997), and an average MgO of 5.8 wt. % (avg basalt: 4.6 wt. %; Price 1997).

The alteration was not as extensive in intrusive and metasedimentary rocks, but these units still have significant potential to host gold mineralization. Many pathfinder elements used for identifying highly altered HCrB, were also observed in intrusive and metasedimentary units. Locally, metasedimentary units exhibit strong alteration (Fig. 6-10a,b; Fig. 6-12d), especially when in contact with Fisher mafic volcanic rocks. Though mineralization occurs in quartz veins within a particular unit, favourable conditions more commonly exist where quartz veins intersect contacts between mafic volcanic, felsic intrusive and metasedimentary rocks.

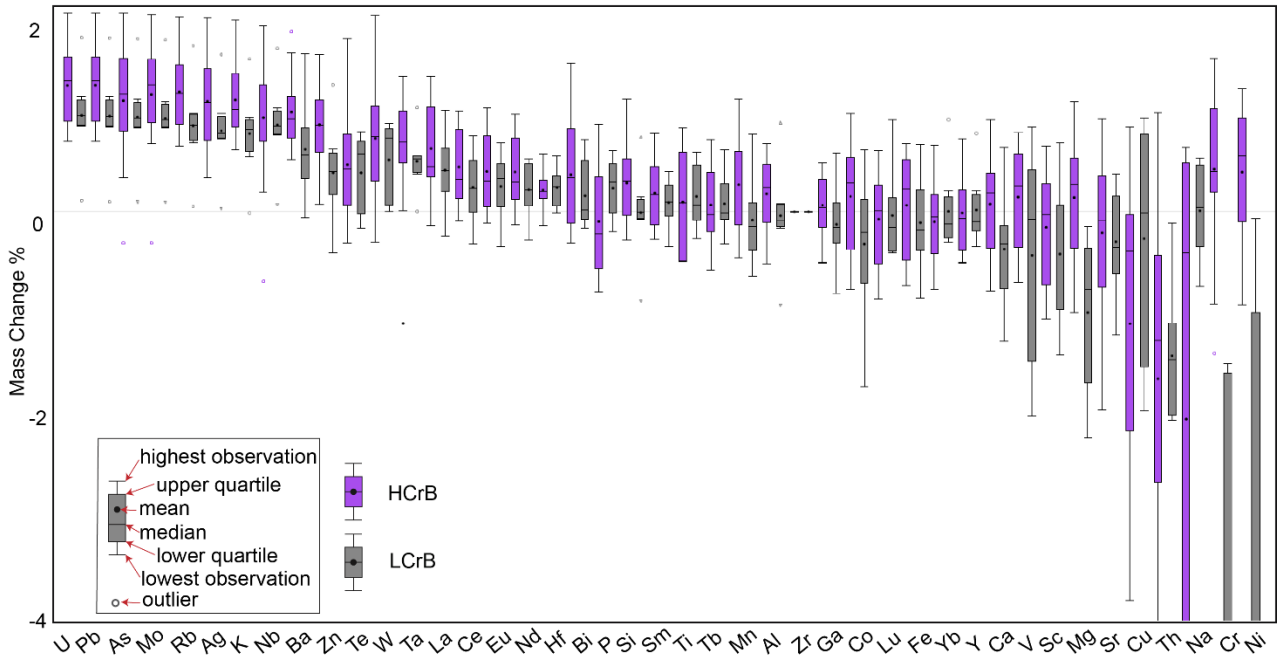

Figure 7-2 Box and whisker plots showing mass changes of major, minor elements, mobile and immobile elements of moderately and highly altered HCrB and LCrB.

The major, minor and trace element variations and particular textures observed in thin section can provide additional insight to hydrothermal fluid conditions. Overall, fluids are not base metal enriched, suggesting hydrothermal fluids were of low salinities, typical of orogenic gold deposits (McCuaig and Kerrich, 1998). Cross-cutting relationships of alteration haloes observed in thin section analysis (Fig.6-5d) and the general lack of distinct mineral zonation suggest multiple hydrothermal fluid events affected the Fisher property. Hydrothermal fluids were likely sourced from metamorphic devolatilization reactions occurring in the greenschist-amphibolite grade transition (Goldfarb, 2015) which were subsequently concentrated along deep fracture systems which focused the migration of fluids (Kerrich and Wyman, 1990)

The presence of diopside potentially suggests higher temperature hydrothermal fluids (525˚C - 700˚C; McCuaig and Kerrich, 1998) were involved, since diopside is not typical of a calc-silicate alteration halo at greenschist-amphibolite grade conditions. K-feldspars were also observed and have been attributed to higher temperature conditions (Cassidy, 1992). Colloform textures (Fig.6-8e) typically form in lower temperature settings (Barrie et al., 2009; Ramdhor, 1969) and likely represent a later cooling phase at the Fisher property.

Chemicals such as K and Rb showed increases in concentrations with proximity to auriferous quartz veins. This chemical gradient provides evidence for increasing fluid/rock ratios and disequilibrium approaching quartz veins (McCuaig and Kerrich, 1998). Tourmaline was observed in various host rocks (Fig.6-4e) and likely represents a hydrothermal fluid constraint rather than a host rock composition constraint. Tourmalines are typically low Cl and F hydroxy varieties indicating that hydrothermal fluids were probably of low Cl and F activities, consistent of those with low-salinities (McCuaig and Kerrich, 1998). Tourmalines also host B, suggesting fluids were boron-enriched, which brings into question the chemistry of source rocks. Studies have suggested

various B-enriched source rocks such as clastic metasediments and carbonate rocks (Lambert-Smith et al., 2016), marine evaporites (Xavier et al., 2008) and other sedimentary rocks, potentially indicating an import source rock for the Fisher deposit was a B-enriched sedimentary rock.

7.3 Comparison to Santoy Deposit

Host rocks:

The following summary is based on data received from Devon Stuebing, SSR Mining (Table 7-1; "Santoy data"). The Santoy Lake basalt (SL-B) is the unit interpreted to host the Santoy deposit (Stuebing, pers. comm., 2020). The volcanic rocks are tholeiitic – transitional and are attributed to Assemblage A (Delaney, 1995). This unit is approximately 500m thick through the Santoy deposit area which thins (~150m) as it continues south towards the Fisher property. A thicker unit (~3km) of this suite exists to the west in the Ray Lake fold. The calc-alkaline basalt (CA-B) is exposed to the north of the Santoy deposit occurring with the Carruthers Lake basalt (CL-B) and minimally exposed along the contact with the Packman Lake pluton. The unit also appears to continue down through the Fisher property. The Carruthers Lake basalt, mainly exposed in the Carruthers Lake synform, and the calc-alkaline basalt are believed to be Assemblage A volcanic rocks. The Felsic A (FA) unit outcrops to the north of the Packman Lake pluton and is attributed to Assemblage A. The Intermediate B (IB) and Felsic B (FB) units have both been interpreted to correspond to Assemblage B and typically occur as relatively thin lenses. The Intermediate B unit is typically found overlying the basal conglomerate unit of Assemblage B (Stuebing, pers. comm., 2020).

To determine whether Fisher host rocks are similar host rocks in the Santoy deposit, geochemical data from Santoy extrusive and intrusive rocks were provided by SSR Mining Inc.

This data (Table 7-1) was received in the format of a maximum and a minimum value of individual elements of each suite. It is important to note that the maximum values do not correspond to a particular rock, rather the highest concentration of each element from any rock type within that suite. Santoy extrusive rocks include two felsic units, an intermediate unit, five basalts including: a calc-alkaline basalt, the Carruthers Lake basalt, the Santoy Lake basalt, a calc-silicate basalt, and a clinopyroxene basalt.

Table 7-1 Maximum and minimum values of major oxides (wt. %) of representative Fisher from this study and Santoy volcanic units.

	Al_2O_3	CaO	Fe_2O_3	K_2O	LOI	MgO	MnO	Na_2O	P_2O_5	SiO_2
Santoy data										
FB-MAX	17.23	2.98	6.02	4.16	1.87	1.12	0.15	5.23	0.19	65.82
FB-MIN	15.98	1.84	5.14	2.70	0.58	0.60	0.11	4.54	0.13	63.33
IB-MAX	18.94	6.85	7.81	3.62	1.17	4.94	0.14	4.24	0.47	80.67
IB-MIN	9.61	0.56	2.49	0.94	0.50	0.72	0.03	1.14	0.05	57.48
FA-MAX	16.22	3.45	8.07	3.73	1.09	1.14	0.17	4.28	0.14	71.00
FA-MIN	12.91	1.37	4.51	1.59	0.19	0.66	0.05	3.11	0.05	63.63
CAB-MAX	18.81	13.63	12.35	3.25	2.18	7.97	0.20	5.20	0.38	60.20
CAB-MIN	14.16	4.85	7.43	0.63	0.19	1.84	0.12	1.00	0.12	46.11
SLB-MAX	20.66	13.63	12.22	3.25	5.03	23.04	0.24	3.91	0.42	62.27
SLB-MIN	7.91	4.90	5.60	0.04	0.13	1.89	0.08	0.41	0.08	44.13
CLB-MAX	21.41	17.94	15.25	3.09	1.75	9.56	0.29	3.82	0.74	60.21
CLB-MIN	12.59	6.49	9.22	0.19	0.15	2.59	0.12	1.16	0.05	47.03
Fisher data										
AND1-MAX	16.60	8.01	10.00	2.43	1.60	5.26	0.15	3.95	0.23	62.70
AND1-MIN	14.40	5.91	6.88	1.24	0.80	3.10	0.11	2.77	0.04	55.80
AND2-MAX	19.00	6.55	7.92	3.21	1.30	3.82	0.13	4.73	0.55	64.60
AND2-MIN	15.20	3.59	4.92	1.69	0.70	2.48	0.06	3.34	0.11	55.40
FV-MAX	14.50	2.17	2.74	3.64	0.90	0.62	0.03	4.59	0.05	75.30
FV-MIN	13.30	1.64	1.59	1.47	0.80	0.61	0.02	3.25	0.01	72.50
HCrB-MAX	18.00	11.10	14.60	1.80	1.40	6.89	0.20	3.76	0.29	55.00
HCrB-MIN	14.60	7.34	8.53	0.27	0.50	3.71	0.13	2.63	0.08	47.00
LCrB-MAX	17.20	10.20	11.80	1.02	1.10	6.61	0.18	3.65	0.50	55.70
LCrB-MIN	15.90	7.14	9.17	0.22	0.40	2.63	0.13	2.62	0.03	53.80

Abbreviations:

FA = Felsic Assemblage A
FB = Felsic Assemblage B
IB = Intermediate Assemblage B
CAB = Calc-Alkaline Basalt
SLB = Santoy Lake Basalt
CLB = Carruthers Lake Basalt

Based on Table 7-1, some initial comparisons can be made. The SiO_2 concentrations of Santoy basalts (CAB, SLB, CLB) range from 44 – 62 wt. %, while those from Fisher (HCrB, LCrB) range from 47 – 57 wt. %. Felsic units exhibit elevated SiO_2 between 63 – 75 wt. %. The Fisher FV has elevated SiO_2 (72 – 75 wt. %), closer to that of the Santoy FA (63 – 71 wt. %). Intermediate units at Fisher typically range in SiO_2 from 55 – 65 wt. % while the IB at Santoy ranges from 57 – 81 wt. %. Based on field associations between Fisher basalts and intermediate volcanic rocks, it is likely that And-1 and And-2 are attributed to Assemblage A, whereas IB has been attributed to Assemblage B.

The use of trace element extended variation diagrams normalized to primordial mantle (Fig. 7-3) is an alternative approach to comparing Fisher and Santoy host rocks. The HCrB tends to correlate best with the Santoy calc-alkaline basalt, while the LCrB correlates better with the Santoy Lake basalt. The LCrB does not have as strong of depletions in Nb, Zr, Hf and Ti which are characteristic of the Santoy calc-alkaline basalt (Fig. 7-3a). The CL-B appears to be relatively depleted in the LREEs relative to other Santoy and Fisher units and is interpreted not to be present at the Fisher property. Both And-1 and And-2 correlate well with the Santoy IB (Fig. 7-3b) but the units correspond to different assemblages. The Fisher rhyolite trace element pattern (Fig. 7-3c) correlates well with the Santoy Felsic A unit relative to the Santoy Felsic B unit.

In summary, the HCrB appears to be the equivalent of the calc-alkaline basalt from the Santoy deposit. The calc-alkaline affinity of the HCrB (Fig. 4-8c,d) may reflect a more mature oceanic arc basalt in the Fisher property area. The LCrB appears to be more similar to the Santoy Lake basalt, thus both the HCrB and LCrB can be assigned to Assemblage A. Geochemically, the trace element patterns of Fisher intermediate volcanic rocks and Santoy intermediate volcanic rocks are identical but field associations have distinguished these as units corresponding to

Assemblage A and Assemblage B, respectively. The Fisher rhyolite has similar trace element patterns and major oxide values to the Santoy Felsic A (Fig. 7-3c); thus, the rhyolite likely corresponds to Santoy Felsic A.

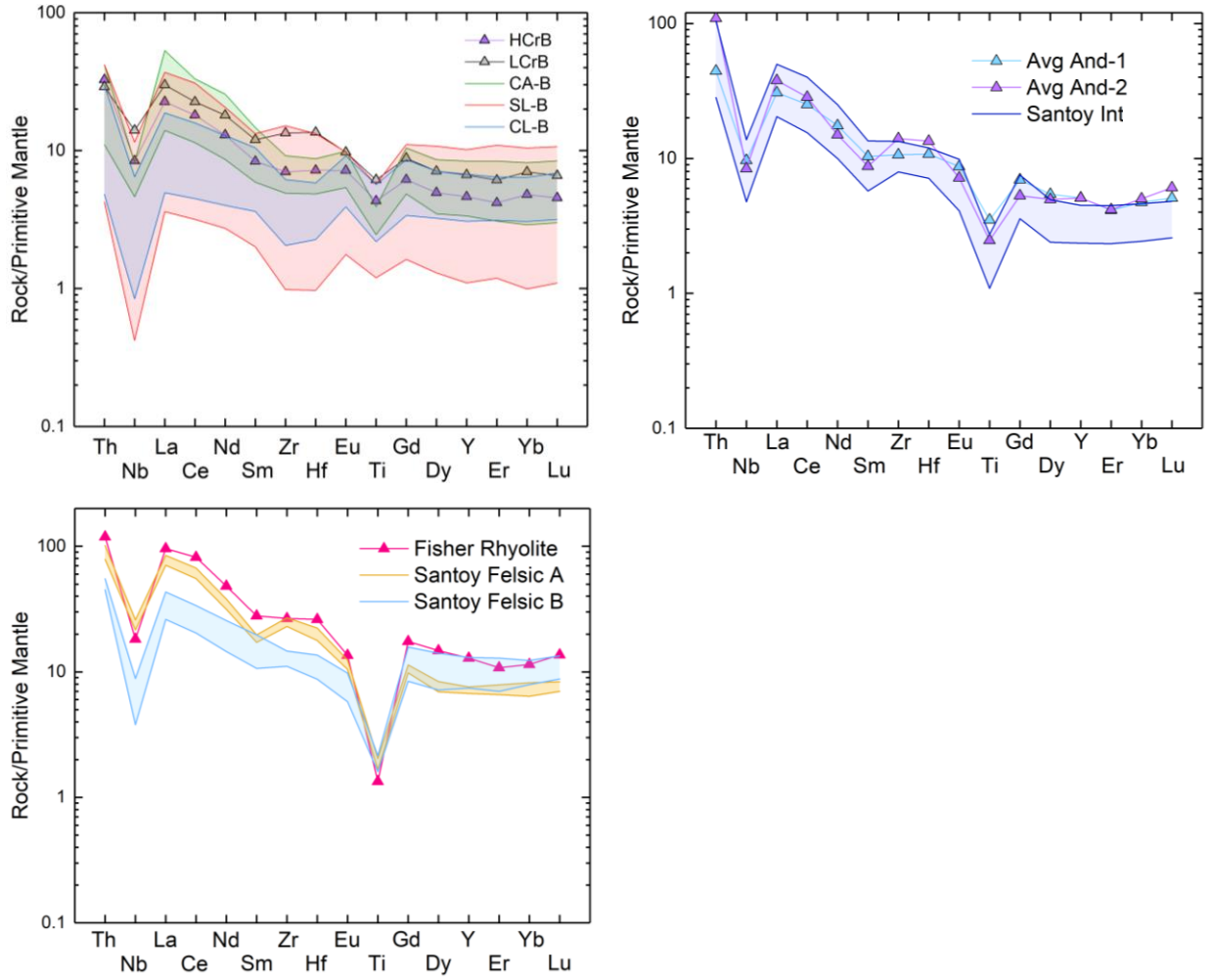

Figure 7-3 Extended variation diagrams of various volcanic rocks from the Fisher property and the Santoy mine area normalized to primitive mantle. Santoy data (unpublished data provided by SSR Mining; Stuebing, pers. comm.). A) The average Fisher Basalt relative to the boundary of the Santoy calc-alkaline basalt. B) Average Andesite-1 and Andesite-2 relative to the Santoy Intermediate Basalt. C) Fisher rhyolite relative to Santoy Felsic A & B units.

Alteration & Mineralization:

Gold mineralization at the Santoy deposit has well-developed calc-silicate alteration haloes surrounding quartz veins. The alteration assemblage includes minerals directly associated with mineralization including diopside, K-feldspar, titanite, epidote, plagioclase, scheelite, zircon, apatite and quartz (Wood, 2016). Actinolite is believed to be related to retrograde reactions while late fracturing was responsible for calcite, sericite, and chlorite formation (Wood, 2016).

The alteration assemblage directly associated with the mineralization phase at Fisher has been studied at greater detail, highlighting the addition of new alteration minerals not indicated at Santoy. Biotite, chlorite and sericite are the most common alteration minerals which consistently occur as haloes around mineralized quartz veins (Fig. 6-2a,e; Fig. 6-3a,b,c; Fig. 6-5a,c,d,f,g; Fig. 6-6a) indicating a synchronous relationship. Biotite and chlorite have variable textural and compositional characteristics (Table 5-1; 5-2), depending on whether they occur in the host rock, the alteration halo or within quartz veins.

Clinozoisite, epidote, diopside and muscovite occur within alteration haloes at Fisher (Fig. 6-2f; Fig. 6-5b,a,g,h; Fig. 6-6a,b,c,d) but no cross-cutting relationships exist amongst them, suggesting that they formed at broadly the same time. At Santoy, diopside typically occurs along quartz vein margins which also include K-feldspar, plagioclase and titanite. Diopside grains are undeformed and locally retrograde to actinolite needles, or within quartz veins with titanite inclusions (Wood, 2016). At Fisher, diopside also occurs along quartz vein margins and within quartz veins and associated with titanite, calcite, biotite, epidote, clinozoisite and hornblende selvages. Titanite occurs as euhedral crystals throughout the host rock, and as anhedral crystals with ilmenite cores (Fig. 5-4d), or as sub-euhedral crystals in the alteration halo (Fig. 6-3b; Fig. 6-

6d). Actinolite was observed as part of the alteration assemblage at both deposits and appears to occur late in the alteration assemblage altering pyrite (Fig. 6-8c). In also occurs as a hornblende core with margins of subhedral actinolite (Fig. 6-6c) or as fine-grained radiating needles from hornblende/actinolite grains (Fig. 6-6d). Due to the association of actinolite with quartz veins, it is likely that actinolite occurs as a result of hydrothermal alteration rather than retrograde metamorphism.

Epidote and clinozoisite alteration at Fisher are abundant in mafic volcanic units. Phases including a unique clinozoisite-quartz symplectite texture (Fig. 6-6c), a euhedral clinozoisite in alteration haloes (Fig. 6-5h) and finer-grained epidote in alteration haloes (Fig. 6-3c). Localized fine-grained tourmaline at Fisher shows a simultaneous relationship with pyrite formation and calcite veining (Fig. 6-4e). Like Santoy, K-feldspar, scheelite and apatite are also considered part of the mineralization phase at Fisher.

Evidence of late calcite, sericite and chlorite alteration associated with fracturing, barren quartz veins and colloform pyrite was observed at the Santoy deposit. While late calcite veins were observed at Fisher (Fig. 6-5e), no evidence of late sericite or chlorite exists. Cross-cutting relationships between quartz veins were observed locally and provide evidence of multiple fluid events. While calcite was only observed as a late fracturing phase at Santoy, it commonly occurs in the mineralization phase at the Fisher deposit as interstitial calcite in pyrite grains (Fig. 6-2d) or along quartz vein margins (Fig.6-5d).

The paragenetic sequence of sulphide minerals and precious metals at Santoy indicates phases of pyrite, chalcopyrite, pyrrhotite, telluride and gold related to the mineralization phase, the retrogression phase and within late fracturing phases. The calc-silicate alteration assemblage was

noted to boudinage where remobilized sulphide minerals, especially intermingled chalcopyrite and pyrrhotite, typically precipitated (Wood, 2016). Bi-tellurides associate with native gold and occur as intergrowths with diopside, quartz and actinolite. Sulphide minerals are interpreted to have been introduced during the main mineralization event and were subsequently remobilized by later deformational events producing localized high-grade gold. Evidence of remobilized sulphide minerals and gold was suggested to be related to a "retrogression phase", while late fracturing is made evident by remobilization of sulphide minerals into late brittle fractures which associates with sericite and chlorite (Wood, 2016). These late veins typically host colloform pyrite but are barren.

Initial textural relationships at the Fisher property indicate the mineralization phase includes pyrrhotite, arsenopyrite, pyrite, chalcopyrite, sphalerite and Bi-tellurides (Fig. 6-1). Chalcopyrite occurs as fracture fills or inclusions in pyrite or pyrrhotite potentially indicating remobilization during post-mineralization deformation where they occur as veinlets in competent pyrite grains (Fig. 6-7d). Bi-tellurides were also noted to occur along pyrite grain boundaries (Fig. 6-8a). Evidence from microprobe work indicates varying degrees of overgrowth textures of euhedral pyrite by (chlorite or actinolite?) where fibrous or fine-grained margins overprint pyrite but the primary euhedral grain shape is preserved (Fig. 6-8c). Both textures likely resulted from hydrothermal alteration late in the paragenetic sequence. Colloform pyrite was also observed at the Fisher property (Fig. 6-8e) but the relationship with barren quartz veins and mineralization phase pyrite is not fully understood at this time.

7.4 Fisher Deposit Model

The geological setting of the gold deposits in the Fisher property can be broadly described as a deposit occurring along a shear zone (Santoy shear zone; Fig. 3-4), which is a second or higher order splay from an early ductile component of the regional crustal scale fault (Tabbernor fault zone; Fig. 3-3), in a greenstone belt (Pine Lake greenstone Belt; Fig. 3-3) and formed in an evolving orogenic belt. Based on these findings, the Fisher deposit is best characterized by an orogenic gold deposit model. An orogenic gold deposit model has also been suggested for the Santoy deposit and Seabee mine (Wood, 2016; Tourigny et al., 2004). In comparison to the Santoy deposit, similar calc-silicate alteration assemblages, and sulphide minerals are observed, which suggests that hydrothermal fluids interacted with similar rock types at both deposits producing relatively consistent deposit models. The mineralization event which produced the gold mineralization at the Santoy deposit, is thus likely the same mineralization event which occurred to form the Fisher deposit. Based on additional data collected here in this study, and the associated interpretations, the following provides additional support to the classification of the Fisher deposit as an orogenic gold deposit.

Spatially, there is a link between gold mineralization and the Santoy shear zone (Fig. 7-4). The exact extent of the Santoy shear zone in the Fisher property is not fully understood. However, it appears that it, and other secondary shear zones, generally trend N-S following major lithological contacts (Fig. 3-4). In general, mineralization tends to occur along contacts between mafic volcanic and intrusive rocks (Fig. 7-5), especially those with a calc-alkaline affinity. Abundant quartz veins (~0.5 – 2m) occur along lithological contacts and thus are steeply dipping, similar to host rock units (Fig. 7-5). The quartz veins are predominantly controlled by foliation due to shearing associated with the Santoy shear zone. Increased strain along the Santoy shear zone likely

prevented injection of hydrothermal fluids. Rather, fluids followed rheological weaknesses along the hanging wall of the Santoy shear zone, between softer metasedimentary and metavolcanic rocks relative to rigid intrusive bodies (Fig. 7-5). These rheologic characteristics were likely key conditions for gold mineralization to occur along discrete channels (Ridley, 1993).

In terms of gold mineralization, precipitation was likely induced by sulfidation reactions in Fe-bearing basalts. The average FeO content of LCrB is 11.96 wt. % FeO and 13.13% wt. % FeO, compared to 8.65% FeO in average basalts (Price, 1997). Fe-rich host rocks are well-known hosts to gold mineralization (Ropchan et al., 2002; Van Hees et al., 1999; Groves and Phillips, 1987). Fisher property rocks are enriched in Mg and Fe and have variations in Cr likely corresponding to differences in fractional crystallization processes. Thus, Fe-Mg bearing host rocks, and potentially those with higher Cr, are favourable for gold mineralization at the Fisher property.

The alteration at the deposit can be summarized by a distal sericite-biotite assemblage (~meters to 10's of meters?) and a proximal (0.2 – 0.5m) calc-silicate alteration assemblage (Fig. 7-4) described comprehensively in Chapter 6. This calc-silicate assemblage is synchronous with and well-developed along auriferous quartz vein margins, especially in the HCrB. The HCrB has mass changes summarized by gains in K, Rb and Ba associated with potassic alteration, gains in Pb, As, W, Mo, Ag, and Zn related to sulphide minerals, trace minerals and likely trace phases in sulphide minerals. Losses in Na and Sr likely correspond to a combination of feldspar destruction by potassic alteration, and primary fractional crystallization processes. In terms of a zonation, +K, Rb, Ba and -Na, Sr are expected distal to the quartz veins and $\pm$ Pb, As, W, Mo, Ag, Zn, Bi, Te, Sb are expected proximal to quartz veins. Sulphide minerals and precious metals associated with mineralized quartz veins include pyrite, chalcopyrite, pyrrhotite, arsenopyrite, sphalerite, Bi-tellurides, and native gold. Initial petrographic textural observations indicate localized

remobilization of chalcopyrite and brecciation of pyrite associated with higher grade Au intersects (13.72 g/T Au over 0.73m; Fig. 6-8b).

In terms of timing of major events in the Fisher property area, a zircon from a titanite grain (both interpreted to be hydrothermal in origin) at the Santoy deposit was analyzed using U-Pb geochronological techniques which provided an age of ~1755 $\pm$ 8.4 Ma (Wood, 2016). Based on the alteration assemblage characteristics at Fisher being similar to those at Santoy, it can be inferred that the same fluids and thus the same mineralization age could also apply to the Fisher property. The various intrusive rocks that intersect volcanic units and commonly occur with increased gold grades are foliation parallel. These intrusive rocks have a foliation likely related to peak metamorphism at ~1807 Ma (Wood, 2016). One possibility is that these intrusive rocks represent feeders to volcanic rocks higher in the stratigraphy. For example, Fisher intrusive such as the gabbro, diorite and granite have very similar Zr/TiO_2 ratios to the HCrB, And-1 and Rhyolite units, respectively. Acquiring age constraints on these intrusive rocks would be a suitable approach to determine their exact origin.

This study presents insights on orogenic gold deposits hosted in Paleoproterozoic, amphibolite grade metamorphic rock. The intersections of high Fe basalts and calc-alkaline intrusions offer an excellent contrast in competencies and chemistry where auriferous quartz veins occur. The calc-silicate alteration assemblage and the structural and lithological setting favor this deposit as orogenic in origin.

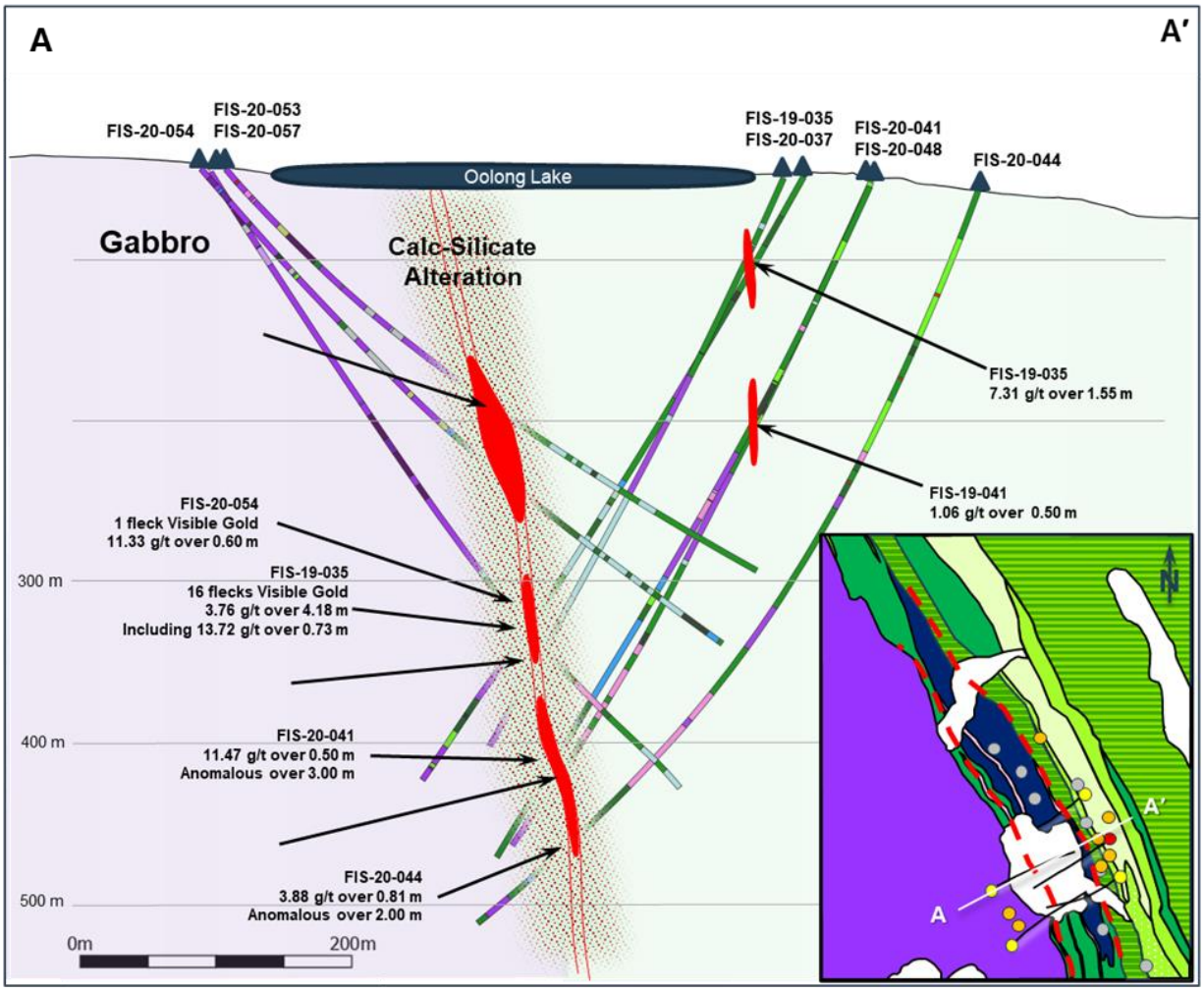

Figure 7-4 Cross section through the "Mac zone" showing Eisler intrusive complex to the left (purple), Assemblage A volcanic rocks on the right (green), the mac vein and associated alteration halo (red) and drill holes with lithologic units intercepted (modified from SSR Mining Inc.).

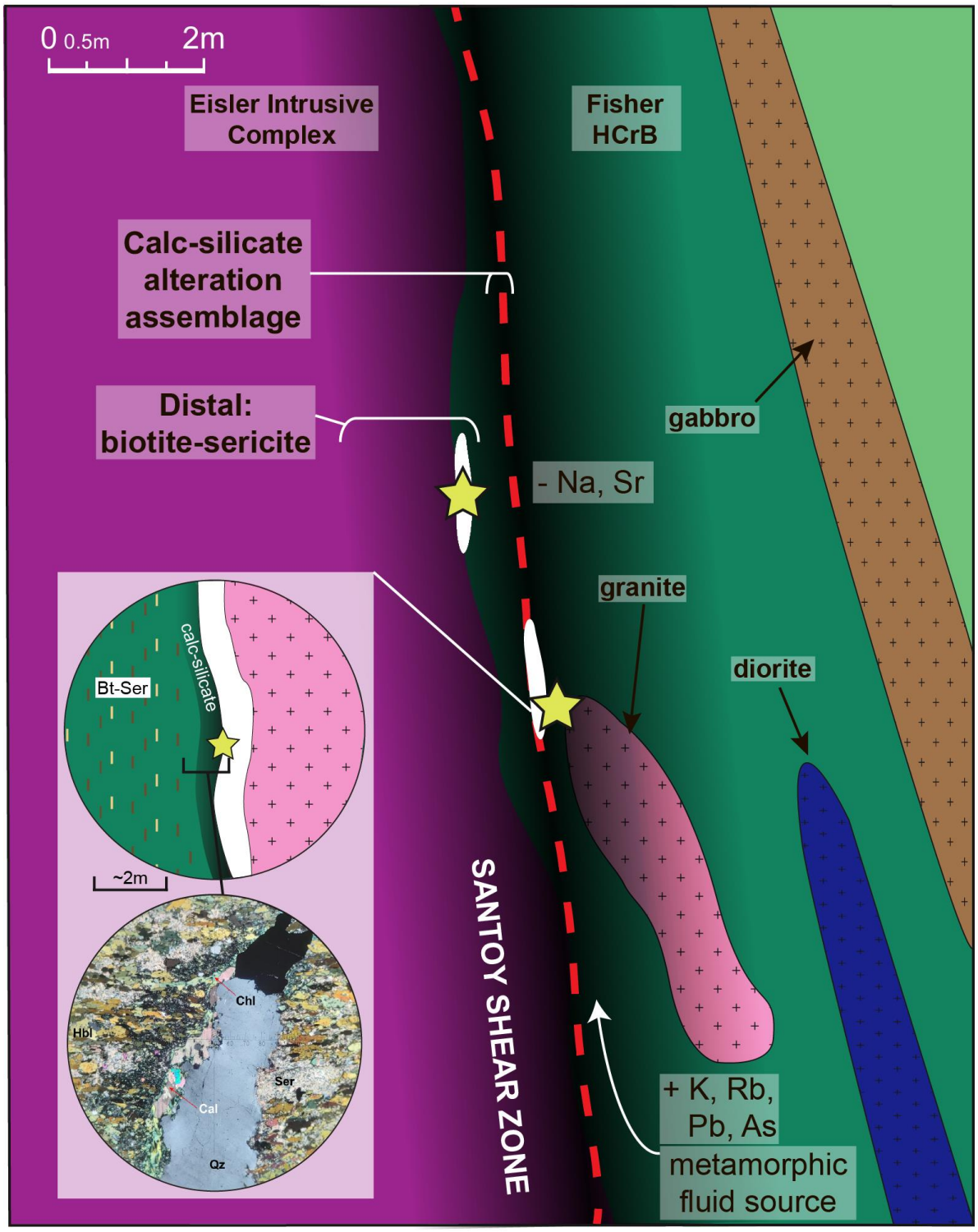

Figure 7-5 Diagrammatic cross-section across the Fisher property, with a simplified genetic model of hydrothermal alteration, mineralization (gold stars), and associations with quartz veins (white), structures (red dotted line) and lithological units.

CHAPTER 8: SUMMARY AND FUTURE RESEARCH

8.1 Summary

This thesis provides a characterization of the various host rocks and corresponding alteration styles at the Fisher property, Saskatchewan, Canada. The area has been metamorphosed to amphibolite facies and is hosted in Paleoproterozoic rocks which presents a unique opportunity to study orogenic gold deposits of this type. Both the recently decommissioned Seabee mine and the actively producing Santoy mine to the north, boast high potential for continued gold production which led SSR Mining Inc. to supporting this research. Integrating different analytical methods including lithogeochemistry, petrography and electron microscopy, provided insight on various processes related to rock formation, subsequent alteration, and mineralization. These findings were then compared to characteristics from the Santoy mine to investigate potential geological relationships between the two deposits.

This research identified six volcanic, five intrusive and multiple sedimentary host rock lithologies based on their respective Zr/Ti ratios. A trend from tholeiitic to calc-alkaline magmatic affinities and negative Nb and Ti anomalies indicate the host rocks formed in a maturing volcanic arc environment. The mineral assemblages observed in petrographic analysis indicate amphibolite facies metamorphism affected all host rocks. In mafic volcanic rocks, this assemblage includes hornblende porphyroblasts in a finer-grained groundmass of relatively equal proportions of quartz and plagioclase, with lesser biotite and chlorite defining the foliation. In felsic intrusive rocks, this assemblage includes a coarse-grained groundmass of varying amounts of quartz and plagioclase feldspar and lesser biotite or muscovite defining foliation. The most common rocks hosting mineralization include the mafic volcanic rocks and the granite unit. Chromium was used to further

differentiate the basalt into a High Cr Basalt (HCrB) and a Low Cr Basalt (LCrB). This Cr variation has been attributed to variations in fractional crystallization from the parent magma. The HCrB tends to have a slightly more calc-alkaline signature relative to the LCrB.

Alteration at the Fisher property can be summarized by a distal sericite-biotite halo and a proximal calc-silicate assemblage. The calc-silicate assemblage occurs on the margins of quartz veins which typically occur along, but are not constrained to, contacts between HCrB and felsic intrusive units. The extent of this proximal halo is small (~50cm) and varies in strength depending on the host rock. In general, intrusive units exhibit minor alteration haloes relative to volcanic and sedimentary packages.

HCrB were identified as a favourable host rock for alteration and mineralization at the Fisher property, though LCrB and metasedimentary rocks were still shown to have strong alteration, and intrusive rocks host high-grade gold. Structural considerations should also be accounted for but were not covered in this research. The HCrB exhibits mass gains in K, Rb, Ba associated with potassic alteration, mass gains in Fe and Mg, likely related to biotite and chlorite alteration and gains in Pb, As, Ag, W, Mo, and Zn reflecting potential pathfinder elements. Mass losses in the unit are mostly constrained to Na which reflects feldspar destruction by potassic alteration and the effects of variations in fractional crystallization between the units. Petrographic observations confirm these geochemical signatures and provide information on additional alteration minerals and textures. The calc-silicate alteration assemblage can be summarized by quartz, biotite, chlorite, sericite, calcite +/- clinozoisite, diopside, actinolite, epidote, K-feldspar, muscovite, titanite, tourmaline and scheelite. Sulphide minerals likely associated with increased Au grades include pyrite, chalcopyrite, pyrrhotite, arsenopyrite and sphalerite. Textural evidence shows gold may

occur associated with brecciation, clinozoisite-quartz symplectite textures which forms on sulphide and quartz vein margins, and with pseudomorphic replacement of pyrite, locally.

Microprobe studies focused on biotite, chlorite, calcite, amphiboles, pyroxenes, titanite, epidote and plagioclase. Mafic volcanic host rock's mineral assemblage was defined by magnesiohornblende, oligoclase-andesine, and a Mg-Fe chlorite. Chlorite phases have the greatest variation of all alteration minerals. Chlorite shows a transition from a Mg-Fe chlorite in host rock chlorites, halo chlorites have increased Fe and vein chlorites are of chamosite (Fe-end member) composition. Though variations in biotite characteristics exist, variations in chemistry between phases were not identified and mostly plotted as annite. The amount of biotite, rather than the chemistry of biotite, appears to be the most useful indicator of proximity to auriferous quartz veins. All carbonate samples were determined to be calcite and showed little variation. Epidote group minerals were of clinozoisite composition and showed variations in respective Al and Fe amounts which likely reflect host rock compositions.

8.2 Recommendations

Findings from this research provide a baseline for additional research should. Interpretations of the paragenetic sequence of sulphide minerals and processes related to ore formation were based on relationships observed in one excellent sample. This presents issues and additional altered/mineralized samples should be collected to improve on the interpretations from this study. Additional samples could also corroborate the alteration characteristics described in Chapter 6.

Timing of mineralization can be constrained using the radiometric dating systems of Re-Os and U-Pb. Re-Os dating on pyrite has been proven to be effective in providing a reasonably precise age (Morelli et al., 2004; Arne et al., 2001), due to its robustness even in higher temperature

regimes (van Acken et al., 2014; Vernon et al., 2014). Though pyrite can include common Os in its structure, a simple correction equation can be used to compensate (Smoliar et al., 1996). Modern analytical techniques (Creaser et al., 1991; Volkening et al., 1991) have also helped with the generally low concentration of both Re and Os in pyrite. Pyrite and arsenopyrite grains from the SGO area present an excellent opportunity to further constrain the mineralization age.

Zircon and titanite grains can be used in U-Pb dating of hydrothermal alteration (Wang et al., 2018; Li et al., 2010; Geisler et al., 2007). A mineralization age of ~1755 $\pm$ 8 Ma was produced at the Santoy deposit (Wood, 2016), thus an age at Fisher could indicate whether similar mineralizing fluids affected the property. U-Pb dating of magmatic zircons from various plutonic suites in the area would be useful to determine crystallization ages of these intrusive rocks and maximum and minimum ages of mineralization based on cross-cutting relationships.

The use of LA-ICP-MS is an effective approach to determine the specific textural setting of Au mineralization and has been applied to orogenic gold deposits globally (Wu et al., 2018; Altigani et al., 2016). Due to the limitations of detection levels in microprobe analysis, the exact location of Au and other trace elements was not established. Based on the increased presence of pyrite associated with high-grade Au samples, it is assumed that Au is hosted in pyrite, but this methodology would provide more insight on that assumption. This study suggested remobilization of Au could have occurred. This and other potential replacement texture would be better constrained with use of LA-ICP-MS (Rottier et al., 2016). Trace elements analysis can also provide insight on the origin of hydrothermal fluids. This technique has been used to differentiate phases, however, based on the minimal chemical variation in phases from microprobe work, this should not be a high priority.

The study of S-isotopes has been used to determine fluid source, transport, and precipitation of Au in orogenic gold deposits (LaFlamme et al., 2018; Wu et al., 2018; Phillips et al., 1986). A useful application of S-isotopes at the Seabee Gold Operation would include reanalysis of S-isotopes from the Seabee mine (Schultz, 1996), and collection of S-isotope data from the Santoy and Fisher deposits. Comparisons of S isotopic data could indicate whether the same fluids which host the Seabee mine are those which also affected the Santoy and Fisher deposits.

Understanding the relationships and occurrences of various lithologic units and their relation to structures is an important aspect which was not covered in this study. A detailed structural analysis of the Santoy deposit (Wood, 2016) presents an opportunity for direct comparisons. Though this study examined the detailed geochemical attributes of host rocks, it would be useful to reaffirm these connections with field relationships. There is also potential to complete more detailed surface mapping to the south and east of the Fisher property.

REFERENCES

Aitchison, J., 1982, The statistical analysis of compositional data: Journal of the Royal Statistical Society. Series B (Methodological), v. 44(2), p. 139-177.

Altigani, M. A. H., Merkle, R. K. W., and Dixon, R. D., 2016, Geochemical identification of episodes of gold mineralisation in the Barberton Greenstone Belt, South Africa: Ore Geology Reviews, v. 75, p. 186–205.

Andrews, A. J., Hugon, H., Durocher, M., Corfu, F., and Lavigne, M. J., 1986, The anatomy of a gold-bearing greenstone belt: Red Lake, northwestern Ontario, Canada: p. 3-22 in Proceedings of Gold ’86, an International Symposium on the Geology of Gold, edited by A J. Macdonald, Konsult International Inc., Toronto, 517p.

Ansdell, K. M., Lucas, S. B., Connors, K., and Stern, R. A., 1995, Kisseynew metasedimentary gneiss belt, Trans- Hudson orogen (Canada): back-arc origin and collisional inversion: Geol., v. 23, p. 1039-1043.

Ansdell, K. M., 2005, Tectonic evolution of the Manitoba-Saskatchewan segment of the Paleoproterozoic Trans-Hudson Orogen, Canada: Canadian Journal of Earth Sciences, v. 42, p. 741–759.

Armbruster, T., Bonazzi, P., Akasaka, M., Bermanec, V., Chopin, C., Gieré, R., Heuss-Assbichler, S., Liebscher, A., Menchetti, S., Pan, Y., and Pasero, M., 2006, Recommended nomenclature of epidote-group minerals: European Journal of Mineralogy, v. 18, p. 551–567.

Arne, D. C., Bierlein, F. P., Morgan, J. W., and Stein, H. J., 2001, Re-Os Dating of Sulfides Associated with Gold Mineralization in Central Victoria, Australia: Economic Geology, v. 96, p. 1455–1459.

Ashton, K. E., and Haidl, F. M., 1998, Geology, NATMAP Shield Margin Project area of Flin Flon Belt, Manitoba/Saskatchewan: accompanying notes to Geol. Surv. Can. Map 1968A / Manit. Energy Mines Map A-98-2 / Sask. Energy Mines, Map 258A, 54p.

Ashton, K. E., 1999, A Proposed Lithotectonic Domainal Re-classification of the Southeastern Reindeer Zone in Saskatchewan: in Summary of Investigations 1999, v. 1, Saskatchewan Geological Survey, Sask. Energy Mines, Misc. Rep. 99-4.1. p. 92–100.

Ashton, K. E., Lewry, J. F., Heaman, L. M., Hartlaub, R. P., Stauffer, M. R., and Tran, H. T., 2005, The Pelican Thrust Zone: basal detachment between the Archean Sask Craton and Paleoproterozoic Flin Flon-Glennie Complex, western Trans-Hudson Orogen: Canadian Journal of Earth Sciences, v. 42, p. 685–706.

Barrie, C. D., Boyce, A. J., Boyle, A. P., Williams, P. J., Blake, K., Wilkinson, J. J., Lowther, M., McDermott, P., and Prior, D. J., 2009, On the growth of colloform textures: A case study of sphalerite from the Galmoy ore body, Ireland: Journal of the Geological Society, v. 166, p. 563–582.

Basnett, R., 1999, Seabee Mine: in Ashton, K.E. and Harper, C.T. (eds.), Minexpo'96 Symposium – Advances in Saskatchewan Geology and Mineral Exploration, Sask. Geol. Soc., Spec. Publ. No. 14, p. 72-79.

Battaglia, S., 1999, Applying X-ray geothermometer diffraction to a chlorite: Clays and Clay Minerals, v. 47, p. 54–63.

Beaumont-Smith, C. J. and Böhm, C. O., 2003, Tectonic evolution and gold metallogeny of the Lynn Lake greenstone belt, Manitoba (NTS 64C10, 11, 12, 14, 15 and 16): in Report of Activities 2003, Manitoba Industry, Trade and Mines, Manitoba Geological Survey, p. 39–49.

Bleeker, W., and Hall, B., 2007, The Slave Craton: Geology and metallogenic evolution: in Goodfellow, W.D., ed., Mineral Deposits of Canada: A Synthesis of Major Deposit-Types, District Metallogeny, the Evolution of Geological Provinces, and Exploration Methods. Geological Association of Canada, Mineral Deposits Division, Special Publication, 5, p. 849-879.

Buccianti, A., and Grunsky, E., 2014, Compositional data analysis in geochemistry: Are we sure to see what really occurs during natural processes: Journal of Geochemical Exploration, v. 141, p. 1-5.

Cabanis, B., and Lecolle, M., 1989, Le diagramme La/10-Y/15-Nb/8: un outil pour la discrimination des séries volcaniques et la mise en évidence des processus de mélange et/ou de contamination crustale: Comptes rendus de l'Académie des sciences. Série 2, Mécanique, Physique, Chimie, Sciences de l'univers, Sciences de la Terre, v.309, p. 2023–2029.

Carpenter, R. L., and Duke, N. A., 2004, Geological setting of the West Meliadine gold deposits, Western Churchill Province, Nunavut, Canada: Explor. Min. Geol, v.13, p. 49–65.

Carpenter, R. L., Duke, N. A., Sandeman, H. S., and Stern, R., 2005, Relative and absolute timing of gold mineralization along the Meliadine trend, Nunavut, Canada: evidence for Paleoproterozoic gold hosted in an Archean greenstone belt: Econ. Geol., v. 100, p. 567–576.

Cassidy, K.F., 1992, Archaean granitoid-hosted gold deposits in greenschist to amphibolite facies terrains: a high P-T to low P-T depositional continuum equivalent to greenstone-hosted deposits: Unpublished Ph.D. thesis, Nedlands, Australia, The University of Western Australia, 296 pp.

Cathelineau, M., 1988, Cation site occupancy in chlorites and illites as a function of temperature: Clay Minerals, v. 23. p. 471–485.

Cattell, R. B., 1966, The scree test for the number of factors: Multivariate Behavioral Research, v. 1, p. 245–276.

Chiarenzelli, J. R., 1989, The Nistowiak and Guncoat Gneisses: implications for the tectonics of the Glennie and La Ronge domains, northern Saskatchewan, Canada: Unpublished Ph.D. thesis, Kansas, USA, University of Kansas, 229 p.

Colvine, A. C., Fyon, J. A., Heather, K. B., Marmont, S., Smith, P. M., and Troop, D. G., 1988, Archean Lode Gold Deposits in Ontario: Ontario Geological Survey, Misc Paper 139, 136 p.

Corrigan, D., Galley, A. G. and Pehrsson, S., 2007, Tectonic evolution and metallogeny of the southwestern Trans-Hudson Orogen: In: Goodfellow, W. D. (ed.) Mineral Deposits of Canada: A Synthesis of Major Deposit-types, District Metallogeny, the Evolution of Geological Provinces, and Exploration Methods. Geological Association of Canada, Mineral Deposits Division, Special Publication, 5, p. 881–902.

Corrigan, D., Pehrsson, S., Wodicka, N., and de Kemp, E., 2009, The Palaeoproterozoic Trans-Hudson Orogen: a prototype of modern accretionary processes: Geological Society, London, Special Publications, 327, p. 457–479.

Creaser, R. A., Papanastassiou, D. A., and Wasserburg, G. J., 1991a, Negative thermal ion mass spectrometry of osmium, rhenium, and iridium: Geochimica et Cosmochimica, v. 55, p. 397-401.

Davies, J., Whitehead, R., 2006, Alkali-alumina and MgO-alumina molar ratios of altered and unaltered rhyolites: Explor. Min. Geol, v. 15, p. 75–88.

Davis, W. J., and Bleeker, W., 1999, Timing of plutonism, deformation, and metamorphism in the Yellowknife Domain, Slave Province, Canada: Canadian Journal of Earth Sciences, v. 36, p. 1169–1187.

Deer, W. A., Howie, R. A. and Zussman, J., 1992, An Introduction to the Rock-forming Minerals: 2nd ed. Harlow: Longman Group UK, 232 p.

Delaney, G.D., 1986, Bedrock geological mapping, Laonil Lake area (part of NTS 63M- 11 and -12): in Summary of Investigations 1986, Saskatchewan Geological Survey, Sask. Energy Mines, Misc. Rep. 86-4, p. 32-41.

Delaney, G.D., 1987, Bedrock geological mapping, Carruthers-Uskik Lakes area: in Summary of Investigations 1987, Saskatchewan Geological Survey, Sask. Energy Mines, Misc. Rep. 87-94, p. 8-17.

Delaney, G. D. and Cutler, S. A. 1992, Geological setting of the 'Santoy Lake' gold camp (part of NTS 63M-11 and -12): in Summary of Investigations 1992, Saskatchewan Geological Survey, Sask. Energy Mines, Misc. Rep. 92-4.

Delaney, G.D. 2016, Geology of the Pine Lake Greenstone Belt Laonil-Uskik Lakes Area (part of NTS 63M-11 and 12): Saskatchewan Geological Survey, Sask Ministry of the Economy, Geoscience Map 240.

Dinel, E., Fowler, A. D., Ayer, J., Still, A., Tylee, K., and Barr, E., 2008, Lithogeochemical and stratigraphic controls on gold mineralization within the metavolcanic rocks of the Hoyle Pond mine, Timmins, Ontario: Economic Geology, v. 103, p. 1341–1363.

Dubosq, R., Schneider, D. A., Camacho, A., and Lawley, C. J. M., 2019, Geochemical and geochronological discrimination of biotite types at the detour lake gold deposit, Canada: Minerals, v. 9, 22p.

Foster M. D., 1960, Interpretation of composition of trioctahedral micas: U.S. Geological Survey Professional Paper, 354B, p. 1-49.

Gaillard, N., Williams-Jones, A. E., Clark, J. R., Lypaczewski, P., Salvi, S., Perrouty, S., Piette-Lauzière, N., Guilmette, C., and Linnen, R. L., 2018, Mica composition as a vector to gold mineralization: Deciphering hydrothermal and metamorphic effects in the Malartic district, Quebec: Ore Geology Reviews, v. 95, p. 789–820.

Gardiner, J. J., 1986, Structural geology of the Lupin gold mine, Northwest Territories: Unpublished M.Sc. thesis, Wolfville, Canada, Acadia University,

Gazley, M. F., Collins, K. S., Hines, B. R., Fisher, L. A., and McFarlane, A., 2015, Application of principal component analysis and cluster analysis to mineral exploration and mine geology and cluster analysis to mineral exploration: AusIMM New Zealand Branch Annual Conference 2015, p. 131–139.

Geisler T., Schaltegger, U., and Tomaschek, F., 2007, Re-equilibration of zircon in aqueous fluids and melts: Elements, v. 3, p. 43–50.

Goldfarb, R. J., Groves, D. I., and Gardoll, S., 2001, Orogenic gold and geologic time: A global synthesis: Ore Geology Reviews, v. 18, p. 1–75.

Goldfarb, R. J., Baker, T., Dubé, B., Groves, D. I., Hart, C. J. R., and Gosselin, P. 2005, Distribution, Character, and Genesis of Gold Deposits in Metamorphic Terrane: In J. W. Hedenquist, J. F. H. Thompson, R. J. Goldfarb, & J. P. Richards (Eds.), One Hundredth Anniversary Volume. Society of Economic Geologists.

Goldfarb, R. J., and Groves, D. I., 2015, Orogenic gold: Common or evolving fluid and metal sources through time: Lithos, v. 233, p. 2–26.

Gosselin, P., Dubé, B., Gosselin, P., and Dubé, B., 2005, Gold deposits of the world: distribution, geological parameters and gold content: Geological Survey of Canada Open File 4895, 1 CD-ROM.

Grant, J. A., 2005, Isocon analysis: A brief review of the method and applications: Physics and Chemistry of the Earth, v. 30, p. 997–1004.

Gresens, R. L., 1967, Composition-volume relationships of metasomatism: Chemical Geology, v. 2, p. 47–65.

Groves, D. I. and Phillips, G. N., 1987, The genesis and tectonic control on Archaean gold deposits of the Western Australian Shield - A metamorphic replacement model: Ore Geology Reviews, v. 2, p. 287-322.

Groves, D. I., Goldfarb, R. J., Gebre-Mariam, M., Hagemann, S. G., and Robert, F., 1998, Orogenic gold deposits: A proposed classification in the context of their crustal distribution and relationship to other gold deposit types: Ore Geology Reviews, v. 13, p. 7–27.

Hall, R., 2002, Cenozoic geological and plate tectonic evolution of SE Asia and the SW Pacific: Computer-based reconstructions, model and animations: Journal of Asian Earth Sciences, v. 20, p. 353–431.

Hallberg, J.A., 1984, A geochemical aid to igneous rock type identification in deeply weathered terrane: Journal of Geochemical Exploration., v. 20, p. 1-8.

Hawthorne, F. C., Oberti, R., Harlow, G. E., Maresch, W. V., Martin, R. F., Schumacher, J. C., and Welch, M. D., 2012, Ima report: Nomenclature of the amphibole supergroup: American Mineralogist, v. 97, p. 2031–2048.

Heaman, L. M., Maxeiner, R. O., and Slimmon, W. L., 1994, U-Pb geochronological investigations in the Trans-Hudson Orogen, Saskatchewan: in Summary of Investigations, 1994, Saskatchewan Energy and Mines Miscellaneous Report 94-4, p. 96-99.

Helmstaedt, H., 1986, Report on the geology and structure of the Seabee and Currie Rose properties, Laonil Lake, Saskatchewan: Placer Development Ltd., internal report, 14 p.

Hoffman, P., 1988, United Plates Of America, The Birth Of A Craton: Early Proterozoic Assembly And Growth Of Laurentia: Annual Review of Earth and Planetary Sciences, v. 16, p. 543-603.

Hood, S. B., Cracknell, M. J., Gazley, M. F., and Reading, A. M., 2019, Element mobility and spatial zonation associated with the Archean Hamlet orogenic Au deposit, Western Australia: Implications for fluid pathways in shear zones: Chemical Geology, v. 514, p. 10–26.

Hardy, F., 1994, Origin, Timing, and Fluid Characteristics Associated with the Paleoproterozoic Jasper Lode-Gold Deposit, Saskatchewan, Canada: Unpublished M.Sc. Thesis, Saskatoon, Canada, University of Saskatchewan, 100p.

Hughes, C.J., 1973, Spilites, keratophyres, and the igneous spectrum: Geological Magazine, v. 109, p. 513-527.

Kerrich, R., and Wyman, D., 1990, Geodynamic setting of mesothermal gold deposits: an association with accretionary tectonic regimes: Geology, v. 18, p. 882–885.

Kishida, A., and Kerrich, R., 1987, Hydrothermal alteration zoning and gold concentration at the Kerr- Addison Archean lode gold deposit, Kirkland Lake, Ontario (Canada): Economic Geology, v. 82, p. 649–690.

Kranidiotis, P., and MacLean, W. H., 1987, Alteration: Phelps Dodge Massive Sulfide Deposit, Matagami, Quebec: Economic Geology, v. 82, p. 1898–1911.

Kuno, H., 1966, Lateral variation of basaltic magma type across continental margins and island arcs: Bulletin of Volcanology, v. 29, p. 195-222.

LaFlamme C., Sugiono D., The´baud N., Caruso S., Fiorentini M., Selvaraja V., Jeon H., Voute F. and Martin L., 2018, Multiple sulfur isotopes monitor fluid evolution in an orogenic gold deposit: Geochim. Cosmochim. Acta 222, p. 436–446.

Laird, J., 1988, Chlorites; metamorphic petrology: Rev. Mineral. Geochem, v. 19, p. 405–453.

Lambert-Smith, J. S., Rocholl, A., Treloar, P. J., and Lawrence, D. M., 2016, Discriminating fluid source regions in orogenic gold deposits using B-isotopes: Geochimica et Cosmochimica Acta, v. 194, p. 57–76.

Lawley, C. J. M., Dubé, B., Mercier-langevin, P., Kjarsgaard, B., Knight, R., and Vaillancourt, D., 2015, Defining and mapping hydrothermal footprints at the BIF-hosted Meliadine gold district, Nunavut, Canada: Journal of Geochemical Exploration, v. 155, p. 33–55.

Lawley, C. J. M., McNicoll, V., Sandeman, H., Pehrsson, S., Simard, M., Castonguay, S., Mercier-Langevin, P., and Dubé, B., 2016, Age and geological setting of the Rankin Inlet greenstone belt and its relationship to the gold endowment of the Meliadine gold district, Nunavut, Canada: Precambrian Research, v. 275, p. 471–495.

Le Maitre, R. W., 1989, A Classification of Igneous Rocks and Glossary of Terms: Recommendations of the IUGS Commission on the Systematics of Igneous Rocks. Oxford: Blackwell.

Lesher, C. M., Gibson, H. L., and Campbell, I. H., 1986, Composition-volume changes during hydrothermal alteration of andesite at Buttercup Hill, Noranda District, Quebec: Geochimica et Cosmochimica Acta, v. 50, p. 2693–2705.

Lewry, J.F., 1977, The geology of the Glennie Lake area, Saskatchewan: Dep. Miner. Resour., Rep. 143, 59 p.

Lewry, J. F., Thomas, D. J., Macdonald, R., and Chiarenzelli, J., 1990, Structural relations in accreted terranes of the Trans-Hudson Orogen, Saskatchewan: telescoping in a collisional regime: in Lewry, J.F. and Stauffer, M.R. (eds.), The Early Proterozoic Trans-Hudson Orogen of North America: Geol. Assoc. Can., Spec. Pap. 37, p. 75- 94.

Lhotka, P. G., and Nesbitt, B. E., 1989, Geology of unmineralized and gold-bearing iron formation, Contwoyto Lake-Point Lake region, Northwest Territories, Canada: Canadian Journal of Earth Sciences, v. 26, p. 46–64.

Li, C. M., Deng, J. F., and Chen, L. H., 2010, Constraint from two stages of zircon on the metallogenic age in the Dongping gold deposit, Zhangxuan area, northern North China: Miner. Depos. Geol, v. 29, p. 265–275.

Lucas, S. B., Stern, R. A., Syme, E. C., Reilly, B. A., and Thomas, D. J., 1996, Intraoceanic tectonics and the development of continental crust: 1.92-1.84 Ga evolution of the Flin Flon Belt, Canada: Geol. Soc. Amer. Bull., v. 108, p. 602-629.

Lucas, S. B., Stern, R. A., Syme, E.C., Zwanzig, H., Bailes, A. H., Ashton, K. E., Maxeiner, R. O., Ansdell, K. M., Lewry, J.F., Ryan, J. J., and Kraus, J., 1997, Tectonics of the southeastern Reindeer Zone, Trans-Hudson Orogen (Manitoba and Saskatchewan): Geological Association of Canada – Mineralogical Association of Canada, Joint Annual Meeting, Program with Abstract, 22, A-93.

McCuaig, T. C., and Kerrich, R., 1998, P-T-t-deformation-fluid characteristics of lode gold deposits: Evidence from alteration systematics: Ore Geology Reviews, v.12, p. 381–453.

McDonough, W. F., Sun, S. S., Ringwood, A. E., Jagoutz, E., and Hofmann, A. W., 1992, Potassium, rubidium, and cesium in the Earth and Moon and the evolution of the Earth's mantle: Geochimica et Cosmochimica Acta, v. 56, p. 1001-1012.

McEwan, B., 2013, Summary of Geological Mapping of the Santoy Mine area during the summer of 2012: internal report, 27p.

McNicoll, V. J., Delaney, G. D., Parrish, R. R., and Heaman, L. M., 1992, U-Pb age determinations from the Glennie Lake Domin, Trans-Hudson Orogen, Saskatchewan: Radiogenic Age and Isotopic Studies: Report 6, Geological Survey of Canada, Paper 92-2, p. 57-72.

Middlemost, E. A., 1994, Naming materials in the magma/igneous rock system: Earth-Science Reviews, v. 37, p. 215-224.

Miyashiro, A., 1974, Volcanic rock series in island arcs and active continental margins: American Journal of Science, v. 274, p. 321–355.

Morelli, R. M., Creaser, R. A., Selby, D., Kelley, K. D., Leach, D. L., and King, A. R., 2004, Re-Os Sulfide Geochronology of the Red Dog Sediment-Hosted Zn-Pb-Ag Deposit, Brooks Range, Alaska: Economic Geology, v. 99, p. 1569–1576.

Morelli, R. M., and Maclachlan, K., 2012, Saskatchewan Gold: Mineralization Styles and Mining History: Saskatchewan Ministry of Energy and Resources, 171p.

Morimoto, N., 1988, Nomenclature of pyroxenes: Schweizerische Mineralogische und Petrographische Mitteilungen, v. 68, p. 95–111.

Nachit, H., Ibhi, A., Abia, E. H., and Ben Ohoud, M., 2005, Discrimation entre biotites magmatiques primaires, biotites rééquilibrées et biotites néoformées: Comptes Rendus - Geoscience, v. 337, p. 1415–1420.

Nicholls, J., 1988, The statistics of Pearce element diagrams and the Chayes closure problem: Contributions to Mineralogy and Petrology, v. 99, p. 11–24.

Pearce, J.A., 1996, A User's Guide to Basalt Discrimination Diagrams: In: Wyman, D.A., Ed., Trace Element Geochemistry of Volcanic Rocks: Applications for Massive Sulphide Exploration, Geological Association of Canada, Short Course Notes, 12, p. 79-113.

Pearce, J. A., 2008, Geochemical fingerprinting of oceanic basalts with applications to ophiolite classification and the search for Archean oceanic crust: Lithos, v. 100, p. 14–48.

Pearce, J.A., 2014, Immobile element fingerprinting of ophiolites: Elements, v. 10, p. 101-108.

Phillips, G. N., Groves, D. I., Neall, F. B., Donnelly, T. H., and Lambert, I. B., 1986, Anomalous sulfur isotope compositions in the Golden Mile, Kalgoorlie: Economic Geology, v. 81, p. 2008–2015.

Piercey, S. J., 2009, Lithogeochemistry of volcanic rocks associated with volcanogenic massive sulphide deposits and applications to exploration in Submarine Volcanism and Mineralization: Modern through Ancient, p. 15–40.

Price, W., 1997, Guidelines and recommended Methods for the Prediction of Metal Leaching and Acid rock Drainage at Minesites in British Columbia: 170p.

Ramdohr, P., 1969, The Ore Minerals and their Intergrowths: Pergamon, Oxford

Ramsay, J. G., and Huber, M. I., 1987, The techniques of modern structural geology: Folds and Fractures, v. 2, Academic Press, London.

Ridley, J., 1993, The relations between mean rock stress and fluid flow in the crust: With reference to vein- and lode-style gold deposits: Ore Geology Reviews, v. 8, p. 23–37.

Ridley, J., 2013, Ore deposit geology, Cambridge University Press.

Robert, F., Brommecker, R., Bourne, B. T., Dobak, P. J., McEwan, C. J., Rowe, R. R., and Zhou, X., 2007, Models and Exploration Methods for Major Gold Deposit Types: Exploration 07: Fifth Decennial International Conference on Mineral Exploration, p. 691–711.

Rollinson, H., 1993, Using geochemical data: evaluation, presentation, interpretation: Longman, Harlow, 352p.

Ropchan J. R., Fowler A. D., Benn K., Ayer J., Berger B., Dahn, R., Labine, R., and Amelin, Y., 2002, Host rock and structural controls on the nature and timing of gold mineralization at the Holloway mine, Abitibi subprovince, Ontario: Economic Geology, v. 97, p. 291–309.

Ross, G. M., Parrish, R. R., Villeneuve, M. E., and Bowring, S. A., 1991, Geophysics and geochronology of the crystalline basement of the Alberta basin, western Canada: Canadian Journal of Earth Sciences, v. 28, p. 512-522.

Rottier B., Kouzmanov K., Wälle M., Bendezú R. and Fontboté L., 2016, Sulfide replacement processes revealed by textural and LA-ICP-MS trace element analyses: example from the early mineralization stages at Cerro de Pasco, Peru: Economic Geology, v. 111, p. 1347–1367.

Saskatchewan Geological Survey, 2003, Geology, and mineral and petroleum resources of Saskatchewan: Sask. Industry and Resources, Misc. Rep. 2003-7, 173p.

Saskatchewan Ministry of Energy and Resources, 2019, Saskatchewan Exploration and Development Highlights 2019: Saskatchewan Geological Survey, Saskatchewan Ministry of Energy and Resources, Miscellaneous Report 2019-2, 18p.

Saunders, A. D. and Tarney, J., 1979, The geochemistry of basalts from a back-arc spreading centre in the East Scoti Sea: Geochemica et Cosmochimica Acta, v. 43, p. 555-572.

Schultz, D. J., 1996, The fluid history of the Seabee mesothermal gold deposit northern Saskatchewan: Unpublished M.Sc. thesis, Saskatoon, Canada, University of Saskatchewan. 122p.

Selby, M., Chartier, D., Liskowich, M., and Kulas, J., 2017, Technical Report for the Seabee Gold Operation, Saskatchewan, Canada, NI 43-101 Report, RPA Canada.

Shiraki, K., 1997, Geochemical Behavior of Chromium: Resource Geology, v. 4, p. 319–330.

Siddorn, J. P., 2011, The Giant-Con gold deposit, a once-linked Archean lode-gold system: Unpublished PhD Thesis, Toronto, Canada, University of Toronto, 330p.

Smoliar, M. I., Walker, R. J., and Morgan, J. W. 1996, Re-Os ages of group IIA, IIIA, IVA and IVB iron meteorites: Science, v. 271, p. 1099-1102.

Spear, F. S., 1993, Metamorphic Phase Equilibria and Pressure-Temperature-Time Paths: Monograph I, Mineralogical Society of America.

Spitz, G. and Darling, R., 1978, Major and minor element lithogeochemical anomalies surrounding the Louvem copper deposit, Val d'Or, Quebec: Canadian Journal of Earth Sciences, v. 15, p. 1161-1169.

Stanley, C. R., and Madeisky, H. E., 1996, Lithogeochemical exploration for metasomatic zones associated with hydrothermal mineral deposits using Pearce element ratio analysis: British Columbia, Canada, Mineral Deposit Research Unit, Short Course Notes on Pearce Element Ratio Analysis, 99p.

Stanley, C., 2013, Molar Element Ratio Analysis of Lithogeochemical Data: A Toolbox for Use in Mineral Exploration and Mining: Proceedings of Exploration 17: Sixth Decennial International Conference on Mineral Exploration, p. 471–494.

Stauffer, M. R., 1984, Manikewan: An early proterozoic ocean in central Canada, its igneous history and orogenic closure: Precambrian Research, v. 25, p. 257–281.

Stern, R. A., Syme, E. C., and Lucas, S. B., 1995, Geochemistry of 1.9 Ga MORB- and OIB-like basalts from the Amisk collage, Flin Flon Belt, Canada: Evidence for an intra-oceanic origin: Geochimica et Cosmochimica Acta, v. 59, p. 3131–3154.

Taiga Gold Corp., 2021, News: Taiga Forms Joint-Venture with SSR Mining, Receives CDN $3,000,000 Cash Payment for Fisher Gold Project, Saskatchewan, January 5, 2021: https://www.taigagold.com/news/taiga-forms-joint-venture-ssr-mining-receives-cdn-3000000-cash-payment-fisher-gold-project.

Thomas, D. J., and Heaman, L. M., 1994, Geologic setting of the Jolu gold mine, Saskatchewan: U-Pb age constraints on plutonism, deformation, mineralization, and metamorphism: Economic Geology, v. 89, p. 1017–1029.

Tourigny, G., 2003, Preliminary structural study of the gold-bearing shear zone system at the Seabee Mine, northern Saskatchewan: Summary of Investigations 2003, Volume 2, Saskatchewan Geological Survey, Sask. Industry Resources, Misc. Rep. 2003-4.2, CD-ROM, Paper B-1, 11p.

Tourigny, G., Chi, G., Yuhasz, C., Olson, R., Berger, J., and Soloman, J., 2004, Structural controls and temperature-pressure conditions of gold-bearing quartz vein systems at the Seabee mine, northern Saskatchewan: Summary of Investigations 2004, Volume 2, Saskatchewan Geological Survey, Sask. Industry and Resources, Misc. Rep. 2004-4.2, CD-ROM, Paper A-2, 18p.

van Acken, D., Su, W., Gao, J., and Creaser, R. A., 2014, Preservation of Re-Os isotope signatures in pyrite throughout low-T, high-P eclogite facies metamorphism: Terra Nova, v. 26, p. 402–407.

Van Hees, E.H.P., Shelton, K.L., McMenamy, T.A., Ross, L.M., Cousens, B.L., Falck, H., Robb, M.E., and Canam, T.W., 1999, Metasedimentary influence on metavolcanic-rock-hosted greenstone gold deposits: Geochemistry of the Giant mine, Yellowknife, Northwest Territories, Canada: Geology, v. 27, p. 71–74.

Völkening, J., Walczyk, T., and Heumann, K. G., 1991, Osmium Isotope Ratio Determinations by Negative Thermal Ionization Mass Spectrometry: International Journal of Mass Spectrometry and Ion Processes, v. 105, p. 147-159.

Wang, R., Jeon, H., and Evans, N.J., 2018, Archaean hydrothermal fluid modified zircons at Sunrise Dam and Kanowna Belle gold deposits, Western Australia: Implications for post-magmatic fluid activity and ore genesis: American Mineralogist, v. 103, p. 1891-1905.

Warren, I., Simmons, S. F., and Mauk, J. L., 2007, Whole-rock geochemical techniques for evaluating hydrothermal alteration, mass changes, and compositional gradients associated with epithermal Au-Ag mineralization: Economic Geology, v. 102, p. 923–948.

Whitney, D. L., and Evans, B. W., 2010, Abbreviations for names of rock-forming minerals: American Mineralogist, v. 95, p. 185–187.

Winchester, J. A., and Floyd, P. A., 1977, Geochemical discrimination of different magma series and their differentiation products using immobile elements: Chemical Geology, v. 20, p. 325–343.

Witvoet, L., Partin, C., Ansdell, K., Carlson, A., 2019, Petrological and Geochemical Comparison of the Eisler and Laonil Lake Intrusive Complexes, Seabee Gold Operation, Saskatchewan: Poster presentation at: 2019 Saskatchewan Geological Open House; 2019 Dec 2 - 4; Saskatoon, SK, Canada.

Wood, C.R., 2016, Structural Study of the Auriferous Santoy Shear Zone, Northeastern Glennie Domain, Saskatchewan: Unpublished M.Sc. thesis, Regina, Canada, University of Regina., 154p.

Xavier, R. P., Wiedenbeck, M., Trumbull, R. B., Dreher, A. M., Monteiro, L. V. S., Rhede, D., de Araújo, C. E. G., and Torresi, I., 2008, Tourmaline B-isotopes fingerprint marine evaporites as the source of high-salinity ore fluids in iron oxide copper-gold deposits, Carajás Mineral Province (Brazil): Geology, v. 36, p. 743–746.

Xing, Y., Brugger, J., Tomkins, A., and Shvarov, Y., 2019, Arsenic evolution as a tool for understanding formation of pyritic gold ores: Geology, v. 47, p. 335–338.

Zane, A., and Weiss, Z., 1998, A procedure for classifying rock-forming chlorites based on microprobe data: Rendiconti Lincei, v. 9, p. 51–56.

Zuo, H., Lu, A., Gu, X., Ma, W., Cui, Y., Yi, L., Lei, H., Wang, Z., Zhang, D., and Liu, J., 2016, Typomorphic feature of chromium sericite in granite hosted gold deposits in Jiaodong Peninsula, China: Applied Clay Science, v. 119, p. 49–58.

Zwanzig, H. V., 1997, Kisseynew metasedimentary gneiss belt, Trans-Hudson orogen (Canada): Back-arc origin and collisional inversion: Geology, v. 25, p. 90-92.

APPENDIX A: GENERAL SAMPLE DETAILS

Table A. Fisher rocks samples and associated drill holes, depths, locality information and lithologic classifications.

Sample ID	Hole ID	Depth (m)	UTM Easting	UTM Northing	Company Lithology	New Lithology	Thin Section (y/n)	Geochem (y/n)	Microprobe (y/n)
CO-2019-1	FIS-18-001	72.8	600767.1	6166989	PYRX	PYRX	yes	yes	no
CO-2019-2	FIS-18-001	244.6	600767.1	6166989	QD	QD	yes	yes	no
CO-2019-3	FIS-18-003	10.3	601195.9	6167042	MV	HCrB	yes	yes	no
CO-2019-4	FIS-18-003	171.3	601195.9	6167042	AMV	AND1	yes	yes	no
CO-2019-5	FIS-18-003	214.4	601195.9	6167042	BSCH	BSCH	yes	yes	no
CO-2019-6	FIS-18-003	238.7	601195.9	6167042	IV	AND1	yes	yes	no
CO-2019-7	FIS-18-003	343.5	601195.9	6167042	FV	AND1	yes	yes	no
CO-2019-8	FIS-18-003	392.3	601195.9	6167042	FGGB	GRD	yes	yes	no
CO-2019-9	FIS-18-003	654.1	601195.9	6167042	MVC	HCrB	yes	yes	no
CO-2019-11	FIS-18-016	157.3	602156	6165130	IV	AND1	yes	yes	no
CO-2019-12	FIS-18-016	286.1	602156	6165130	MV	AND2	yes	yes	no
CO-2019-13	FIS-18-016	379.5	602156	6165130	ISMV	AND1	yes	yes	no
CO-2019-14	FIS-18-016	514.2	602156	6165130	AMV	AND1	yes	yes	no
CO-2019-15	FIS-18-017	317.3	603370	6162978	IV	HCrB	yes	yes	no
CO-2019-16	FIS-18-017	393.5	603370	6162978	MV	HCrB	yes	yes	no
CO-2019-17	FIS-18-017	409.1	603370	6162978	TON	MetaSED	yes	yes	no
CO-2019-18	FIS-18-017	526	603370	6162978	GAB	AND2	yes	yes	no
CO-2019-19	FIS-18-017	623.5	603370	6162978	AMV	AND2	yes	yes	yes
CO-2019-20	FIS-18-017	673.5	603370	6162978	FV	FV	yes	yes	no
CO-2019-21	FIS-18-017	720	603370	6162978	QD	GAB	yes	yes	no
CO-2019-22	FIS-18-018	55.1	602798	6163905	IMV	MV	yes	yes	no
CO-2019-23	FIS-18-018	186.3	602798	6163905	BSS	BSCH	yes	yes	no
CO-2019-24	FIS-18-018	358.2	602798	6163905	MVCL	PYRX	yes	yes	no
CO-2019-25	FIS-18-018	620.7	602798	6163905	IV	LCrB	yes	yes	no
CO-2019-26	FIS-18-028	44.7	604138	6160239	MGMV	LCrB	yes	yes	no
CO-2019-28	FIS-18-028	231.8	604138	6160239	MV	HCrB	yes	yes	yes
CO-2019-29	FIS-18-028	237.6	604138	6160239	CSCH	CSCH	yes	yes	no
CO-2019-30	FIS-18-028	320.2	604138	6160239	GAB	GAB	yes	yes	no
CO-2019-31	FIS-18-022	60.7	604183	6160406	GAB	GAB	yes	yes	no
CO-2019-32	FIS-18-022	112.8	604183	6160406	AMV	LCrB	yes	yes	no
CO-2019-33	FIS-18-022	191.1	604183	6160406	PYRX	PYRX	yes	yes	yes
CO-2019-34	FIS-18-022	314.5	604183	6160406	MV	HCrB	yes	yes	yes
CO-2019-35	FIS-18-022	422.4	604183	6160406	GRD	MetaSED	yes	yes	no
CO-2019-36	FIS-18-023	78.1	604154	6160271	MVCL	VCLST	yes	yes	no
CO-2019-37	FIS-18-023	83.8	604154	6160271	GAB	GAB	yes	yes	no
CO-2019-38	FIS-18-023	211	604154	6160271	MV	HCrB	yes	yes	no
CO-2019-39	FIS-18-023	238.5	604154	6160271	GRD	MetaSED	yes	yes	no
CO-2019-48	FIS-18-021	249	604154	6160271	GRD	GRNT	yes	yes	yes
CO-2019-49	FIS-18-021	249.5	604154	6160271	GRD	GRNT	no	yes	no
CO-2019-50	FIS-18-021	251.1	604154	6160271	GRD	GRNT	no	yes	no
CO-2019-51	FIS-18-021	255.1	604154	6160271	GRD	GRNT	no	yes	no
CO-2019-52	FIS-18-021	255.3	604154	6160271	GRD	GRNT	no	yes	no
CO-2019-53	FIS-19-035	102	603981.7	6161456	MV	LCrB	no	yes	no
CO-2019-54	FIS-19-035	106.49	603981.7	6161456	MV	LCrB	yes	yes	no
CO-2019-55	FIS-19-035	107.45	603981.7	6161456	MV	HCrB	yes	yes	yes
CO-2019-56	FIS-19-035	107.65	603981.7	6161456	MV	MetaSED	yes	yes	no
CO-2019-57	FIS-19-035	108.35	603981.7	6161456	MV	AND1	yes	yes	no
CO-2019-58	FIS-19-030	135.5	604132.7	6160681	MV	LCrB	no	yes	no
CO-2019-59	FIS-19-030	136.6	604132.7	6160681	QZDIO	DIO	no	yes	no
CO-2019-60	FIS-19-030	138.3	604132.7	6160681	QZDIO	LCrB	yes	yes	no
CO-2019-61	FIS-19-030	139.1	604132.7	6160681	QZDIO	LCrB	yes	yes	yes

Table A. Fisher rocks samples and associated drill holes, depths, locality information and lithologic classifications.

Sample ID	Hole ID	Depth (m)	UTM Easting	UTM Northing	Company Lithology	New Lithology	Thin Section (y/n)	Geochem (y/n)	Microprobe (y/n)
CO-2019-62	FIS-19-030	141.2	604132.67	6160680.7	QZDIO	LCrB	no	yes	no
CO-2019-63	FIS-18-024	28.2	604123	6160492	MV	LCrB	no	yes	no
CO-2019-64	FIS-18-024	28.5	604123	6160492	MV	LCrB	yes	yes	no
CO-2019-65	FIS-18-024	29.4	604123	6160492	MV	LCrB	no	yes	no
CO-2019-66	FIS-18-024	30.6	604123	6160492	MV	FV	no	yes	no
CO-2019-67	FIS-18-024	32.7	604123	6160492	QZDIO	HCrB	yes	yes	no
CO-2019-68	FIS-18-021	314.8	604154	6160271	MV	MetaSED	no	yes	no
CO-2019-69	FIS-18-021	316.1	604154	6160271	MV	MetaSED/HCrB	yes	yes	yes
CO-2019-70	FIS-18-021	318.5	604154	6160271	MV	HCrB	no	yes	no
CO-2019-71	FIS-18-021	328.5	604154	6160271	MV	MetaSED	no	yes	no
CO-2019-72	FIS-18-021	329.2	604154	6160271	QZDIO	MetaSED	yes	yes	no
CO-2019-73	FIS-18-021	329.8	604154	6160271	QZDIO	MetaSED	no	yes	no
CO-2019-74	FIS-18-024	185.8	604123	6160492	GRD	GRNT	yes	yes	no
CO-2019-75	FIS-18-024	189.3	604123	6160492	GRD	AND1	no	yes	no
CO-2019-76	FIS-18-020	182.5	604154	6160271	MV	GRNT	no	yes	no
CO-2019-77	FIS-18-020	184.4	604154	6160271	MV	GRNT	yes	yes	no
CO-2019-78	FIS-18-020	184.86	604154	6160271	MV	GRNT	no	yes	no
CO-2019-79	FIS-18-020	185.5	604154	6160271	GRD	DIO	no	yes	no
CO-2019-80	FIS-18-021	55.3	604154	6160271	GAB	DIO	no	yes	no
CO-2019-81	FIS-18-021	55.9	604154	6160271	GAB	DIO	yes	yes	yes
CO-2019-82	FIS-18-021	56.6	604154	6160271	GAB	DIO	no	yes	no
CO-2019-83	FIS-18-021	57.2	604154	6160271	GAB	DIO	yes	yes	no
CO-2019-84	FIS-18-021	58.7	604154	6160271	GAB	DIO	no	yes	no
CO-2019-85	FIS-18-028	60.8	604154	6160271	GAB	DIO	no	yes	no
CO-2019-86	FIS-18-028	306.5	604138	6160239	MV	HCrB	yes	yes	no
CO-2019-87	FIS-18-028	307.5	604138	6160239	MV	HCrB	yes	yes	no
CO-2019-88	FIS-18-023	309.5	604138	6160239	MV	HCrB	no	yes	no
CO-2019-92	FIS-18-023	181.5	604154	6160271	MV	HCrB	no	yes	no
CO-2019-93A	FIS-18-023	182.3	604154	6160271	MV	HCrB	yes	yes	yes
CO-2019-93B	FIS-18-023	182.3	604154	6160271	MV	HCrB	no	yes	no
CO-2019-94	FIS-18-023	182.3	604154	6160271	MV	HCrB	yes	no	no
CO-2019-114	surface	-	603120	6163318	MV Cglm	MetaSED	yes	yes	no
CO-2019-115	surface	-	603581	6161710	MV	MV	yes	yes	no
CO-2019-116	surface	-	603384	6162975	MV	HCrB	no	yes	no
CO-2019-117	surface	-	603854	6161835	Dacitic Tuff	VCLST	yes	yes	no
CO-2019-118	surface	-	604265	6161670	Tonalite	GRD	yes	yes	no
CO-2019-119	surface	-	604585	6161373	Felsic SED	MetaSED	yes	yes	no
CO-2019-120	surface	-	604107	6160399	MV	HCrB	no	yes	no
CO-2019-121	surface	-	604310	6159077	MV	HCrB	no	yes	no
CO-2019-122	surface	-	603219	6166953	DIO	GRD	no	yes	no
CO-2019-123	surface	-	603954	6161125	MV	HCrB	yes	yes	no
CO-2019-124	surface	-	605492	6158451	Int VCL	VCLST	yes	yes	no
CO-2019-125	surface	-	605300	6158362	Hyp Phyric Sill	DIO	yes	yes	no
CO-2019-126	surface	-	605040	6158355	Felsic Tuff	VCLST	yes	yes	no
CO-2019-127	surface	-	604096	6161365	FV	AND2	no	yes	no
CO-2019-128	surface	-	604091	6160249	MV	HCrB	no	yes	no
CO-2019-129	surface	-	604091	6160249	GRD	GRNT	no	yes	no
CO-2019-130	surface	-	604561	6161318	VC/SED	AND2	yes	yes	no
CO-2019-131	surface	-	603954	6161125	GRD	GRNT	no	yes	no
CO-2019-132	surface	-	676107	6068472	DIO	DIO	no	yes	no

APPENDIX B: LITHOGEOCHEMICAL DATA

Table B ICP-OES and ICP-MS lithogeochemical results of Fisher property rocks.

Sample ID				CO-2019-03	CO-2019-16	CO-2019-34	CO-2019-38	CO-2019-120	CO-2019-123	CO-2019-128	CO-2019-15	CO-2019-28
Hole ID				FIS-18-003	FIS-18-017	FIS-18-022	FIS-18-023	Surface	Surface	Surface	FIS-18-017	FIS-18-028
Depth (m)				10.3	393.5	314.5	211	-	-	-	317.3	231.8
UTM Zone 13N Northing				6167042	6162978	6160406	6160271	6160399	6161125	6160249	6162978	6160239
UTM Zone 13N Easting				601195.9	603370	604183	604154	604107	603954	604091	603370	604138
Lithology				HCrB	HCrB	HCrB	HCrB	HCrB	HCrB	HCrB	HCrB	HCrB
Alteration Intensity				L	L	L	L	L	L	L	M	M
			Detection Limit									
SiO_2	(%)	ICP-OES	0.10%	55	50.1	47	50.7	54	50.6	50.7	51.4	47.8
TiO_2	(%)	ICP-OES	0.01%	0.6	0.84	1.33	1.38	1	1.03	1.64	0.67	1.61
Al_2O3	(%)	ICP-OES	0.01%	18	17.1	15.5	15.7	16.1	15.7	14.6	13.7	16.8
Fe_2O_3	(%)	ICP-OES	0.01%	8.53	10.2	14.6	13	10.3	11.7	14.4	9.89	13.5
MnO	(%)	ICP-OES	0.01%	0.13	0.14	0.2	0.16	0.15	0.16	0.18	0.19	0.18
MgO	(%)	ICP-OES	0.01%	3.71	5.96	6.89	5.19	4.58	6.18	5.49	9.84	5.78
CaO	(%)	ICP-OES	0.01%	7.34	11.1	10	8.6	7.73	9.94	8.67	8.6	8.78
Na_2O	(%)	ICP-OES	0.01%	3.76	2.81E+00	2.9	2.94	3.66	2.63	3	2.44	3.29
K_2O	(%)	ICP-OES	0.01%	1.8	0.94	0.43	0.69	0.85	0.27	0.38	1.88	0.71
P_2O_5	(%)	ICP-OES	0.01%	0.2	0.08	0.18	0.29	0.25	0.24	0.21	0.1	0.38
LOI	(%)	ICP-OES	0.10%	1.4	0.7	0.9	0.5	0.8	0.8	0.7	1.2	0.8
SUM	(%)	ICP-OES	0.10%	100.47	99.97	99.93	99.15	99.42	99.25	99.97	99.91	99.63
Ag	(ppm)	ICP-MS	0.1 ppm	2	0.6	0.6	0.7	0.05	0.05	0.05	1.1	0.8
As	(ppm)	ICP-MS	0.1 ppm	2.8	2.1	2.1	3.7	0.05	0.05	0.05	2.8	2.3
Ba	(ppm)	ICP-MS	1 ppm	524	268	110	375	398	116	108	349	324
Be	(ppm)	ICP-MS	0.1 ppm	8	7.7	9.4	9.1	0.3	0.05	0.05	8	7.9
Bi	(ppm)	ICP-MS	0.1 ppm	0.3	0.2	0.1	0.1	0.05	0.05	0.05	0.2	0.05
C	(ppm)	ICP-MS	0.01 ppm	0.18	0.05	0.09	<0.01	-	-	-	0.03	0.07
Cd	(ppm)	ICP-MS	0.1 ppm	0.05	0.2	0.3	0.5	0.1	0.05	0.2	0.1	0.3
Ce	(ppm)	ICP-MS	1 ppm	39	17	19	38	26	25	28	27	26
Co	(ppm)	ICP-MS	0.1 ppm	23.2	36	38.3	38.4	30.4	35	39	41.6	34.5
Cr	(ppm)	ICP-OES	2 ppm	84	142	156	63	67	124	62	379	106
Cs	(ppm)	ICP-MS	0.1 ppm	1.3	1	0.3	0.3	0.05	2.2	0.05	14.7	0.5
Cu	(ppm)	ICP-MS	0.1 ppm	80.2	69.2	62.9	68.2	40.4	52.3	78.5	18.6	29.8
Dy	(ppm)	ICP-MS	0.01 ppm	3.19	3.32	3.82	6.13	5.06	4.64	4.23	2.72	4.32
Er	(ppm)	ICP-MS	0.01 ppm	1.65	1.92	2.09	3.09	2.57	2.6	2.81	1.26	2.32
Eu	(ppm)	ICP-MS	0.01 ppm	1.02	0.96	1.14	1.67	1.34	1.04	1.25	1.21	1.51
Ga	(ppm)	ICP-MS	0.1 ppm	16.3	15.3	16.8	18	19.7	17.2	20.1	13.8	17.2
Gd	(ppm)	ICP-MS	0.01 ppm	2.83	2.46	2.7	4.94	3.78	3.48	3.65	2.52	3.78
Ge	(ppm)	ICP-MS	0.1 ppm	1.4	1.3	1.4	1.3	0.3	0.3	0.4	1.1	1.1
Hf	(ppm)	ICP-MS	0.1 ppm	1.9	1.5	1.6	2.4	2.7	2.2	1.9	1.6	1.7
Hg	(ppm)	ICP-MS	0.1 ppm	0.05	0.05	0.2	0.05	0.05	0.05	0.05	0.05	0.2
Ho	(ppm)	ICP-MS	0.01 ppm	0.69	0.82	0.9	1.37	0.92	0.92	0.96	0.56	0.96
La	(ppm)	ICP-MS	1 ppm	17	6	7	16	11	10	10	11	10
Lu	(ppm)	ICP-MS	0.01 ppm	0.36	0.32	0.43	0.6	0.41	0.42	0.35	0.19	0.39
Mo	(ppm)	ICP-MS	0.1 ppm	2.1	1.2	1.3	1.3	0.4	0.05	0.05	1.5	1
Nb	(ppm)	ICP-MS	1 ppm	4	2	3	5	3	1	1	2	4
Nd	(ppm)	ICP-MS	0.1 ppm	18.5	8.8	12.7	22.3	18.9	16.2	17.1	14.9	15.9
Ni	(ppm)	ICP-MS	1 ppm	22	56	64	60	62	62	45	96	66
Pb204	(ppm)	ICP-MS	0.01 ppm	0.155	1.05E-01	0.115	0.096	0.072	5.00E-04	5.00E-04	0.089	0.092
Pb206	(ppm)	ICP-MS	0.02 ppm	2.09	1.02	0.843	0.834	1.39	0.441	0.246	0.505	0.823
Pb207	(ppm)	ICP-MS	0.02 ppm	1.69	0.882	0.855	0.69	1.53	0.619	0.475	0.429	0.806
Pb208	(ppm)	ICP-MS	0.02 ppm	3.92	2.08	1.8	1.93	3.46	1.38	1.25	0.986	1.98
PbSUM	(ppm)	ICP-MS	0.02 ppm	7.85	4.08	3.62	3.55	6.46	2.44	1.95	2.01	3.7
Pr	(ppm)	ICP-MS	0.01 ppm	4.66	2.01	2.91	5.26	3.84	3.43	4	3.54	3.85
Rb	(ppm)	ICP-MS	0.1 ppm	41.3	10.6	4.6	16.3	18.2	2.7	3.6	78.5	14
S	(ppm)	ICP-MS	0.01 ppm	<0.01	0.11	0.17	0.18	-	-	-	0.04	0.12
Sb	(ppm)	ICP-MS	1 ppm	1	1	0.5	3	0.5	0.5	0.5	0.5	0.5
Sc	(ppm)	ICP-OES	2 ppm	21	29	34	26	23	33	31	31	27
Se	(ppm)	ICP-MS	1 ppm	0.5	0.5	1	6	1	3	0.5	12	11
Sm	(ppm)	ICP-MS	0.01 ppm	3.46	2.38	2.66	5.8	4.31	4.19	3.51	3.37	3.98
Sn	(ppm)	ICP-MS	0.1 ppm	4.7	4.6	1.8	1.4	0.05	0.05	0.05	3.3	5.2
Sr	(ppm)	ICP-MS	1 ppm	482	323	341	426	326	365	424	459	535
Ta	(ppm)	ICP-MS	0.01 ppm	0.54	0.36	0.3	0.7	0.3	0.13	0.16	0.34	0.43
Tb	(ppm)	ICP-MS	0.01 ppm	0.48	0.49	0.51	0.79	0.57	0.55	0.62	0.38	0.64
Te	(ppm)	ICP-MS	0.1 ppm	0.1	0.05	0.05	0.05	0.05	0.05	0.05	0.05	0.05
Th	(ppm)	ICP-MS	0.01 ppm	5.38	2.51	0.58	2.05	5.72	4.6	2.19	3.56	0.73
Tm	(ppm)	ICP-MS	0.01 ppm	0.28	0.26	0.36	0.52	0.5	0.41	0.43	0.2	0.4
U	(ppm)	ICP-MS	0.01 ppm	2.2	1.79	0.24	0.75	0.005	0.005	0.03	2.24	0.17
V	(ppm)	ICP-OES	2 ppm	152	225	358	283	174	246	315	242	308
W	(ppm)	ICP-MS	1 ppm	17	9	1	1	0.5	0.5	0.5	8	2
Y	(ppm)	ICP-MS	0.01 ppm	20.4	20.2	24.9	36.7	25.8	25.6	23.4	14.4	26.8
Yb	(ppm)	ICP-MS	0.01 ppm	2.1	1.83	2.19	3.16	2.68	3.04	2.37	1.24	2.12
Zn	(ppm)	ICP-MS	1 ppm	102	93	135	114	64	62	87	116	124
Zr	(ppm)	ICP-MS	2 ppm	65	54	55	95	106	97	64	57	70

Table B ICP-OES and ICP-MS lithogeochemical results of Fisher property rocks.

Sample ID				CO-2019-55	CO-2019-70	CO-2019-88	CO-2019-92	CO-2019-116	CO-2019-68	CO-2019-71	CO-2019-86	CO-2019-87
Hole ID				FIS-19-035	FIS-18-021	FIS-18-021	FIS-18-023	Surface	FIS-18-021	FIS-18-021	FIS-18-028	FIS-18-028
Depth (m)				107.45	318.5	55.3	181.5	-	314.8	328.5	306.5	307.5
UTM Zone 13N Northing				6161455.94	6160271	6160271	6160271	6162975	6160271	6160271	6160239	6160239
UTM Zone 13N Easting				603981.747	604154	604154	604154	603384	604154	604154	604138	604138
Lithology				HCrB	HCrB	HCrB	HCrB	HCrB	HCrB	HCrB	HCrB	HCrB
Alteration Intensity				M	M	M	M	M	H	H	H	H
			Detection Limit									
SiO_2	(%)	ICP-OES	0.10%	52	49.4	50.9	55.8	52.9	51.7	51.1	50.7	61.1
TiO_2	(%)	ICP-OES	0.01%	0.84	1.29	1.15	0.74	0.57	0.79	0.94	1.11	0.87
Al_2O3	(%)	ICP-OES	0.01%	14.9	15.5	15.5	15.9	16.8	15.9	14.3	15	13.1
Fe_2O_3	(%)	ICP-OES	0.01%	11.2	12.8	10.9	7.66	10.7	9.18	10.6	11.4	8.28
MnO	(%)	ICP-OES	0.01%	0.18	0.16	0.16	0.12	0.17	0.17	0.18	0.16	0.14
MgO	(%)	ICP-OES	0.01%	6.49	6.96	7.06	4.95	5.66	5.02	7.08	7.05	3.69
CaO	(%)	ICP-OES	0.01%	8.75	7.61	8.41	7.69	9.85	8.28	9.03	9.84	6.77
Na_2O	(%)	ICP-OES	0.01%	3.30E+00	2.67	2.96	0.36	2.22	1.68	0.51	1.89	1.11
K_2O	(%)	ICP-OES	0.01%	1.09	2.25	1.56	4.58	0.8	5.49	4.05	1.57	3.01
P_2O_5	(%)	ICP-OES	0.01%	0.16	0.21	0.21	0.17	0.16	0.15	0.17	0.24	0.17
LOI	(%)	ICP-OES	0.10%	1	1	1.3	1.9	0.7	1.6	2.1	1	1.7
SUM	(%)	ICP-OES	0.10%	99.91	99.85	100.11	99.87	100.53	99.96	100.06	99.96	99.94
Ag	(ppm)	ICP-MS	0.1 ppm	0.4	0.5	0.4	0.6	0.05	0.6	0.3	0.4	0.4
As	(ppm)	ICP-MS	0.1 ppm	1.1	1.9	4.8	21.7	0.05	9.2	20.3	10.4	8.5
Ba	(ppm)	ICP-MS	1 ppm	400	456	191	584	404	1160	535	364	601
Be	(ppm)	ICP-MS	0.1 ppm	9.9	9.4	10.1	10.1	0.05	11.1	9.4	8.8	11.4
Bi	(ppm)	ICP-MS	0.1 ppm	3.4	0.05	0.05	0.05	0.05	0.05	0.05	0.05	0.05
C	(ppm)	ICP-MS	0.01 ppm	-	-	-	-	-	-	-	-	-
Cd	(ppm)	ICP-MS	0.1 ppm	0.6	0.05	0.6	0.6	0.05	0.6	0.6	0.4	0.7
Ce	(ppm)	ICP-MS	1 ppm	24	24	54	33	60	40	27	47	36
Co	(ppm)	ICP-MS	0.1 ppm	32.3	45.9	39.7	28.2	32.4	25	43.4	43.3	24.1
Cr	(ppm)	ICP-OES	2 ppm	220	194	253	157	121	205	199	232	78
Cs	(ppm)	ICP-MS	0.1 ppm	8.9	2.2	0.8	0.8	1	1.4	1.2	1	1.4
Cu	(ppm)	ICP-MS	0.1 ppm	10.4	44.5	37.8	672	95.2	18.7	7.1	27.8	47.6
Dy	(ppm)	ICP-MS	0.01 ppm	3.77	3.9	3.68	3.19	2.63	3.81	4.34	3.62	6
Er	(ppm)	ICP-MS	0.01 ppm	2.31	2.19	2	1.76	1.82	2.01	2.48	2.19	3.28
Eu	(ppm)	ICP-MS	0.01 ppm	1.1	0.99	1.43	1.16	1.01	1.56	1.1	1.38	1.28
Ga	(ppm)	ICP-MS	0.1 ppm	13.1	15.3	13.9	16.3	16.2	17.3	13.4	13.9	14.4
Gd	(ppm)	ICP-MS	0.01 ppm	3.19	4.19	4.9	4.34	2.63	4.05	4.23	5.02	5.57
Ge	(ppm)	ICP-MS	0.1 ppm	0.05	0.05	0.05	0.05	0.3	0.05	0.05	0.05	0.05
Hf	(ppm)	ICP-MS	0.1 ppm	2.5	2.4	1.7	3.4	1.5	3.2	1.5	2.1	3.9
Hg	(ppm)	ICP-MS	0.1 ppm	0.05	0.05	0.05	0.05	0.05	0.05	0.3	0.05	0.05
Ho	(ppm)	ICP-MS	0.01 ppm	0.86	0.9	0.76	0.77	0.65	0.85	0.97	0.9	1.32
La	(ppm)	ICP-MS	1 ppm	12	12	42	18	28	22	14	32	17
Lu	(ppm)	ICP-MS	0.01 ppm	0.42	0.26	0.3	0.24	0.31	0.3	0.36	0.33	0.69
Mo	(ppm)	ICP-MS	0.1 ppm	2.3	2.2	2.7	3.3	0.7	2.4	2	2.9	1.4
Nb	(ppm)	ICP-MS	1 ppm	9	8	9	7	0.5	10	8	6	9
Nd	(ppm)	ICP-MS	0.1 ppm	15	15.8	32.8	20.7	29.4	26.3	16.4	25.8	22
Ni	(ppm)	ICP-MS	1 ppm	103	141	106	66	38	78	103	133	53
Pb204	(ppm)	ICP-MS	0.01 ppm	0.091	0.444	0.235	0.527	0.04	1.3	1.88	0.325	0.324
Pb206	(ppm)	ICP-MS	0.02 ppm	1.14	5.42	3.62	8.44	0.704	18.8	23.8	7.42	6.04
Pb207	(ppm)	ICP-MS	0.02 ppm	0.799	5.98	2.94	8.64	0.752	18.7	25.5	5.67	4.82
Pb208	(ppm)	ICP-MS	0.02 ppm	1.44	13.8	6.29	18.8	2.04	43.1	57	11.5	10
PbSUM	(ppm)	ICP-MS	0.02 ppm	3.47	25.6	13.1	36.4	3.53	81.9	108	24.9	21.2
Pr	(ppm)	ICP-MS	0.01 ppm	3.1	3.54	8.07	4.7	7.48	5.63	3.85	6.13	5.22
Rb	(ppm)	ICP-MS	0.1 ppm	36.7	54.9	30.3	83.2	13.9	88.8	87	36.3	68.9
S	(ppm)	ICP-MS	0.01 ppm	-	-	-	-	-	-	-	-	-
Sb	(ppm)	ICP-MS	1 ppm	3	3	3	4	0.5	3	4	3	3
Sc	(ppm)	ICP-OES	2 ppm	28	26	29	18	31	21	27	27	19
Se	(ppm)	ICP-MS	1 ppm	0.5	0.5	8	0.5	5	0.5	0.5	6	3
Sm	(ppm)	ICP-MS	0.01 ppm	3.06	3.78	6.13	3.98	4.16	4.44	3.88	4.35	4.82
Sn	(ppm)	ICP-MS	0.1 ppm	1.8	1	1.3	1.8	0.05	2.3	1.6	0.9	1.1
Sr	(ppm)	ICP-MS	1 ppm	322	371	319	249	443	336	198	178	139
Ta	(ppm)	ICP-MS	0.01 ppm	0.22	0.23	0.26	0.26	0.005	0.45	0.25	0.25	0.67
Tb	(ppm)	ICP-MS	0.01 ppm	0.41	0.49	0.5	0.43	0.29	0.54	0.52	0.49	0.66
Te	(ppm)	ICP-MS	0.1 ppm	0.5	0.05	0.05	0.05	0.05	0.8	0.05	0.05	0.05
Th	(ppm)	ICP-MS	0.01 ppm	2.52	1.02	1.92	1.92	12.8	2.79	1.11	1.66	2.62
Tm	(ppm)	ICP-MS	0.01 ppm	0.36	0.3	0.41	0.27	0.26	0.4	0.45	0.37	0.54
U	(ppm)	ICP-MS	0.01 ppm	2.53	1.17	15.3	6.94	0.28	2.6	1.63	26.8	16.7
V	(ppm)	ICP-OES	2 ppm	231	273	276	179	240	189	248	285	178
W	(ppm)	ICP-MS	1 ppm	2	0.5	0.5	9	0.5	4	0.5	0.5	0.5
Y	(ppm)	ICP-MS	0.01 ppm	21.6	21.7	20	18.3	14.7	21.3	24.3	22.1	33.1
Yb	(ppm)	ICP-MS	0.01 ppm	2.89	2.68	2.05	2.16	1.73	2.49	2.72	2.6	4.04
Zn	(ppm)	ICP-MS	1 ppm	141	184	159	116	142	356	270	233	180
Zr	(ppm)	ICP-MS	2 ppm	78	87	67	107	73	118	55	73	139

Table B Table B ICP-OES and ICP-MS lithogeochemical results of Fisher property rocks.

Sample ID				CO-2019-93A	CO-2019-93B	CO-2019-121	CO-2019-25	CO-2019-26	CO-2019-32	CO-2019-54	CO-2019-58	CO-2019-22
Hole ID				FIS-18-023	FIS-18-023	Surface	FIS-18-018	FIS-18-028	FIS-18-022	FIS-19-035	FIS-19-030	FIS-18-018
Depth (m)				182.3	182.3	-	620.7	44.7	112.8	106.49	135.5	55.1
UTM Zone 13N Northing				6160271	6160271	6159077	6163905	6160239	6160406	6161455.94	6160680.73	602798
UTM Zone 13N Easting				604154	604154	604310	602798	604138	604183	603981.747	604132.674	6163905
Lithology				HCrB	HCrB	HCrB	LCrB	LCrB	LCrB	LCrB	LCrB	LCrB
Alteration Intensity				H	H	H	L	L	L	L	L	M
			Detection Limit									
SiO_2	(%)	ICP-OES	0.10%	60.1	55.6	52.3	53.8	55.7	51.2	54.6	53.8	57
TiO_2	(%)	ICP-OES	0.01%	0.92	0.79	1.32	0.54	1.4	2.01	0.77	1.32	0.83
Al_2O3	(%)	ICP-OES	0.01%	10.9	15	15.4	16.2	16.3	15.6	17.2	15.9	15.2
Fe_2O_3	(%)	ICP-OES	0.01%	8.14	7.78	11.8	9.17	11.5	14	10.6	11.8	12.8
MnO	(%)	ICP-OES	0.01%	0.19	0.15	0.19	0.13	0.18	0.15	0.14	0.18	0.1
MgO	(%)	ICP-OES	0.01%	4.32	5	4.55	6.61	2.63	5.23	3.6	3.64	3.11
CaO	(%)	ICP-OES	0.01%	9.55	8.4	9.54	10.2	7.15	7.61	7.14	7.71	3.25
Na_2O	(%)	ICP-OES	0.01%	0.24	0.3	1.14	2.62E+00	3.39	2.9	3.57	3.65E+00	2.59
K_2O	(%)	ICP-OES	0.01%	3.82	4.66	2.99	0.22	0.71	0.44	1.02	0.63	3.57
P_2O_5	(%)	ICP-OES	0.01%	0.22	0.17	0.23	0.03	0.5	0.65	0.16	0.4	0.21
LOI	(%)	ICP-OES	0.10%	1.4	2	1.2	0.6	0.4	0.8	1.1	0.7	0.4
SUM	(%)	ICP-OES	0.10%	99.8	99.85	100.66	100.12	99.86	100.59	99.9	99.73	99.06
Ag	(ppm)	ICP-MS	0.1 ppm	1.1	1.5	0.4	0.7	0.8	0.6	0.5	0.3	0.6
As	(ppm)	ICP-MS	0.1 ppm	58.3	24.9	0.05	2.6	1.8	3.1	2.5	1.7	1.8
Ba	(ppm)	ICP-MS	1 ppm	630	499	914	59	269	190	489	198	1910
Be	(ppm)	ICP-MS	0.1 ppm	9	9.4	0.05	8.3	8.4	7.5	8.7	9.1	8.4
Bi	(ppm)	ICP-MS	0.1 ppm	0.05	0.05	0.05	0.05	0.05	0.05	0.05	0.05	0.05
C	(ppm)	ICP-MS	0.01 ppm	-	-	-	0.01	0.08	0.04	-	-	0.03
Cd	(ppm)	ICP-MS	0.1 ppm	1	1	0.1	0.3	0.4	0.3	0.2	0.4	0.2
Ce	(ppm)	ICP-MS	1 ppm	19	33	32	33	36	48	24	41	46
Co	(ppm)	ICP-MS	0.1 ppm	21.5	31.6	30.2	33	21.3	32.4	37.1	30.5	29.1
Cr	(ppm)	ICP-OES	2 ppm	278	185	60	19	10	6	36	14	22
Cs	(ppm)	ICP-MS	0.1 ppm	0.5	0.8	0.05	0.5	0.5	0.3	11.9	0.7	1.8
Cu	(ppm)	ICP-MS	0.1 ppm	24.8	43.2	16	40	26.6	42	105	62.9	290
Dy	(ppm)	ICP-MS	0.01 ppm	2.87	3.66	5.43	2.65	5.74	6.88	4.45	5.34	3.93
Er	(ppm)	ICP-MS	0.01 ppm	1.62	2.04	3.57	1.2	2.59	3.38	2.79	2.57	2.2
Eu	(ppm)	ICP-MS	0.01 ppm	1.12	1.4	1.32	0.78	1.82	2.09	1.17	1.87	1.75
Ga	(ppm)	ICP-MS	0.1 ppm	10.4	15.6	18.3	15.1	18.5	21.3	15.1	15.8	18.1
Gd	(ppm)	ICP-MS	0.01 ppm	3	4.36	5.4	2.39	5.16	5.59	3.99	4.73	3.83
Ge	(ppm)	ICP-MS	0.1 ppm	0.05	0.05	0.5	1	1	1.3	0.05	0.05	0.6
Hf	(ppm)	ICP-MS	0.1 ppm	1.6	2.9	3.7	1.2	2.3	2.9	2.4	3.1	3.1
Hg	(ppm)	ICP-MS	0.1 ppm	0.05	0.05	0.05	0.1	0.4	0.2	1.6	0.6	0.05
Ho	(ppm)	ICP-MS	0.01 ppm	0.61	0.86	1.21	0.56	1.23	1.46	1.18	1.13	0.92
La	(ppm)	ICP-MS	1 ppm	16	20	12	15	16	20	13	22	22
Lu	(ppm)	ICP-MS	0.01 ppm	0.27	0.35	0.55	0.28	0.58	0.6	0.57	0.33	0.46
Mo	(ppm)	ICP-MS	0.1 ppm	3.3	3.1	0.05	1.2	1.9	1.6	2.2	2	1.9
Nb	(ppm)	ICP-MS	1 ppm	8	7	2	3	6	6	9	12	4
Nd	(ppm)	ICP-MS	0.1 ppm	12.7	20.1	19.7	15.5	22.6	26.4	15.1	27	23
Ni	(ppm)	ICP-MS	1 ppm	84	78	39	38	8	1	24	15	14
Pb204	(ppm)	ICP-MS	0.01 ppm	0.652	1.18	0.091	0.131	0.1	5.00E-04	0.128	0.122	0.115
Pb206	(ppm)	ICP-MS	0.02 ppm	8.81	15.6	1.46	1.58	0.907	0.462	1.15	0.774	1.05
Pb207	(ppm)	ICP-MS	0.02 ppm	8.97	16.8	1.47	1.41	0.724	0.541	1.12	0.666	0.712
Pb208	(ppm)	ICP-MS	0.02 ppm	20	38.2	3.45	3.39	1.82	1.02	2.67	1.75	1.74
PbSUM	(ppm)	ICP-MS	0.02 ppm	38.4	71.7	6.47	6.51	3.55	1.98	5.07	3.31	3.62
Pr	(ppm)	ICP-MS	0.01 ppm	2.81	4.63	4.25	4.56	4.99	6.14	3	6.09	5.96
Rb	(ppm)	ICP-MS	0.1 ppm	74	89.3	49.2	3.4	17.1	7.7	33.8	11.4	79.4
S	(ppm)	ICP-MS	0.01 ppm	-	-	-	0.01	0.07	0.26	-	-	0.11
Sb	(ppm)	ICP-MS	1 ppm	4	4	0.5	0.5	0.5	0.5	4	3	0.5
Sc	(ppm)	ICP-OES	2 ppm	16	20	27	29	22	29	25	28	22
Se	(ppm)	ICP-MS	1 ppm	0.5	1	6	6	19	11	11	9	17
Sm	(ppm)	ICP-MS	0.01 ppm	2.78	4.43	4.35	2.43	5.01	6.37	3.65	4.74	4.51
Sn	(ppm)	ICP-MS	0.1 ppm	0.9	1	0.05	1.6	2	4.8	1.4	1.4	2.4
Sr	(ppm)	ICP-MS	1 ppm	180	215	198	229	374	294	383	392	114
Ta	(ppm)	ICP-MS	0.01 ppm	0.11	0.5	0.19	0.29	0.74	0.65	0.16	0.48	0.46
Tb	(ppm)	ICP-MS	0.01 ppm	0.38	0.48	0.74	0.4	0.89	1.06	0.57	0.63	0.64
Te	(ppm)	ICP-MS	0.1 ppm	0.2	0.1	0.05	0.05	0.05	0.05	0.05	0.05	0.05
Th	(ppm)	ICP-MS	0.01 ppm	0.63	1.72	6.94	1.07	1.27	6.68	2.53	2.29	3.77
Tm	(ppm)	ICP-MS	0.01 ppm	0.3	0.3	0.52	0.23	0.49	0.5	0.53	0.42	0.34
U	(ppm)	ICP-MS	0.01 ppm	4.35	5.59	0.8	0.87	0.7	3.73	1.6	1.23	2.28
V	(ppm)	ICP-OES	2 ppm	149	194	294	175	118	330	234	225	188
W	(ppm)	ICP-MS	1 ppm	19	10	1	2	2	1	0.5	0.5	6
Y	(ppm)	ICP-MS	0.01 ppm	15.9	19	30.2	14.9	33.1	42	27.7	26.6	24.5
Yb	(ppm)	ICP-MS	0.01 ppm	1.96	2.38	3.25	1.31	3.12	3.29	3.5	2.82	2.21
Zn	(ppm)	ICP-MS	1 ppm	153	231	100	88	118	103	121	134	133
Zr	(ppm)	ICP-MS	2 ppm	50	101	140	43	84	114	89	112	101

Table B ICP-OES and ICP-MS lithogeochemical results of Fisher property rocks.

Sample ID				CO-2019-53	CO-2019-59	CO-2019-62	CO-2019-65	CO-2019-61	CO-2019-63	CO-2019-64	CO-2019-66	CO-2019-36
Hole ID				FIS-19-035	FIS-19-030	FIS-19-030	FIS-18-024	FIS-19-030	FIS-18-024	FIS-18-024	FIS-18-024	FIS-18-023
Depth (m)				102	136.6	141.2	29.4	139.1	28.2	28.5	30.6	78.1
UTM Zone 13N Northing				6161455.94	6160680.73	6160680.73	6160492	6160680.73	6160492	6160492	6160492	6160271
UTM Zone 13N Easting				603981.747	604132.674	604132.674	604123	604132.674	604123	604123	604123	604154
Lithology				LCrB	LCrB	LCrB	LCrB	LCrB	LCrB	LCrB	LCrB	MVCL
Alteration Intensity				M	M	M	M	H	H	H	H	M
			Detection Limit									
SiO_2	(%)	ICP-OES	0.10%	52	55.7	51.8	51.8	55.5	55.2	52.8	51.3	48.8
TiO_2	(%)	ICP-OES	0.01%	0.83	1.27	2.75	1.84	1.07	1.06	1.15	1.87	1.07
Al_2O3	(%)	ICP-OES	0.01%	18.8	17.2	15.5	14.7	16.2	14.7	17	14.7	16.5
Fe_2O_3	(%)	ICP-OES	0.01%	11.2	10.2	12.3	13.4	9.2	9.83	11	13.3	12.3
MnO	(%)	ICP-OES	0.01%	0.17	0.16	0.22	0.16	0.16	0.15	0.11	0.16	0.15
MgO	(%)	ICP-OES	0.01%	3.35	2.73	2.68	4.19	2.36	4.11	3.23	4.31	8.08
CaO	(%)	ICP-OES	0.01%	9.21	6.08	7.28	8.91	6.83	9	6.92	7.82	10.1
Na_2O	(%)	ICP-OES	0.01%	2.22	4.51	3.17	3.28	2.48	2.03	2.39	4.33	2.63
K_2O	(%)	ICP-OES	0.01%	1.27	0.92	2.19	0.98	4.33	2.56	3.32	0.93	0.12
P_2O_5	(%)	ICP-OES	0.01%	0.14	0.54	0.79	0.49	0.46	0.26	0.31	0.45	0.07
LOI	(%)	ICP-OES	0.10%	0.6	0.6	1.3	0.5	1	0.9	1.3	0.7	0.6
SUM	(%)	ICP-OES	0.10%	99.79	99.91	99.98	100.25	99.59	99.8	99.53	99.87	100.42
Ag	(ppm)	ICP-MS	0.1 ppm	0.3	0.4	0.6	0.2	0.4	0.4	0.3	0.3	0.5
As	(ppm)	ICP-MS	0.1 ppm	3.4	3.1	3.5	2.3	2.8	1.5	2.2	1.9	1.9
Ba	(ppm)	ICP-MS	1 ppm	726	243	696	174	761	578	757	161	41
Be	(ppm)	ICP-MS	0.1 ppm	9.2	10.3	9.6	10.2	9.6	9.2	10.8	9.7	8
Bi	(ppm)	ICP-MS	0.1 ppm	0.05	0.05	0.7	0.05	0.2	0.05	0.05	0.05	0.05
C	(ppm)	ICP-MS	0.01 ppm	-	-	-	-	-	-	-	-	0.02
Cd	(ppm)	ICP-MS	0.1 ppm	0.2	0.05	0.7	0.05	0.05	0.4	0.2	0.05	0.4
Ce	(ppm)	ICP-MS	1 ppm	26	41	59	33	72	31	24	36	86
Co	(ppm)	ICP-MS	0.1 ppm	31.7	22.1	19.3	33.8	25	28.1	40	34.3	50
Cr	(ppm)	ICP-OES	2 ppm	38	5	1	2	4	52	48	1	224
Cs	(ppm)	ICP-MS	0.1 ppm	6.4	0.7	1.4	2.4	2.4	1	2.1	1.9	0.1
Cu	(ppm)	ICP-MS	0.1 ppm	66	19.2	113	749	81.2	84.5	17.8	37.7	61.1
Dy	(ppm)	ICP-MS	0.01 ppm	4.34	4.81	9.56	4.47	4.54	3.97	4.1	5.03	2.62
Er	(ppm)	ICP-MS	0.01 ppm	3.11	2.57	5.89	2.85	2.65	2.71	2.35	2.63	1.12
Eu	(ppm)	ICP-MS	0.01 ppm	1.01	2.14	2.31	1.53	2.14	1.23	1.09	1.65	0.97
Ga	(ppm)	ICP-MS	0.1 ppm	15.2	16.2	19.1	16	15.9	13.8	16.4	17.3	15.4
Gd	(ppm)	ICP-MS	0.01 ppm	3.35	6.13	10.1	5	5.7	4.18	4.46	5.44	2.23
Ge	(ppm)	ICP-MS	0.1 ppm	0.05	0.05	0.05	0.05	0.05	0.05	0.05	0.05	0.8
Hf	(ppm)	ICP-MS	0.1 ppm	1.9	2.6	23.1	3.2	3.2	3.1	3.1	2.9	1.2
Hg	(ppm)	ICP-MS	0.1 ppm	0.05	0.2	0.9	0.05	0.05	0.2	0.05	0.05	0.4
Ho	(ppm)	ICP-MS	0.01 ppm	1.18	1.11	2.4	1.23	1	1.12	0.85	1.14	0.54
La	(ppm)	ICP-MS	1 ppm	14	22	29	18	40	16	12	19	3
Lu	(ppm)	ICP-MS	0.01 ppm	0.52	0.34	0.94	0.51	0.33	0.38	0.38	0.4	0.19
Mo	(ppm)	ICP-MS	0.1 ppm	2	2.4	3.2	0.9	2.1	1.6	1.3	0.9	1.2
Nb	(ppm)	ICP-MS	1 ppm	9	12	24	10	10	9	9	9	2
Nd	(ppm)	ICP-MS	0.1 ppm	13.7	24.4	41.8	22.4	38.9	19.4	17	24.6	7.7
Ni	(ppm)	ICP-MS	1 ppm	13	7	5	0.5	7	52	58	0.5	178
Pb204	(ppm)	ICP-MS	0.01 ppm	0.079	0.061	0.044	0.038	0.071	3.20E-02	0.033	0.091	3.60E-02
Pb206	(ppm)	ICP-MS	0.02 ppm	1.21	1.12	0.838	0.69	1.24	0.838	0.738	1	0.493
Pb207	(ppm)	ICP-MS	0.02 ppm	0.98	0.971	0.662	0.836	0.862	0.75	0.694	0.909	0.539
Pb208	(ppm)	ICP-MS	0.02 ppm	2.56	2.39	2.05	1.67	2.23	1.9	1.6	1.94	1.14
PbSUM	(ppm)	ICP-MS	0.02 ppm	4.82	4.54	3.6	3.23	4.4	3.52	3.07	3.95	2.2
Pr	(ppm)	ICP-MS	0.01 ppm	3	5.49	8.55	4.83	9.28	4.2	3.32	4.89	1.77
Rb	(ppm)	ICP-MS	0.1 ppm	32.8	16.2	45.5	13.9	76	44.3	72.1	13.7	0.8
S	(ppm)	ICP-MS	0.01 ppm	-	-	-	-	-	-	-	-	0.09
Sb	(ppm)	ICP-MS	1 ppm	3	3	3	3	3	3	3	6	0.5
Sc	(ppm)	ICP-OES	2 ppm	32	19	22	30	18	24	26	33	22
Se	(ppm)	ICP-MS	1 ppm	0.5	0.5	0.5	35	11	0.5	2	0.5	4
Sm	(ppm)	ICP-MS	0.01 ppm	3.19	5.59	9.3	4.77	6.77	4.85	3.9	4.82	2.22
Sn	(ppm)	ICP-MS	0.1 ppm	1.4	1.4	2.2	1.2	1.4	1.4	1.6	1.6	1.2
Sr	(ppm)	ICP-MS	1 ppm	274	507	280	293	279	236	247	379	447
Ta	(ppm)	ICP-MS	0.01 ppm	0.19	0.45	1.2	0.29	0.3	0.24	0.26	0.22	0.19
Tb	(ppm)	ICP-MS	0.01 ppm	0.5	0.6	1.3	0.73	0.59	0.61	0.53	0.66	0.41
Te	(ppm)	ICP-MS	0.1 ppm	0.05	0.05	0.4	0.05	0.2	0.4	0.1	0.1	0.2
Th	(ppm)	ICP-MS	0.01 ppm	2.53	2.18	2.69	1.54	2.42	1.64	1.52	1.94	15.6
Tm	(ppm)	ICP-MS	0.01 ppm	0.54	0.44	0.98	0.47	0.48	0.42	0.41	0.45	0.24
U	(ppm)	ICP-MS	0.01 ppm	3.87	2.29	3.13	1.7	1.31	1.21	1.38	1.43	0.6
V	(ppm)	ICP-OES	2 ppm	281	115	153	327	86	228	251	375	222
W	(ppm)	ICP-MS	1 ppm	0.5	6	7	4	12	3	0.5	0.5	0.5
Y	(ppm)	ICP-MS	0.01 ppm	27.3	26.9	57	27.2	25.1	26	21.4	27.8	14.3
Yb	(ppm)	ICP-MS	0.01 ppm	3.78	2.78	7.45	3.02	2.74	2.86	2.8	3.28	1.18
Zn	(ppm)	ICP-MS	1 ppm	134	128	122	115	85	91	109	120	138
Zr	(ppm)	ICP-MS	2 ppm	57	116	882	99	111	107	97	86	41

Table B ICP-OES and ICP-MS lithogeochemical results of Fisher property rocks.

Sample ID				CO-2019-06	CO-2019-11	CO-2019-13	CO-2019-14	CO-2019-57	CO-2019-04	CO-2019-07	CO-2019-76	CO-2019-78
Hole ID				FIS-18-003	FIS-18-016	FIS-18-016	FIS-18-016	FIS-19-035	FIS-18-003	FIS-18-003	FIS-18-020	FIS-18-020
Depth (m)				238.7	157.3	379.5	514.2	108.35	171.3	343.5	182.5	184.86
UTM Zone 13N Northing				6167042	6165130	6165130	6165130	6161456	6167042	6167042	6160271	6160271
UTM Zone 13N Easting				601196	602156	602156	602156	603982	601196	601196	604154	604154
Lithology				AND1	AND1	AND1	AND1	AND1	AND1	AND1	AND1	AND1
Alteration Intensity				L	L	L	L	L	M	M	H	H
			Detection Limit									
SiO_2	(%)	ICP-OES	0.10%	57.3	62.7	57.8	55.8	58.8	63.4	52.1	60.3	54.8
TiO_2	(%)	ICP-OES	0.01%	0.74	0.43	0.4	0.78	0.92	0.59	1.21	0.62	0.72
Al_2O3	(%)	ICP-OES	0.01%	15.7	14.4	14.9	16.6	14.4	14.7	17.2	15.8	16.1
Fe_2O_3	(%)	ICP-OES	0.01%	7.62	6.88	8.52	8.63	10	7.33	10	6.52	7.96
MnO	(%)	ICP-OES	0.01%	0.11	0.12	0.14	0.12	0.15	0.12	0.11	0.1	0.16
MgO	(%)	ICP-OES	0.01%	4.57	3.1	5.26	3.65	3.36	1.67	3.68	3.57	4.56
CaO	(%)	ICP-OES	0.01%	7.21	5.91	8.01	7.74	6.16	3.9	6.02	6.4	7.28
Na_2O	(%)	ICP-OES	0.01%	3.95	3.32	2.77	3.16	3.58	4.31	4.2	0.4	0.41
K_2O	(%)	ICP-OES	0.01%	1.43	1.95	1.24	2.43	1.29	3.19	3.15	4.99	3.58
P_2O_5	(%)	ICP-OES	0.01%	0.15	0.05	0.04	0.17	0.23	0.21	0.7	0.16	0.16
LOI	(%)	ICP-OES	0.10%	1.5	1.6	0.9	0.8	1	0.4	1.7	1.3	4
SUM	(%)	ICP-OES	0.10%	100.28	100.46	99.98	99.88	99.89	99.82	100.07	100.16	99.73
Ag	(ppm)	ICP-MS	0.1 ppm	1.8	0.9	1.3	0.8	0.6	1.9	1.9	2.5	0.5
As	(ppm)	ICP-MS	0.1 ppm	2.4	3.4	2.7	2.1	2.2	2.6	7.5	77.3	45.4
Ba	(ppm)	ICP-MS	1 ppm	566	785	757	634	420	959	889	387	1600
Be	(ppm)	ICP-MS	0.1 ppm	9	7.3	8.2	9.1	9.8	7.6	8.6	9.2	10.6
Bi	(ppm)	ICP-MS	0.1 ppm	0.2	0.1	0.1	0.2	0.6	0.4	0.3	0.05	0.05
C	(ppm)	ICP-MS	0.01 ppm	0.14	0.21	0.04	0.05	-	0.07	0.02	-	-
Cd	(ppm)	ICP-MS	0.1 ppm	0.5	0.4	0.2	0.3	0.4	0.2	0.3	0.2	0.6
Ce	(ppm)	ICP-MS	1 ppm	49	21	15	37	44	36	111	36	38
Co	(ppm)	ICP-MS	0.1 ppm	23.8	19.3	29.8	25	26.6	14.6	25.7	25.2	20.9
Cr	(ppm)	ICP-OES	2 ppm	98	70	170	137	56	21	38	107	138
Cs	(ppm)	ICP-MS	0.1 ppm	1.6	2.4	2.1	5.9	5.4	2.4	5.1	0.6	1
Cu	(ppm)	ICP-MS	0.1 ppm	23.6	4.6	46.8	54.2	408	210	116	87.6	5.8
Dy	(ppm)	ICP-MS	0.01 ppm	3.15	2.56	1.89	4.63	5.48	3.78	5.36	3.49	3.73
Er	(ppm)	ICP-MS	0.01 ppm	1.23	1.25	1.1	1.98	3.26	2.09	2.31	1.7	2.06
Eu	(ppm)	ICP-MS	0.01 ppm	1.68	0.76	0.67	1.47	1.48	1.1	2.54	1.31	1.49
Ga	(ppm)	ICP-MS	0.1 ppm	17.5	13.8	12.8	17	14.5	16.2	18.6	16.3	16
Gd	(ppm)	ICP-MS	0.01 ppm	4	2.1	1.61	3.76	5.58	3.19	6.95	3.69	4.94
Ge	(ppm)	ICP-MS	0.1 ppm	1.3	1	1.1	1.4	0.05	1.3	0.8	0.05	0.05
Hf	(ppm)	ICP-MS	0.1 ppm	2.8	1.9	1.5	3.4	4.4	3.3	5.1	3.2	3.2
Hg	(ppm)	ICP-MS	0.1 ppm	0.05	0.05	0.05	0.05	0.05	0.05	0.05	0.05	0.05
Ho	(ppm)	ICP-MS	0.01 ppm	0.62	0.55	0.47	1.03	1.3	0.87	1.25	0.62	0.85
La	(ppm)	ICP-MS	1 ppm	21	9	8	18	22	16	50	18	20
Lu	(ppm)	ICP-MS	0.01 ppm	0.24	0.28	0.28	0.47	0.53	0.4	0.41	0.27	0.4
Mo	(ppm)	ICP-MS	0.1 ppm	1.4	1.3	1.6	5.1	2.1	1.5	2.5	1	2.8
Nb	(ppm)	ICP-MS	1 ppm	4	3	1	4	10	5	14	9	10
Nd	(ppm)	ICP-MS	0.1 ppm	23.4	11	7.5	19.4	24	18	52.2	21.4	23.6
Ni	(ppm)	ICP-MS	1 ppm	36	17	30	54	30	10	24	50	60
Pb204	(ppm)	ICP-MS	0.01 ppm	0.113	0.046	0.235	0.141	0.078	0.271	0.223	1.83	1.56E+00
Pb206	(ppm)	ICP-MS	0.02 ppm	1.68	1.64	1.55	1.53	1.31	2.5	3.22	25.6	20.7
Pb207	(ppm)	ICP-MS	0.02 ppm	1.2	1.09	1.36	1.15	0.962	1.86	2.51	27.2	21.7
Pb208	(ppm)	ICP-MS	0.02 ppm	2.88	3.12	2.96	3.1	2.45	4.38	5.33	60.6	49.3
PbSUM	(ppm)	ICP-MS	0.02 ppm	5.87	5.89	6.11	5.92	4.8	9	11.3	115	93.2
Pr	(ppm)	ICP-MS	0.01 ppm	6.26	2.87	1.96	5.02	5.74	4.65	13.5	5.07	5.39
Rb	(ppm)	ICP-MS	0.1 ppm	60.9	33.9	39.4	91.3	27.2	86.9	101	92.4	95.4
S	(ppm)	ICP-MS	0.01 ppm	0.05	<0.01	0.01	0.1	-	0.02	0.51	-	-
Sb	(ppm)	ICP-MS	1 ppm	1	1	1	1	3	2	3	3	4
Sc	(ppm)	ICP-OES	2 ppm	17	17	25	22	19	12	17	15	17
Se	(ppm)	ICP-MS	1 ppm	0.5	10	13	4	0.5	17	5	7	0.5
Sm	(ppm)	ICP-MS	0.01 ppm	5.01	2.05	1.38	4.66	5.98	3.83	8.76	3.83	4.27
Sn	(ppm)	ICP-MS	0.1 ppm	5.8	4.6	1.8	1.7	25.5	2.5	2.5	1.1	1.3
Sr	(ppm)	ICP-MS	1 ppm	652	278	305	347	335	295	656	198	244
Ta	(ppm)	ICP-MS	0.01 ppm	0.48	0.45	0.36	0.52	0.41	0.57	1.21	0.28	0.48
Tb	(ppm)	ICP-MS	0.01 ppm	0.48	0.37	0.26	0.68	0.7	0.59	0.9	0.43	0.48
Te	(ppm)	ICP-MS	0.1 ppm	0.05	0.8	0.2	0.05	0.05	0.05	0.05	0.05	0.05
Th	(ppm)	ICP-MS	0.01 ppm	3.72	4.06	3.11	3.06	3.28	5.95	7.94	1.89	2.15
Tm	(ppm)	ICP-MS	0.01 ppm	0.25	0.22	0.18	0.44	0.47	0.32	0.46	0.24	0.36
U	(ppm)	ICP-MS	0.01 ppm	2	2.28	5.04	1.48	1.76	2.9	5.11	2.27	3.73
V	(ppm)	ICP-OES	2 ppm	161	123	170	164	184	70	189	144	158
W	(ppm)	ICP-MS	1 ppm	13	10	9	10	9	14	13	6	6
Y	(ppm)	ICP-MS	0.01 ppm	18.1	15.9	11.6	27.3	31.1	24.4	32.6	16.7	23.6
Yb	(ppm)	ICP-MS	0.01 ppm	1.62	1.5	1.18	2.39	3.85	2.4	2.84	1.71	2.56
Zn	(ppm)	ICP-MS	1 ppm	104	75	91	113	134	96	126	252	187
Zr	(ppm)	ICP-MS	2 ppm	99	65	53	120	146	119	217	109	116

Table B ICP-OES and ICP-MS lithogeochemical results of Fisher property rocks.

Sample ID				CO-2019-12	CO-2019-130	CO-2019-18	CO-2019-19	CO-2019-127	CO-2019-20	CO-2019-67	CO-2019-05	CO-2019-23
Hole ID				FIS-18-016	Surface	FIS-18-017	FIS-18-017	Surface	FIS-18-017	FIS-18-024	FIS-18-003	FIS-18-018
Depth (m)				286.1	-	526	623.5	-	673.5	32.7	214.4	186.3
UTM Zone 13N Northing				6165130	6161318	6162978	6162978	6161365	6162978	6160492	6167042	6163905
UTM Zone 13N Easting				602156	604561	603370	603370	604096	603370	604123	601195.9	602798
Lithology				AND2	AND2	AND2	AND2	AND2	FV	FV	BSCH	BSCH
Alteration Intensity				L	L	L	L	M	L	L	L	L
			Detection Limit									
SiO_2	(%)	ICP-OES	0.10%	62.3	58.6	55.4	64.6	61.5	75.3	72.5	50.3	53.8
TiO_2	(%)	ICP-OES	0.01%	0.61	0.76	0.55	0.46	0.44	0.29	0.24	0.51	0.57
Al_2O3	(%)	ICP-OES	0.01%	17.3	15.9	19	15.2	16.4	13.3	14.5	14.7	15.8
Fe_2O_3	(%)	ICP-OES	0.01%	6.12	7.89	7.92	4.92	6.57	1.59	2.74	10.6	11
MnO	(%)	ICP-OES	0.01%	0.06	0.11	0.09	0.13	0.11	0.03	0.02	0.14	0.24
MgO	(%)	ICP-OES	0.01%	2.48	3.82	3.33	2.65	2.02	0.62	0.61	9.31	6.39
CaO	(%)	ICP-OES	0.01%	3.59	6.55	5	4.67	5.24	1.64	2.17	5.74	8.53
Na_2O	(%)	ICP-OES	0.01%	3.98	3.34	4.73	3.44	2.56	3.25	4.59	2.46	2.01
K_2O	(%)	ICP-OES	0.01%	2.82	1.69	2.27	3.21	2.31	3.64	1.47	2.93	0.83
P_2O_5	(%)	ICP-OES	0.01%	0.12	0.2	0.55	0.11	0.12	0.005	0.05	0.07	0.07
LOI	(%)	ICP-OES	0.10%	0.7	0.8	1.3	1	2	0.8	0.9	2.7	1
SUM	(%)	ICP-OES	0.10%	100.08	99.66	100.14	100.39	99.27	100.46	99.79	99.46	100.24
Ag	(ppm)	ICP-MS	0.1 ppm	0.8	0.05	0.8	0.7	0.05	1	0.3	1.8	0.6
As	(ppm)	ICP-MS	0.1 ppm	2.1	0.05	4.4	3.2	0.05	1.8	9	2.5	2.9
Ba	(ppm)	ICP-MS	1 ppm	1740	632	329	1100	411	1120	930	513	521
Be	(ppm)	ICP-MS	0.1 ppm	8.3	1.8	8.4	8.7	0.05	10.1	10.5	13.5	7.7
Bi	(ppm)	ICP-MS	0.1 ppm	0.4	0.05	0.6	0.2	0.05	0.1	0.05	0.4	0.5
C	(ppm)	ICP-MS	0.01 ppm	0.03	-	0.1	0.14	-	0.1	-	0.09	0.06
Cd	(ppm)	ICP-MS	0.1 ppm	0.3	0.3	0.5	0.5	0.05	0.4	0.5	0.2	0.3
Ce	(ppm)	ICP-MS	1 ppm	55	49	76	46	41	145	47	13	18
Co	(ppm)	ICP-MS	0.1 ppm	21.7	24.5	22	13.9	26.5	1.6	6	39.4	34.9
Cr	(ppm)	ICP-OES	2 ppm	7	115	7	98	32	10	8	475	231
Cs	(ppm)	ICP-MS	0.1 ppm	4	0.5	60.9	7.3	1.6	3.7	1.2	28.6	2.4
Cu	(ppm)	ICP-MS	0.1 ppm	415	40.2	100	3.3	90.7	14.6	49.7	354	70.9
Dy	(ppm)	ICP-MS	0.01 ppm	5.04	5.36	3.89	2.29	3.25	10.9	2.75	1.92	2.46
Er	(ppm)	ICP-MS	0.01 ppm	2.66	3.77	1.87	1.35	2.86	5.17	1.78	0.9	1.38
Eu	(ppm)	ICP-MS	0.01 ppm	1.35	1.24	1.91	1.06	0.93	2.28	0.92	0.6	0.99
Ga	(ppm)	ICP-MS	0.1 ppm	16.7	20.8	18.3	15.3	17.2	18.9	12.2	17.6	15
Gd	(ppm)	ICP-MS	0.01 ppm	4.47	5.2	4.63	1.83	3.61	10.4	3.01	1.65	2.01
Ge	(ppm)	ICP-MS	0.1 ppm	1.6	0.3	1	0.8	0.2	2.3	0.05	1.5	1.6
Hf	(ppm)	ICP-MS	0.1 ppm	4.7	4.9	3.8	3.6	2.8	8.1	4.6	1.2	1.4
Hg	(ppm)	ICP-MS	0.1 ppm	0.05	0.05	0.05	0.05	0.05	0.05	0.8	0.05	0.05
Ho	(ppm)	ICP-MS	0.01 ppm	1.05	1.1	0.86	0.46	0.79	2.16	0.78	0.46	0.57
La	(ppm)	ICP-MS	1 ppm	27	22	37	25	19	66	30	5	8
Lu	(ppm)	ICP-MS	0.01 ppm	0.6	0.61	0.36	0.3	0.56	1.01	0.35	0.26	0.33
Mo	(ppm)	ICP-MS	0.1 ppm	1.6	0.8	9.5	1.9	0.05	2	2.2	7.2	1.3
Nb	(ppm)	ICP-MS	1 ppm	7	5	6	5	2	13	10	3	2
Nd	(ppm)	ICP-MS	0.1 ppm	24	26.4	34.3	16.5	22.1	65.4	18.6	7.3	9.3
Ni	(ppm)	ICP-MS	1 ppm	4	66	12	38	14	5	10	172	58
Pb204	(ppm)	ICP-MS	0.01 ppm	0.121	0.05	0.133	0.047	0.1	0.026	0.094	0.126	0.201
Pb206	(ppm)	ICP-MS	0.02 ppm	1.61	1.15	1.58	1.31	2.55	1.02	2.76	1.01	2.35
Pb207	(ppm)	ICP-MS	0.02 ppm	0.792	1.16	1.09	0.946	2.45	0.521	1.29	0.859	2.11
Pb208	(ppm)	ICP-MS	0.02 ppm	1.8	2.78	2.42	2.6	5.67	1.42	3.52	1.88	4.67
PbSUM	(ppm)	ICP-MS	0.02 ppm	4.33	5.14	5.22	4.9	10.8	2.99	7.66	3.88	9.34
Pr	(ppm)	ICP-MS	0.01 ppm	6.83	6.71	9.44	4.82	5.32	18.3	5.37	1.71	2.4
Rb	(ppm)	ICP-MS	0.1 ppm	66.9	42.4	461	88.1	61.3	64.4	43.3	730	22.8
S	(ppm)	ICP-MS	0.01 ppm	0.05	-	0.36	<0.01	-	<0.01	-	2.46	0.08
Sb	(ppm)	ICP-MS	1 ppm	1	0.5	1	1	0.5	1	5	1	1
Sc	(ppm)	ICP-OES	2 ppm	13	18	8	10	19	6	4	33	32
Se	(ppm)	ICP-MS	1 ppm	2	5	2	0.5	4	4	0.5	7	0.5
Sm	(ppm)	ICP-MS	0.01 ppm	5.11	5.77	5.22	2.67	4.22	12.4	4.19	1.7	2.35
Sn	(ppm)	ICP-MS	0.1 ppm	1.4	0.2	1.8	1.6	0.05	3.5	0.9	19.2	4.5
Sr	(ppm)	ICP-MS	1 ppm	137	332	465	279	140	102	195	249	392
Ta	(ppm)	ICP-MS	0.01 ppm	0.79	0.47	0.7	0.65	0.22	1.58	0.66	0.34	0.18
Tb	(ppm)	ICP-MS	0.01 ppm	0.74	0.66	0.66	0.38	0.44	1.55	0.39	0.31	0.39
Te	(ppm)	ICP-MS	0.1 ppm	0.05	0.05	0.2	0.2	0.05	0.05	0.05	0.4	0.4
Th	(ppm)	ICP-MS	0.01 ppm	6.67	4.86	5.7	11.9	5.23	10.1	12.4	2.51	1.77
Tm	(ppm)	ICP-MS	0.01 ppm	0.43	0.58	0.33	0.25	0.45	0.85	0.29	0.15	0.2
U	(ppm)	ICP-MS	0.01 ppm	3.42	1.88	2.32	3.47	1.45	2.72	5.22	0.74	0.81
V	(ppm)	ICP-OES	2 ppm	21	120	97	82	124	1	31	232	235
W	(ppm)	ICP-MS	1 ppm	10	0.5	7	6	0.5	6	0.5	14	3
Y	(ppm)	ICP-MS	0.01 ppm	31.5	32.4	25.7	14.7	24.5	58.5	19.6	12	16.4
Yb	(ppm)	ICP-MS	0.01 ppm	3.4	3.9	2.12	1.56	3.23	5.66	2.61	1.1	1.5
Zn	(ppm)	ICP-MS	1 ppm	62	55	78	111	100	48	48	135	157
Zr	(ppm)	ICP-MS	2 ppm	177	189	169	137	106	298	163	37	50

Table B ICP-OES and ICP-MS lithogeochemical results of Fisher property rocks.

Sample ID				CO-2019-117	CO-2019-124	CO-2019-126	CO-2019-29	CO-2019-21	CO-2019-30	CO-2019-31	CO-2019-37
Hole ID				Surface	Surface	Surface	FIS-18-028	FIS-18-017	FIS-18-028	FIS-18-022	FIS-18-023
Depth (m)				-	-	-	237.6	720	320.2	60.7	83.8
UTM Zone 13N Northing				6161835	6158451	6158355	6160239	6162978	6160239	6160406	6160271
UTM Zone 13N Easting				603854	605492	605040	604138	603370	604138	604183	604154
Lithology				VCLST	VCLST	VCLST	CSCH	GAB	GAB	GAB	GAB
Alteration Intensity				L	L	L	L	L	L	L	L
			Detection Limit								
SiO_2	(%)	ICP-OES	0.10%	68	68.4	69	46.9	52.3	48.2	50.6	51
TiO_2	(%)	ICP-OES	0.01%	0.34	0.42	0.4	0.91	1.97	1.32	0.72	1.32
Al_2O3	(%)	ICP-OES	0.01%	14.1	13.3	14.2	16.9	13.9	15.6	16.9	14.7
Fe_2O_3	(%)	ICP-OES	0.01%	5	6.86	6.42	11.3	13.8	13.4	9.16	12
MnO	(%)	ICP-OES	0.01%	0.1	0.12	0.1	0.15	0.13	0.18	0.12	0.15
MgO	(%)	ICP-OES	0.01%	1.04	0.9	0.73	9.31	4.28	6.9	7.22	6.12
CaO	(%)	ICP-OES	0.01%	2.96	2.17	1.56	9.85	7.63	8.9	11.8	9.09
Na_2O	(%)	ICP-OES	0.01%	2.24	3.74	3.37E+00	2.13	3.71	3	2.52	3.1
K_2O	(%)	ICP-OES	0.01%	3.66	2.58	3.66	1.01	0.95	0.51	0.17	0.38
P_2O_5	(%)	ICP-OES	0.01%	0.05	0.1	0.08	0.16	0.43	0.23	0.11	0.14
LOI	(%)	ICP-OES	0.10%	1.9	0.9	0.4	1.3	0.9	0.9	0.8	2
SUM	(%)	ICP-OES	0.10%	99.39	99.49	99.92	99.92	100	99.14	100.12	100
Ag	(ppm)	ICP-MS	0.1 ppm	0.05	0.05	0.05	0.7	0.9	1	0.5	0.9
As	(ppm)	ICP-MS	0.1 ppm	0.05	0.05	0.1	2.6	6.3	4.3	3	5.1
Ba	(ppm)	ICP-MS	1 ppm	835	1090	636	252	252	135	94	103
Be	(ppm)	ICP-MS	0.1 ppm	2.1	1	0.05	7.7	8.3	7.5	8.5	7.9
Bi	(ppm)	ICP-MS	0.1 ppm	0.05	0.05	0.05	0.05	0.05	0.2	0.05	0.05
C	(ppm)	ICP-MS	0.01 ppm	-	-	-	0.05	0.04	0.05	0.07	0.3
Cd	(ppm)	ICP-MS	0.1 ppm	0.05	0.05	0.2	0.5	0.4	0.4	0.05	0.05
Ce	(ppm)	ICP-MS	1 ppm	54	58	52	16	43	20	14	16
Co	(ppm)	ICP-MS	0.1 ppm	3.6	5.1	2.6	50.9	33.1	44.5	38.4	42.3
Cr	(ppm)	ICP-OES	2 ppm	19	10	7	252	25	163	398	95
Cs	(ppm)	ICP-MS	0.1 ppm	1.6	0.4	0.8	1	3.1	0.5	0.5	0.7
Cu	(ppm)	ICP-MS	0.1 ppm	13.2	8.9	7.9	44.2	73.8	64	82.8	53.5
Dy	(ppm)	ICP-MS	0.01 ppm	6.47	7.65	7.22	2.67	6.73	4.34	2.73	3.09
Er	(ppm)	ICP-MS	0.01 ppm	5.38	5.62	4.53	1.36	3.58	2.16	1.24	1.64
Eu	(ppm)	ICP-MS	0.01 ppm	1.16	1.48	1.49	1.06	1.86	1.41	0.79	1.05
Ga	(ppm)	ICP-MS	0.1 ppm	16.6	18	17.2	14.2	18.6	16.7	15.4	17.2
Gd	(ppm)	ICP-MS	0.01 ppm	5.5	6.08	5.84	2.46	5.7	3.41	1.97	2.5
Ge	(ppm)	ICP-MS	0.1 ppm	0.3	0.4	0.4	0.9	1.4	1.2	1	1.1
Hf	(ppm)	ICP-MS	0.1 ppm	5.1	4	4.3	1.2	4.4	2.3	1.4	1.9
Hg	(ppm)	ICP-MS	0.1 ppm	0.05	0.05	0.05	0.2	0.05	0.05	0.1	0.05
Ho	(ppm)	ICP-MS	0.01 ppm	1.52	1.73	1.57	0.6	1.51	0.96	0.54	0.72
La	(ppm)	ICP-MS	1 ppm	29	28	22	6	19	7	6	7
Lu	(ppm)	ICP-MS	0.01 ppm	0.82	0.95	0.7	0.25	0.74	0.44	0.18	0.3
Mo	(ppm)	ICP-MS	0.1 ppm	1.5	0.1	0.05	1.2	1.6	1.6	1.7	1.5
Nb	(ppm)	ICP-MS	1 ppm	3	3	2	3	5	3	2	2
Nd	(ppm)	ICP-MS	0.1 ppm	28.4	30.6	31.2	10	23.8	13	8.5	10
Ni	(ppm)	ICP-MS	1 ppm	0.5	1	2	195	21	123	108	59
Pb204	(ppm)	ICP-MS	0.01 ppm	0.106	5.00E-04	0.092	0.134	0.176	0.232	0.147	1.15E-01
Pb206	(ppm)	ICP-MS	0.02 ppm	2.52	0.884	2.56	0.671	0.844	2.18	0.445	0.498
Pb207	(ppm)	ICP-MS	0.02 ppm	2.13	0.68	1.97	0.808	0.708	1.97	0.437	0.626
Pb208	(ppm)	ICP-MS	0.02 ppm	5.19	1.64	4.98	1.94	1.99	4.54	1.13	1.1
PbSUM	(ppm)	ICP-MS	0.02 ppm	9.95	3.21	9.61	3.56	3.72	8.93	2.16	2.33
Pr	(ppm)	ICP-MS	0.01 ppm	7.33	7.48	7.46	2.32	6.02	3.05	2.05	2.35
Rb	(ppm)	ICP-MS	0.1 ppm	77.8	35.6	64.1	21.6	17.3	10.2	1.5	5.9
S	(ppm)	ICP-MS	0.01 ppm	-	-	-	0.11	0.28	0.16	0.08	0.12
Sb	(ppm)	ICP-MS	1 ppm	0.5	0.5	0.5	0.5	3	1	1	1
Sc	(ppm)	ICP-OES	2 ppm	11	15	14	20	29	26	29	30
Se	(ppm)	ICP-MS	1 ppm	1	3	3	5	10	8	4	4
Sm	(ppm)	ICP-MS	0.01 ppm	5.63	6.36	7.1	2.24	5.72	3.46	2.12	2.46
Sn	(ppm)	ICP-MS	0.1 ppm	0.4	0.05	0.05	4.5	3	1	1	1.4
Sr	(ppm)	ICP-MS	1 ppm	124	218	57	424	422	464	408	412
Ta	(ppm)	ICP-MS	0.01 ppm	0.45	0.32	0.3	0.19	0.66	0.31	0.24	0.23
Tb	(ppm)	ICP-MS	0.01 ppm	0.89	1.07	0.89	0.44	1.1	0.73	0.42	0.47
Te	(ppm)	ICP-MS	0.1 ppm	0.05	0.05	0.05	0.05	0.05	2.1	0.05	0.05
Th	(ppm)	ICP-MS	0.01 ppm	12.7	5.98	5.95	0.56	2.13	0.61	0.59	0.67
Tm	(ppm)	ICP-MS	0.01 ppm	0.82	0.88	0.73	0.2	0.57	0.32	0.23	0.28
U	(ppm)	ICP-MS	0.01 ppm	3.04	1.04	1.43	0.73	1.52	0.7	0.57	0.63
V	(ppm)	ICP-OES	2 ppm	22	1	1	177	338	249	161	277
W	(ppm)	ICP-MS	1 ppm	2	0.5	0.5	1	6	2	0.5	0.5
Y	(ppm)	ICP-MS	0.01 ppm	42.2	48.2	37.8	15.8	40.6	25.8	14.8	20.5
Yb	(ppm)	ICP-MS	0.01 ppm	5.57	6.2	5.27	1.28	4.08	2.42	1.43	1.79
Zn	(ppm)	ICP-MS	1 ppm	82	42	120	145	114	138	91	102
Zr	(ppm)	ICP-MS	2 ppm	182	147	145	50	183	83	53	75

Table B ICP-OES and ICP-MS lithogeochemical results of Fisher property rocks.

Sample ID				CO-2019-81	CO-2019-82	CO-2019-125	CO-2019-132	CO-2019-80	CO-2019-83	CO-2019-85	CO-2019-84
Hole ID				FIS-18-021	FIS-18-021	Surface	Surface	FIS-18-021	FIS-18-021	FIS-18-021	FIS-18-021
Depth (m)				55.9	56.6	-	-	55.3	57.2	60.8	58.7
UTM Zone 13N Northing				6160271	6160271	6158362		6160271	6160271	6160271	6160271
UTM Zone 13N Easting				604154	604154	605300		604154	604154	604154	604154
Lithology				DIO	DIO	DIO	DIO	DIO	DIO	DIO	DIO
Alteration Intensity				L	L	L	L	M	M	M	H
			Detection Limit								
SiO_2	(%)	ICP-OES	0.10%	59.4	59.4	55.5	55.8	59.4	56.6	58	58.2
TiO_2	(%)	ICP-OES	0.01%	1.07	1.01	0.78	0.52	1.04	1.12	1	1.18
Al_2O3	(%)	ICP-OES	0.01%	15.5	15.5	17.3	15.6	16	16.3	15	15.8
Fe_2O_3	(%)	ICP-OES	0.01%	8.6	8.63	7.94	9.51	8.72	9.81	10.1	9.55
MnO	(%)	ICP-OES	0.01%	0.13	0.12	0.11	0.13	0.12	0.13	0.14	0.13
MgO	(%)	ICP-OES	0.01%	2.25	2.18	4.55	5.42	2.28	2.28	2.96	2.54
CaO	(%)	ICP-OES	0.01%	5.47	5.54	8	8.6	4.76	5.86	5.81	5.45
Na_2O	(%)	ICP-OES	0.01%	3.63	3.18	3.55	2.58	3.93	2.6	3.85	3.32
K_2O	(%)	ICP-OES	0.01%	2.23	2.75	1.43	0.95	1.93	3.51	1.31	2.15
P_2O_5	(%)	ICP-OES	0.01%	0.42	0.4	0.22	0.13	0.43	0.44	0.45	0.48
LOI	(%)	ICP-OES	0.10%	1.1	1.2	0.9	0.7	1.1	1.2	1.2	1
SUM	(%)	ICP-OES	0.10%	99.8	99.91	100.28	99.94	99.71	99.85	99.82	99.8
Ag	(ppm)	ICP-MS	0.1 ppm	0.4	0.3	0.4	0.05	0.3	0.4	0.3	0.2
As	(ppm)	ICP-MS	0.1 ppm	2.7	3.5	0.05	0.05	3.5	2.5	3.4	1.8
Ba	(ppm)	ICP-MS	1 ppm	560	685	486	617	520	929	374	527
Be	(ppm)	ICP-MS	0.1 ppm	9.6	11.8	0.05	0.05	10.3	10.2	10.3	9.3
Bi	(ppm)	ICP-MS	0.1 ppm	0.05	0.05	0.05	0.05	0.05	0.05	0.05	0.05
C	(ppm)	ICP-MS	0.01 ppm	-	-	-	-	-	-	-	-
Cd	(ppm)	ICP-MS	0.1 ppm	0.4	0.2	0.2	0.2	0.3	0.6	0.6	0.2
Ce	(ppm)	ICP-MS	1 ppm	43	44	38	26	47	43	45	41
Co	(ppm)	ICP-MS	0.1 ppm	17	18.9	27.5	31.7	17.8	18.8	26.6	23.6
Cr	(ppm)	ICP-OES	2 ppm	8	7	75	145	9	9	12	11
Cs	(ppm)	ICP-MS	0.1 ppm	0.6	0.7	0.4	0.6	0.6	0.7	0.6	0.5
Cu	(ppm)	ICP-MS	0.1 ppm	31.6	48.1	34.2	76.2	22.5	63.5	44.2	18.4
Dy	(ppm)	ICP-MS	0.01 ppm	6.21	6.75	3.34	2.48	6.31	6.29	6.64	5.94
Er	(ppm)	ICP-MS	0.01 ppm	3.32	3.39	1.81	1.67	3.6	3.53	3.84	3.72
Eu	(ppm)	ICP-MS	0.01 ppm	1.53	1.71	1.2	0.97	1.97	1.83	1.76	1.94
Ga	(ppm)	ICP-MS	0.1 ppm	16.3	16.1	20.4	15.3	15.3	16.8	16.5	16.4
Gd	(ppm)	ICP-MS	0.01 ppm	6.26	6.8	3.67	2.5	5.79	7.4	7.22	6.39
Ge	(ppm)	ICP-MS	0.1 ppm	0.05	0.05	0.1	0.2	0.05	0.05	0.05	0.05
Hf	(ppm)	ICP-MS	0.1 ppm	4.6	5	3.1	1.1	4.2	4.1	3.9	3.2
Hg	(ppm)	ICP-MS	0.1 ppm	0.05	0.05	0.05	0.05	0.05	0.05	0.05	0.05
Ho	(ppm)	ICP-MS	0.01 ppm	1.38	1.42	0.7	0.57	1.5	1.45	1.68	1.52
La	(ppm)	ICP-MS	1 ppm	23	27	17	11	27	22	22	21
Lu	(ppm)	ICP-MS	0.01 ppm	0.48	0.66	0.19	0.25	0.52	0.62	0.58	0.54
Mo	(ppm)	ICP-MS	0.1 ppm	1.7	1.8	0.3	0.7	2.1	5.9	4.6	2.6
Nb	(ppm)	ICP-MS	1 ppm	10	10	2	0.5	10	10	8	10
Nd	(ppm)	ICP-MS	0.1 ppm	27.1	26.2	21.2	16.6	28.8	27.2	27.9	28.6
Ni	(ppm)	ICP-MS	1 ppm	14	18	95	34	12	14	17	18
Pb204	(ppm)	ICP-MS	0.01 ppm	0.115	0.114	0.097	0.034	0.126	0.074	0.017	5.10E-02
Pb206	(ppm)	ICP-MS	0.02 ppm	1.22	0.824	1.27	0.7	0.884	0.785	0.975	0.777
Pb207	(ppm)	ICP-MS	0.02 ppm	1.02	1.23	1.29	0.679	0.956	0.603	0.775	0.755
Pb208	(ppm)	ICP-MS	0.02 ppm	2.52	2.13	2.89	1.76	2.08	1.72	2.04	1.65
PbSUM	(ppm)	ICP-MS	0.02 ppm	4.87	4.3	5.54	3.18	4.05	3.18	3.8	3.23
Pr	(ppm)	ICP-MS	0.01 ppm	6.04	6.2	4.73	3.48	6.64	6.09	6.43	6.03
Rb	(ppm)	ICP-MS	0.1 ppm	44.2	56	32.6	23.2	37.5	61.4	28.8	41.7
S	(ppm)	ICP-MS	0.01 ppm	-	-	-	-	-	-	-	-
Sb	(ppm)	ICP-MS	1 ppm	4	6	0.5	0.5	4	3	3	4
Sc	(ppm)	ICP-OES	2 ppm	16	16	18	30	15	17	18	16
Se	(ppm)	ICP-MS	1 ppm	0.5	0.5	1	1	0.5	0.5	9	4
Sm	(ppm)	ICP-MS	0.01 ppm	5.72	5.62	3.7	3.34	5.76	6.33	6.04	6.96
Sn	(ppm)	ICP-MS	0.1 ppm	1.3	1.2	0.05	0.05	1.3	1.7	1.2	1.1
Sr	(ppm)	ICP-MS	1 ppm	303	245	509	520	270	208	327	263
Ta	(ppm)	ICP-MS	0.01 ppm	0.45	0.43	0.32	0.005	0.51	0.33	0.38	0.48
Tb	(ppm)	ICP-MS	0.01 ppm	0.77	0.83	0.47	0.34	0.8	0.82	0.78	0.83
Te	(ppm)	ICP-MS	0.1 ppm	1.6	0.05	0.05	0.05	0.2	0.5	0.05	0.2
Th	(ppm)	ICP-MS	0.01 ppm	1.85	2.15	4.76	3.81	2.29	1.95	3.96	1.84
Tm	(ppm)	ICP-MS	0.01 ppm	0.62	0.6	0.25	0.27	0.66	0.57	0.63	0.69
U	(ppm)	ICP-MS	0.01 ppm	2.1	1.58	1.73	0.43	2.46	2.2	3.16	1.64
V	(ppm)	ICP-OES	2 ppm	109	138	145	217	134	130	173	150
W	(ppm)	ICP-MS	1 ppm	0.5	0.5	0.5	0.5	0.5	5	0.5	0.5
Y	(ppm)	ICP-MS	0.01 ppm	33.4	36.8	17.1	14	35.2	35.1	36.5	35.4
Yb	(ppm)	ICP-MS	0.01 ppm	3.79	4.82	2.05	1.91	4.22	3.96	4.37	4.2
Zn	(ppm)	ICP-MS	1 ppm	101	98	45	55	115	87	127	143
Zr	(ppm)	ICP-MS	2 ppm	154	163	137	67	127	134	129	128

Table B ICP-OES and ICP-MS lithogeochemical results of Fisher property rocks.

Sample ID				CO-2019-49	CO-2019-51	CO-2019-52	CO-2019-79	CO-2019-48	CO-2019-75	CO-2019-129	CO-2019-131	CO-2019-50
Hole ID				FIS-18-021	FIS-18-021	FIS-18-021	FIS-18-020	FIS-18-021	FIS-18-020	Surface	Surface	FIS-18-021
Depth (m)				249.5	255.1	255.3	185.5	249	189.3	-	-	251.1
UTM Zone 13N Northing				6160271	6160271	6160271	6160271	6160271	6160492	6160249	6161125	6160271
UTM Zone 13N Easting				604154	604154	604154	604154	604154	604123	604091	603954	604154
Lithology				GRNT	GRNT	GRNT	GRNT	GRNT	GRNT	GRNT	GRNT	GRNT
Alteration Intensity				L	L	L	L	M	M	H	H	H
			Detection Limit									
SiO_2	(%)	ICP-OES	0.10%	74.6	72	75.1	74.1	76.2	73.3	74.8	73.1	72.7
TiO_2	(%)	ICP-OES	0.01%	0.13	0.16	0.12	0.19	0.2	0.17	0.18	0.22	0.14
Al_2O3	(%)	ICP-OES	0.01%	13.8	14.5	13.4	13.8	12.8	13.8	14.4	15.3	14.8
Fe_2O_3	(%)	ICP-OES	0.01%	2.32	3.24	2.23	2.32	1.99	2.81	1.62	1.93	2.21
MnO	(%)	ICP-OES	0.01%	0.05	0.04	0.04	0.07	0.04	0.07	0.02	0.02	0.03
MgO	(%)	ICP-OES	0.01%	0.12	0.36	0.21	0.25	0.15	0.17	0.31	0.6	0.21
CaO	(%)	ICP-OES	0.01%	1.7	1.19	1.49	2.1	1.65	1.81	2.02	1.99	1.4
Na_2O	(%)	ICP-OES	0.01%	4.69	5.68	4.78	4.07	4.69	4.7	5.12	6	4.94
K_2O	(%)	ICP-OES	0.01%	1.63	1.33	1.48	2.05	1.24	1.74	0.64	0.29	2.31
P_2O_5	(%)	ICP-OES	0.01%	0.01	0.02	0.01	0.03	0.01	0.02	0.02	0.02	0.01
LOI	(%)	ICP-OES	0.10%	0.8	1.5	0.9	1.1	1	1.2	0.6	0.3	1.2
SUM	(%)	ICP-OES	0.10%	99.85	100.02	99.76	100.08	99.97	99.79	99.73	99.77	99.95
Ag	(ppm)	ICP-MS	0.1 ppm	0.4	0.4	0.4	0.6	0.6	0.1	0.05	0.05	0.3
As	(ppm)	ICP-MS	0.1 ppm	1.8	2.3	0.8	12.8	2.5	3	0.05	0.05	1.8
Ba	(ppm)	ICP-MS	1 ppm	578	446	492	710	597	769	580	38	1020
Be	(ppm)	ICP-MS	0.1 ppm	9.7	12.4	10	10.2	11.7	10.1	1.4	0.05	11.1
Bi	(ppm)	ICP-MS	0.1 ppm	0.05	0.3	0.05	0.05	0.9	0.05	0.05	0.05	0.05
C	(ppm)	ICP-MS	0.01 ppm	-	-	-	-	-	-	-	-	-
Cd	(ppm)	ICP-MS	0.1 ppm	0.05	0.3	0.5	0.5	0.2	0.2	0.2	0.2	0.4
Ce	(ppm)	ICP-MS	1 ppm	71	68	68	90	102	57	38	39	68
Co	(ppm)	ICP-MS	0.1 ppm	1.7	4.9	2.2	3.4	2.3	2.1	2	4	1.8
Cr	(ppm)	ICP-OES	2 ppm	16	20	25	43	13	10	19	21	15
Cs	(ppm)	ICP-MS	0.1 ppm	0.6	0.5	0.7	0.4	0.6	0.8	0.05	0.6	0.5
Cu	(ppm)	ICP-MS	0.1 ppm	16.6	53.5	12	3.8	75.8	4.2	7.7	10.3	43.8
Dy	(ppm)	ICP-MS	0.01 ppm	7.72	7.58	7.49	5.95	9.37	7.24	1.7	2.64	8.1
Er	(ppm)	ICP-MS	0.01 ppm	4.73	4.88	5.34	4.18	5.47	4.29	1.14	1.82	4.91
Eu	(ppm)	ICP-MS	0.01 ppm	1.26	1.17	1.46	1.38	1.45	1.22	0.87	0.66	1.5
Ga	(ppm)	ICP-MS	0.1 ppm	14.9	16.6	15.9	14.2	14.2	15.2	14.6	12.8	15.1
Gd	(ppm)	ICP-MS	0.01 ppm	8.24	7.62	7.72	5.79	7.53	6.8	1.89	1.98	8.42
Ge	(ppm)	ICP-MS	0.1 ppm	0.05	0.05	0.05	0.05	0.05	0.05	0.2	0.3	0.05
Hf	(ppm)	ICP-MS	0.1 ppm	6.7	7.4	7.2	6.4	6.4	6	3.6	4.1	7.9
Hg	(ppm)	ICP-MS	0.1 ppm	0.7	0.6	0.4	0.8	0.4	0.05	0.05	0.05	1.4
Ho	(ppm)	ICP-MS	0.01 ppm	1.94	1.57	2.01	1.49	2.1	1.81	0.36	0.61	1.89
La	(ppm)	ICP-MS	1 ppm	32	33	34	54	47	29	23	23	31
Lu	(ppm)	ICP-MS	0.01 ppm	0.97	0.64	1	0.76	1.03	0.7	0.17	0.24	0.76
Mo	(ppm)	ICP-MS	0.1 ppm	1.6	4.2	2.4	2.5	3.2	2.4	0.05	0.3	3.5
Nb	(ppm)	ICP-MS	1 ppm	17	17	16	11	22	13	1	1	18
Nd	(ppm)	ICP-MS	0.1 ppm	35.6	35.2	35.2	41.6	42.6	32.1	15	15.2	36.1
Ni	(ppm)	ICP-MS	1 ppm	13	12	11	10	14	7	2	5	12
Pb204	(ppm)	ICP-MS	0.01 ppm	0.09	0.04	0.005	0.142	0.3	0.063	0.037	5.00E-04	0.142
Pb206	(ppm)	ICP-MS	0.02 ppm	1.82	1.24	1	3.15	5.54	1.34	1.66	1.32	2.24
Pb207	(ppm)	ICP-MS	0.02 ppm	0.991	0.754	0.831	2.68	3.66	0.942	0.769	0.5	1.1
Pb208	(ppm)	ICP-MS	0.02 ppm	2.77	1.57	2.05	6.36	9.28	2.16	2.67	1.96	2.56
PbSUM	(ppm)	ICP-MS	0.02 ppm	5.67	3.61	3.88	12.3	18.8	4.5	5.13	3.78	6.03
Pr	(ppm)	ICP-MS	0.01 ppm	8.7	8.22	8.43	11	11.6	7.4	4.42	4.08	8.62
Rb	(ppm)	ICP-MS	0.1 ppm	32.1	25.9	28.4	34.3	30.6	37.4	11.8	3.8	40
S	(ppm)	ICP-MS	0.01 ppm	-	-	-	-	-	-	-	-	-
Sb	(ppm)	ICP-MS	1 ppm	4	3	3	4	3	3	0.5	0.5	4
Sc	(ppm)	ICP-OES	2 ppm	4	4	4	5	4	5	1	3	4
Se	(ppm)	ICP-MS	1 ppm	0.5	0.5	0.5	0.5	11	2	2	2	1
Sm	(ppm)	ICP-MS	0.01 ppm	7.46	7.72	7.6	7.42	7.38	5.67	2.37	2.46	8.23
Sn	(ppm)	ICP-MS	0.1 ppm	3.2	2.2	2.5	1.8	6	2.2	0.05	0.05	4.3
Sr	(ppm)	ICP-MS	1 ppm	157	112	134	163	149	142	250	202	146
Ta	(ppm)	ICP-MS	0.01 ppm	0.96	1.12	1.13	0.59	1.14	0.74	0.3	0.27	1.19
Tb	(ppm)	ICP-MS	0.01 ppm	1.15	0.93	0.87	0.89	1.09	0.88	0.2	0.31	1.02
Te	(ppm)	ICP-MS	0.1 ppm	0.2	0.05	0.2	0.8	0.05	0.05	0.05	0.05	0.05
Th	(ppm)	ICP-MS	0.01 ppm	8.19	6.69	6.05	6.2	11.9	3.15	6.51	7.8	7.42
Tm	(ppm)	ICP-MS	0.01 ppm	0.95	0.87	0.84	0.81	0.82	0.74	0.14	0.28	0.79
U	(ppm)	ICP-MS	0.01 ppm	3.22	3.92	3.5	2.37	5.17	2.06	2.27	3.76	6.52
V	(ppm)	ICP-OES	2 ppm	5	24	19	75	19	13	1	21	5
W	(ppm)	ICP-MS	1 ppm	0.5	0.5	0.5	0.5	0.5	0.5	0.5	0.5	0.5
Y	(ppm)	ICP-MS	0.01 ppm	49.8	41.3	50.8	38.7	52.8	43.9	11.5	16.1	48.7
Yb	(ppm)	ICP-MS	0.01 ppm	6.26	5.7	6.51	5.16	5.63	5.67	1.45	2.3	6.51
Zn	(ppm)	ICP-MS	1 ppm	52	45	51	60	91	87	32	0.5	54
Zr	(ppm)	ICP-MS	2 ppm	199	224	198	220	195	221	126	180	232

Table B ICP-OES and ICP-MS lithogeochemical results of Fisher property rocks.

Sample ID				CO-2019-74	CO-2019-77	CO-2019-122	CO-2019-02	CO-2019-08	CO-2019-118	CO-2019-24	CO-2019-33	CO-2019-01
Hole ID				FIS-18-020	FIS-18-020	Surface	FIS-18-001	FIS-18-003	Surface	FIS-18-018	FIS-18-022	FIS-18-001
Depth (m)				185.8	184.4	-	244.6	392.3	-	358.2	191.1	72.8
UTM Zone 13N Northing				6160492	6160271		6166989	6167042	6161670	6163905	6160406	6166989
UTM Zone 13N Easting				604123	604154		600767.1	601195.9	604265	602798	604183	600767.1
Lithology				GRNT	GRNT	QD	QD	QD	QD	PYRX	PYRX	PYRX
Alteration Intensity				H	H	L	M	M	H	L	L	M
			Detection Limit									
SiO_2	(%)	ICP-OES	0.10%	72.9	82.6	62.3	67.2	56.8	80.7	48.4	47.6	48
TiO_2	(%)	ICP-OES	0.01%	0.18	0.12	0.58	0.34	0.65	0.5	0.44	1.16	0.39
Al_2O3	(%)	ICP-OES	0.01%	14.2	8.14	15.6	16.3	16.6	8.72	11.8	13.3	10.6
Fe_2O_3	(%)	ICP-OES	0.01%	2.75	2.18	4.76	3.35	7.87	4.15	12.2	14.8	10.5
MnO	(%)	ICP-OES	0.01%	0.04	0.05	0.06	0.04	0.13	0.08	0.19	0.18	0.16
MgO	(%)	ICP-OES	0.01%	0.24	0.96	3.7	1.26	4.61	0.42	12.2	12	15.5
CaO	(%)	ICP-OES	0.01%	1.37	1.7	4.8	3.96	6.49	1.76	11.7	7.61	11
Na_2O	(%)	ICP-OES	0.01%	3.88	0.35	4.4	4.72	3.31	0.61	1.56	2.27	1.19
K_2O	(%)	ICP-OES	0.01%	3.51	3.34	2.6	1.75	2.24	2.4	0.49	0.45	1.06
P_2O_5	(%)	ICP-OES	0.01%	0.02	0.01	0.26	0.06	0.22	0.06	0.005	0.26	0.01
LOI	(%)	ICP-OES	0.10%	1	0.7	0.6	0.6	0.8	0.7	1.1	0.9	1.7
SUM	(%)	ICP-OES	0.10%	100.09	100.15	99.66	99.58	99.72	100.1	100.08	100.53	100.11
Ag	(ppm)	ICP-MS	0.1 ppm	0.7	10.1	0.05	3	1.7	0.1	0.7	0.6	2.9
As	(ppm)	ICP-MS	0.1 ppm	7.1	341	0.05	2.7	2.5	0.05	1.2	1.1	2
Ba	(ppm)	ICP-MS	1 ppm	1220	195	639	535	865	878	95	122	290
Be	(ppm)	ICP-MS	0.1 ppm	11.5	9.5	0.8	9.2	7.6	0.05	7.7	7.9	8
Bi	(ppm)	ICP-MS	0.1 ppm	0.05	0.05	0.05	0.3	0.2	0.05	0.05	0.2	0.6
C	(ppm)	ICP-MS	0.01 ppm	-	-	-	<0.01	0.03	-	0.02	0.01	0.04
Cd	(ppm)	ICP-MS	0.1 ppm	0.2	0.9	0.2	0.5	0.3	0.05	0.3	0.4	0.5
Ce	(ppm)	ICP-MS	1 ppm	77	44	90	36	66	78	8	19	15
Co	(ppm)	ICP-MS	0.1 ppm	2	3.6	16.9	9.1	25.6	4.8	58.1	72.2	61.9
Cr	(ppm)	ICP-OES	2 ppm	9	16	159	28	187	79	904	361	1160
Cs	(ppm)	ICP-MS	0.1 ppm	0.8	0.6	1.8	1.4	2.3	0.8	2.5	0.9	6.5
Cu	(ppm)	ICP-MS	0.1 ppm	43.3	23.5	98.2	7.5	21	0.7	53.7	57.5	136
Dy	(ppm)	ICP-MS	0.01 ppm	7.61	4.22	2.82	1.11	3.78	2.87	1.8	2.99	1.94
Er	(ppm)	ICP-MS	0.01 ppm	4.72	2.32	1.46	0.36	1.82	1.6	1.03	1.43	1.11
Eu	(ppm)	ICP-MS	0.01 ppm	1.49	0.75	1.81	0.74	1.58	0.96	0.5	1.06	0.66
Ga	(ppm)	ICP-MS	0.1 ppm	16.2	8.9	21.2	18.7	17.7	10.6	10.7	13.9	10
Gd	(ppm)	ICP-MS	0.01 ppm	7.26	4.07	4.7	1.57	3.96	3.18	1.35	2.56	1.57
Ge	(ppm)	ICP-MS	0.1 ppm	0.05	0.05	0.1	0.8	1.1	0.2	1.1	1.3	1.7
Hf	(ppm)	ICP-MS	0.1 ppm	8.5	3.7	5.8	2.5	4.1	4.6	0.6	1.7	0.6
Hg	(ppm)	ICP-MS	0.1 ppm	0.05	0.05	0.05	0.05	0.05	0.05	0.05	0.1	0.05
Ho	(ppm)	ICP-MS	0.01 ppm	1.78	0.9	0.51	0.18	0.76	0.58	0.43	0.6	0.5
La	(ppm)	ICP-MS	1 ppm	42	22	39	19	32	40	3	9	4
Lu	(ppm)	ICP-MS	0.01 ppm	0.8	0.3	0.14	0.12	0.36	0.27	0.19	0.28	0.18
Mo	(ppm)	ICP-MS	0.1 ppm	6.2	5.1	1.6	1.4	1.6	0.05	2.5	2	1.3
Nb	(ppm)	ICP-MS	1 ppm	13	10	6	4	11	4	1	2	3
Nd	(ppm)	ICP-MS	0.1 ppm	39.9	22.5	43.7	12.6	27.5	30.4	5.6	12	6.4
Ni	(ppm)	ICP-MS	1 ppm	7	15	83	14	62	11	127	296	414
Pb204	(ppm)	ICP-MS	0.01 ppm	0.073	35.5	0.132	0.24	0.218	0.146	0.048	0.052	0.137
Pb206	(ppm)	ICP-MS	0.02 ppm	1.92	467	2.9	7.7	2.21	2.7	0.308	0.622	5
Pb207	(ppm)	ICP-MS	0.02 ppm	1.35	494	2.19	1.98	1.62	2.37	0.408	0.769	1.52
Pb208	(ppm)	ICP-MS	0.02 ppm	3.28	1110	5.57	3.42	3.89	5.86	1.2	1.56	2.67
PbSUM	(ppm)	ICP-MS	0.02 ppm	6.62	2110	10.8	13.3	7.94	11.1	1.96	3	9.32
Pr	(ppm)	ICP-MS	0.01 ppm	10.1	5.77	11.1	3.99	8.14	8.59	1.31	2.89	1.56
Rb	(ppm)	ICP-MS	0.1 ppm	62.5	50.5	64.7	34.3	67.2	51.8	42.3	7.9	66.8
S	(ppm)	ICP-MS	0.01 ppm	-	-	-	<0.01	0.01	-	<0.01	0.12	<0.01
Sb	(ppm)	ICP-MS	1 ppm	4	10	0.5	2	1	0.5	0.5	0.5	2
Sc	(ppm)	ICP-OES	2 ppm	5	3	9	5	17	4	48	23	34
Se	(ppm)	ICP-MS	1 ppm	7	0.5	6	12	12	1	5	8	1
Sm	(ppm)	ICP-MS	0.01 ppm	7.38	4.55	7.68	1.7	5.33	4.97	1.27	2.41	1.55
Sn	(ppm)	ICP-MS	0.1 ppm	3	1.1	0.05	1.3	4.3	0.05	1.4	1.6	1.2
Sr	(ppm)	ICP-MS	1 ppm	114	56	861	641	519	131	224	354	346
Ta	(ppm)	ICP-MS	0.01 ppm	0.82	0.49	0.53	0.54	1.08	0.49	0.17	0.3	0.45
Tb	(ppm)	ICP-MS	0.01 ppm	0.96	0.61	0.48	0.17	0.59	0.45	0.26	0.45	0.3
Te	(ppm)	ICP-MS	0.1 ppm	0.05	0.05	0.05	0.05	0.9	0.05	0.05	0.3	0.4
Th	(ppm)	ICP-MS	0.01 ppm	7.18	3.24	10.3	6.38	8.32	20	0.78	0.8	10.1
Tm	(ppm)	ICP-MS	0.01 ppm	0.78	0.4	0.18	0.1	0.33	0.22	0.16	0.22	0.22
U	(ppm)	ICP-MS	0.01 ppm	2.74	1.96	3.75	39.7	3.46	2.01	0.4	1.35	22.1
V	(ppm)	ICP-OES	2 ppm	26	15	86	48	123	89	260	240	208
W	(ppm)	ICP-MS	1 ppm	0.5	0.5	0.5	15	12	0.5	3	2	17
Y	(ppm)	ICP-MS	0.01 ppm	43.9	24.4	14	5.07	22.2	15.9	11.3	18.2	12.1
Yb	(ppm)	ICP-MS	0.01 ppm	5.53	2.81	1.07	0.44	2.16	1.81	1.14	1.46	1.3
Zn	(ppm)	ICP-MS	1 ppm	62	119	24	63	141	0.5	105	152	103
Zr	(ppm)	ICP-MS	2 ppm	277	142	253	89	162	174	24	59	22

Table B ICP-OES and ICP-MS lithogeochemical results of Fisher property rocks.

Sample ID				CO-2019-17	CO-2019-35	CO-2019-39	CO-2019-56	CO-2019-114	CO-2019-119	CO-2019-69	CO-2019-72	CO-2019-73
Hole ID				FIS-18-017	FIS-18-022	FIS-18-023	FIS-19-035	surface	surface	FIS-18-021	FIS-18-021	FIS-18-021
Depth (m)				409.1	422.4	238.5	107.65	-	-	316.1	329.2	329.8
UTM Zone 13N Northing				6162978	6160406	6160271	6161455.94	6163318	6161373	6160271	6160271	6160271
UTM Zone 13N Easting				603370	604183	604154	603981.747	603120	604585	604154	604154	604154
Lithology				MetaSED	MetaSED	MetaSED	MetaSED	MetaSED	MetaSED	MetaSED	MetaSED	MetaSED
Alteration Intensity				L	L	L	L	L	L	H	H	H
			Detection Limit									
SiO_2	(%)	ICP-OES	0.10%	74.8	75.3	74.7	63.6	49	64.4	47.8	76	77.6
TiO_2	(%)	ICP-OES	0.01%	0.13	0.13	0.13	0.8	0.58	0.53	0.75	0.15	0.18
Al_2O3	(%)	ICP-OES	0.01%	13.9	13.5	13.4	15.3	17.1	14.7	19.5	11.4	13
Fe_2O_3	(%)	ICP-OES	0.01%	2.11	1.86	2.1	7.89	10.9	8.09	10.2	2.78	1.8
MnO	(%)	ICP-OES	0.01%	0.01	0.02	0.03	0.1	0.17	0.39	0.12	0.04	0.01
MgO	(%)	ICP-OES	0.01%	0.19	0.21	0.23	1.39	5.85	1.75	4.4	0.9	0.43
CaO	(%)	ICP-OES	0.01%	2.07	1.67	2.1	3.21	11	3.64	6.58	1.42	0.5
Na_2O	(%)	ICP-OES	0.01%	5.06	4.82	4.69	4.77	3.68	4.1	0.99	1.13	0.49
K_2O	(%)	ICP-OES	0.01%	0.96	1.53	1.16	1.46	0.75	1.46	6.91	4.59	4.14
P_2O_5	(%)	ICP-OES	0.01%	0.005	0.005	0.005	0.3	0.12	0.1	0.15	0.03	0.03
LOI	(%)	ICP-OES	0.10%	0.5	1	1	1	1	0.6	2.4	1.4	1.7
SUM	(%)	ICP-OES	0.10%	99.73	100.04	99.54	99.82	100.15	99.76	99.8	99.84	99.88
Ag	(ppm)	ICP-MS	0.1 ppm	0.8	0.8	0.6	0.6	0.05	0.05	1.2	0.8	0.7
As	(ppm)	ICP-MS	0.1 ppm	1.9	9.3	25.3	2.5	0.05	0.05	4.5	1100	34.9
Ba	(ppm)	ICP-MS	1 ppm	541	761	597	536	262	941	1220	390	326
Be	(ppm)	ICP-MS	0.1 ppm	7.1	8.6	8.8	8.5	0.05	0.05	9.7	9.8	9.5
Bi	(ppm)	ICP-MS	0.1 ppm	0.05	0.05	0.2	0.4	0.3	0.4	0.05	0.05	0.05
C	(ppm)	ICP-MS	0.01 ppm	0.06	0.19	0.21	-	-	-	-	-	-
Cd	(ppm)	ICP-MS	0.1 ppm	0.2	0.4	0.2	0.5	0.05	0.3	0.2	0.4	0.2
Ce	(ppm)	ICP-MS	1 ppm	81	49	40	74	28	41	52	53	53
Co	(ppm)	ICP-MS	0.1 ppm	4	2.1	3.2	13.3	37	15.6	24.9	2.5	3.5
Cr	(ppm)	ICP-OES	2 ppm	15	12	13	7	92	20	118	8	7
Cs	(ppm)	ICP-MS	0.1 ppm	1.1	0.3	0.4	3.9	8.6	0.1	1.9	0.6	0.4
Cu	(ppm)	ICP-MS	0.1 ppm	16.1	8.5	10.9	55.2	148	219	61.2	34.8	15.7
Dy	(ppm)	ICP-MS	0.01 ppm	7.33	3.4	3.41	6.64	2.96	5.79	5.43	5.2	6.04
Er	(ppm)	ICP-MS	0.01 ppm	3.87	1.77	1.7	3.85	2.18	3.47	3.09	3.36	4.26
Eu	(ppm)	ICP-MS	0.01 ppm	1.49	0.76	0.77	2.14	0.84	1.2	1.84	1.22	1.31
Ga	(ppm)	ICP-MS	0.1 ppm	18.3	14.4	14.6	16.3	16.6	16.1	22	11.7	14.2
Gd	(ppm)	ICP-MS	0.01 ppm	5.39	3.21	3.02	6.53	2.41	4.81	5.39	5.58	4.98
Ge	(ppm)	ICP-MS	0.1 ppm	1.2	0.8	1	0.05	0.1	0.4	0.05	0.05	0.05
Hf	(ppm)	ICP-MS	0.1 ppm	5.7	4.3	4.2	6.6	0.9	2.9	5.1	6.2	6.3
Hg	(ppm)	ICP-MS	0.1 ppm	0.05	0.1	0.2	0.9	0.05	0.05	0.5	0.05	0.05
Ho	(ppm)	ICP-MS	0.01 ppm	1.81	0.82	0.74	1.59	0.67	1.29	1.13	1.27	1.62
La	(ppm)	ICP-MS	1 ppm	29	25	17	46	13	18	28	27	29
Lu	(ppm)	ICP-MS	0.01 ppm	0.68	0.43	0.41	0.59	0.28	0.62	0.39	0.47	0.65
Mo	(ppm)	ICP-MS	0.1 ppm	1.5	4.9	3.7	2.9	0.6	0.3	26.6	1.3	1.2
Nb	(ppm)	ICP-MS	1 ppm	8	4	7	15	0.5	0.5	12	11	12
Nd	(ppm)	ICP-MS	0.1 ppm	29.8	19.7	14.4	38.2	14.8	22.9	31.5	27.9	30.2
Ni	(ppm)	ICP-MS	1 ppm	5	12	7	13	28	0.5	91	12	11
Pb204	(ppm)	ICP-MS	0.01 ppm	0.134	0.136	0.197	0.038	0.031	5.00E-04	1.8	6.43	1.5
Pb206	(ppm)	ICP-MS	0.02 ppm	1.16	1.38	2.12	1.21	0.764	0.964	25.8	87.8	18.4
Pb207	(ppm)	ICP-MS	0.02 ppm	0.946	1.19	1.65	1.05	0.673	0.589	28.8	95.6	19.8
Pb208	(ppm)	ICP-MS	0.02 ppm	2.1	2.62	3.79	2.61	1.76	1.67	64.4	208	43.6
PbSUM	(ppm)	ICP-MS	0.02 ppm	4.34	5.33	7.75	4.9	3.23	3.2	121	397	83.4
Pr	(ppm)	ICP-MS	0.01 ppm	7.63	5.49	4.6	8.8	3.85	5.53	7.17	6.84	7.28
Rb	(ppm)	ICP-MS	0.1 ppm	17.9	26.2	26.4	26.4	28.1	19.7	115	61.6	56.4
S	(ppm)	ICP-MS	0.01 ppm	0.05	0.08	0.14	-	-	-	-	-	-
Sb	(ppm)	ICP-MS	1 ppm	1	0.5	2	3	0.5	0.5	4	5	4
Sc	(ppm)	ICP-OES	2 ppm	4	1	1	14	31	21	18	4	4
Se	(ppm)	ICP-MS	1 ppm	0.5	5	6	0.5	8	6	0.5	0.5	0.5
Sm	(ppm)	ICP-MS	0.01 ppm	6.81	3.4	3.31	7.24	2.87	5.89	6.22	5.07	5.54
Sn	(ppm)	ICP-MS	0.1 ppm	1.3	1.8	1.9	1.9	0.05	0.05	2.2	2	1.3
Sr	(ppm)	ICP-MS	1 ppm	146	157	128	307	398	182	329	94	46
Ta	(ppm)	ICP-MS	0.01 ppm	1.18	0.72	0.89	0.48	0.005	0.1	0.6	0.6	0.69
Tb	(ppm)	ICP-MS	0.01 ppm	1.2	0.52	0.51	0.91	0.41	0.76	0.66	0.72	0.79
Te	(ppm)	ICP-MS	0.1 ppm	0.05	0.2	0.05	0.05	0.05	0.1	0.05	0.05	0.05
Th	(ppm)	ICP-MS	0.01 ppm	8.56	4.38	3.3	3.66	34.9	11.5	3.31	3.33	5.3
Tm	(ppm)	ICP-MS	0.01 ppm	0.72	0.39	0.36	0.67	0.32	0.57	0.49	0.53	0.72
U	(ppm)	ICP-MS	0.01 ppm	2.18	2.11	2.22	1.63	0.39	1.63	2.73	2.11	2.85
V	(ppm)	ICP-OES	2 ppm	3	1	2	60	228	95	163	21	18
W	(ppm)	ICP-MS	1 ppm	7	1	0.5	0.5	0.5	0.5	5	1	3
Y	(ppm)	ICP-MS	0.01 ppm	46.6	24.2	21.3	39.7	16.5	31.3	31.8	34.8	39
Yb	(ppm)	ICP-MS	0.01 ppm	4.77	2.51	1.96	4.7	2.1	4.01	3.85	4.12	4.49
Zn	(ppm)	ICP-MS	1 ppm	53	42	55	89	71	220	204	159	57
Zr	(ppm)	ICP-MS	2 ppm	191	157	142	223	52	117	176	192	213

APPENDIX C: ELECTRON MICROPROBE DATA

Table C-1 Electron microprobe analysis results for biotite phases at the Fisher property analyzed at the University of Calgary.

Phase	B_1	B_1	B_1	B_1	B_1	B_1	B_1	B_1	B_1	B_1
Sample	CO-2019-55	CO-2019-55	CO-2019-55	CO-2019-55	CO-2019-69	CO-2019-69	CO-2019-69	CO-2019-69	CO-2019-69	CO-2019-81B
Rock Type	HCrB	HCrB	HCrB	HCrB	MetaSed	MetaSed	MetaSed	MetaSed	MetaSed	DIO
SiO_2 (in wt%)	36.97	37.07	36.28	35.86	36.02	36.30	36.75	36.62	36.35	35.40
TiO_2	2.30	2.39	2.09	2.11	1.83	1.90	1.81	1.67	1.92	2.16
Al_2O_3	16.78	16.77	16.82	17.02	19.25	19.00	19.17	18.83	18.75	16.32
FeO	19.34	19.31	19.14	19.40	16.38	16.92	15.82	15.85	16.08	22.75
MnO	0.43	0.37	0.38	0.36	0.29	0.29	0.32	0.25	0.33	0.34
MgO	10.60	10.42	10.41	10.37	11.78	11.40	12.29	12.05	12.01	9.21
BaO	0.19	0.22	0.26	0.39	0.14	0.19	0.12	0.20	0.17	0.41
CaO	0.09	0.09	0.01	0.04	0.03	0.03	0.01	0.03	0.01	0.03
Na_2O	0.08	0.11	0.11	0.05	0.11	0.05	0.05	0.11	0.07	0.09
K_2O	9.34	9.31	9.51	8.95	9.93	9.79	9.92	9.97	9.89	9.43
F	0.02	0.02	0.02	0.00	0.00	0.03	0.00	0.00	0.02	0.03
Cl	0.09	0.08	0.10	0.05	0.05	0.03	0.04	0.04	0.05	0.06
(OH)	3.81	3.90	4.92	5.42	4.22	4.08	3.71	4.41	4.37	3.82
Total	96.22	96.12	95.11	94.58	95.79	95.95	96.29	95.60	95.64	96.20
Atoms per formula unit calculated on the basis of 11 O + 2(F, Cl, OH, O)										
Si	2.80	2.81	2.79	2.75	2.72	2.73	2.74	2.75	2.74	2.74
Al_{IV}	1.05	1.05	1.04	1.11	1.26	1.24	1.24	1.21	1.22	1.06
Al_{VI}	0.45	0.45	0.48	0.43	0.45	0.44	0.45	0.46	0.44	0.43
Fe^{3+}	0.27	0.26	0.27	0.28	0.09	0.10	0.09	0.10	0.11	0.34
Fe^{2+}	0.96	0.97	0.96	0.97	0.94	0.97	0.90	0.90	0.91	1.13
Mg	1.21	1.18	1.23	1.20	1.33	1.27	1.36	1.35	1.36	1.09
Ti	0.13	0.14	0.12	0.12	0.10	0.11	0.10	0.10	0.11	0.13
Mn	0.03	0.02	0.02	0.02	0.02	0.02	0.02	0.02	0.02	0.02
K	0.89	0.89	0.90	0.88	0.94	0.93	0.93	0.94	0.93	0.91
Na	0.01	0.02	0.02	0.01	0.02	0.01	0.01	0.02	0.01	0.01
Ba	0.01	0.01	0.01	0.01	0.00	0.01	0.00	0.01	0.00	0.01
Ca	0.01	0.01	0.00	0.00	0.00	0.00	0.00	0.00	0.00	0.00
F	0.02	0.01	0.05	0.00	0.00	0.01	0.00	0.00	0.02	0.03
Cl	0.01	0.01	0.01	0.01	0.01	0.00	0.01	0.01	0.01	0.01
OH	1.65	1.63	1.70	1.69	1.77	1.75	1.76	1.77	1.75	1.72
O^{2-}	0.32	0.34	0.24	0.30	0.23	0.23	0.23	0.23	0.22	0.24
Total (*apfu*)	9.81	9.79	9.84	9.79	9.87	9.83	9.84	9.84	9.86	9.87
Fe^{3+}/Fe_{tot}	0.22	0.21	0.22	0.22	0.09	0.09	0.09	0.10	0.10	0.23
Fe/Fe+Mg	0.504	0.509	0.499	0.509	0.438	0.456	0.420	0.425	0.428	0.575
Species[a]	annite	annite	annite	annite	phlogopite	phlogopite	phlogopite	phlogopite	phlogopite	annite

[a] Species from Deer et al. (1992)

Table C-1 Electron microprobe analysis results for biotite phases at the Fisher property analyzed at the University of Calgary.

Phase	B_1	B_1	B_2	B_2	B_2	B_2	B_2	B_2	B_2	B_2
Sample	CO-2019-81B	CO-2019-81B	CO-2019-55	CO-2019-55	CO-2019-55	CO-2019-55	CO-2019-55	CO-2019-55	CO-2019-55	CO-2019-61
Rock Type	DIO	DIO	HCrB	HCrB	HCrB	HCrB	HCrB	HCrB	HCrB	LCrB
SiO_2 (in wt%)	35.68	35.32	34.72	35.25	34.67	36.05	35.97	35.29	34.82	33.68
TiO_2	1.96	2.02	1.45	1.62	1.62	1.49	1.41	1.48	1.38	1.59
Al_2O_3	16.04	16.40	15.51	15.34	15.50	15.58	15.47	16.02	15.76	14.97
FeO	22.30	22.61	25.95	25.64	26.50	23.36	23.72	23.77	26.56	24.91
MnO	0.29	0.33	0.30	0.28	0.30	0.33	0.30	0.22	0.23	0.34
MgO	9.33	8.99	7.64	8.01	7.48	9.70	9.83	8.82	8.48	9.60
BaO	0.12	0.28	0.80	0.39	0.35	0.22	0.15	0.19	0.44	0.05
CaO	0.02	0.04	0.00	0.00	0.02	0.06	0.07	0.09	0.00	0.37
Na_2O	0.14	0.12	0.04	0.06	0.04	0.07	0.07	0.17	0.06	0.05
K_2O	9.47	9.34	9.26	9.18	8.92	8.90	8.94	8.96	8.56	6.16
F	0.00	0.00	0.03	0.05	0.03	0.00	0.00	0.02	0.02	0.00
Cl	0.05	0.05	0.04	0.05	0.07	0.11	0.07	0.09	0.05	0.05
(OH)	4.62	4.52	4.29	4.17	4.53	4.17	4.04	4.93	3.66	8.25
Total	95.39	95.50	95.73	95.86	95.50	95.85	95.97	95.10	96.36	91.76
Atoms per formula unit calculated on the basis of 11 O + 2(F, Cl, OH, O)										
Si	2.77	2.74	2.73	2.75	2.73	2.77	2.76	2.75	2.70	2.66
Al_{IV}	1.02	1.06	0.97	0.95	0.96	0.95	0.97	0.99	1.00	1.11
Al_{VI}	0.45	0.44	0.46	0.46	0.47	0.47	0.43	0.47	0.44	0.28
Fe^{3+}	0.31	0.33	0.48	0.45	0.48	0.45	0.43	0.40	0.52	0.60
Fe^{2+}	1.13	1.14	1.22	1.23	1.27	1.06	1.10	1.14	1.20	1.05
Mg	1.10	1.07	0.94	0.97	0.93	1.14	1.13	1.05	1.01	1.09
Ti	0.12	0.12	0.09	0.10	0.10	0.09	0.08	0.09	0.08	0.10
Mn	0.02	0.02	0.02	0.02	0.02	0.02	0.02	0.01	0.02	0.02
K	0.92	0.91	0.91	0.90	0.88	0.86	0.87	0.88	0.84	0.72
Na	0.02	0.02	0.01	0.01	0.01	0.01	0.01	0.02	0.01	0.01
Ba	0.00	0.01	0.02	0.01	0.01	0.01	0.00	0.01	0.01	0.00
Ca	0.00	0.00	0.00	0.00	0.00	0.00	0.01	0.01	0.00	0.03
F	0.00	0.00	0.03	0.03	0.03	0.00	0.00	0.02	0.01	0.00
Cl	0.01	0.01	0.01	0.01	0.01	0.01	0.01	0.01	0.01	0.01
OH	1.74	1.73	1.82	1.79	1.80	1.76	1.78	1.76	1.83	1.64
O^{2-}	0.26	0.26	0.14	0.17	0.17	0.22	0.21	0.20	0.16	0.35
Total (*apfu*)	9.86	9.86	9.86	9.85	9.85	9.81	9.81	9.83	9.83	9.66
Fe^{3+}/Fe_{tot}	0.22	0.22	0.28	0.27	0.27	0.30	0.28	0.26	0.30	0.36
Fe/Fe+Mg	0.567	0.579	0.644	0.633	0.653	0.568	0.573	0.595	0.631	0.601
Species[a]	annite	annite	annite	annite	annite	annite	annite	annite	annite	annite

[a] Species from Deer et al. (1992)

Table C-1 Electron microprobe analysis results for biotite phases at the Fisher property analyzed at the University of Calgary.

Phase	B_2	B_2	B_2	B_2	B_2	B_2	B_2	B_2	B_3	B_3
Sample	CO-2019-61	CO-2019-61	CO-2019-48	CO-2019-48	CO-2019-48	CO-2019-81B	CO-2019-81B	CO-2019-81B	CO-2019-55	CO-2019-55
Rock Type	LCrB	LCrB	GRNT	GRNT	GRNT	DIO	DIO	DIO	HCrB	HCrB
SiO_2 (in wt%)	33.50	34.68	34.41	34.67	34.79	34.37	34.47	34.57	36.41	35.34
TiO_2	1.16	1.43	3.11	2.92	3.21	1.78	1.89	1.95	2.18	2.18
Al_2O_3	15.72	15.29	16.95	17.38	16.83	15.73	15.97	15.89	15.69	15.69
FeO	24.10	22.73	24.91	24.49	24.88	25.67	25.95	26.12	22.23	20.72
MnO	0.32	0.38	0.50	0.40	0.35	0.28	0.29	0.29	0.23	0.29
MgO	9.77	9.33	5.91	6.35	6.07	8.55	7.81	7.67	10.74	10.72
BaO	0.07	0.07	0.50	0.46	0.31	0.15	0.39	0.31	0.34	0.23
CaO	0.27	0.20	0.03	0.02	0.02	0.00	0.05	0.06	0.08	0.10
Na_2O	0.09	0.05	0.09	0.10	0.08	0.03	0.06	0.08	0.20	0.27
K_2O	6.73	8.68	9.21	9.34	9.24	8.86	8.98	8.69	8.65	8.69
F	0.00	0.00	0.00	0.02	0.06	0.04	0.04	0.01	0.00	0.07
Cl	0.08	0.06	0.13	0.11	0.13	0.05	0.04	0.04	0.08	0.11
(OH)	8.22	7.13	4.31	3.78	4.10	4.53	4.10	4.33	3.21	5.65
Total	91.80	92.89	95.71	96.25	95.96	95.50	95.93	95.69	96.82	94.41
Atoms per formula unit calculated on the basis of 11 O + 2(F, Cl, OH, O)										
Si	2.65	2.74	2.73	2.72	2.75	2.69	2.70	2.71	2.76	2.75
Al_{IV}	1.11	1.03	1.05	1.08	1.03	1.04	1.05	1.04	1.00	1.03
Al_{VI}	0.35	0.39	0.53	0.53	0.54	0.42	0.43	0.43	0.40	0.41
Fe^{3+}	0.56	0.39	0.37	0.33	0.33	0.44	0.43	0.44	0.44	0.40
Fe^{2+}	1.04	1.11	1.28	1.28	1.31	1.25	1.27	1.27	0.97	0.95
Mg	1.14	1.11	0.79	0.82	0.80	1.03	0.94	0.92	1.22	1.27
Ti	0.08	0.09	0.18	0.17	0.19	0.10	0.11	0.12	0.12	0.13
Mn	0.02	0.03	0.03	0.03	0.02	0.02	0.02	0.02	0.01	0.02
K	0.74	0.89	0.89	0.90	0.89	0.88	0.89	0.87	0.83	0.85
Na	0.01	0.01	0.01	0.01	0.01	0.00	0.01	0.01	0.03	0.04
Ba	0.00	0.00	0.02	0.01	0.01	0.00	0.01	0.01	0.01	0.01
Ca	0.02	0.02	0.00	0.00	0.00	0.00	0.00	0.01	0.01	0.01
F	0.00	0.00	0.00	0.05	0.07	0.02	0.02	0.00	0.00	0.04
Cl	0.01	0.01	0.02	0.01	0.02	0.01	0.01	0.01	0.01	0.01
OH	1.73	1.74	1.63	1.66	1.62	1.80	1.77	1.75	1.66	1.63
O^{2-}	0.26	0.25	0.35	0.27	0.29	0.17	0.21	0.24	0.33	0.31
Total (*apfu*)	9.72	9.81	9.90	9.89	9.88	9.87	9.86	9.84	9.81	9.85
Fe^{3+}/Fe_{tot}	0.35	0.26	0.22	0.20	0.20	0.26	0.25	0.26	0.31	0.30
Fe/Fe+Mg	0.583	0.575	0.676	0.663	0.673	0.620	0.644	0.650	0.537	0.514
Species[a]	annite	annite	annite	annite	annite	annite	annite	annite	annite	annite

[a] Species from Deer et al. (1992)

Table C-1 Electron microprobe analysis results for biotite phases at the Fisher property analyzed at the University of Calgary.

Phase	B_3	B_3	B_3	B_3
Sample	CO-2019-55	CO-2019-81B	CO-2019-81B	CO-2019-81B
Rock Type	HCrB	DIO	DIO	DIO
SiO_2 (in wt%)	36.41	34.39	34.80	34.68
TiO_2	2.15	1.95	1.78	1.90
Al_2O_3	15.66	15.73	15.85	15.89
FeO	20.96	24.99	24.53	24.95
MnO	0.28	0.24	0.33	0.28
MgO	10.95	8.39	8.64	8.37
BaO	0.16	0.23	0.28	0.33
CaO	0.10	0.02	0.00	0.02
Na_2O	0.21	0.06	0.13	0.05
K_2O	8.80	9.25	9.28	9.05
F	0.00	0.00	0.02	0.00
Cl	0.09	0.05	0.04	0.05
(OH)	4.28	4.71	4.35	4.44
Total	95.74	95.30	95.67	95.57
Atoms per formula unit calculated on the basis of 11 O + 2(F, Cl, OH, O)				
Si	2.78	2.71	2.72	2.71
Al_{IV}	1.00	1.04	1.03	1.03
Al_{VI}	0.41	0.42	0.43	0.43
Fe^{3+}	0.39	0.40	0.40	0.42
Fe^{2+}	0.95	1.25	1.21	1.22
Mg	1.25	1.02	1.04	1.01
Ti	0.12	0.12	0.11	0.11
Mn	0.02	0.02	0.02	0.02
K	0.85	0.91	0.91	0.89
Na	0.03	0.01	0.02	0.01
Ba	0.00	0.01	0.01	0.01
Ca	0.01	0.00	0.00	0.00
F	0.00	0.00	0.02	0.00
Cl	0.01	0.01	0.00	0.01
OH	1.65	1.78	1.78	1.78
O^{2-}	0.34	0.21	0.20	0.22
Total (*apfu*)	9.82	9.90	9.89	9.86
Fe^{3+}/Fe_{tot}	0.29	0.24	0.25	0.25
Fe/Fe+Mg	0.516	0.617	0.607	0.618
Species[a]	annite	annite	annite	annite

[a] Species from Deer et al. (1992)

Table C-2 Electron microprobe analysis results for chlorite phases at the Fisher property analyzed at the University of Calgary.

Phase	C_1	C_1	C_1	C_1	C_1	C_1	C_1	C_1
Sample	CO-2019-55	CO-2019-55	CO-2019-55	CO-2019-55	CO-2019-55	CO-2019-55	CO-2019-61	CO-2019-61
Rock Type	HCrB	HCrB	HCrB	HCrB	HCrB	HCrB	LCrB	LCrB
SiO_2 (in wt%)	24.63	24.95	25.35	24.98	25.65	25.90	26.14	25.50
TiO_2	0.04	0.04	0.06	0.01	0.04	0.04	0.04	0.13
Al_2O_3	19.90	19.95	19.43	20.04	20.34	20.08	18.13	18.43
FeO	33.69	31.01	31.50	30.98	31.88	33.30	27.92	28.86
MnO	0.47	0.51	0.58	0.55	0.60	0.54	0.43	0.48
MgO	9.36	11.21	11.39	11.46	11.40	10.37	14.10	13.21
BaO	0.00	0.07	0.10	0.03	-	-	0.00	0.00
CaO	0.02	0.03	0.00	0.01	0.05	0.06	0.01	0.06
Na_2O	0.00	0.14	0.03	0.05	-	-	0.04	0.02
K_2O	0.03	0.11	0.04	0.04	-	-	0.12	0.22
F	0.00	0.03	0.08	0.00	-	-	0.04	0.00
Cl	0.02	0.06	0.01	0.02	-	-	0.03	0.03
(OH)	11.85	11.91	11.46	11.83	10.04	9.72	13.03	13.08
Total	88.16	88.11	88.58	88.18	89.96	90.28	87.00	86.93
Atoms per formula unit calculated on the basis of 28 oxygens								
Si	5.43	5.42	5.49	5.42	5.46	5.53	5.66	5.57
Ti	0.01	0.01	0.01	0.00	0.01	0.01	0.01	0.02
Al	5.17	5.11	4.96	5.13	5.10	5.05	4.62	4.74
Fe	6.21	5.64	5.70	5.62	5.68	5.94	5.05	5.27
Mn	0.09	0.09	0.11	0.10	0.11	0.10	0.08	0.09
Mg	3.07	3.63	3.68	3.71	3.62	3.30	4.55	4.30
Ba	0.00	0.01	0.01	0.00	-	-	0.00	0.00
Ca	0.00	0.01	0.00	0.00	0.01	0.01	0.00	0.01
Na	0.00	0.03	0.01	0.01	-	-	0.01	0.00
K	0.00	0.01	0.01	0.01	-	-	0.02	0.03
F	0.00	0.02	0.05	0.00	-	-	0.03	0.00
Cl	0.01	0.02	0.01	0.01	-	-	0.01	0.01
H	2.00	2.00	2.00	2.00	2.00	2.00	2.00	2.00
Total (*apfu*)	21.98	22.01	22.02	22.01	21.98	21.94	22.03	22.04
Al_{IV}	2.57	2.58	2.51	2.58	2.54	2.47	2.34	2.43
Al_{VI}	2.59	2.54	2.45	2.55	2.56	2.58	2.28	2.31
X_{Mg}	0.331	0.392	0.392	0.397	0.389	0.357	0.474	0.449
Species[a]	Fe-chlorite	Fe-chlorite	Fe-chlorite	Fe-chlorite	Fe-chlorite	Fe-chlorite	Fe-Mg chlorite	Fe-Mg chlorite

[a] Species from Zane and Weiss (1988)

Table C-2 Electron microprobe analysis results for chlorite phases at the Fisher property analyzed at the University of Calgary.

Phase	C_1	C_1	C_1	C_1	C_1	C_1	C_1	C_1	C_1	C_1
Sample	CO-2019-55	CO-2019-55	CO-2019-48	CO-2019-48	CO-2019-48	CO-2019-48	CO-2019-81B	CO-2019-81B	CO-2019-81B	CO-2019-81B
Rock Type	HCrB	HCrB	GRNT	GRNT	GRNT	GRNT	DIO	DIO	DIO	DIO
SiO_2 (in wt%)	25.66	25.84	29.03	29.98	29.71	30.72	26.62	26.59	26.49	26.35
TiO_2	0.05	0.08	0.00	0.00	0.00	0.01	0.04	0.05	0.06	0.02
Al_2O_3	19.65	20.02	14.65	15.46	15.08	15.08	19.89	20.34	20.15	20.81
FeO	32.48	30.44	37.51	38.30	37.38	38.22	30.13	30.98	31.75	33.21
MnO	0.54	0.58	0.17	0.16	0.17	0.17	0.63	0.53	0.55	0.57
MgO	11.02	12.03	6.50	6.98	6.85	6.89	12.02	11.76	10.56	9.91
BaO	-	-	-	-	-	-	-	-	-	-
CaO	0.02	0.03	0.20	0.20	0.19	0.20	0.02	0.01	0.05	0.01
Na_2O	-	-	-	-	-	-	-	-	-	-
K_2O	-	-	-	-	-	-	-	-	-	-
F	-	-	-	-	-	-	-	-	-	-
Cl	-	-	-	-	-	-	-	-	-	-
(OH)	10.59	11.00	11.94	8.91	10.63	8.71	10.66	9.74	10.39	9.14
Total	89.41	89.00	88.06	91.10	89.37	91.29	89.34	90.26	89.61	90.87
Atoms per formula unit calculated on the basis of 28 oxygens										
Si	5.52	5.52	6.48	6.45	6.51	6.58	5.64	5.59	5.64	5.57
Ti	0.01	0.01	0.00	0.00	0.00	0.00	0.01	0.01	0.01	0.00
Al	4.98	5.04	3.86	3.92	3.89	3.81	4.97	5.04	5.06	5.18
Fe	5.84	5.44	7.00	6.89	6.84	6.85	5.34	5.45	5.65	5.87
Mn	0.10	0.10	0.03	0.03	0.03	0.03	0.11	0.09	0.10	0.10
Mg	3.53	3.83	2.16	2.24	2.23	2.20	3.80	3.69	3.35	3.12
Ba	0.00	0.00	0.00	0.00	0.00	0.00	0.00	0.00	0.00	0.00
Ca	0.00	0.01	0.05	0.05	0.05	0.05	0.01	0.00	0.01	0.00
Na	-	-	-	-	-	-	-	-	-	-
K	-	-	-	-	-	-	-	-	-	-
F	-	-	-	-	-	-	-	-	-	-
Cl	-	-	-	-	-	-	-	-	-	-
H	2.00	2.00	2.00	2.00	2.00	2.00	2.00	2.00	2.00	2.00
Total (*apfu*)	21.98	21.95	21.59	21.59	21.55	21.51	21.87	21.88	21.82	21.84
Al_{IV}	2.48	2.48	1.52	1.55	1.49	1.42	2.36	2.41	2.36	2.43
Al_{VI}	2.50	2.56	2.34	2.38	2.40	2.39	2.61	2.64	2.70	2.75
X_{Mg}	0.377	0.413	0.236	0.245	0.246	0.243	0.416	0.404	0.372	0.347
Species[a]	Fe-chlorite	Fe-chlorite	Fe-chlorite	Fe-chlorite	Fe-chlorite	Fe-chlorite	Fe-chlorite	Fe-chlorite	Fe-chlorite	Fe-chlorite

[a] Species from Zane and Weiss (1988)

Table C-2 Electron microprobe analysis results for chlorite phases at the Fisher property analyzed at the University of Calgary.

Phase	C_1	C_1	C_2	C_2	C_2	C_2	C_2	C_2	C_2	C_2	C_2
Sample	CO-2019-81B	CO-2019-81B	CO-2019-55	CO-2019-55	CO-2019-61	CO-2019-69	CO-2019-69	CO-2019-48	CO-2019-48	CO-2019-48	CO-2019-4
Rock Type	DIO	DIO	HCrB	HCrB	LCrB	MetaSed	MetaSed	GRNT	GRNT	GRNT	GRNT
SiO_2 (in wt%)	26.46	26.25	28.34	28.26	31.31	32.53	31.92	25.02	25.33	25.06	25.35
TiO_2	0.08	0.07	0.57	0.60	0.00	0.00	0.02	0.12	0.10	0.12	0.07
Al_2O_3	20.52	20.91	15.38	15.10	15.45	15.35	15.27	20.41	20.38	20.90	20.83
FeO	32.75	33.62	39.41	39.56	32.61	34.36	33.37	40.07	39.85	39.56	38.74
MnO	0.57	0.59	0.28	0.25	0.53	0.45	0.46	0.47	0.50	0.40	0.39
MgO	10.27	9.89	4.71	4.60	6.77	6.94	6.47	3.69	4.19	4.32	4.85
BaO	-	-	0.11	0.06	-	-	-	-	-	-	-
CaO	0.02	0.01	0.04	0.08	0.66	0.62	0.65	0.01	0.01	0.01	0.04
Na_2O	-	-	0.06	0.07	-	-	-	-	-	-	-
K_2O	-	-	1.86	1.73	-	-	-	-	-	-	-
F	-	-	0.00	0.00	-	-	-	-	-	-	-
Cl	-	-	0.05	0.04	-	-	-	-	-	-	-
(OH)	9.33	8.66	9.20	9.67	12.67	9.75	11.86	10.22	9.63	9.63	9.73
Total	90.67	91.34	90.81	90.34	87.33	90.25	88.14	89.78	90.37	90.37	90.28
Atoms per formula unit calculated on the basis of 28 oxygens											
Si	5.59	5.53	6.28	6.30	6.82	6.88	6.90	5.57	5.59	5.52	5.56
Ti	0.01	0.01	0.09	0.10	0.00	0.00	0.00	0.02	0.02	0.02	0.01
Al	5.11	5.19	4.02	3.97	3.97	3.83	3.89	5.36	5.30	5.43	5.39
Fe	5.79	5.92	7.30	7.38	5.94	6.08	6.03	7.46	7.36	7.29	7.11
Mn	0.10	0.11	0.05	0.05	0.10	0.08	0.08	0.09	0.09	0.07	0.07
Mg	3.23	3.11	1.56	1.53	2.20	2.19	2.08	1.22	1.38	1.42	1.59
Ba	-	-	0.01	0.01	-	-	-	-	-	-	-
Ca	0.00	0.00	0.01	0.02	0.15	0.14	0.15	0.00	0.00	0.00	0.01
Na	-	-	0.01	0.01	-	-	-	-	-	-	-
K	-	-	0.26	0.25	-	-	-	-	-	-	-
F	-	-	0.00	0.00	-	-	-	-	-	-	-
Cl	-	-	0.02	0.01	-	-	-	-	-	-	-
H	2.00	2.00	2.00	2.00	2.00	2.00	2.00	2.00	2.00	2.00	2.00
Total (*apfu*)	21.84	21.87	21.62	21.62	21.19	21.20	21.15	21.73	21.74	21.75	21.73
Al_{IV}	2.41	2.47	1.72	1.70	1.18	1.12	1.10	2.43	2.41	2.48	2.44
Al_{VI}	2.70	2.72	2.30	2.27	2.79	2.71	2.79	2.93	2.89	2.95	2.95
X_{Mg}	0.359	0.344	0.176	0.172	0.270	0.265	0.257	0.141	0.158	0.163	0.182
Species[a]	Fe-chlorite	Fe-chlorite	Fe-chlorite	Fe-chlorite	Fe-chlorite	Fe-chlorite	Fe-chlorite	Fe-chlorite	Fe-chlorite	Fe-chlorite	Fe-chlorit

[a] Species from Zane and Weiss (1988)

Table C-3 Electron microprobe analysis results for titanites at the Fisher property analyzed at the University of Calgary.

Phase	T_1	T_1	T_1	T_1	T_1	T_2	T_2	T_2	T_2	T_2
Sample	CO-2019-93A	CO-2019-93A	CO-2019-93A	CO-2019-81B	CO-2019-81B	CO-2019-55	CO-2019-55	CO-2019-55	CO-2019-55	CO-2019-6
Rock Type	HCrB	HCrB	HCrB	DIO	DIO	HCrB	HCrB	HCrB	HCrB	LCrB
SiO_2 (wt.%)	30.60	30.41	30.64	30.83	30.70	30.78	30.71	30.86	30.70	31.06
TiO_2	34.30	34.72	34.84	37.31	36.69	36.08	36.08	36.51	37.46	36.55
Al_2O_3	2.96	2.78	2.70	1.49	1.84	2.48	2.45	2.22	1.83	2.61
FeO	1.36	1.28	1.27	0.67	0.63	0.89	0.95	0.77	0.68	0.47
CaO	29.35	29.31	29.41	28.99	29.19	29.45	29.45	29.57	29.26	29.41
V_2O_3	0.80	0.85	0.77	0.65	0.65	0.77	0.78	0.86	0.80	0.84
Total	99.37	99.35	99.63	99.93	99.70	100.45	100.41	100.79	100.74	100.95
Atoms per formula unit calculated on the basis of 5 oxygens										
Si	1.01	1.01	1.01	1.01	1.01	1.01	1.01	1.01	1.00	1.01
Ti	0.85	0.87	0.87	0.92	0.91	0.89	0.89	0.90	0.92	0.89
Al	0.12	0.11	0.10	0.06	0.07	0.10	0.09	0.09	0.07	0.10
Fe	0.04	0.04	0.04	0.02	0.02	0.02	0.03	0.02	0.02	0.01
Ca	1.04	1.04	1.04	1.02	1.03	1.03	1.03	1.03	1.02	1.02
V	0.01	0.01	0.01	0.01	0.01	0.01	0.01	0.01	0.01	0.01
Total (*apfu*)	3.07	3.07	3.07	3.04	3.05	3.06	3.06	3.05	3.04	3.05

Phase	T_2	T_2	T_2	T_2	T_3	T_3	T_3	T_3	T_3	T_3
Sample	CO-2019-61	CO-2019-61	CO-2019-81B	CO-2019-81B	CO-2019-61	CO-2019-61	CO-2019-61	CO-2019-61	CO-2019-93A	CO-2019-93.
Rock Type	LCrB	LCrB	DIO	DIO	LCrB	LCrB	LCrB	LCrB	HCrB	HCrB
SiO_2 (wt.%)	30.60	30.41	30.64	30.83	30.70	30.78	30.71	30.86	30.70	31.06
TiO_2	34.30	34.72	34.84	37.31	36.69	36.08	36.08	36.51	37.46	36.55
Al_2O_3	2.96	2.78	2.70	1.49	1.84	2.48	2.45	2.22	1.83	2.61
FeO	1.36	1.28	1.27	0.67	0.63	0.89	0.95	0.77	0.68	0.47
CaO	29.35	29.31	29.41	28.99	29.19	29.45	29.45	29.57	29.26	29.41
V_2O_3	0.80	0.85	0.77	0.65	0.65	0.77	0.78	0.86	0.80	0.84
Total	99.37	99.35	99.63	99.93	99.70	100.45	100.41	100.79	100.74	100.95
Atoms per formula unit calculated on the basis of 5 oxygens										
Si	1.01	1.01	1.01	1.01	1.01	1.01	1.01	1.01	1.00	1.01
Ti	0.85	0.87	0.87	0.92	0.91	0.89	0.89	0.90	0.92	0.89
Al	0.12	0.11	0.10	0.06	0.07	0.10	0.09	0.09	0.07	0.10
Fe	0.04	0.04	0.04	0.02	0.02	0.02	0.03	0.02	0.02	0.01
Ca	1.04	1.04	1.04	1.02	1.03	1.03	1.03	1.03	1.02	1.02
V	0.01	0.01	0.01	0.01	0.01	0.01	0.01	0.01	0.01	0.01
Total (*apfu*)	3.07	3.07	3.07	3.04	3.05	3.06	3.06	3.05	3.04	3.05

Table C-4 Electron microprobe analysis results for calcite phases at the Fisher property analyzed at the University of Calgary.

Phase	Cal_1	Cal_1	Cal_1	Cal_1	Cal_1	Cal_1	Cal_1
Sample	CO-2019-55	CO-2019-55	CO-2019-55	CO-2019-55	CO-2019-55	CO-2019-55	CO-2019-48
Rock Type	HCrB	HCrB	HCrB	HCrB	HCrB	HCrB	GRNT
CO_2 (wt.%)	44.28	43.67	44.38	43.84	44.52	44.33	46.78
FeO	0.73	0.68	1.09	1.02	1.44	0.72	0.40
MnO	0.35	0.31	0.37	0.33	0.49	0.40	0.42
MgO	0.00	0.00	0.00	0.00	0.00	0.00	0.38
CaO	54.64	55.34	54.16	54.81	53.55	54.56	52.02
Total	100.00	100.00	100.00	100.00	100.00	100.00	100.00
Atoms per formula unit calculated on the basis of 3 oxygens							
C	1.51	1.50	1.51	1.50	1.51	1.51	1.54
Fe	0.01	0.01	0.01	0.01	0.02	0.01	0.00
Mn	0.00	0.00	0.00	0.00	0.01	0.00	0.00
Mg	0.00	0.00	0.00	0.00	0.00	0.00	0.01
Ca	0.73	0.74	0.72	0.74	0.71	0.73	0.67
Total (*apfu*)	2.25	2.25	2.25	2.25	2.24	2.25	2.23

Phase	Cal_1	Cal_2	Cal_2	Cal_2	Cal_2	Cal_2	Cal_2
Sample	CO-2019-48	CO-2019-55	CO-2019-55	CO-2019-55	CO-2019-61	CO-2019-61	CO-2019-81B
Rock Type	GRNT	HCrB	HCrB	HCrB	LCrB	LCrB	DIO
CO_2 (wt.%)	46.63	45.22	45.17	45.25	43.95	44.84	45.01
FeO	0.23	1.02	0.89	0.89	0.11	0.20	0.47
MnO	0.40	0.41	0.31	0.43	0.34	0.51	0.64
MgO	0.21	0.00	0.00	0.00	0.04	0.06	0.18
CaO	52.54	53.36	53.64	53.43	55.57	54.40	53.70
Total	100.00	100.00	100.00	100.00	100.00	100.00	100.00
Atoms per formula unit calculated on the basis of 3 oxygens							
C	1.54	1.52	1.52	1.52	1.50	1.51	1.52
Fe	0.00	0.01	0.01	0.01	0.00	0.00	0.00
Mn	0.00	0.00	0.00	0.00	0.00	0.01	0.01
Mg	0.00	0.00	0.00	0.00	0.00	0.00	0.00
Ca	0.68	0.70	0.71	0.70	0.74	0.72	0.71
Total (*apfu*)	2.23	2.24	2.24	2.24	2.25	2.24	2.24

Table C-4 Electron microprobe analysis results for calcite phases at the Fisher property analyzed at the University of Calgary.

Phase	Cal_2	Cal_2	Cal_2	Cal_2	Cal_2	Cal_2	Cal_2	Cal_2
Sample	CO-2019-81B	CO-2019-81B	CO-2019-69	CO-2019-69	CO-2019-69	CO-2019-93A	CO-2019-93A	CO-2019-93A
Rock Type	DIO	DIO	MetaSed	MetaSed	MetaSed	HCrB	HCrB	HCrB
CO_2 (wt.%)	43.75	43.88	44.98	44.06	44.35	44.48	43.61	43.79
FeO	0.05	0.05	0.95	0.92	0.86	0.17	0.17	0.12
MnO	0.50	0.64	1.15	1.20	1.22	0.52	0.48	0.56
MgO	0.06	0.02	0.62	0.63	0.56	0.14	0.15	0.13
CaO	55.64	55.42	52.30	53.19	53.01	54.70	55.60	55.40
Total	100.00	100.00	100.00	100.00	100.00	100.00	100.00	100.00
Atoms per formula unit calculated on the basis of 3 oxygens								
C	1.50	1.50	1.52	1.50	1.51	1.51	1.50	1.50
Fe	0.00	0.00	0.01	0.01	0.01	0.00	0.00	0.00
Mn	0.01	0.01	0.01	0.01	0.01	0.01	0.01	0.01
Mg	0.00	0.00	0.01	0.01	0.01	0.00	0.00	0.00
Ca	0.75	0.74	0.69	0.71	0.71	0.73	0.75	0.74
Total (*apfu*)	2.25	2.25	2.24	2.25	2.25	2.25	2.25	2.25

Table C-5 Electron microprobe analysis results for epidote-group minerals at the Fisher property analyzed at the University of Calgary.

Phase	Ep_1	Ep_1	Ep_1	Ep_1	Ep_1	Ep_1	Ep_1	Ep_1	Ep_2	Ep_2	Ep_2
Sample	CO-2019-61	CO-2019-61	CO-2019-61	CO-2019-81B	CO-2019-81B	CO-2019-69	CO-2019-69	CO-2019-93A	CO-2019-61	CO-2019-61	CO-2019-61
Rock Type	LCrB	LCrB	LCrB	DIO	DIO	MetaSed	MetaSed	HCrB	LCrB	LCrB	LCrB
SiO_2 (wt.%)	38.13	38.27	38.07	38.26	37.88	39.81	40.37	36.36	38.41	38.41	38.45
TiO_2	0.02	0.13	0.03	0.00	0.05	1.33	1.35	0.13	0.01	0.01	0.00
Al_2O_3	23.06	23.20	23.49	23.42	23.04	21.76	21.92	18.84	23.60	23.87	23.95
Fe_2O_3	13.20	12.62	12.05	12.57	13.02	5.65	6.06	17.00	12.27	11.51	11.75
MnO	0.23	0.35	0.18	0.38	0.31	0.04	0.07	0.53	0.37	0.19	0.22
CaO	23.73	23.19	23.49	23.33	22.97	22.11	22.26	21.81	23.59	23.97	23.81
Total	98.38	97.75	97.31	97.96	97.26	90.70	92.03	94.67	98.25	97.95	98.18
Atoms per formula unit calculated on the basis of 12.5 oxygens											
Si	3.02	3.04	3.04	3.04	3.03	3.31	3.31	3.05	3.04	3.04	3.04
Ti	0.00	0.01	0.00	0.00	0.00	0.08	0.08	0.01	0.00	0.00	0.00
Al	2.16	2.17	2.21	2.19	2.17	2.13	2.12	1.86	2.20	2.23	2.23
Fe	0.79	0.76	0.72	0.75	0.78	0.35	0.37	1.07	0.73	0.69	0.70
Mn	0.02	0.02	0.01	0.03	0.02	0.00	0.01	0.04	0.02	0.01	0.01
Ca	2.02	1.98	2.01	1.99	1.97	1.97	1.96	1.96	2.00	2.03	2.02
H	1.00	1.00	1.00	1.00	1.00	1.00	1.00	1.00	1.00	1.00	1.00
Total (*apfu*)	9.00	8.98	8.99	8.99	8.98	8.86	8.86	8.98	8.99	9.00	9.00
Species[a]	clnz	clnz	clnz	clnz	clnz	clnz	clnz	clnz	clnz	clnz	clnz

"clnz" = Clinozoisite

[a] Species from Armbruster et al. (2006)

Table C-6 Electron microprobe analysis results for pyroxenes at the Fisher property analyzed at the University of Calgary.

Phase	pyroxene	pyroxene	pyroxene	pyroxene
Sample	CO-2019-61	CO-2019-61	CO-2019-61	CO-2019-61
Rock Type	LCrB	LCrB	LCrB	LCrB
SiO_2 (in wt%)	51.24	51.36	50.99	51.55
TiO_2	0.00	0.01	0.04	0.02
Al_2O_3	0.55	0.54	0.88	0.91
Cr_2O_3	0.02	0.00	0.00	0.00
FeO	14.31	14.09	13.40	14.44
MnO	1.03	1.00	0.90	0.91
MgO	9.36	9.32	9.66	9.32
CaO	23.54	23.74	23.54	23.71
Na2O	0.27	0.28	0.32	0.28
Total	100.32	100.34	99.72	101.13
Atoms per formula unit calculated on the basis of 6 oxygens				
Si	1.96	1.97	1.96	1.96
Ti	0.00	0.00	0.00	0.00
Al	0.02	0.02	0.04	0.04
Fe^{3+}	0.07	0.06	0.07	0.06
Cr^{3+}	0.001	0.000	0.000	0.000
Fe^{2+}	0.39	0.39	0.36	0.40
Mn	0.03	0.03	0.03	0.03
Mg	0.53	0.53	0.55	0.53
Ca	0.97	0.97	0.97	0.96
Na	0.02	0.02	0.02	0.02
Total (*apfu*)	4.00	4.00	4.00	4.00
Wo	51	51	51	51
En	28	28	29	28
Fs	21	20	19	21
Species[a]	diopside	diopside	diopside	diopside

[a] Species from Morimoto (1988)

Table C-7 Electron microprobe analysis results for amphiboles at the Fisher property analyzed at the University of Saskatchewan.

Phase	amphibole	amphibole	amphibole	amphibole	amphibole	amphibole	amphibole	amphibole	amphibole	amphibole
Sample	CO-2019-33	CO-2019-33	CO-2019-33	CO-2019-33	CO-2019-33	CO-2019-33	CO-2019-33	CO-2019-33	CO-2019-33	CO-2019-33
Rock Type	PYRX	PYRX	PYRX	PYRX	PYRX	PYRX	PYRX	PYRX	PYRX	PYRX
SiO_2 (in wt%)	51.71	51.36	46.68	46.00	51.78	42.18	51.01	47.80	55.03	46.21
TiO_2	0.18	0.30	0.18	0.43	0.03	0.57	0.20	0.48	0.00	0.53
Al_2O_3	5.55	7.28	4.74	8.61	1.11	12.00	4.85	11.79	0.91	13.85
Cr_2O_3	0.06	0.09	0.04	0.02	0.05	0.02	0.00	0.00	0.02	0.03
FeO	15.84	15.06	15.52	13.72	18.13	11.74	16.37	13.49	17.63	12.73
MnO	0.32	0.31	0.38	0.22	0.46	0.17	0.35	0.19	0.47	0.18
MgO	16.99	15.67	16.94	15.06	20.58	12.11	17.43	13.29	20.74	12.07
CaO	4.82	6.07	4.58	8.66	0.49	11.24	4.56	9.41	0.00	10.67
Na_2O	0.69	0.82	0.63	1.12	0.10	1.55	0.64	1.48	0.07	1.81
K_2O	0.04	0.07	0.06	0.13	0.01	0.11	0.09	0.12	0.01	0.17
Cl	0.02	0.01	0.02	0.02	0.02	0.03	0.02	0.02	0.00	0.02
Total	96.22	97.02	89.78	94.00	92.76	91.73	95.50	98.07	94.88	98.28
Atoms per formula unit calculated on the basis of 23 oxygens										
Si	7.51	7.40	7.35	6.94	7.81	6.55	7.50	6.87	8.02	6.65
Ti	0.02	0.03	0.02	0.05	0.00	0.07	0.02	0.05	0.00	0.06
Al	0.95	1.24	0.88	1.53	0.20	2.20	0.84	2.00	0.16	2.35
Cr^{3+}	0.01	0.01	0.01	0.00	0.01	0.00	0.00	0.00	0.00	0.00
Fe^{2+}	1.92	1.81	2.04	1.73	2.29	1.52	2.01	1.62	2.15	1.53
Mn	0.04	0.04	0.05	0.03	0.06	0.02	0.04	0.02	0.06	0.02
Mg	3.68	3.36	3.97	3.39	4.63	2.80	3.82	2.85	4.51	2.59
Ca	0.75	0.94	0.77	1.40	0.08	1.87	0.72	1.45	0.00	1.65
Na	0.19	0.23	0.19	0.33	0.03	0.47	0.18	0.41	0.02	0.51
K	0.01	0.01	0.01	0.03	0.00	0.02	0.02	0.02	0.00	0.03
H	2.00	2.00	2.00	2.00	2.00	2.00	2.00	2.00	2.00	2.00
Total (*apfu*)	17.09	17.07	17.29	17.42	17.10	17.53	17.16	17.30	16.91	17.38
Al^{IV}	0.49	0.60	0.65	1.06	0.19	1.45	0.50	1.13	-0.02	1.35
Al^{VI}	0.46	0.63	0.22	0.47	0.01	0.75	0.34	0.87	0.18	1.00
X_{Mg}	0.657	0.650	0.661	0.662	0.669	0.648	0.655	0.637	0.677	0.628
Species[a]	cum	mghbl	cum	mghbl	cum	mghbl	cum	mghbl	cum	mghbl

"cum" = Cummingtonite, "mghbl" = Magnesiohornblende

[a] Species from Leake et al. (1997)

Table C-7 Electron microprobe analysis results for amphiboles at the Fisher property analyzed at the University of Saskatchewan.

Phase	amphibole	amphibole	amphibole	amphibole	amphibole	amphibole	amphibole	amphibole	amphibole
Sample	CO-2019-33	CO-2019-33	CO-2019-33	CO-2019-33	CO-2019-28A2	CO-2019-28A2	CO-2019-28A2	CO-2019-28A2	CO-2019-28A
Rock Type	PYRX	PYRX	PYRX	PYRX	HCrB	HCrB	HCrB	HCrB	HCrB
SiO_2 (in wt%)	44.45	48.00	47.39	47.15	44.01	42.24	44.94	45.63	44.66
TiO_2	0.54	0.41	0.42	0.40	0.61	0.53	0.00	0.53	0.63
Al_2O_3	14.30	10.38	11.16	10.99	10.50	9.25	11.67	9.58	11.39
Cr_2O_3	0.06	0.06	0.07	0.00	0.00	0.03	0.14	0.05	0.02
FeO	12.54	13.07	13.66	13.90	16.81	17.28	16.51	15.57	16.26
MnO	0.18	0.22	0.17	0.28	0.26	0.31	0.30	0.35	0.35
MgO	11.65	14.56	13.93	14.05	10.46	10.83	9.86	11.02	10.85
CaO	10.76	9.04	9.22	9.04	12.15	12.34	12.20	12.02	12.00
Na_2O	1.96	1.23	1.41	1.35	0.93	0.79	0.94	0.90	1.06
K_2O	0.15	0.13	0.12	0.10	1.18	0.91	1.23	0.36	0.48
Cl	0.03	0.02	0.02	0.03	0.05	0.04	0.00	0.03	0.04
Total	96.61	97.11	97.56	97.30	96.98	96.53	97.70	96.03	97.73
Atoms per formula unit calculated on the basis of 23 oxygens									
Si	6.53	6.95	6.86	6.86	7.51	7.40	7.35	6.94	7.81
Ti	0.06	0.04	0.05	0.04	0.02	0.03	0.02	0.05	0.00
Al	2.48	1.77	1.90	1.88	0.95	1.24	0.88	1.53	0.20
Cr^{3+}	0.01	0.01	0.01	0.00	0.01	0.01	0.01	0.00	0.01
Fe^{2+}	1.54	1.58	1.65	1.69	1.92	1.81	2.04	1.73	2.29
Mn	0.02	0.03	0.02	0.03	0.04	0.04	0.05	0.03	0.06
Mg	2.55	3.14	3.01	3.05	3.68	3.36	3.97	3.39	4.63
Ca	1.69	1.40	1.43	1.41	0.75	0.94	0.77	1.40	0.08
Na	0.56	0.34	0.40	0.38	0.19	0.23	0.19	0.33	0.03
K	0.03	0.02	0.02	0.02	0.01	0.01	0.01	0.03	0.00
H	2.00	2.00	2.00	2.00	2.00	2.00	2.00	2.00	2.00
Total (*apfu*)	17.46	17.30	17.35	17.36	17.09	17.07	17.29	17.42	17.10
Al^{IV}	1.47	1.05	1.14	1.14	0.49	0.60	0.65	1.06	0.19
Al^{VI}	1.00	0.72	0.76	0.74	0.46	0.63	0.22	0.47	0.01
X_{Mg}	0.623	0.665	0.645	0.643	0.657	0.650	0.661	0.662	0.669
Species[a]	mghbl	mghbl	mghbl	mghbl	cum	mghbl	cum	mghbl	cum

"cum" = Cummingtonite, "mghbl" = Magnesiohornblende

[a] Species from Leake et al. (1997)

Table C-7 Electron microprobe analysis results for amphiboles at the Fisher property analyzed at the University of Saskatchewan.

Phase	amphibole	amphibole	amphibole	amphibole	amphibole	amphibole	amphibole	amphibole	amphibole
Sample	CO-2019-28A2	CO-2019-28A2	CO-2019-28A2	CO-2019-19	CO-2019-19	CO-2019-19	CO-2019-19	CO-2019-34	CO-2019-34
Rock Type	HCrB	HCrB	HCrB	AND2	AND2	AND2	AND2	HCrB	HCrB
SiO_2 (in wt%)	45.73	46.54	45.91	45.32	45.71	45.38	45.33	45.42	50.08
TiO_2	0.55	0.11	0.55	0.74	0.65	0.62	0.61	0.69	0.43
Al_2O_3	10.17	10.64	10.75	9.97	9.06	8.96	8.77	10.65	8.15
Cr_2O_3	0.01	0.08	0.03	0.00	0.09	0.09	0.09	0.07	0.02
FeO	15.60	14.92	16.09	17.33	17.09	16.75	17.09	15.55	13.97
MnO	0.32	0.35	0.32	0.58	0.73	0.66	0.67	0.24	0.28
MgO	11.62	11.04	9.94	9.72	10.12	10.40	9.72	10.46	12.45
CaO	12.06	12.32	12.13	11.77	11.73	11.65	11.71	12.09	12.21
Na_2O	0.93	0.95	0.99	1.14	1.10	1.20	1.09	0.95	0.69
K_2O	0.38	0.33	0.41	1.04	0.91	0.89	0.85	1.07	0.68
Cl	0.03	0.03	0.03	0.05	0.04	0.03	0.04	0.05	0.03
Total	97.41	97.31	97.15	97.66	97.23	96.63	95.96	97.24	98.99
Atoms per formula unit calculated on the basis of 23 oxygens									
Si	6.55	6.79	6.84	6.80	6.88	6.87	6.92	6.78	7.20
Ti	0.07	0.06	0.06	0.08	0.07	0.07	0.07	0.08	0.05
Al	2.20	1.78	1.89	1.76	1.61	1.60	1.58	1.87	1.38
Cr^{3+}	0.00	0.00	0.00	0.00	0.01	0.01	0.01	0.01	0.00
Fe^{2+}	1.52	1.94	2.00	2.18	2.15	2.12	2.18	1.94	1.68
Mn	0.02	0.04	0.04	0.07	0.09	0.08	0.09	0.03	0.03
Mg	2.80	2.57	2.21	2.17	2.27	2.35	2.21	2.33	2.67
Ca	1.87	1.92	1.94	1.89	1.89	1.89	1.92	1.93	1.88
Na	0.47	0.27	0.29	0.33	0.32	0.35	0.32	0.27	0.19
K	0.02	0.07	0.08	0.20	0.18	0.17	0.17	0.20	0.12
H	2.00	2.00	2.00	2.00	2.00	2.00	2.00	2.00	2.00
Total (*apfu*)	17.53	17.43	17.34	17.50	17.48	17.52	17.46	17.44	17.22
Al^{IV}	1.45	1.21	1.16	1.20	1.12	1.13	1.08	1.22	0.80
Al^{VI}	0.75	0.56	0.72	0.57	0.49	0.47	0.50	0.65	0.58
X_{Mg}	0.648	0.570	0.524	0.500	0.514	0.525	0.503	0.545	0.614
Species[a]	mghbl	mghbl	mghbl	eden	mghbl	eden	mghbl	mghbl	mghbl

"mghbl" = Magnesiohornblende, "eden" = edenite

[a] Species from Leake et al. (1997)

Table C-8 Electron microprobe analysis results for chlorites at the Fisher property analyzed at the University of Saskatchewan.

Phase	chlorite	chlorite	chlorite	chlorite	chlorite	chlorite	chlorite
Sample	CO-2019-28A2	CO-2019-28A2	CO-2019-28A2	CO-2019-28A2	CO-2019-33	CO-2019-33	CO-2019-34
Rock Type	HCrB	HCrB	HCrB	AND2	AND2	AND2	HCrB
SiO_2 (in wt%)	27.52	25.14	23.99	25.64	25.30	29.13	26.57
TiO_2	0.01	0.05	0.08	0.09	0.34	0.08	0.08
Al_2O_3	19.66	18.08	17.73	19.79	20.75	21.20	19.49
Cr_2O_3	0.02	0.06	0.03	0.03	0.05	0.04	0.02
FeO	23.03	38.89	38.33	26.44	12.32	13.75	22.46
MnO	0.29	0.20	0.18	0.16	0.05	0.05	0.21
MgO	15.99	4.58	4.89	13.27	21.62	23.44	17.17
CaO	0.00	0.06	0.27	0.41	0.03	0.03	0.07
Na_2O	0.00	0.00	0.03	0.04	0.13	0.02	0.00
K_2O	0.00	0.01	0.00	0.02	0.70	0.03	0.04
Cl	0.00	0.03	0.02	0.02	0.06	0.01	0.01
Total	86.51	87.10	85.55	85.91	81.37	87.78	86.10
Atoms per formula unit calculated on the basis of 28 oxygens							
Si	5.79	5.77	5.63	5.57	5.42	5.73	5.62
Ti	0.00	0.01	0.01	0.01	0.06	0.01	0.01
Al	4.87	4.89	4.91	5.07	5.23	4.91	4.86
Fe^{3+}	0.00	0.00	0.00	0.00	0.00	0.00	0.00
Fe^{2+}	4.05	7.47	7.53	4.80	2.21	2.26	3.97
Mn	0.05	0.04	0.04	0.03	0.01	0.01	0.04
Mg	5.01	1.57	1.71	4.30	6.90	6.87	5.41
Ca	0.00	0.02	0.07	0.10	0.01	0.01	0.02
Na	0.00	0.00	0.01	0.02	0.06	0.01	0.00
Cr^{3+}	0.00	0.01	0.00	0.00	0.12	0.00	0.01
K	0.00	0.00	0.00	0.00	0.00	0.00	0.00
H	2.00	2.00	2.00	2.00	2.00	2.00	2.00
Total (*apfu*)	21.78	21.78	21.91	21.89	22.00	21.81	21.94
Al^{IV}	2.21	2.23	2.37	2.43	2.58	2.27	2.38
Al^{VI}	2.64	2.24	2.52	2.62	2.62	2.62	2.47
X_{Mg}	0.553	0.174	0.185	0.472	0.758	0.752	0.577
Species[a]	Fe-Mg chlorite	Fe-chlorite	Fe-chlorite	Fe-Mg chlorite	Mg-chlorite	Mg-chlorite	Fe-Mg chlorite

[a] Species from Zane and Weiss (1988)

Table C-9 Electron microprobe analysis results for feldspars at the Fisher property analyzed at the University of Saskatchewan.

Phase	feldspar	feldspar	feldspar	feldspar	feldspar
Sample	CO-2019-33	CO-2019-19	CO-2019-19	CO-2019-28A2	CO-2019-34
Rock Type	PYRX	AND2	AND2	HCrB	HCrB
SiO_2 (in wt%)	58.83	61.73	61.20	61.03	54.80
TiO_2	0.00	0.01	0.00	0.00	0.02
Al_2O_3	26.50	24.92	24.95	24.69	28.94
Cr_2O_3	0.01	0.05	0.00	0.00	0.00
FeO	0.17	0.08	0.06	0.14	0.10
MnO	0.01	0.00	0.02	0.05	0.01
MgO	0.02	0.00	0.00	0.00	0.00
CaO	8.73	5.87	6.02	6.50	11.94
Na_2O	6.24	7.85	8.05	7.85	4.70
K_2O	0.05	0.22	0.12	0.09	0.10
Cl	0.01	0.00	0.00	0.00	0.00
Total	100.57	100.74	100.41	100.36	100.62
Atoms per formula unit calculated on the basis of 8 oxygens					
Si	2.63	2.73	2.71	2.71	2.47
Ti	0.00	0.00	0.00	0.00	0.00
Al	1.40	1.30	1.30	1.29	1.54
Cr^{3+}	0.00	0.00	0.00	0.00	0.00
Fe^{2+}	0.01	0.00	0.00	0.01	0.00
Mn	0.00	0.00	0.00	0.00	0.00
Mg	0.00	0.00	0.00	0.00	0.00
Ca	0.42	0.28	0.29	0.31	0.58
Ba	0.00	0.00	0.00	0.00	0.00
Na	0.54	0.67	0.69	0.68	0.41
K	0.00	0.01	0.01	0.00	0.01
Total (*apfu*)	5.00	5.00	5.00	5.00	5.00
An (mol %)	43.47	28.86	29.04	31.24	58.05
Ab	56.23	69.85	70.28	68.27	41.35
Or	0.29	1.28	0.68	0.49	0.60
Species[a]	andesine	oligoclase-andesine	oligoclase-andesine	oligoclase-andesine	labradorite

[a] Species from Deer, Howie and Zussman (1992)

Table C-10 Electron microprobe analysis results for titanites at the Fisher property analyzed at the University of Saskatchewan.

Phase	Titanite	Titanite	Titanite	Titanite	Titanite	Titanite	Titanite
Sample	CO-2019-28A2	CO-2019-28A2	CO-2019-28A2	CO-2019-28A2	CO-2019-19	CO-2019-34	CO-2019-34
Rock Type	HCrB	HCrB	HCrB	HCrB	AND2	HCrB	HCrB
SiO_2 (wt.%)	30.60	30.41	30.64	30.83	30.70	30.78	30.71
TiO_2	34.30	34.72	34.84	37.31	36.69	36.08	36.08
Al_2O_3	2.96	2.78	2.70	1.49	1.84	2.48	2.45
FeO	1.36	1.28	1.27	0.67	0.63	0.89	0.95
CaO	29.35	29.31	29.41	28.99	29.19	29.45	29.45
V_2O_3	0.80	0.85	0.77	0.65	0.65	0.77	0.78
Total	99.37	99.35	99.63	99.93	99.70	100.45	100.41
Atoms per formula unit calculated on the basis of 5 oxygens							
Si	1.02	1.11	1.03	1.02	1.04	1.00	1.01
Ti	0.94	0.83	0.93	0.95	0.93	0.97	0.96
Al	0.05	0.04	0.04	0.03	0.05	0.04	0.03
Cr	0.00	0.00	0.00	0.00	0.00	0.00	0.00
Fe^{+2}	0.02	0.02	0.02	0.02	0.00	0.01	0.01
Mn	0.00	0.00	0.00	0.00	0.00	0.00	0.00
Mg	0.00	0.00	0.00	0.00	0.00	0.00	0.00
Ca	0.97	1.04	0.99	0.99	0.99	0.98	0.99
Na	0.00	0.00	0.00	0.00	0.00	0.00	0.00
K	0.00	0.00	0.00	0.00	0.00	0.00	0.00
Total (*apfu*)	3.02	3.04	3.02	3.01	3.01	3.00	3.01